Proceedings of the OHP2013 colloquium

# Improving the performances of current optical interferometers & future designs

**23-27 September 2013**

**Edited by** L. Arnold, H. Le Coroller, J. Surdej
Observatoire de Haute-Provence - UMS Pythéas

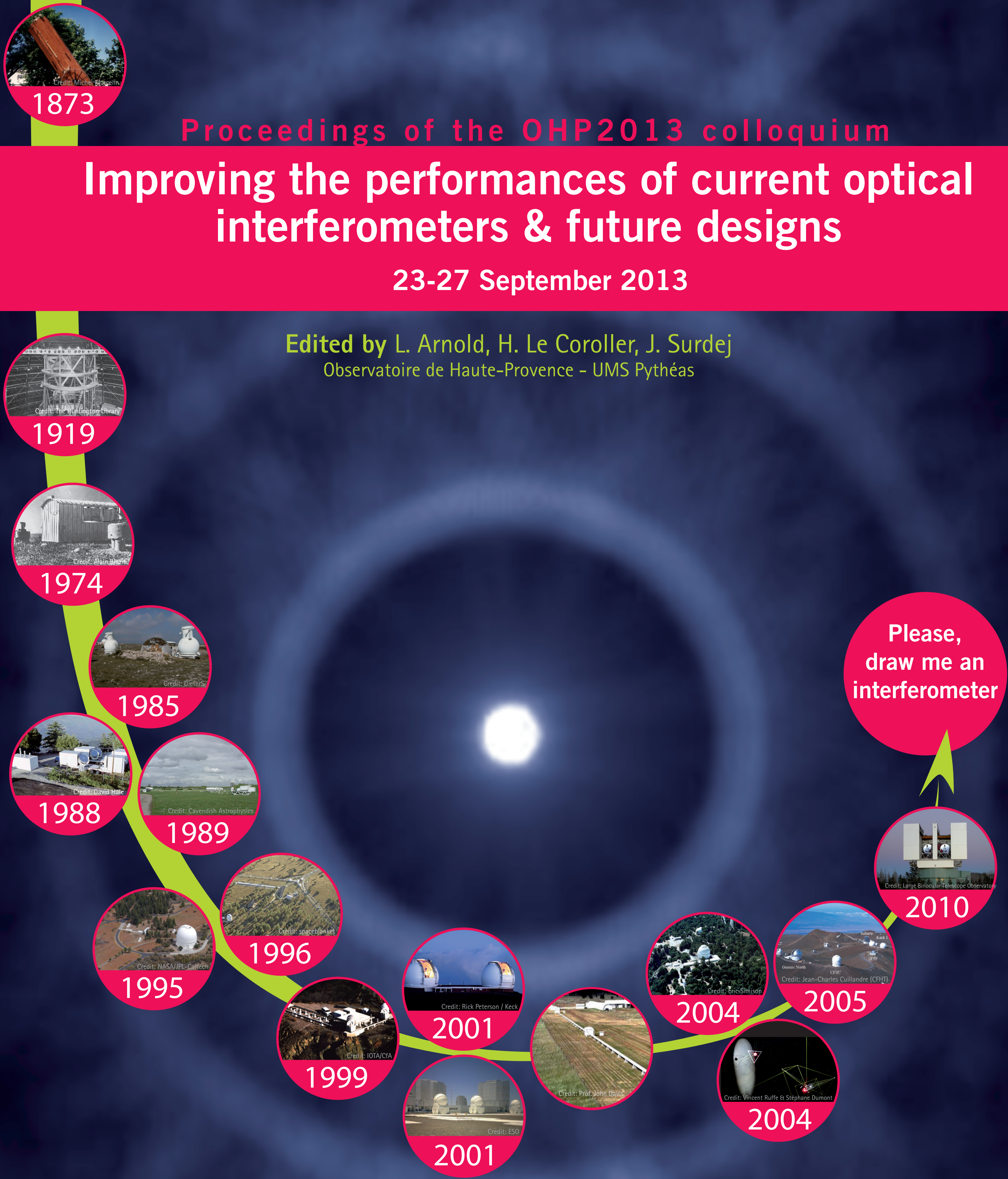


http://www.obs-hp.fr/~hlecorol/workshopOHP/

Unité Mixte de Service PYTHEAS
Provence-Alpes-Côte d'Azur
ASHRA Action Spécifique Haute Résolution Angulaire
Aix-Marseille université
optitec
GRAM
CONSEIL GÉNÉRAL ALPES DE HAUTE-PROVENCE
IAU C54 Endorsed

# Abstract

The number of astrophysical studies making use of interferometers has steadily increased during the past 15 years. Nevertheless, the performances of interferometers are still limited: their sensitivity does not exceed magnitude V=12, and their imaging capability could yet be improved by increasing the number of telescopes/sub-apertures. In the context of the ELTs, it is not certain how future interferometry projects will be financed. However, interferometry remains the only way to observe compact astrophysical objects at very high angular resolution (< milliarcsecond), like gravitational micro-lensing events, central engines of AGNs, proto-planetary disks, exoplanets, etc. The aim of this workshop was to review and discuss the development of technologies that could improve the performances of current and future interferometers: new optical designs; techniques to improve the accuracy of measurements (visibility, closure-phase, etc.); progress on delay-line performances; solutions without delay-lines; technologies for larger apertures at lower cost (ex: lightweight replica mirrors); optimized beam combiners (integrated optic, pupil densifier, etc.); fringe tracking systems; laser telemetry applied to interferometry; heterodyne interferometry; progress in heterodyne detection using new technologies (laser comb, time propagation technologies, etc.); progress in image reconstruction techniques; progress in nulling interferometry; and important science cases that could benefit from progress in interferometry (report of observations at the limit of current interferometers). Nearly 50 oral presentations have been delivered, followed by very lively discussions which eventually emerged with the proposition to organize the *Planet Formation Interferometer/Imager* (PFI) project. The present proceedings reflect most of the highlights of this international colloquium.

Happy terrestrial interferometrists... OHP, 27 september 2013.

## Table of contents

A roundtable with the EII/ASHRA/Interferometry Forum groups was organized that evening by Jean Surdej. The main elements of this discussion are given in the colloquium recommendations at the end of this volume, p. 277.

## Foreword

The main motivation in organizing the international colloquium entitled *Improving the performances of current optical interferometers & future designs* at the Haute-Provence Observatory (France) on 23-27 September 2013, comes from the obvious fact that the performances of present day interferometers are still very limited: their sensitivity does not go beyond the magnitude V=12, and their imaging capability could yet be improved by increasing the number of telescopes/sub-apertures. Many interesting astrophysical objects remain out of reach. Moreover, in the context of the ELTs, it is not certain how future interferometry projects will be financed. However, interferometry remains the only way to observe compact astrophysical objects with a very high angular resolution (< milliarcsecond). High angular resolution should still improve, for quite some time, our knowledge on the detailed content of the Universe, for example by imaging and characterizing proto-planetary disks, exo-planets, the central engines of AGN, etc.

The main goal of this international colloquium was to discuss the following key points for future interferometers:
⋆ new optical designs,
⋆ techniques to improve the accuracy of the measurements (visibility, closure-phases, etc.),
⋆ progress on delay-line performances,
⋆ solutions without delay-lines,
⋆ technologies that could allow larger apertures at lower cost (ex: lightweight replica mirrors),
⋆ optimized beam combiners (integrated optics, temporal hypertelescope, pupil densifier, etc.),
⋆ fringe tracking systems,
⋆ laser telemetry applied to interferometry,
⋆ heterodyne interferometry,
⋆ discussion on how to improve the performances of the heterodyne detection using new technologies (laser comb, time propagation technologies, etc.),
⋆ progress in image reconstruction techniques (strategy about the ideal UV coverage depending on the observed astrophysical objects, etc.),
⋆ progress in the field of nulling interferometry,
⋆ important science cases that could benefit from progress in interferometry (report of observations at the limit of the performances of the present systems).

The main topics covered during this colloquium were organized in nine sessions as follows:
⋆ Session 1. Science and Technology context
⋆ Session 2. Current Interferometers and future development for these facilities
⋆ Session 3. Poster Session
⋆ Session 4. Optimized beam combiners for present and future interferometers

⋆ Session 5. Discussion on the future of interferometry
⋆ Session 6. Unique science and technologies that will allow to design future interferometers with extremely high performances
⋆ Session 7. Metrology and astrometry with extremely high accuracy
⋆ Session 8. Problems related to the sensitivity of interferometers and quality of the observables in interferometry
⋆ Session 9. Progress in data reduction and image reconstruction techniques

The members of the Scientific Organizing Committee included: Hervé Le Coroller (OHP/Pytheas, France, Chair), Fabien Malbet (IPAG, France, Co-Chair), Jean-Philippe Berger (ESO, Chili), Olivier Chesneau (Lagrange, Observatoire de la Côte d'Azur, France), Michel Lintz (ARTEMIS, Observatoire de la Côte d'Azur, France), Bertrand Mennesson (JPL, California, USA), John Monnier (University of Michigan, USA), Guillaume Montagnier (OHP, France), Claire Moutou (LAM, France), Jörg-Uwe Pott (Max-Planck Institut, Heidelberg, Germany), Jean Surdej (Université de Liège, Belgium), and Gerard Van Belle (Lowell Observatory, USA). The Local Organizing Committee was composed of members from the Haute-Provence Observatory: Luc Arnold, Thierry Botti, Nathalie Bressand, Nathalie Desmons, Mélody Didier, Anne-Marie Galliano, Andrée Laloge, Hervé Le Coroller (Chair), Guillaume Montagnier and Jean-Paul Payan.

A large number of astronomers and engineers (around 50) from all over the world (13 countries) took active part in this meeting. Nearly 50 oral presentations have been delivered, followed by very lively discussions which eventually emerged with the proposition to organize the "Planet Formation Interferometer/Imager" (PFI) project. Stimulating general conclusions were also given by Jörg-Uwe Pott. All these presentations are accessible in the form of pdf and video files via the link:
http://interferometer.osupytheas.fr/index.php?page=OHP2013.

The present proceedings reflect most of the highlights of the colloquium. It is our pleasure to thank the members of the SOC, of the LOC and colleagues from the Haute-Provence Observatory in general for having participated to the very good organization of this colloquium. We also thank the CNRS for their financial help and the European Interferometry Initiative (OPTICON) for partially supporting the attendance of several members of the working group "Future of Interferometry in Europe".

Saint-Michel-l'Observatoire, 16 February 2014
The editors, Jean Surdej, Hervé Le Coroller and Luc Arnold

*Improving the performances of current optical interferometers & future designs*
*Proceedings of Haute Provence Observatory Colloquium (23-27 September 2013)*
*Edited by L. Arnold, H. Le Coroller & J. Surdej*

# Session 1. Science and technology context

Chair: Jean-Philippe Berger
Monday afternoon, Sept. $23^{th}$

*Improving the performances of current optical interferometers & future designs*
*Proceedings of Haute Provence Observatory Colloquium (23-27 September 2013)*
*Edited by L. Arnold, H. Le Coroller & J. Surdej*

# Summary of the science discussions during the Special Session "Science with present and future interferometers" and ASTRONET session at EWASS2013

J. Surdej[1], J.-U. Pott[2], & O. Chesneau[3]

[1] *Institute of Astrophysics and Geophysics, Allée du 6 août 17, 4000 Liège 1 (Sart Tilman), Belgium*

[2] *Max Planck Institute for Astronomy, Koenigstuhl 17, 69117 Heidelberg, Germany*

[3] *Hippolyte Fizeau Laboratory, University of Nice & Observatoire de la Côte d'Azur, Boulevard de l'Observatoire, 06304 Nice, France*

**Abstract.** The main goal and achievement of the Special Session "Science with present and future interferometers" and "ASTRONET" session at EWASS2013 (European Week of Astronomy and Space Science; 10 and 11 July 2013, Turku, Finland) were to bring together Europe's scientists using the openly available interferometric facilities (like VLTI and CHARA) to hear about the current results, but also to discuss the future of this technique in the light of the upcoming ELTs and other future facilities (GAIA, ALMA, SKA, etc.).

## 1. Summary

The excellent list of speakers responded enthusiastically to the challenge of summarizing their work and highlight scientific results to a wider audience. The breadth of science being exploited by modern optical arrays is impressively long, and extended from rather classical domains (instigation of stellar diameters and binarity) to high angular resolution images of stellar surfaces, resolving the origins of planet formation in young stellar disks, solving some of the mysteries of enigmatic, rare and complex sources, learning about fundamental parameters of black hole feeding. Clearly, in the age of gigantic all-sky surveys, optical and infrared interferometry plays the complementary role of a giant night sky microscope, capable of resolving very fine details in a considerable number of astronomical key objects.

The invited speakers reported several examples of those incremental sensitivity improvements of modern interferometers over the last years. These have now allowed to conduct sample studies of statistical sizes leading to transformational insights in the areas of star formation and feeding of active black holes in galactic nuclei.

At the end of the session, a detailed review of the scientific productivity of the VLTI was given as a start to discuss ways into the future. The well attended session showed the interest of the wider astronomical community in the technique, in particular where long baselines, and high spectral resolution of spectro-interferometry allow access to new observables of physical processes in and around stars and black holes. The last decades of technological groundwork has lead to a maturity, which in the short term future will give the upcoming commissioning of the next generation of VLTI and CHARA instruments a higher scientific impact.

In addition, for the longer term future, we are now in a position to plan on robust technological grounds for a new or significantly enhanced facility, with laser-guide star adaptive optics assisted large telescopes with several 100m long baselines. Such a new facility, responding to the astronomers demand for even higher dynamic range interferometric imaging and improved sky coverage than offered today, will critically rely on the international community and community networks.

The complete list of talks is available as pdf and video files via the webpage: http://www.ss7.ulg.ac.be/programme.php

Please visit the "Planet Formation Imager" web page

http://planetformationimager.org for some more recent and important actions taken following the present 2013 international Colloquium at the Haute-Provence Observatory.

*Improving the performances of current optical interferometers & future designs*
*Proceedings of Haute Provence Observatory Colloquium (23-27 September 2013)*
*Edited by L. Arnold, H. Le Coroller & J. Surdej*

# 2013 Interferometry Forum Report

Gerard van Belle[1], Stephen Ridgway[2], Theo ten Brummelaar[3]

[1]*Lowell Observatory, 1400 West Mars Hill Road, Flagstaff, Arizona, USA 86001*

[2]*National Optical Astronomy Observatories, P.O. Box 26732, Tucson, Arizona, USA 85726*

[2]*Georgia State University, CHARA Array, P.O. Box 48, Altadena, California, USA 91023*

**Abstract.** The 2013 Interferometry Forum was organized around a list of topics - each topic had a moderator and an archivist. Each participant in the forum had one or more assignments - this was not a meeting for passive participation. The following summaries are a slightly edited version of those notes; conclusions and recommendations are presented at the end of the document.[1]

## 1. Discussions from Friday, March 15, 2013

### 1.1 Forum Concept Presentation and Initial Discussion

*Moderator: van Belle; Archivist: Baines*

The **2013 Optical Interferometry Forum** was a special opportunity to get together and talk about a technique that is both important to our various areas of expertise, and scientifically productive. The interferometry community has this opportunity only infrequently and incompletely, so having a more focused event with adequate time for discussion was, we felt, important. The attendance for the Forum was solicited from throughout the community and largely self-selecting; the organizers (Steve Ridgway, Gerard van Belle, Theo ten Brummelaar, Guy Perrin) accepted every request for attendance.

The rationale for the Forum can be summed up in two sides to the issue:

We live in a time of **Great Disturbances**: Big things are happening in astronomy that unsettle the status quo and make it challenging to develop and use the technique of optical interferometry. In the United States, this in particular includes the Decadal Review, and even the detailed plans laid out therein arent quite happening as expected because of funding issues. On the European

[1]An expanded version of the Forum Report may be found online at the IAU Commission 54 website, http://iau-c54.wikispaces.com/2013+Interferometry+Forum.

side, if the need for high spatial resolution is correctly described in the Science Vision document of ASTRONET, its declination in the Infrastructure Roadmap is clearly postponed. Development of JWST and the next generation of large ground-based telescopes require lots of resources, and operating costs of new facilities that are coming online (such as ALMA) have a large impact as well.

We also live in a time of **Great Opportunities**: There will be a time after JWST. The CHARA Array is soldiering along, the NPOI upgrades are poised to revitalize the instrument, VLTI has upgrades under development, there are new efforts in LBTI and MROI, and China is developing Dome A. The scientific productivity of the existing facilities is robust and unique.

All these circumstances inspired the organizers to put this forum together. The intent was to supplement the SPIE meetings (but not to supplant them). The annual CHARA Science Review meetings have been going on for a while and are growing in scope; this idea grew out of those meetings. Future versions of this Forum may grow into an 'official' interferometry meeting.

The questions we aimed to address by the end of the Forum:

– How do we envision this forum as related to other existing structure, such as the IAU, USIC, OLBIN, EII? We shouldnt duplicate those efforts.

– Do we want future meetings? Are they associated with the SPIE or other meetings? Are they combined with the interferometry schools in Europe?

– Do we want proceedings? The answer is probably yes. What are those written products?

– How do we best construct a plan for the future?

### 1.2 Active Plans of Current Facilities

*Moderator: Herbst; Archivist: Baron*

Active instrumentation plans and/or statuses of the following facilities were presented (and are detailed in the expanded forum report): the Very Large Telescope Interferometer (VLTI); the Navy Precision Optical Interferometer (NPOI); the Georgia State University (GSU) Center for High Angular Resolution Astronomy (CHARA) Array; the Large Binocular Telescope (LBT); the Sydney University Stellar Interferometer (SUSI); New Mexico Tech's (NMT) Magdalena Ridge Optical Interferometer (MROI); Berkeley's Infrared Stellar Interferometer (ISI); the Keck Interferometer (KI); the OHANA (Optical Hawaiian Array for Nanoradian Astronomy) effort; the Cambridge Optical Aperture Synthetic Telescope (COAST); A. Labeyries 'hypertelescope' project ongoing in France; and NASA Goddard's Balloon Experimental Twin Telescope for Infrared Interferometry (BETTII).

### 1.3 Significant Developments in Technology - Achieved or Needed

*Moderator: Buscher; Archivist: Berger*

New technology developments should be driven not only by the main scientific requirements but also by what is technically feasible - there is an interactive relationship between the science and the technology. For optical long baseline interferometry the main science necessities are to raise the limiting magnitudes, to improve the imaging capability, to allow for faint companion detection and characterization and to a lesser extent to allow scientific polarimetric measurements and astrometry.

One of the considerable advances in the coming years will be the arrival of new technology detectors such as the SELEX currently being test-developed at ESO in collaboration with other partners. These detectors should provide kHz readout possibilities with sub-electron read noise. Finally, multi-telescope phase-tracking systems should enable long integrations.

Pushing the aperture synthesis imaging capability requires more telescopes. The development of low-cost telescopes that are reliable, resistant to vibrations and possibly relocatable would help with this. Beam transportation through fiber optics could be further studied. At the central laboratory multi-telescope combiners will be needed with spatial/modal filtering capabilities and improved calibration capability of temporal effects.

### 1.4 Funding and Other Practical Matters

*Moderator: Wishnow; Archivist: Creech-Eakman*

The various interferometry groups reported on current and near-term funding. There is not a surfeit of funding or human resources, particularly for all US-based facilities. The results of the top-level 2010 Astrophysics Decadal report have made it very difficult to obtain operational funding from US funding agencies, except in the case that this funding comes from PI based proposals for scientific experiments or new technologies. While the primary source of funding in the US for present-day interferometric science is NSF, we have previously benefitted (and some still do) from funds garnered via: the Defense Department (ONR, NRL, DARPA), NASA, and some state and institutional funds. As a community we have experienced limited success from philanthropic groups. While it appears that US-based facilities will continue to approach all of the same funding agencies, it is clear that operational support is not something most of these funding agencies are able or are eager to support.

In Europe the funding for VLTI is exclusively through ESO, and individual interferometer backends (e.g., beamcombiners and detectors) are provided by the community-funded national organizations or international partnerships. The status of the individual projects is fairly complex in almost all cases, and there is no clear path to medium and long-term funding.

### 1.5 Long Term Perspective on Astronomy Programs - Relation of Interferometry to Other Facilities

*Moderator: Mourard; Archivist: Tuthill*

The lesson from projects and programs that have been successful in securing resources both for construction and for ongoing science support is that broad based community support is required to drive major investment. It is not clear that the interferometry community has been successful in such community building (or even community awareness) for the science we do. In order to launch major initiatives, often decades of careful lobbying and awareness raising are required.

The formal process by which this is done is usually through national or transnational planning processes such as the Decadal Plan in the US or the ASTRONET 2020-40 exercise in Europe. Here we take the latter as an example (these exercises usually come up with broadly common science themes which are judged to be top priorities). In general, it was recognized that interferometry was poorly represented in such exercises on both sides of the Atlantic. The onus is on the interferometry community to attempt to make the case for a stronger presence in future exercises of this type.

Analysis of the four main ASTRONET science cases with highlighting of items especially relevant to optical interferometry: Do we understand the extremes of the Universe? How do galaxies form and evolve? What is the origin and evolution of stars and planets? How do we fit in?

The good news is that interferometry, as presently formulated, does seem directly applicable to large parts of two of the four major themes from ASTRONET. There was discussion (although no consensus) on the question as to whether it is more important to play to those strengths we already do well, or to try to expand to tick more of the boxes with our instruments. In the end this decision may be taken out of our hands by technical arguments - the parts of astronomy we dont contribute to are hard for fundamental detection reasons.

It was recognized that none of the present crop of major instruments could be considered to be fully "mature", and in this sense we can expect a continuing strong growth in science even with no major new investment at the scale of a major facility.

## 1.6 Next-Generation Interferometric Science - Opportunities and Requirements

*Moderator: Berger; Archivist: Petrov*

The discussion started by asking the instrument or facility representatives to say a few words about: their scientific drivers, what kind of trend they see in their use, and their subjective feeling of success. A broad range of instruments and programs was quoted. The following is an attempt to isolate some key points.

*Old and new science goals and trends.* We have evolved from "fundamental parameters" (diameters, masses, distances) to "general stellar astrophysics". There is an (unfinished) evolution from performance to science driven designs. We have not delivered all that we initially promised. We have actually delivered much more. For example, we have (a) solved "old" astrophysical problems and modified new ones; (b) provided images on complex objects with unexpected shapes. One major field has been abandoned: the direct detection and characterization of extrasolar planets. More precisely, this field has abandoned us: ground and space interferometry are not expected to be a major contributor to this topic any more. This has a major impact on the long term plans for major interferometers. There is an open discussion about the real future of extragalactic applications: is it enough to increase the limiting magnitudes; when do we need to move to much larger baselines; is there a major science case beyond AGNs and QSOs?

*Marketing strategy.* We discussed the need to advertise attractive science goals, with the risk of overselling our potential and being eventually punished for it. Even if we had to abandon some topics, we have not really oversold the potential of interferometry, which has delivered a fair deal of what it promised plus a large sample of unplanned results. Another discussion about our "marketing" strategy is about the necessity to insert our science potential into the large objectives of the ASTRONET or US Decadal prospective. We need to place interferometry in this global landscape if we want to obtain substantial resources.

However, by doing so, we might harm some important "basic" science and blind ourselves to new perspectives. These debates about "marketing" are not closed.

*Past and present perspective.* Ten years ago, Optical Interferometry was a difficult technique, with very few results, and a grandiose future, with a long term path: the "small interferometers", then VLTI-KI, then DARWIN-SIM, then some kind of OVLA. Now, optical interferometry is a difficult technique, with a lot of results, great expectations for the 2015-2020 period, and a dim future. After the 2nd generation VLTI instruments (e.g. GRAVITY) and the completion/extension of the US arrays, the horizon is opaque. We need a long term perspective: our grail could be a super interferometer, imaging very faint targets with dense u-v coverage and kilometric baselines, or as this might be overwhelmingly expensive, we could switch to two more "modest" projects: (a) A very good imaging interferometer, with very dense u-v coverage, but relatively less demanding in sensitivity and maybe resolution (a super CHARA or NPOI+ or MROI+); (b) An interferometer shaped for very faint sources at very high angular resolution, with a smaller number of larger apertures (a super VLTI, not necessarily on Paranal). We have the tools to specify and evaluate such concepts, but we need to coordinate this evaluation and to agree on the criteria and the procedure.

## 2. Discussions from Saturday, March 16, 2013

### 2.1 Forum Concept - Discussion Continues

*Moderator: ten Brummelaar; Archivist: Schmitt*

The general consensus was that, while having a gathering on this topic was productive, a specific set of outcomes from this meeting was necessary. Who are we and why are we here? Is this meeting to plan for more planning meetings? Are we working towards an optical VLA? Towards a space mission? Are we simply trying to stay alive? It seemed that all of these things applied.

What can we do that no one else can do? Is there a need for a global and unified vision? ESO is "only a small part of our user base"; in the USA the next decadal review already looms large on the horizon. There was broad agreement that a unified global vision is required.

Do we do this under an IAU Banner? Yes. The IAU, not only Commission 54, should take a role in leading and guiding, or at the least coordinating and endorsing, the development of this vision.

How do we best sell ourselves to the community? The potential user base is larger than most people think.

Should there be a publication or written statement from this meeting? Yes; there was broad agreement that we should have a written record of this discussion. The forum chairs will put together an executive summary to be distributed amongst the forum members and published in some manner, on the OLBIN email list at a minimum.

Is this the forum for building a long term science case? Yes; we should think on the time scales ranging from a few years through to the time of the next decadal survey and even longer. A consensus is needed in order to promote a big instrument like an OVLA. ALMA is be a good example. A roadmap for future developments is needed. The US and EU roadmaps are not well coordinated, which should be changed. The IAU C54 Chair should appoint a panel chair to coordinate this work.

In order to prepare for a major facility in the future, it is necessary to do a lot of preparation over many years. In order to make this preparation happen, it is necessary to begin working now or soon.

This forum is not an alternative to the SPIE but offers an opportunity for interaction that has not been achieved at the SPIE. There was a consensus that the forum should be repeated in an annual or biennial pace. Considerations for possible future forum meetings:

- In SPIE years, it is possible to have a Forum meeting separate from but adjacent to the SPIE, or to have a segment of the SPIE meeting devoted to Forum activities.

- What about non-SPIE years? One option is to have it in non-SPIE years, possibly as an additional meeting during the CHARA meetings. The CHARA annual science meeting has developed over the years, and this year includes NPOI. What direction might it go in the future? Perhaps it could extend its scope to include at least some aspects of activities at other facilities.

Part of the value of this meeting is the relatively small attendance and the resulting intense participation by attendees. Should the meeting size be limited in the future? Should future Forum participation remain self selected?

### 2.2 Interferometry User and Operator Experience

*Moderator: Delplancke; Archivist: Stencel*

The following topics related to the status of various facilities - the VLTI, Keck-I, CHARA, NPOI, MROI, LBTI and LINC NIRVANAwere addressed: Is the facility an open user and/or a proprietary user facility? How is the time allocated? How organized are the data acquisition and reduction? Is user support available? Are the data archived? And is the archive publicly available? What were the difficult things that went well and what were the easy things that turned out to be difficult?

The advantage of having an open user community or at least to partially opening a facility to all users is the increased the scientific return. Some proprietary facilities are sitting on unreduced data due to lack of available manpower.

The usefulness of OIFITS data format was discussed. The advantages are that imaging data packages are based on that format and that it allows combining observations from different facilities (e.g. CHARA and VLTI). However, in the case of some very specialized instruments, the current format is not enough. We should consider whether improvements to OIFITS are needed and whether its use should continue to be recommended. The availability of good data reduction packages, properly supported, is essential if we want to widen our user community.

To attract external interest, proprietary and new facilities could host an online catalog of observed target and calibrator objects, even if making OIFITS or equivalent data generally available comes (much) later.

### 2.3 Blue Sky Thinking

*Moderator: Eisner; Archivist: Payne*

We need to identify high profile science goals that only interferometry can attack. If the science is compelling enough but is out of the reach of current facilities, we may be able to promote a new facilityspace- or ground-based, as the science dictatesas a single experiment (e.g., the Event Horizon Telescope). When new facilities are built, they often work well beyond the original science goals. But we also need to identify science goals that get the most out of current facilities. HST is a good example.

Example science goals that were discussed: such as precision astrometry in dense fields and low-mass exoplanets in clusters. Science of interest outside astronomy that may yield support, eg. wide angle astrometry is of interest to the Navy and should be of interest to NASA (GAIA will not hit the bright stars needed for navigation). Basic limits need to be recognized: sensitivity to low surface brightness features (galaxies for example have very low surface brightness, although this may not be as true of emerging galaxies) often requires good u, v coverage; using longer baselines leads to less flux per resolution element, which may drive a need for larger apertures. Technological possibilities to be explored: increasing aperture diameter: bigger is better (modulo AO problems); more apertures: improves u,v coverage at the possible cost in sensitivity and the certainty of higher expense; etc. Site considerations: High? Cold? Space?

### 2.4 International Collaborations and Coordination

*Moderator: Armstrong; Archivist: Herbst*

*Hardware Collaboration.* Instrumental collaborations are more difficult than observational collaborations. One of the primary obstacles to instrumental collaboration is the perception that, e.g., a proposal to VLTI must have a European PI. In actuality, ESO evaluates proposals without regard to where they come from, but allocation considers PI institution. Being Co-I is the route to follow. Instrumental collaboration at CHARA has taken the form of outside users, many of them European, bringing instrumentation to CHARA. This approach has worked well in making CHARA scientifically productive.

*Observational Collaboration.* Our interferometer facilities are complementary in interesting ways. One example is CHARA and NPOI baselines for visible imaging. Another is VLTI and CHARA baselines for near-IR imaging. If multiple facilities can be utilized in coordination to produce better science, it will benefit not just the particular project, but the entire community. It was suggested that CHARA and ESO might coordinate to offer access to both the ESO AT's and the CHARA Array for proposals which need both.

*Collaboration on Software.* Is there a regime between highly instrument-specific data-processing and high-level imaging on which collaboration would be useful? Collaboration could range from exchange of approaches to production of software. An EII collaboration with moderate funding from ESO has started, focused on coordinating image reconstruction algorithms, developing cookbooks and making how they work clearer. The above-mentioned JMMC OI database is partially funded through this EII grant.

### 2.5 The Role of Formal and Informal Community Organizations and Networking

*Moderator: Mozurkewich; Archivist: Elias*

Communication among the various groups around the world is lacking. Better communication is required for the survival of optical interferometry, successfully funding next generation instruments, and organizing for the next decadal review. Getting together every two years at an SPIE meeting is not sufficient. OLBIN has been the communications vehicle in the past, but there has been very little recent activity. It was proposed to upgrade OLBIN to a wiki, which is newer technology. It was also proposed to start a Facebook page for more rapid dissemination of relevant information. Both the wiki and the Facebook page would be run under the auspices of IAU Commission 54.

In Europe, EII is the voice of the VLTI community; it makes recommendations to ESO. It has been proposed to resurrect the moribund USIC as the US equivalent to EII to speak on behalf of the optical interferometry community to NSF and the next decadal review. EII runs workshops and schools. Is that possible for USIC? It was also suggested that EII, USIC, and possibly other groups organize for global planning. What do groups have in common, how do their efforts complement each other, and how can we coordinate more effectively to revitalize the field?

*Plans for Future Activities.* One model: an interferometry science & technology meeting (ISTM): the Annual CHARA Science Review has evolved (for 2013) into CHARA-NPOI. Should it evolve further into an ISTM? Frequency: annually to every two years? For the latter, the SPIE 'off' years could be when a larger ISTM is held.

*Future forum details.* Keeping the attendance modest, to ∼20 people, is helpful to streamline discussion & interactions. Complete or nearly-completely representation from world interferometry groups is desirable. Such future forums could be adjunct to SPIE or ISTM meetings, just as the 2013 Forum was adjacent on the calendar to the CHARA-NPOI meeting.

## 3. Conclusions

- Interferometry has gone from an exotic technique with promise, to a demonstrated technique with a steadily growing technical capability, a large and active community, and significant impact on stellar physics.

- Opening access to a wider community has demonstrated benefits. Opening to a wider community is also due to the availability of data preparation, data calibration, data reduction and data interpretation packages, in a word, documented, reliable and well behaved user-friendly software.

- Funding. In Europe, VLTI funding, including some development, is currently stable. France, through its funding by INSU of, e.g., JMMC, plays a supportive role for OI interferometry well beyond its contribution to ESO funding. Interferometry in the U.S. is not strongly supported by the Decadal report, and there are reduced opportunities at NSF but there is a possible future "mid-scale" funding opportunity. In the next 10+ years, the interferometry community must make the most of existing facilities and their obvious extensions.

- Possible facility options for the future on the decade+ time-scale include: Moderate development from existing facilities to much enhanced imaging capability; moderate development to fainter target capability.

– Possible options on the decade++ time-scale include: Major development of a super-facility; now is the time to build a consensus for the next major development.

– An International Interferometry Forum is needed and has numerous important roles.

## 4. Recommendations

– The Forum should have both on-going and annual activities.

– The Forum should develop a charter.

– The Forum should use the IAU banner as a Commission 54 activity; the Forum should engage IAU officers and members in Forum work.

– The Forum should hold annual meetings: Adjacent to SPIE in SPIE years; in alternate years adjacent to CHARA-NPOI meetings or schools.

– The Forum should publish Forum reports, including from this meeting.

– The Forum should foster long-term development of interferometry science directions.

– Roadmaps are needed - including U.S.-Europe coordination of roadmaps - which requires U.S. entity to develop roadmap.

– USIC should be revived, to develop a national consensus and to represent the U.S. to Europe.

– We encourage making catalogs of observed targets available.

– We encourage improved archive access.

– The U.S. community should consider "webinars" as a low-cost implementation of interferometry schools.

– U.S. PI's should be encouraged to propose to VLTI.

– Joint facility access – CHARA-VLTI, CHARA-NPOI, NPOI-VLTI – should be studied.

– The scope of the CHARA-NPOI meetings should be expanded, at least in SPIE off-years.

– OLBIN should be rebuilt in a supportable form, perhaps as a wiki.

– The community should make use of social media, including starting and maintaining an interferometry Facebook page.

## 5. Draft Forum "Charter" of the International Interferometry Forum

The Forum will organize occasions and channels for communication, facilitate coordination in planning, and encourage and promote opportunities for technical and scientific collaboration, both within and beyond the interferometry community.

The Forum will operate as an element of IAU Commission 54. The commission officers will take initiative and personal responsibility for ensuring some Forum activities. These will include: organizing annual Forum gatherings, continuation of the online OLBIN functionality in a more sustainable incarnation, and implementation of social media networking opportunities.

Forum participation will be open to the community. The IAU officers will call on and benefit from the support of Forum participants in carrying out their Forum responsibilities.

## 6. 2013 Forum Participants

Tom Armstrong (NRL); Jean-Philippe Berger (ESO); Fabien Baron (UMich / GSU); Jim Benson (USNO-FS); David Buscher (Univ. Cambridge); Michelle Creech-Eakman (NMT); Francoise Delplancke (ESO); Joshua Eisner (U. Arizona); Nicholas Elias (OAMS); Tom Herbst (MPIA-Heidelberg); Don Hutter (USNO-FS); Fabien Malbet (Grenoble); Denis Mourard (OCA); David Mozurkewich (Seabrook Engineering); Ifan Payne (NMT); Guy Perrin (Paris-Meudon); Romain Petrov (U. Nice); Steve Ridgway (NOAO); Robert Stencel (DU); Theo ten Brummelaar (GSU); Peter Tuthill (Univ. Sydney); Gerard van Belle (Lowell); Ed Wishnow (Berkeley SSL)

*Acknowledgements.* The editors of the 2013 Forum Report gratefully acknowledge the contributions of all of the forum participants.

*Improving the performances of current optical interferometers & future designs*
*Proceedings of Haute Provence Observatory Colloquium (23-27 September 2013)*
*Edited by L. Arnold, H. Le Coroller & J. Surdej*

# Session 2. Current interferometers and future development for these facilities

Chair: Victor Garcia & Gerard Van Belle
Tuesday, Sept. $24^{th}$


Gerard van Belle
Chair: Session
Ed Wishnow

*Improving the performances of current optical interferometers & future designs*
*Proceedings of Haute Provence Observatory Colloquium (23-27 September 2013)*
*Edited by L. Arnold, H. Le Coroller & J. Surdej*

# Intensity Interferometry with Cherenkov Telescope Arrays: Prospects for submilliarcsecond optical imaging

Dainis Dravins

*Lund Observatory, Box 43, SE-22100 Lund, Sweden (dainis@astro.lu.se)*

**Abstract.** Intensity interferometry measures the second-order coherence of light. Very rapid (nanosecond) fluctuations are correlated between separate telescopes, without any optical connection. This makes the method insensitive to atmospheric turbulence and optical imperfections, permitting observations over long baselines, and at short wavelengths. The required large telescopes are becoming available as those primarily erected to study gamma rays: the planned Cherenkov Telescope Array (https://www.cta-observatory.org/) envisions many tens of telescopes distributed over a few square km. Digital signal handling enables very many baselines to be simultaneously synthesized between many pairs of telescopes, while stars may be tracked across the sky with electronic time delays, synthesizing an optical interferometer in software. Simulations indicate limiting magnitudes around m(v)=8, reaching a resolution of 30 microarcseconds in the violet. Since intensity interferometry provides only the modulus (not phase) of any spatial frequency component of the source image, image reconstruction requires phase retrieval techniques. As shown in simulations, full two-dimensional images can be retrieved, provided there is an extensive coverage of the (u,v)-plane, such as will be available once the number of telescopes reaches numbers on the order of ten.

The material presented at the conference has recently been published and the author proposes to the reader the references below.

## References

D. Dravins, S. LeBohec, H. Jensen, P. D. Nuñez: Stellar Intensity Interferometry: Prospects for sub-milliarcsecond optical imaging New Astronomy Reviews 56, 143-167 (2012); http://dx.doi.org/10.1016/j.newar.2012.06.001, preprint http://arxiv.org/abs/1207.0808

D. Dravins, S. LeBohec, H. Jensen, P. D. Nuñez, for the CTA Consortium: Optical Intensity Interferometry with the Cherenkov Telescope Array Astroparticle Physics 43, 331-347 (2013); http://dx.doi.org/10.1016/j.astropartphys.2012.04.017, preprint http://arxiv.org/abs/1204.3624

*Improving the performances of current optical interferometers & future designs*
*Proceedings of Haute Provence Observatory Colloquium (23-27 September 2013)*
*Edited by L. Arnold, H. Le Coroller & J. Surdej*

# The Very Large Telescope Interferometer: status and plans

J.-P. Berger[1], A. Mérand[1]

[1]*European Southern Observatory*

**Abstract.** The Very Large Interferometer is undergoing an important mutation. In this paper we present an update on the status of the VLTI and a description of the technical roadmap to prepare for the arrival of its second generation instruments GRAVITY and MATISSE.

## 1. Introduction

### 1.1 VLTI Infrastructure

The Very Large Telescope Interferometer (VLTI) is located in Cerro Paranal, Chile. It provides the VLT with an interferometric capability. With the maximum baselines in operation (i.e $\approx$ 150m) angular resolution of the order of 2 milliarcseconds in the near-infrared and 10 milli-arcseconds in the mid-infrared can be reached. As of today the interferometric infrastructure of the VLTI consists of the following main elements (see Haguenauer et al. 2012 for a detailed description):

- Four Unit telescopes (UTs, 8m diameter) providing up to four simultaneous beams to the VLTI beam combination laboratory;
- Four relocatable Auxiliary telescopes (ATs, 1.8m diameter) providing an enhanced uv plane coverage capability;
- Six delay lines in their tunnel with the distributing optics;
- Four adaptive optics system at each UT focus (MACAO);
- A beam combination laboratory where focal instrumentation is located including beam compression, beam selection and routing, infrared-tip/tilt sensor, coherent four beam source and fringe tracker. (FINITO).

### 1.2 Observing and telescope configurations

VLTI users go through the exact same proposal submission and OB preparation process as for the other VLT instruments. The VLTI users can rely on two main observing modes Service and Visitor. The first guarantees that the observations will be repeated by VLTI astronomers until the data quality has reached the

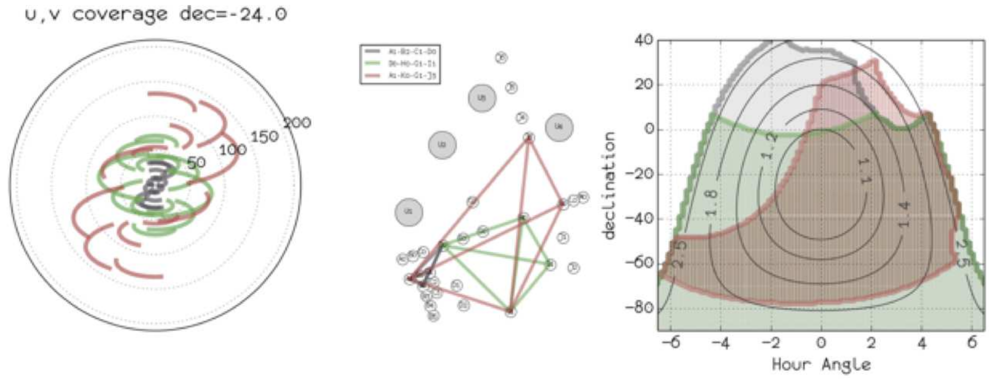


Figure 1.: *Currently offered AT stations and corresponding u,v and sky coverage for a source at dec −24° for the three telescope quadruplets*

guaranteed level. The second one is usually allocated in situations where the expertise of the PI is requested on the mountain or if the time has been allocated through a GTO[1] agreement. It allows the observing strategy to be optimised based on a real-time appreciation of the situation but does not guarantee the best seeing conditions. All raw data are immediately stored in the ESO archive.

In order to provide the possibility of a well covered u,v plane the PI can choose among three AT telescope quadruplets (currently A1-B2-C1-D0, D0-H0-G1-I1, A1-G1-J3-K0) and the four fixed UTs (c.f. figure 1). The quality of the u,v mapping will depend on the position of the source in the sky which can be a strong limitation if the location is in the North (declination $\geq 10°$). This is due to a combination of technical constraints i.e delay line stroke ($\approx$ 100m), pupil relay (field of view), beam distribution. Moreover, the AT relocation capability is limited to two per days which sets the limit of how many reconfigurations can be done. The reader is referred to the presentations by Antoine Merand in the VLTI community days (http://vlti-pionier.sciencesconf.org/) for a better understanding of the configurations constraints.

### 1.3 Instrumentation

In addition to the ongoing PRIMA project there are currently three instruments in operation at Paranal. MIDI and AMBER are official instruments that can be operated either in service or visitor mode under the responsibility of ESO. PIONIER, the most recent one, is a visitor instrument also offered to the community.

**PRIMA** PRIMA is a VLTI infrastructure project that was motivated by three main science cases:

1. providing AMBER and MIDI with better sensitivity through on/off axis infrared two telescope fringe tracking;

[1] Guaranteed Time Observations

2. enabling narrow-angle astrometry at the ten microarcsecond level in order to detect the exoplanet-induced wobble of host-stars (a project led by the ESPRI science consortium);

3. experimenting phase referencing imaging with AMBER and MIDI by measuring the astrometric distance of the science object with a joint reference source.

In order to reach that goal the PRIMA infrastructure project had to develop a series of new subsystems for the VLTI:

– a fast data transmission ring network (RMN);

– four star separator systems on the UTs and the ATs that provide dual feed capability and allow the light of two objects separated by up to 30" (science and reference) to be sent to the VLTI combination lab;

– four differential delay lines to record the fringes on both dual feed targets;

– two two-telescope fringe sensor units operating in the K band (FSU-A, FSU-B);

– PRIMET a two telescope metrology system linking both FSUs and measuring the internal optical path difference up to the ATs M2 mirrors.

PRIMA is currently almost fully operational in its two telescope configuration. However the astrometric commissioning process of PRIMA has been interrupted in 2011 because some major issues with the metrology endpoints were identified that precluded to reach the final astrometric performances. The following years, an in-depth technical and system analysis has lead to several recommendations on how to reach the accuracy goals. In particular the recommendation to push the metrology endpoints to the M2 space was pointed out as a significant improvement. The PRIMA team implemented several of these recommendations and was able to carry on the first astrometric measurements with the new metrology endpoints in october 2013. While the improvement in performance was very significant (e.g $\approx 100\mu$arcsec on a single one hour measurement and with two bright sources) it was still not sufficient for the exoplanet science case. Based on the results the PRIMA team proposed a full recovery plan that will be presented for evaluation in the context of a "gate review" process

**MIDI** [2] is a mid-infrared (N band) two telescope beam combiner that provides two observing modes HIGH SENS and SCI PHOT that allow the observer to choose to privilege sensitivity or photometric calibration (i.e precision). Two spectral resolutions PRISM (R=30) and GRISM (R=230) are available. MIDI can also provide self-coherencing, i.e track its own fringes. MIDI's performance on the ATs have considerably improved with the use of the PRIMA-FSU that compensates the random atmospheric optical path difference fluctuations. A gain of a factor of a $\approx 5-10$ in sensitivity is currently reported. MIDI will eventually be decommissioned to make way to MATISSE.

[2] see http://www.eso.org/sci/facilities/paranal/instruments/midi/overview.html for an overview

**AMBER** [3] is a three telescope beam combiner originally planned to cover the J,H and K bands with small, medium and high spectral resolutions. The user can choose between Low Resolution (35, J,H,K filters), Medium Resolution (1500, H, K filters) and High Spectral Resolution (12000, K band). In practice, due to the sensitivity to fast atmospheric conditions of the fringe tracker FINITO, and probably coupling issues at those short wavelengths the J band is not exploitable and high spectral resolution is limited to K band. The Medium and High spectral resolution often require the external fringe tracker FINITO to be operational. Like MIDI, AMBER possesses a self-coherencing algorithm that allows the fringes to be centered with low frequency correction. AMBER provides visibility and closure phases measurements together with differential visibilities, phases and closure phases. Mérand et al. (2012) have demonstrated how the phase measurements of FINITO could be used for an *a posteriori* calibration of the visibilities. The improvement is very significant in low spectral resolution and relies on the computation of a *jitter* corrective term for each AMBER frame measurement. More recently a Fourier method developed at Observatoire de la Côte d'Azur was demonstrated to lead to significant improvement in sensitivity. However the quality of calibration is currently under review at ESO.

**PIONIER** [4] stands for Precision Integrated-Optics Near-infrared Imaging ExpeRiment. PIONIER is a 4-telescope visitor instrument for the VLTI that combines four ATs or four UTs using an integrated optics combiner. It provides low spectral resolution in H band (1, 3 or 7 spectral channels) and occasionally in the K band. PIONIER is designed for imaging with a specific emphasis on fast fringes recording to allow precision closure-phases and visibilities to be measured. It is currently offered to the whole VLTI community either in visitor or delegated visitor mode. The latter mode is a contribution from ESO that allows the PI to have its observations carried by one of the VLTI operations astronomers. PIONIER data are now stored officially in the ESO raw data archive.

### 1.4 Operations statistics

Figure 2 summarizes in three plots some VLTI statistics extracted from the night-logs since 2004. The top figure represents the distribution of night status between No Operation, Commissioning, Technical time, Service and Visitor mode. The middle one describes the scientific science time breakdown between the four instruments operated at VLTI (VINCI, MIDI, AMBER and PIONIER). The last one represents the distribution of time-loss. All these quantities are given as a function of time.

Two main conclusions emerge from these plots:

– the technical time losses at VLTI have been brought to a very low level (≈10%) thanks to a considerable investment of system engineering;

– the fraction of time devoted to science has considerably increased and represents on average now 70% of the observing time;

[3] see http://www.eso.org/sci/facilities/paranal/instruments/amber/overview.html for an overview

[4] http://ipag.osug.fr/twiki/bin/view/Ipag/Projets/Pionier/WebHome

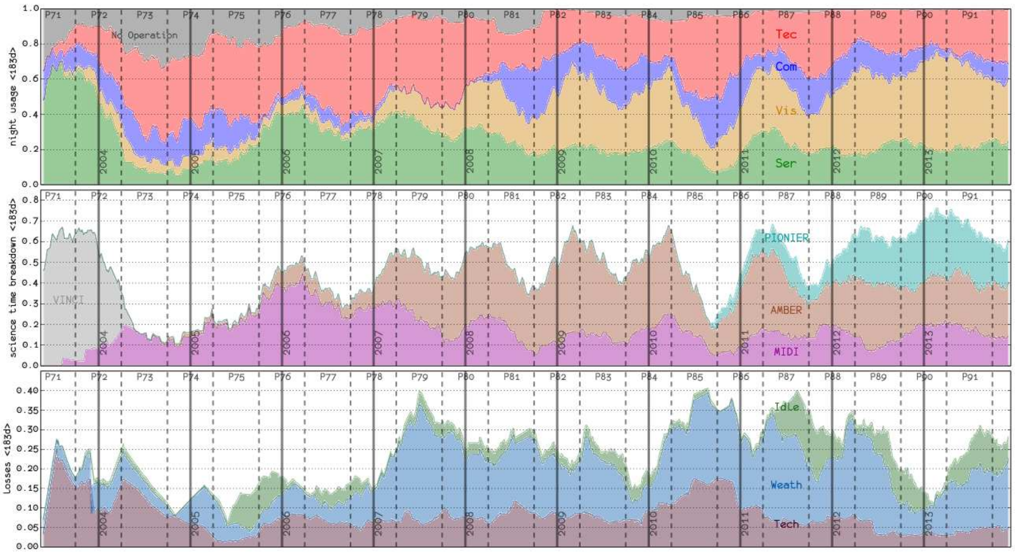


Figure 2.: *Operational statistics for VLTI (see text).*

## 1.5 VLTI 1.0: Lessons learnt

The last years has demonstrated that bringing such a complex infrastructure to an operational level requested an significant investment in system engineering to hunt down systematically any sources of unreliability. Considerable progresses have been made in the delay-lines, ATs, tip/tilt sensors, global setup procedures etc. Without this effort VLTI would still be plagued with significant technical downtime.

**Weather** Cerro Paranal is known to be a fast seeing site. High seeing will lead to the degradation of the amount of light couple into the AMBER, FINITO or PIONIER singlemode fibers. Low temporal coherence times affect severely the capability to fringe track and therefore reach interesting limiting magnitudes or spectral resolutions. Statistics on weather measurements show the following:

– January/February is the best time for interferometric observations (low seeing but high coherence time);

– July/August in general correspond to very fast turbulence;

The weather-induced limitations have lead to define seeing constraints 0.6”, 0.8” and 1.0” in the call for proposals that will determine the limiting magnitude. This is currently an important limitation in VLTI overall performance. It is a strong incentive to develop NAOMI and adaptive optics system for the ATs and a robust four telescope fringe tracker.

**Imaging** The interest of carrying on image reconstruction out of interferometric data is motivated by the fact that these will bring additional value to the astrophysical interpretation. In particular the usual limitation of model-fitting techniques relies in the strong *a priori* knowledge on the object brightness distribution. Aperture synthesis aims at reducing as much as possible a priori information in the analysis process.

Experience has shown that a large and efficient u,v coverage is mandatory to carry on such an effort. VLTI offers the possibility to use four quadruplets of auxiliary telescopes and combine it with earth-rotation synthesis to pave the u,v plane. This has proven successful in a handful of cases in the AMBER case but the advent of four telescope combination with PIONIER has clearly shown a quantitative jump in efficiency. The operational constraints of allowing four telescope reconfigurations are strong. Only two can be moved per day, if wind conditions permit and are accompanied with the subsequent telescope pointing models.

**Performance.** Performance is an umbrella term that encompasses sensitivity, observing efficiency, robustness to internal or atmospheric conditions. VLTI has a very decent transmission that is regularly monitored and is of the order of 30% in K. However the final throughput efficiency is given also by the instrument transmission. In particular the coupling into single mode fibres is a strong factor. A significant effort has been put into improving AMBER's limiting magnitude by conducting a full realignment of its internal optics. More recently the introduction of differential birefringence compensators inspired by PIONIER's have a allowed the polarising beam splitters to be removed. Overall AMBER has gained about two magnitudes in sensitivity over the course of the last few years. The addition of a self-coherencing mode in AMBER has permitted the centering of the fringes. This has lead to significant improvement of visibility and closure phase accuracy. The FINITO fringe tracker, operating in the H band, has enabled to exploit the high spectral resolution of AMBER. Unfortunately its performances are overall disappointing because of high detector readout noise, throughput and a significant sensitivity to atmospheric flux coupling dropouts. More recently PRIMA Fringe Sensor Unit (FSU), operating in the K band, has demonstrated the capability to track on K$\approx 8$ sources and has been offered in combination with MIDI (K band is better suited for MIDI "red" objects than the FINITO H band). The sensitivity has been shown to increase by a factor of $\approx 5-10$. This is obtained through a posteriori coherent integration of the signal (Pott et al. 2012). Unfortunately, vibrations in the UTs prevent the efficient use of the fringe sensor on the UTs. Therefore this possibility is currently used mostly on the ATs.

**Scheduling** The VLTI users are currently offered full freedom in their choice of telescope configurations and instrument parameters. The current scheduling is based first on the highest ranked visitor mode. This can generate clear conflicts between proposals with different goals. For example an imaging proposal will privilege fast u,v coverage while temporal monitoring will request several measurements on regular temporal sampling with the same telescope configuration. This is currently an important limitation since it has conducted to reject highly ranked service mode proposals because the telescope configuration was not available at the time of the planned observations.

**Vibrations** Vibrations have been identified as the major performance offender for VLTI instruments when used on the UTs. Among the three currently offered instruments AMBER is suffering the most since it has shorter wavelengths than MIDI (hence a similar vibration jitter will lead to stronger contrast decrease and transfer function instability) and lower frame rates than PIONIER. Both tip/tilt and piston vibrations contributions have been measured. Systematics studies of the possible sources of vibrations (telescopes, instruments, wind) have lead to a much clearer picture of their origins. Both active and passive strategies have been employed to tackle the problem and have lead to significant performance improvement (see Haguenauer et al. 2012 and Poupar et al. 2010 for detailed information). Instruments are now monitored and their design corrected once vibration contributors are identified. Accelerometers are in place and are used to provide the measurements for an active optical path compensation. However, a recent internal study was able to study the vibrations once all VLT instruments of the UT1-UT3 pair were shutdown and concluded that the level of vibrations remained sufficiently high to be incompatible with GRAVITY's request. Reducing it further would require a dedicated active control covering all the optical path thanks to a metrology system. As of this writing the exact nature of such a control system has not been defined but could find inspiration from the solution adopted at Keck Interferometer.

## 2. Scientific use of VLTI

At the end of 2012 approximately 205 PIs had submitted proposals to use the VLTI. Among this list 137 were recurrent users (i.e. had more than 1 program). The PIs home institution belonged to 22 countries (see fig. 3) showing that VLTI had succeeded in reaching out a wider community than the core interferometric institutions.

The angular resolutions and precisions permitted by VLTI AMBER and MIDI ($\approx 2$ mas in the K band, 10 mas in the N band) have lead mostly to studies of circumstellar environments and fewer stellar surfaces ones which very often are only marginally resolved. However prior to that, VINCI the VLTI commissioning instrument with its accurate precision measurements was extensively used to reach a number of milestones. Among those achievements VINCI was used establish a precise measurement of the surface-brightness relationships in dwarf stars (Kervella et al. 2004). The traditional strengths of the VLTI are the studies of giants/supergiants, hot stars, evolved stars, young-stellar objects, massive young stars, $\mathrm{B}_e, [e]$ with astronomical unit resolution (or even better). In particular, AMBER, with its spectral resolution has permitted several emission lines to be spatially resolved in diverse environments. This was done either directly through visibility measurements but also through the powerful spectro-astrometry technique. This lead to the discoveries of wind emission around intermediate-mass young stars (Herbig AeBe), shocks in Novae, Keplerian rotation in $\mathrm{B}_e$ disks etc. MIDI was used to probe the dust distribution and composition in circumstellar environments. Of particular significance was the discovery of a dependence of the fraction of dust crystallinity as a function of the distance from the star in young stellar objects disks which is related with the dust processing and probably the planet formation process. MIDI has now surveyed a significant amount of young intermediate mass stars of all evolutionary status as well as evolved stars.

One of the most spectacular achievements of VLTI was to provide, through MIDIs mid-infrared observations, the possibility to survey the brightest Active

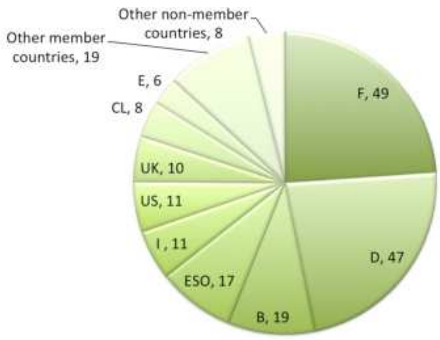


Figure 3.: *Number of VLTI proposal PIs per country.*

Galactic Nuclei with milli-arcseconds resolution. These observations challenged the traditional image of a dusty torus obscuring the view to the central hot accretion disk and black hole by revealing an important variety of objects and in particular in some cases evidence for strong polar elongations most probably caused by winds. The challenge of the AGN unification model is certainly not a small feat and should pursue with the arrival of MATISSE.

## 3. Preparing for the second generation instruments

### 3.1 Instrumentation

**GRAVITY** (Eisenhauer et al. 2011) is a four telescope beam combining instrument operating in the K band. It includes a science combiner and a fringe tracking combiner. GRAVITY allows for "standard" interferometric observation like AMBER or PIONIER but also narrow-angle astrometric observations. The later mode requires the presence of a reference source in the $\approx 2$" field of view of the VLTI on the UTs.

The top science case of GRAVITY is focused on the Galactic Center and aims at tackling the following topics:

- uncovering the true nature of Sgr A* flares probing spacetime close to the black-hole (BH) horizon;
- testing General Relativity with stellar orbits and ultimately in the strong gravity regime;
- address the paradox of youth of galactic center stars.

But GRAVITY is also a powerful spectro-imager with milli-arcsecond resolution that will open new scientific avenues from the measurements of AGN's broad-line regions to the detection of young-stellar objects jets at the spatial scales where they form.

GRAVITY requires a significant modification of the VLTI infrastructure in order to reach the astrometric capability. The following subsystems will have to be implemented:

– infrared wavefront sensors for the MACAO adaptive optics at each UT focus in order to peer through extinct environments (e.g the Galactic Center);

– star separators (STS) at each telescope focus (UTs and ATs) in order to feed the adaptive optics systems (UTs) and to provide a pupil control capability thanks to the STS' variable curvature mirrors;

– a metrology system that projects a laser light all-the-way down to the primary space (telescope spiders) where the optical path distance will be measured.

GRAVITY is currently scheduled to begin operations in $\approx$ 2016.

**MATISSE** is a four telescope beam combiner that will be operating in the L, M and N bands. It will be opening the $[3, 5]\mu$m window for the first time in interferometry offering a unique window at warm $\approx$ 700K dusty and gaseous environments (spectral resolutions 30, 50, 2000). The spatial scales probed will correspond to those of ALMA at its maximum resolution providing a complementary insight at the properties of stellar environments. With MATISSE the considerable increase in u,v coverage will be instrumental to lift the usual degeneracies one is faced with when using a few two-telescope observations.

MATISSE is particularly expected in the following domains:

– circumstellar environments of young low and intermediate mass stars;

– formation of massive stars (usually deeply embedded);

– exozodiacal dusty disks;

– dusts and winds from evolved stars;

– the close environments of hot stars;

– the dusty environment of active galactic nuclei.

In particular the imaging capability of MATISSE is expected to play a role in revealing the exact morphology of AGNs mid-infrared and confirm the recently discovered elongated structure along the polar axis (Hoenig et al. 2013) that could be attributed to a wind component. This could trigger a significant revision of the unification scenario.

Matisse is currently scheduled to begin operations in $\approx$ 2017.

**PIONIER** is expected to stay on the mountain after the laboratory has been adapted to GRAVITY and MATISSE. A specific location has to be found in the laboratory. A possible evolution for PIONIER could be to implement medium resolution (e.g a few 100) to enable observations of dusty environments with dusty molecular composition such as Mira stars.

### 3.2 Challenges for the VLTI

In the coming year the VLTI will be confronted with several important challenges starting with the preparation of the infrastructure for GRAVITY and MATISSE. This includes, among others, the completion of all STS, the laboratory modification, the re-commissioning of the ensemble together with a revision of operational procedures.

Following that four main challenges will have to be tackled.

**The challenge of performance.** In order to improve VLTI instruments overall performances a certain number of actions are considered.

1. provide ATs with an adaptive optics system called NAOMI to reduce VLTI sensitivity to weather conditions and in particular to improve the coupling into single-mode instruments and limit the flux dropouts in fringe trackers. The project is currently preparing for PDR at the fall 2014;

2. an active, metrology-based, vibration control is currently considered for the UTs. It should start with a phase A study.

3. a second generation fringe tracker was initially envisioned. It is mandatory for MATISSE to reach its ultimate performances. Based on resources constraints it is currently delayed. It is expected that the GRAVITY fringe tracker will bring significant expertise once in operation.

Another item relevant of performance will be the overall capability to schedule programs. A modification of the scheduling to better address this problem will probably lead to certain limitations in the configuration flexibility offered to the PI with the advantage of better scheduling of more OBs. Increasing service mode is another way to improve the scientific return and best-seeing exploitation at the VLTI.

**The challenge of imaging.** Paving homogeneously the u,v plane is a critical demand of imaging programs. The currently offered configurations are probably not far from the optimum of what can be realistically done operationally. Some progress can probably be made in offering better u,v-filling ones. The possibility to choose between four telescope out of two UTs and four ATs is an interesting idea that is currently being evaluated but that will probably be facing hard technical limitations (different static opd, beam stopping etc.).

The preparation and observing tools will have to evolve since a typical imaging program will request several tens (hundreds ?) of OBs. Following the progresses of the program throughout the service mode schedule will be a first challenge. The user will have also to generate an important quantity of OBs in a user-friendly way. Finally image reconstruction softwares will have to become widely available although it is very probably that the expertise on how to use them correctly will remain the knowledge of a few.

From the astrophysical point of view the temporal variability of the objects will be a strong constraint in the scheduling. It is probable that it will hard to get a full u,v configuration in less than three weeks.

**The challenge of narrow angle astrometry** The PRIMA team has accumulated a lot of expertise in understanding issues related to the calibration of astrometric measurements. GRAVITY's astrometric requirements will be equally tough even though in practice the exact system implementation and requests are not identical. The PRIMA knowledge will have to be passed onto the GRAVITY project

**The challenge of growing the community** A considerable effort has been done to provide the VLTI users with easy to use observation preparation and data reduction software. Both ESO and Jean-Marie Mariotti Center (JMMC) are accompanying the users. However optical interferometry still requires a significant technical knowledge. Increasing the community of users will require to carry-on a significant effort to provide services similar to ALMA nodes. The accessibility to reduced data directly from the archive or to specialists capable of reducing the data or carrying on the image reconstruction should be an ambitious goal set in agreement between the community and ESO.

## 4. Concluding remarks

As can be seen it is very probably the next decade will be busy bringing VLTI and its three instrument GRAVITY, MATISSE and PIONIER to their full performance.

It is hard to project the VLTI in the Extremely Large Telescope era not knowing exact timescales. However one can envision a few incentives to continue the exploitation of VLTI:

- no faint companion instrument has been contemplated so far at VLTI. Although PIONIER has shown very good capability at searching for companion it is clear that there is an important margin of progress if the instrument is properly designed for this sole purpose.
- the combination of the intrinsically diffraction limited VLTI observations, the spectro astrometry technique and maximum baselines of 150m will keep VLTI has the european instrument with the highest resolving power. Going towards shorter wavelengths (e.g the visible) with high spectral resolution, while challenging, could open new windows complementary to other techniques such as asteroseismology. This could pave the way of direct characterisation of stellar surfaces in the transit missions context.
- extending the array combination capability to six or eight telescope, while probably unrealistic in the current funding situation, would probably be a considerable progress to restore the true complexity of close circumstellar environments and in particular monitoring time-variable astrophysical flows (accretion, winds, jets, shocks) on the scale of a few days. It would also reduce considerable the telescope reconfiguration requirements on the mountain.

## References

Eisenhauer et al. 2011, Msngr, 143

Haguenauer et al. 2012, SPIE 8445
Hoenig et al. 2013, ApJ, 771
Kervella et al. 2004, A&A, 426
Mérand et al. 2012, SPIE 8445
Pott et al. 2012, SPIE 8445
Poupar et al. 2010, SPIE 7734

*Improving the performances of current optical interferometers & future designs*
*Proceedings of Haute Provence Observatory Colloquium (23-27 September 2013)*
*Edited by L. Arnold, H. Le Coroller & J. Surdej*

# Near Term Plans for Upgrades at the CHARA Array

Theo ten Brummelaar

*Georgia State University - The CHARA Array, PO Box 48, Mount Wilson CA 91023, U.S.A. (theo@chara-array.org)*

**Abstract.** The CHARA Array of Georgia State University has now been performing regular science observations for a decade and our list of collaborators continues to expand. Nevertheless, apart from the addition of beam combiners contributed by these collaborators there has been no major upgrade of the CHARA facilities since it's construction. In this talk I will describe the current status of the CHARA Array hardware and then describe the upgrades currently being built or planned. Active upgrade projects include our Adaptive Optics program funded by the National Science Foundation, and a new collaboration with the Max Planck Institute for Radio Astronomy in Bonn to upgrade the detector systems for the CLASSIC/CLIMB beam combiner. I will also discuss our plans for other future upgrades to the CHARA Array facilities.

The material presented at the conference has recently been published and the author proposes to the reader the references below.

## References

ten Brummelaar, Theo A.; Sturmann, Judit; McAlister, Harold A.; Sturmann, Laszlo; Turner, Nils H.; Farrington, Chris D.; Schaefer, Gail; Goldfinger, P. J.; Kloppenborg, Brian 2012, "Data analysis for the CHARA Array CLIMB beam combiner", in Optical and Infrared Interferometry III. Proceedings of the SPIE, Volume 8445, article id. 84453C, 13 pp.

McAlister, Harold A.; ten Brummelaar, Theo A.; Ridgway, Stephen T.; Gies, Douglas R.; Sturmann, Judit; Sturmann, Laszlo; Turner, Nils H.; Schaefer, Gail H.; Boyajian, Tabetha S.; Farrington, Christopher D.; Goldfinger, P. J.; Webster, Larry 2012, "Recent technical and scientific highlights from the CHARA Array", in Optical and Infrared Interferometry III. Proceedings of the SPIE, Volume 8445, article id. 84450H, 13 pp.

*Improving the performances of current optical interferometers & future designs*
*Proceedings of Haute Provence Observatory Colloquium (23-27 September 2013)*
*Edited by L. Arnold, H. Le Coroller & J. Surdej*

## Design Optimization Considerations for the MROI

M. J. Creech-Eakman[1,2], D. F. Buscher[1,3], C. A. Haniff[1,3] & MROI team

[1]*Magdalena Ridge Observatory Interferometer, NMT, Socorro, NM, 87801*

[2]*New Mexico Institute of Mining and Technology, Socorro, NM, 87801*

[3]*Cavendish Laboratory, Astrophysics Group, University of Cambridge, Cambridge, UK*

**Abstract.** The Magdalena Ridge Observatory Interferometer (MROI) has been conceived to be a 10 element 1.4m aperture imaging interferometer working in the optical and near-infrared and located at a altitude of 10,500 feet in the mountains of south-central New Mexico. When designing the MROI, we attempted to take lessons learned from the design of other similar facilities and specifically considered sensitivity, speed of data collection, scalability and mobility of the design, along with polarization preservation and imaging capabilities to attain the present model for the facility. Several papers detailing the specifics of the design of the MROI and the philosophy behind the certain choices or trade-offs have been published in the past few years. These references and those listed therein are listed below.

### References

Buscher, D. F. et al., 2013,"The Conceptual Design of the Magdalena Ridge Observatory Interferometer", Journal of Astronomical Instrumentation, 2, 2, 1340001.

Creech-Eakman, M. J. et al., 2012, "The Magdalena Ridge Observatory interferometer: a status update", in Proc. of SPIE, Optical and Infrared Interferometry III, 8445, 84450P.

Jurgenson, C. A. et al., 2013, "ICONN - the Infrared Coherencing Nearest Neighbor Tracker", Journal of Astronomical Instrumentation, 2, 2, 1340006.

Santoro, F. G., et al., 2012, "Final mechanical and opto-mechanical design of the Magdalena Ridge Observatory Interferometer", in Proc. of SPIE, Optical and Infrared Interferometry III, 8445, 8445E.

*Improving the performances of current optical interferometers & future designs*
*Proceedings of Haute Provence Observatory Colloquium (23-27 September 2013)*
*Edited by L. Arnold, H. Le Coroller & J. Surdej*

# Update on the LBTI: a versatile high-contrast and high-resolution infrared imager for a 23-m telescope

D. Defrère[1], P. Hinz[1], A. Skemer[1], P. Arbo[1], V. Bailey[1], G. Brusa[1], T. Connors[1], E. Downey[1], O. Durney[1], J. Eisner[1], P. Grenz[1], B. Hoffmann[1], J. Hill[1], J. Leisenring[1], T. McMahon[1], B. Mennesson[3], R. Millan-Gabet[2], M. Montoya[1], M. Nash[1], M. Skrutskie[4], R. Sosa[1], and V. Vaitheeswaran[1]

[1]*Steward Observatory, University of Arizona, 633 N. Cherry Avenue, 85721 Tucson, USA*

[2]*NASA Exoplanet Science Center (NExSci), California Institute of Technology, 770 South Wilson Avenue, Pasadena CA 91125, USA*

[3]*Jet Propulsion Laboratory, California Institute of Technology 4800 Oak Grove Drive, Pasadena CA 91109-8099, USA*

[4]*University of Virginia, Department of Astronomy, 530 McCormick Road, Charlottesville, VA 22904-4325, USA*

**Abstract.** The Large Binocular Telescope Interferometer (LBTI) is a strategic instrument of the LBT designed for high-sensitivity, high-contrast, and high-resolution infrared imaging of nearby nearby planetary systems. It combines the two 8.4-m apertures of the LBT in various ways including direct (non-interferometric) or Fizeau imaging, non-redundant aperture masking, and nulling interferometry. First fringe-tracked observations were obtained in December 2013. We report in this paper on the status and recent progress of the LBTI with a particular focus on interferometry.

## 1. Introduction

The LBTI is a NASA-funded interferometric instrument designed to coherently combine the two 8-m primary mirrors of the LBT for high-sensitivity, high-contrast, and high-resolution infrared imaging ($\geq 3\mu$m). It is developed and operated by the University of Arizona and based on the heritage of the Bracewell Infrared Nulling Cryostat (BLINC) on the MMT (see e.g., Hinz et al. 2000). It is equipped with two scientific cameras: LMIRcam (the L and M Infrared Camera) covering the 3-5$\mu$m range and NOMIC (Nulling Optimized Mid-Infrared Camera) covering the 7-25$\mu$m range. The main scientific goals are to determine the brightness and prevalence of exozodiacal dust and image giant planets around nearby main-sequence stars. Two surveys are currently being carried out in that respect: an exozodiacal dust survey called HOSTS (Hunt for Observable Signatures of Terrestrial Planetary Systems, Weinberger et al. 2014) and a planet

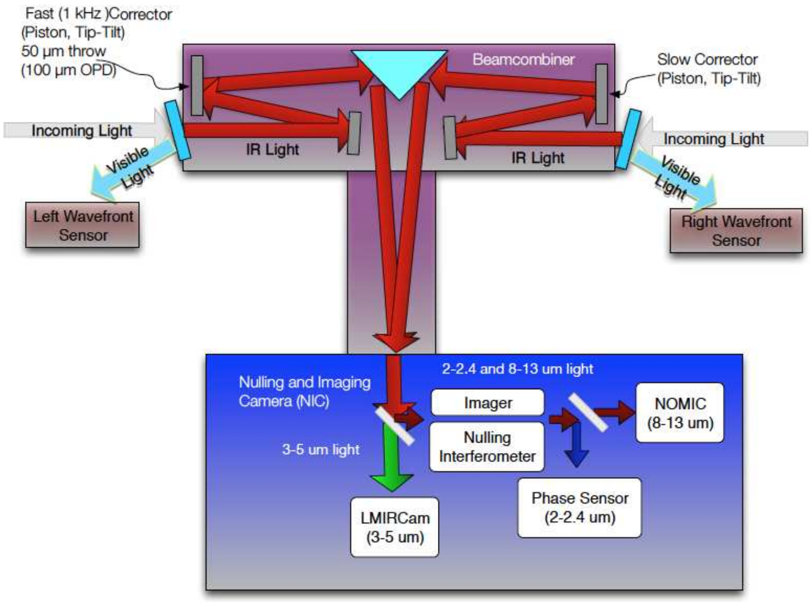


Figure 1.: *Components of the LBTI shown with the optical path through the beam combiner and the NIC cryostat. Starlight is reflected on LBT primaries, secondaries, and tertiaries before coming into this diagram on the top right and top left. The visible light is reflected on the entrance window and used for adaptive optics while the infrared light is transmitted into LBTI, where all subsequent optics are cryogenic. The beam combiner directs the light with steerable mirrors and can adjust pathlength for interferometry. Inside the NIC cryostat, 3-5µm light is directed to LMIRCam for exoplanet imaging, 2.0-2.4µm light is directed to the phase sensor, which measures the differential tip/tilt and phase between the two primary mirrors, and 8-13µm light is directed to NOMIC for Fizeau imaging or nulling interferometry.*

survey called LEECH (LBTI Exozodi Exoplanet Common Hunt, Skemer et al. 2014). We describe in this paper the different interferometric modes implemented in the LBTI and show some early results.

## 2. The instrument

The LBTI consists of a universal beam combiner (UBC) located at the bent center Gregorian focal station and a cryogenic Nulling Infrared Camera (NIC). The UBC provides a combined focal plane from the two LBT apertures while the precise overlapping of the beams is done in the NIC cryostat. The optical design for NIC uses reflective optics to accommodate the wide wavelength range that the LBTI covers. Both the short and the long wavelength channels have an intermediate pupil plane for cold baffling, and nulling beam combination or coronagraphy, as well as an intermediate focal plane for insertion of slits or obscuration spots.

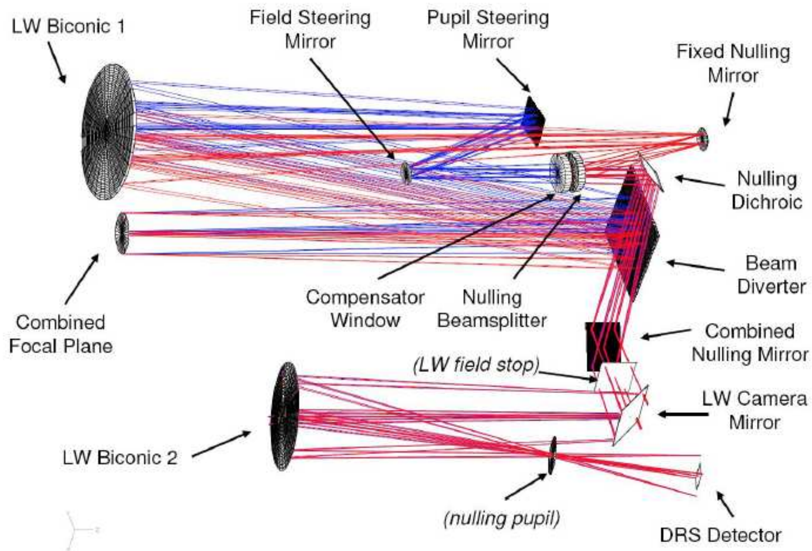


Figure 2.: *Optical layout of NOMIC. The light enters from the left side, is reflected by the beam diverter and reimaged by LWBC 1. A set of flat mirrors overlap the two beams on a beamsplitter. One output of the interferometer is relayed via LWBC 2 to the science detector.*

Besides the two science cameras, the NIC cryostat also houses a K-band fast readout camera (Phasecam) to sense phase variations between the LBT apertures and carry out fringe tracking. A range of cryogenic actuators and alignment mechanisms have been developed to carry out fine alignment of the interferometer and to feed the several channels of NIC. Figure 1 shows the optical path through the UBC and NIC. The three cameras are described hereafter.

- LMIRCAM is the mid-infrared optimized science camera equipped with a Hawaii-2RG detector which has a very fine plate-scale (0.01arcsec/pixel) to sufficiently sample the LBT's interferometric PSF. It contains various filter options, including L-band, M-band, PAH-on (at 3.3 $\mu$m), PAH-off, Br$\alpha$, and $H_2O$ ice. A grism for low resolution spectroscopy (R$\sim$350), a vector-vortex coronagraph (AGPM, Mawet et al. 2013), and non-redundant aperture masks are also available. The first observations made by overlapping the light from both telescopes have been published recently (Skemer et al. 2014).

- NOMIC is the long-wavelength camera used in particular for nulling interferometry. Figure 2 shows the optical path from the combined focal plane to the Raytheon Aquarius Detector. The detector is a 1024x1024 Blocked Impurity Band (BIB) hybrid array with 30-$\mu$m pixels. The optics provides a field of view of 12 arcsecs with pixels of 0.018 arcsecs in size. $\lambda/D$ for an individual aperture is 0.27 arcsecs at 11$\mu$m. For Fizeau interferometry with the two apertures, it is 0.10 arcsecs (or 5.5 pixels).

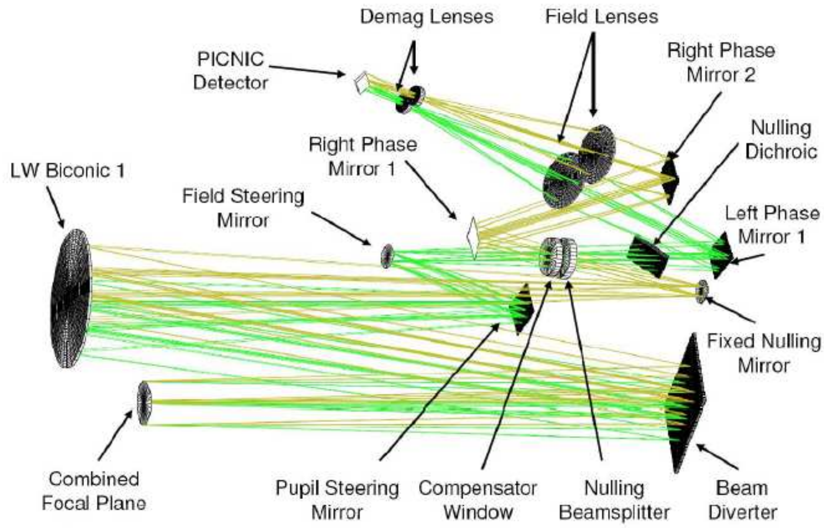


Figure 3.: *Optical layout of Phasecam. The outputs of the nulling beamsplitter are directed via several lenses to two quadrants of a PICNIC detector.*

– PHASECAM is the near-infrared camera equipped with a PICNIC detector that is used for fringe sensing. It receives the light from both interferometric outputs whether the long wavelength channel is in nulling or imaging mode. The only difference is a dichroic which is inserted after the LW biconic 1. A set of reimaging lens are placed at the pupil to create a FOV of 10 arcsecs. Several filter wheels are placed in the beam. One provides for varying neutral density filter to be placed in the the wheel. A second wheel provides for filtering or insertion of a low-dispersion prism into the beam. The reimaging lens are mounted on a wheel to allow for insertion of a second set of lenses that can reimage the pupil, rather than the star.

More information about the cameras and the design of NIC can be found in Hinz et al. (2008) and Skrutskie et al. (2010).

## 3. Interferometric observations

The LBT is an ideal platform for interferometric observations because the individual telescopes are installed on a single steerable mount. This design does not require long delay lines and contains relatively few warm optical elements which provides an exceptional sensitivity. The interferometric combination can be performed in image plane for Fizeau imaging or in pupil-plane for nulling interferometry. These two different modes are described hereafter and illustrated with some commissioning results.

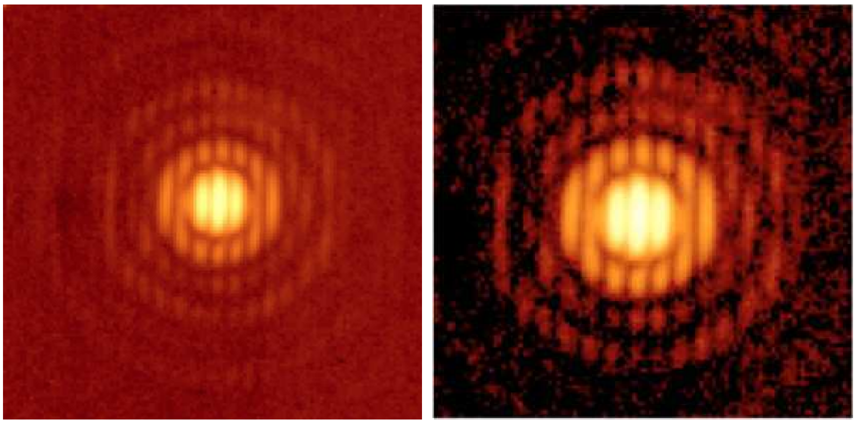

Figure 4.: *Fizeau interferometric PSF at 4.0 $\mu$m and 11.0 $\mu$m obtained respectively with LMIRcam and NOMIC.*

### 3.1 Fizeau interferometry

Fizeau interferometric imaging is available on both science channels separately or simultaneously. Since the high angular resolution direction is always parallel to the horizon and perpendicular to the parallactic angle, aperture synthesis is achieved by sky rotation and provides the resolution of 22.8-m telescope. Fig. 4 shows the interferometric PSF obtained at 4.0 $\mu$m with LMIRcam (left) and at 11.0 $\mu$m with NOMIC (right).

### 3.2 Nulling interferometry

Nulling interferometry is a technique proposed by Bracewell 35 years ago to image extra-solar planets (Bracewell 1978). The basic principle is to combine the beams coming from two distinct telescopes in phase opposition so that a dark fringe appears on the line of sight, which strongly reduces the stellar emission while transmitting the flux of off-axis sources located at angular spacings which are a multiple of $\lambda/b$ (where $b$ is the distance between the telescope and $\lambda$ the wavelength of observation). The technique has now been successfully used on sky both in the near-infrared (Mennesson et al. 2011) and the mid-infrared (e.g., Stock et al. 2010, Millan-Gabet et al. 2011) and the performance required to directly detect exoEarths demonstrated on laboratory testbeds (Martin et al. 2012).

Nulling interferometry with the LBTI was first achieved in September 2012 without fringe and tip/tilt stabilization. The null measurements were randomly fluctuating between constructive and destructive interference, following the random atmospheric pathlength variations. In December 2013, first fringe-tracked nulling observations were obtained on several bright stars. A 4-min null sequence is shown in Fig. 6 with its corresponding null histogram. The goal of these observations was to demonstrate null stabilization rather than a deep null depth (the optical pathlength difference coarsely adjusted). Tools to optimize the null depth and stability are currently being tested.

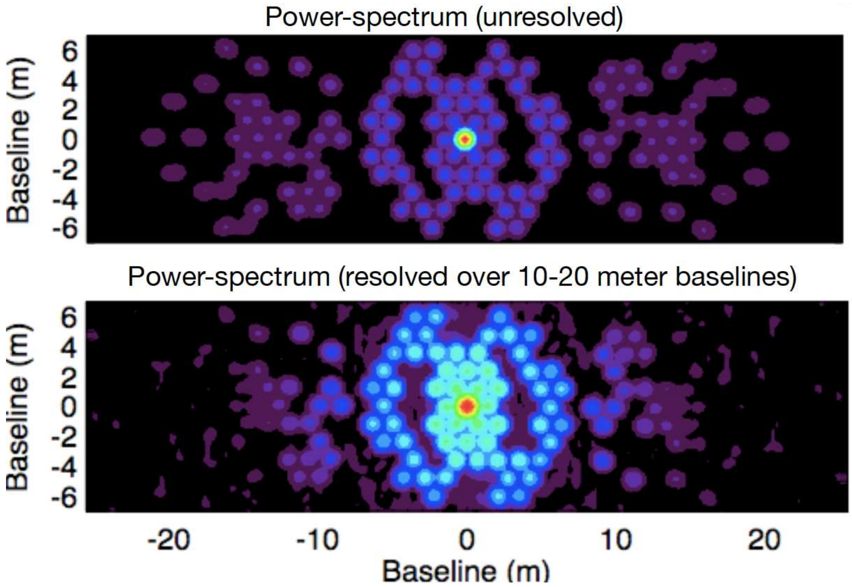


Figure 5.: *Example of non-redundant aperture masking observation with the LBTI. The figure shows the power spectrum of an unresolved calibrator (top) and a bright, previously imaged, YSO (bottom). The latter is heavily resolved especially on baselines longer than approximately 10m.*

### 3.3 Non-redundant aperture masking

The L-band channel of NIC currently contains two non-redundant aperture masks, one with 12 holes and one with 24 holes. An example of observation is shown in Fig. 5 for two relatively bright objects (L<4): an unresolved calibrator (top) and a bright, previously imaged, YSO (bottom) which is heavily resolved especially on baselines longer than about 10m. The observations were achieved without AO correction nor fringe tracking and a short enough integration time was used to freeze the atmospheric piston. AO correction and fringe-tracking are now available and will enable the same sort of data for fainter objects. Image reconstruction is currently under progress.

### 3.4 Fringe tracking

Fringe tracking is performed in the near-infrared portion of NIC and uses the PICNIC camera described above (see optical layout in Fig. 3). A range of optics can be used to create different setups for pathlength and tip/tilt sensing, including the use of relative intensity between the two interferometric outputs, dispersed fringes, or an image of the combined pupils. A large (80 pixel) pupil image of the starlight can be formed for diagnostics, as well as stellar images, and small (18 pixel) pupils. H or K band filters can be used. These various optics allow a flexible approach to phase sensing. So far, fringe sensing has been mainly performed using an image of pupil fringes (equivalent to wedge fringes). Because of dispersion between 2 $\mu$m and 10 $\mu$m in the beamsplitter, a well overlapped

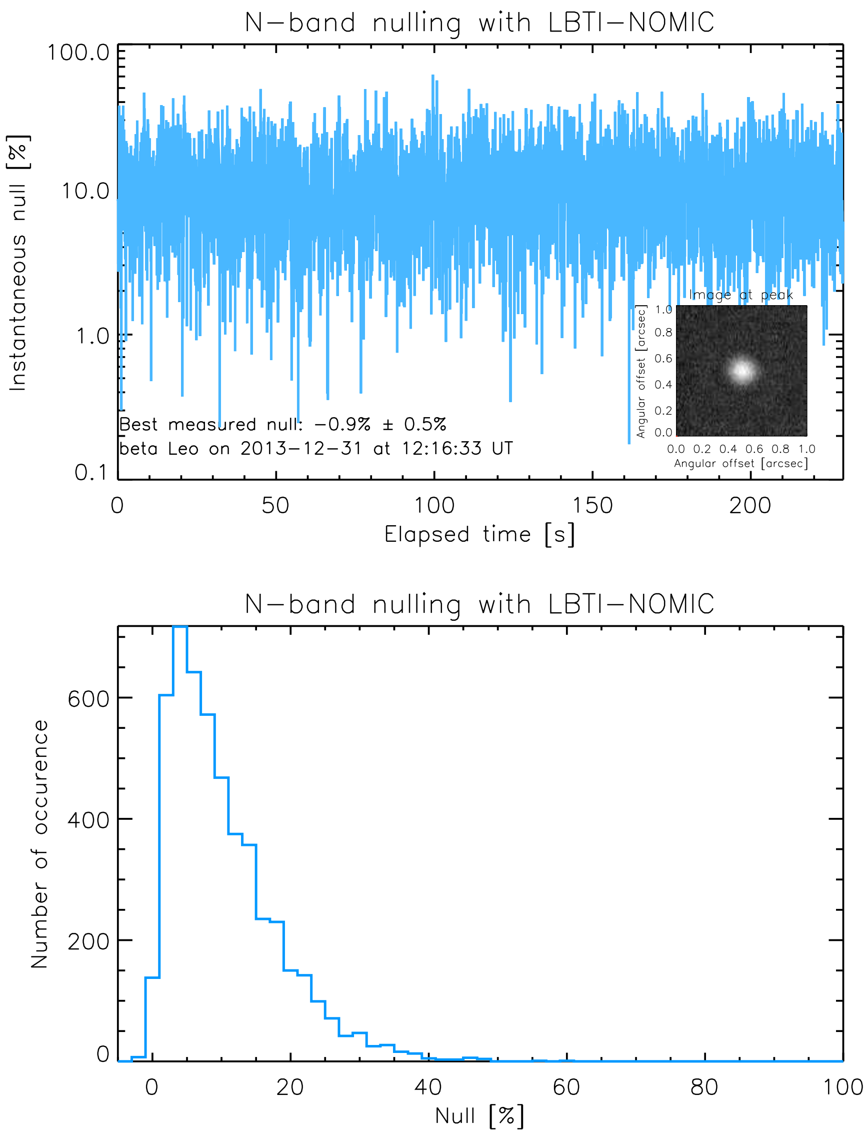


Figure 6.: *One of the first fringe-tracked null sequence obtained on December 31st 2013 at N-band (top figure). The bottom figure shows the corresponding null histogram which peaks at a null of ∼5%.*

set of images at 10 $\mu$m corresponds to a tilt difference of roughly 3 fringes across the pupil at 2 $\mu$m. This has the nice feature of providing a signal in the Fourier plane well separated from the zero-frequency component and allow us to separate tip-tilt and phase variations via a Fourier transform of the detected light. The magnitude of the Fourier transform gives a measurement of the tip/tilt while the phase of the Fourier transform gives a measurement of the optical path delay.

Fringe tracking has been carried out at 1kHz so far and could go as fast as 4 kHz in the near future.

## 4. Status and schedule

The LBTI has reached several important milestones over the past few years and is on good tracks toward routine coherent imaging observations. First fringes were obtained in October 2010, just one month after the installation on the telescope, dual-aperture AO-corrected fringes in April 2012, and first nulling observations in September 2012. The first fringe-tracked observations were obtained in December 2013 using a technique equivalent to group-delay tracking. Most of the efforts are now focused on implementing phase tracking and improving the null depth and stability.

## References

Bracewell 1978, Nature, 274, 780
Hinz P. et al., 2001, SPIE, 4006, 349
Hinz P. et al., 2008, SPIE, 7013
Martin et al., 2012, AO,51, 2907
Mawet D. et al., 2013, SPIE, 8864
Mennesson et al., 2011, ApJ, 243, 178
Millan-Gabet et al., 2011, ApJ, 734, 67
Skemer A. et al., 2014, ApJ, accepted
Skemer A. et al., 2014, IAU, 299, 70
Skrutskie et al., 2010, SPIE, 7735
Stock et al., 2010, ApJ, 724, 1238
Weinberger A. et al., 2014, AAS, 223, 350

*Improving the performances of current optical interferometers & future designs*
*Proceedings of Haute Provence Observatory Colloquium (23-27 September 2013)*
*Edited by L. Arnold, H. Le Coroller & J. Surdej*

# Mid-infrared heterodyne interferometry with the Infrared Spatial Interferometer

E. H. Wishnow

*Space Sciences Laboratory and Department of Physics, University of California, Berkeley, CA 94720, USA (wishnow@ssl.berkeley.edu)*

**Abstract.** The Infrared Spatial Interferometer (ISI) is a three telescope array located at Mt. Wilson. It is a unique mid-IR system that uses heterodyne detection with CO2 lasers as local oscillators. Mid-IR measurements of red supergiant stars and Asymptotic Giant Branch stars have been conducted for about 20 years. The ISI provides precision measurements of stellar sizes and asymmetries, and also measurements of the dust shells surrounding these stars. We have observed changes of these quantities over time periods of weeks to decades. A new high-speed digital spectrometer-correlator has recently been built. It will provide a new capability to measure stellar visibilities on-and-off individual molecular spectral lines. These spectro-interferometric measurements will help determine the nature of extended stellar atmospheres.

The material presented at the conference has recently been published and the author proposes to the reader the references below.

## References

V. Ravi, E. H. Wishnow, C. H. Townes, S. Lockwood, H. Mistry, K. Tatebe 2011, The Non-Uniform, Dynamic Atmosphere of Betelgeuse Observed at Mid-Infrared Wavelengths, ApJ, 740, 24

Edward Wishnow, Charles Townes, Vikram Ravi, Sean Lockwood, Hemma Mistry, Walt Fitelson, William Mallard, Dan Werthimer 2011, Observations of Late-Type Stars with the Infrared Spatial Interferometer, in 16th Cambridge Workshop proceedings on Cool Stars, Stellar Systems, and the Sun, Eds. C.K. Johns-Krull, M.K. Browning, A.A. West, ASP Conf. Series, Vol 448, p. 207

E. H. Wishnow, W. Mallard, V. Ravi, S. Lockwood, W. Fitelson, D. Werthimer, C. H. Townes 2010, Mid-Infrared Interferometry with High Spectral Resolution, in Proc. SPIE Vol. 7734, article id. 773409, Eds. W.C. Danchi, F. Delplancke, J. Rajagopal

*Improving the performances of current optical interferometers & future designs*
*Proceedings of Haute Provence Observatory Colloquium (23-27 September 2013)*
*Edited by L. Arnold, H. Le Coroller & J. Surdej*

# A possible future for space-based interferometry

L. Labadie[1], A. Léger[2], F. Malbet[3], W. C. Danchi[4], B. Lopez[5]

[1] *Physikalisches Institut, Universität zu Köln, Zülpicher Str. 77, 50937 Köln, Germany*

[2] *Institut d'Astrophysique Spatiale, UMR 8617 CNRS, Bât. 121, Université Paris-Sud, 91405 Orsay, France*

[3] *UJF-Grenoble 1, CNRS-INSU, Institut de Planétologie et d'Astrophysique de Grenoble (IPAG) UMR 5274, 38041 Grenoble, France*

[4] *NASA/Goddard Space Flight Center, Greenbelt, MD 20771, USA*

[5] *Laboratoire Lagrange, CNRS UMR 7293, UNSA Observatoire de la Côte d'Azur, BP 4229, 06304 Nice Cedex 4, France*

**Abstract.** We address the question of space interferometry following the recent outcome of the science themes selection by ESA for the L2/L3 missions slots. We review the current context of exoplanetary sciences and its impact for an interferometric mission. We argue that space interferometry will make a major step forward when the scientific communities interested in this technique will merge their efforts into a coherent technology development plan.

## 1. Introduction

In the late nineties and early 2000, the possibility of flying a large infrared interferometric space mission to search for Earth planets in the habitable zone of Solar-type stars and characterize them had materialized in the Darwin/TPF mission. In its most developed state the concept was based on a formation-flying four-telescope array operating as a nulling interferometer in the 6–20 $\mu$m wavelength range. The project was largely followed within the interferometric community and beyond, although there were never a full consensus – for many reasons, among which its cost – if that would be *the* mission concept on which to set programatic priorities. Both the European and US space agencies invested significant resources on these projects in order to improve the technological readiness of the mission. In 2007, the Darwin project was presented as a response to the ESA call for L1 missions (Léger et al. 2007). It was a 4×2-m telescope interferometer planned to do spectroscopy of ∼200 nearby Earth-size exoplanets over a 5-year mission lifetime. Unfortunately the proposal was not selected for further

study, but the AWG and SSAC[1] committees recommended "to initiate the technology development for Darwin". Such a comment was surprising considering the technological development that had already taken place in the last ten years for Darwin/TPF. Obviously this was not enough for the mission to be selected, in particular considering the state of the art of the formation-flying technology needed for the mission.
After 2007 the context has significantly evolved in terms of scientific results in exoplanetology and mission concepts, and activities in nulling interferometry slowly faded. In 2013 a new call for science themes in the perspective of the L2/L3 missions was issued by ESA, to which the exoplanetology community responded in a cohesive way (Quirrenbach et al. 2013) by putting together a proposal to search for habitable distant worlds. The selection of the gravitational wave and X-ray astrophysics as core science themes for the L2/L3 missions further delayed the possibility of building a space-based interferometric observatory for infrared high-angular resolution astronomy. Here we review the case of space-based interferometry in the new context of exoplanetary sciences and beyond the original objectives of Darwin/TPF.

## 2. Space interferometry and the link to exoplanetary science

### 2.1 Overview of the current landscape

In the last 15 years, numerous RV and transit surveys have evidenced the strong diversity of planetary systems around main-sequence stars, which only partially reflects our long standing view inspired by our Solar System. This diversity is largely observed in terms of size, mass, composition, temperature and orbit. It is not the goal of this section to discuss in detail the physical and chemical properties of the different classes of planets, but rather giving a qualitative overview of these properties as this could determine the need – or not – for an interferometric facility.

– **mass/size:** The search for smaller and lighter planets is a natural continuation of the surveys that explored the population of Hot-Jupiters. High-precision radial velocity surveys with $\sim 1\,\mathrm{m.s^{-1}}$ resolution and high-precision photometry of transits with COROT and Kepler allowed exploration of the lower-end of the exoplanetary mass distribution, bringing a new light onto the nature and properties of the extrasolar planets population. New RV measurements have entered the domain of Neptunes ($\sim$10–50 $M_\oplus$), Super-Earths ($\sim$2–10 $M_\oplus$) and Earth-mass ($\sim$0.5–2 $M_\oplus$) planets (cf. Mayor et al. (2009), Dumusque et al. (2012)[2] with HARPS). Transits measurements have constrained the radii of exoplanets, starting from the first measured Super-Earth (Corot-7b, Léger et al. 2009) down to sub-Mercury size planets (Kepler-37b, Barclay et al. 2013). Earth-like similarities – in mass and radius – have therefore been discovered (cf. www.exoplanets.eu), however limited to the case of short-orbit planets which are the most effectively commonly objects with these techniques. The combination of mass and radius observations have permitted measurement of the mean density even for the small-

[1] *Astronomy Working Group* and *Space Science Advisory Committee*

[2] The effective RV detection of Alpha-Centauri Bb has been questioned by Hatzes et al. (2013).

est planets, bringing first insight on their internal composition.

– **frequency:** Current statistics point out the probable high-occurrence rate of Earths and Super-Earths around FGKM stars, with ∼20 % occurrence rate around FGK stars (Howard et al. 2010; Fressin et al. 2013) and up to 50 % occurrence around M stars (Bonfils et al. 2013; Dressing et al. 2013). As mentioned earlier, these numbers must be taken with some precaution as they often correspond to extrapolations from the short-period planets effectively detected (i.e. P<50 days). The recent results obtained by HARPS, Corot and Kepler suggest that "small" planets, if detectable, are quite frequent. Theoretical modeling of the planetary Initial Mass Function (IMF) by the time the protoplanetary disk vanishes and under the core-accretion scenario seems to support this idea (Mordasini et al. 2009). In the context of a direct spectroscopy mission, this reservoir of planets would be have to be volume-limited to the closest objects (typically within ∼20 pc) because of SNR considerations. The plot of Fig. 1 shows the mass histogram of planets around F,G,K,(M) dwarfs within 20 pc and was built using data form the exoplanets.eu website. The case where M dwarfs are included is displayed separately (in blue) becasue of the observational and scientific challenge they represent. The graph indicates a bimodal distribution with a minimum at $\sim 30\,M_{\oplus}$, similarly to what is observed for the full population of planets around FGKM stars.

– **Earths, Super-Earths and HZ within 20 pc:** Although the spectroscopic characterization of Neptunes and Jupiters with H-He-rich atmospheres is intrinsically interesting for comparative planetology, the case of small rocky-core planets with potential habitable atmospheres ($CO_2$-$N_2$-$H_2O$-$O_2$) is central to address the question of habitability, provided we are able to detect them and take a spectrum of the exoplanet with adequate resolution. Hence we concentrate here on the case of Earths and Super-Earths (SE) by analyzing the population of

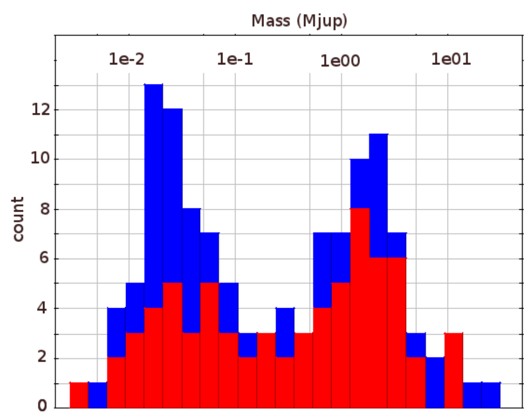


Figure 1.: *Mass histogram for planets orbiting main sequence stars within 20 pc built with data from exoplanet.eu. Red bars correspond to planets orbiting F,G,K stars, while blue bars include the M dwarfs.*

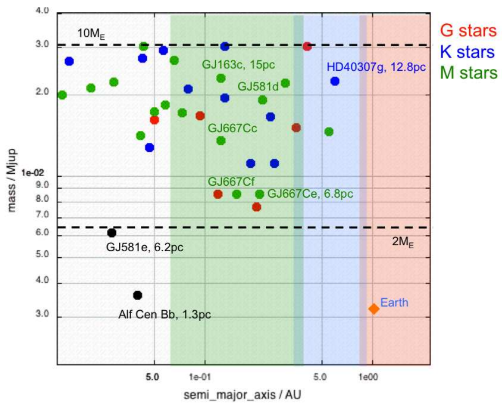


Figure 2.: *Separation in AU for all Earths and Super-Earths detected within 20 pc. The color code reports to G, K and M stars. The position of our Earth is shown for comparison.*

currently detected Earths and SE within 20 pc and its relevance to the Habitable Zone (HZ). Fig. 2 displays the minimum mass of a planet up to 10 $M_\oplus$ – taken as an upper limit for the mass of a Super-Earth – as a function of the separation from the host star in AU. It concerns all the Earths and Super-Earths detected within 20 pc which have been so far only detected only around G, K and M stars. Their position with respect to the HZ of their respective star – in green, blue and red – is shown as well. Without discussing the observational biases of the technique leading to this plot, we see that 1) SE constitute a considerable reservoir of targets for spectroscopic follow-up as they are more easily detected than their low-mass counterparts; 2) the M stars correspond to the sample with the larger number of detected planets lying in their HZ; 3) The number of detected nearby (Super)Earths per year shows a rising trend and we can reasonably expect that this sample will further increase (cf. Fig. 3).
Planets in the HZ of M-dwarfs has often been presented has a difficult case for habitability due to tidal locking and strong stellar flares/UV radiation field (e.g. Kasting 1993; France et al. 2013). Not surprisingly other studies suggest that such conditions do not exclude the possibility for a planet to be habitable (cf. Haberle et al. 1996; Pierrehumbert 2011; Segura et al. 2010). Considering that there are roughly ten times more nearby M dwarfs than G dwarfs (Chabrier 2003) and that $\eta_\oplus$ increases with later spectral type, it does not appear justified for a future mission to exclude M dwarfs from its list of targets (see Sect. 2.3 for the instrumental implications).
We also wish to stress here the fact that the overlap between the concepts of Habitable Zone – in its classical description – is a matter of debate within the exoplanet community. Should we focus on the HZ to characterize habitable planets, or not? That is the question! There is a long-standing ongoing debate on this point, which is difficult to solve because of the current lack of evidence for signs of habitability. New theories as “Superhabitable Worlds” have been pulled in

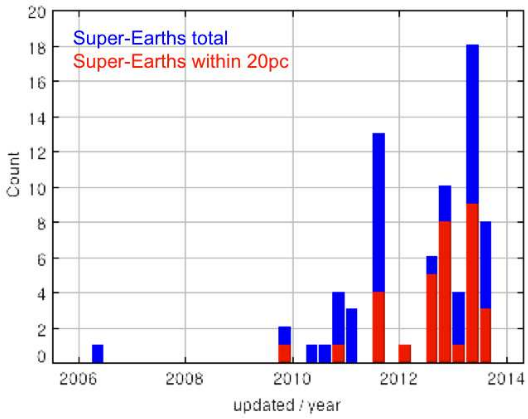


Figure 3.: *Time evolution histogram illustrating the detection rate of Super-Earths.*

the discussion (Heller & Armstrong 2014) and need to be followed, as they might have a significant impact on the future design of a spectroscopic mission.

## 2.2 Summarizing points

We summarize hereafter the pertinent points that will help us to make the case of infrared interferometry in the field of exoplanets.

– Both observational and theoretical studies suggest that the occurrence of small Earths and Super-Earths planets around F,G,K,M is higher than for more massive Neptunes and Jupiters. Provided suitable observatories are able to detect them, we will benefit of a large reservoir of candidates to address the question of habitability through spectroscopy. Because of the profound scientific importance of this question, it is meaningful to address the design of a future L-class spectroscopic mission with the prime objective of characterizing Earths and Super-Earths rather than Extrasolar Giant Planets (EGPs) atmospheres.

– How far should Earths and Super-Earths candidates to direct spectroscopy be picked up? The population of small planets discovered by Kepler are inaccessible to a spectroscopic mission because to distant and faint. It is generally assumed that for direct spectroscopy of Earths and Super-Earths by a 1 G€ mission it is necessary to choose targets within $\sim$20 pc in order to ensure a high enough signal-to-noise.

– Is there a preferential main sequence star spectral type that will be targeted by a future spectroscopic mission? A first level of answer is to consider that a future spectroscopy mission will be designed to characterize already detected Earths and Super-Earths around whatever spectral type, hoping that the sample of small planets within 20 pc will be large enough. Within a more selective approach, while G and K stars can be considered as natural targets, the case of M and F dwarfs deserves some more attention. As mentioned earlier, the close environment of M dwarfs appears quite extreme for habitability, but this is still a matter of debate. On the positive side, the requirement on the planet/star contrast is relaxed compared to earlier spectral types, and despite the small angular size of their Habitable Zone, the latter remains accessible with an interferometer (cf. Section 2.3). Furthermore, the high number of nearby M dwarfs[3] coupled with an expected higher $\eta_\oplus$ ($\sim 50\%$) and to the increasing observing survey capabilities of small planets around them is a convincing fact for including M stars in the targets sample of a future mission. F stars are brighter and with a wider HZ, but rarer in the solar neighborhood. While intrinsically interesting as well – they are included in both the Darwin (Kaltenegger et al. 2010, K10) and in the NEAT (Malbet et al. 2012, M12) catalogs – only new data delivered by TESS and PLATO will reliably inform us on the frequency of small planets around F stars. Key information will also be delivered by the LBTI, which will contribute to quantify the level of exoplanetary dust potentially masking the faint signal of planets candidate to spectroscopy.

– What is the optimal spectral range where to operate? From a purely scientific point of view, this is an unsolvable question. While broad and deep molecular bands can be traced in the mid-infrared (e.g. $CO_2$, $O_3$), $H_2O$ and $O_2$ features could be detected in the UV-Optical-NIR domains with R$\sim$100 with concepts like LUVOIR (Kouveliotou et al. 2013). From the mission concept point of view, it remains that if the mid-IR is the spectral range of interest, only the interferometric design will have the capability to resolve the HZ around the coolest main sequence stars.

### 2.3 Instrumental concepts to access the Habitable Zone

The spectroscopic characterization of exoplanets *in the HZ* of their host star is relevant for the question of habitability based on liquid water. In the recent years, comparative exoplanetology via transit spectroscopy such as proposed by the EChO mission has raised significant interest in the community. The goal is to achieve infrared low-resolution spectroscopy of a variety of short-period ($\sim$tens of days) and warm (>400 K) transiting Neptunes and Jupiters around solar-type stars. When constraining the case of small planets with thin atmospheres orbiting within the HZ of their host, the requirement for a sufficient SNR and a star/planet contrast smaller than $10^{-5}$ practically limit the observations to one or two M stars within 10 pc[4] (cf. EChO proposal). For the spectroscopy of longer-period planets, direct detection techniques are better adapted as they can offer immediate and unambiguous identification of spectroscopic features. Concretely this translates into either a coronographic or interferometric space mission as this has been developed in the proposal to the ESA call for an L3 mission. Fig. 4 shows for all the F,G,K,M stars of the Darwin catalog (Kaltenegger et al. 2010) the radius of the Habitable Zone in milliarcseconds as a function of the distance to the

[3]We list, respectively, 351 Ms, 536 Ks, 235 Gs and 107 Fs within 30 pc (K10); 82 Ks, 65 Gs, and 53 Fs within 20 pc (M12); 248 Ms, 44 Ks, 20 Gs, 6 Fs within 10 pc (www.recons.org).

[4]Assuming a population of $\sim$250 Ms within 10 pc, a $\eta_\oplus$ $\sim$50% and a $\sim$1% transiting probability leads to 1.25 planet.

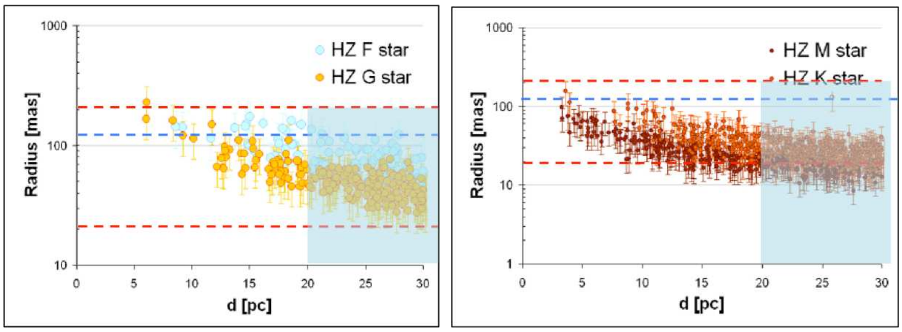


Figure 4.: *Overview of the accessible habitable zones as a function of distance and spectral types for an optical coronograph and an infrared interferometer, with respectively blue and red horizontal dashed line. (adapted from Kaltenegger et al. 2010)*

star up to 20 pc. The horizontal dashed lines define the upper and lower angular resolution limits for the habitable zones that can be spatially resolved in the two following cases: the blue dashed line sets the $2.5\times\lambda/D$ IWA limit of a 2.5-m

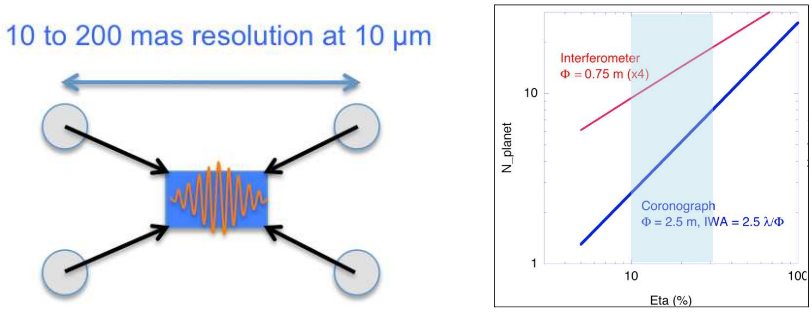


Figure 5.: *Left: schematic of the architecture of a descoped Emma-array configuration for an interferometer with 0.75-m diameter apertures. Right: number of habitable Earth/Super-Earth planets detected via optical coronogaphy and infrared interferometry as a function of $\eta_\oplus$ for FGK stars. This graph assumes prior detection, 5-year mission lifetime for spectroscopy, and R=20 at 10 $\mu$m (A. Léger, private comm.).*

coronograph operating at $\lambda$=0.7 $\mu$m (although $4\times\lambda/D$ would be more realistically feasible). Only the points above this line correspond to a directly accessible HZ. The red lines set the upper and lower resolution limit of an interferometer operating at 10 $\mu$m with a baseline tunable from 5 to 50 m.
From simple considerations on the achievable angular resolution, it appears that only the interferometric approach allows the observation of a large number of stars, *as long as the habitable zone is the main target of the mission.* In the case of K and M spectral types – which are of high scientific importance – the habitable

zone is practically inaccessible with a coronographic mission. Furthermore, the *true* value of the $\eta_\oplus$ parameter will have a crucial impact on the number of Earths and Super-Earths that could be characterized with one or the other concept. Léger et al. (priv. comm.) have estimated the number of habitable planets that can be spectroscopically characterized by interferometry or coronography. The concepts adopted for the comparison are a coronograph as described above on one side and a four-telescope interferometer with 0.75 m apertures as depicted in Fig. 5 on the other side. The details of the assumptions made on the sources of noise for the two approaches are developed in a forthcoming paper. The plot of Fig. 5 underlines the different outcomes between the coronograph and the interferometer in terms of spectroscopy of nearby habitable Super-Earths by a factor 3 to 4, which is a significant factor in the low statistics case.

### 2.4 An exoplanet interferometer in the current context

A space-based interferometer dedicated to the characterization of habitable Earths will only focus on already detected nearby planets. Therefore what is the expected reservoir of Earth-like planet in the next decades? Several ground-based survey programs are already running or will be started in the coming years to detect habitable Earths and Super-Earths around M dwarfs with instruments such as ESPRESSO, CARMENES, or HARPS using precision RV techniques. This will potentially result in the detection of ∼100 small habitable planets out of which ∼1-2% will be transiting their host. These surveys will also monitor hotter F, G and K stars to detect any Super-Earth (essentially non-habitable) up to larger distances. From space where high-photometric accuracy can be achieved, CHEOPS will attempt to record the light dip of small Super-Earths orbiting bright stars and already detected by RV surveys, which will deliver new insights onto the density of these objects. Similarly to Kepler and COROT, the recently selected M3 mission PLATO will conduct blind searches of habitable Earths and Super-Earths even around bright and nearby stars, which was so far not observable with the two predecessors missions, and will build up on the heritage of GAIA in the field of exoplanets. A similar mission – TESS – is under development on the US side. Since the EChO mission was not selected for the M3 slot, a short term opportunity for transit spectroscopy of exoplanets resides in the NASA candidate mission FINESS, for which its main goal is comparative exoplanetology. More punctual but nevertheless important studies in the field of exoplanets characterization will be conducted with the 30-m + class ground-based telescopes, while JWST will spectroscopically characterize transiting planets around M dwarfs.
From the perspective of a direct spectroscopy mission for which nearby habitable Earth and Super-Earths would be the primary targets, a problem remains: all the stars that will be monitored via the aforementioned surveys are carefully chosen for their low stellar activity in order to leave the RV and photometric signals unaffected by stellar noise. This means that the sample of stars within 20 pc hosting a planet will be incomplete in terms of follow-up targets for direct spectroscopy. Circumventing this problem can be achieved by using high-precision astrometry of nearby stars, a technique that is almost unaffected by astrometric jitter noise at the level needed to detect a $1\,M_\oplus$ planet around a Solar-type star. This approach is chosen by the NEAT mission (Malbet et al. 2012), a candidate mission for a potential M4 slot and would be able to conduct a complete census

of nearby Earths and Super-Earths within 20 pc.

In summary, despite a current context which for many reasons is unfavorable to space interferometry, it appears that unless of a major breakthrough in the development of both large and cheap space-based collectors, space interferometry in the 4–20 $\mu$m mid-infrared range remains the best concept for *the low-resolution spectroscopic search of biomarkers in the atmosphere of a significant number ($\gtrsim$10) of nearby Earths and Super-Earths in the HZ of their host stars.* The weak point of this approach still remains at a technological level.

## 3. Space interferometry beyond exoplanetary science

We can reasonably affirm without too many risks that the uniqueness of space interferometry for characterizing planets in the habitable zone of solar-type stars is, *as a principle*, uncontested within the Exoplanet community for the reasons presented above. However, following the Darwin/TPF decade, there is now little support to the idea that this route should be followed as a priority. The scientific achievements obtained with the RV and transits techniques, or with ground-based coronography on large telescopes has refrained part of the community to invest more resources for space-based nulling interferometry in regard to its complexity and cost. The outcome of the recent L2/L3 selection process has flagged positively the technical feasibility of a spectroscopy mission such as proposed by Quirrenbach et al. (2013), but stressed that the cost associated with the technological development was beyond the envelope of an L-class mission, leading to its non-selection. Even considering the topic of Formation Flying (FF) for which the PRISMA and PROBA-3 missions will provide a major boost, the maturity is not considered to be reached for a large FF array. Several reports have been written on the technological readiness for a mid-IR flagship mission (e.g. Lawson et al. 2009) and provide a good starting point to plan a future technology roadmap.
Interestingly, other key topics connected to galactic and extragalactic science may require the use of space-based interferometry (Sauvage et al. 2013). At longer wavelengths, the far-infrared community developed the case for an interferometric observatory to go beyond the resolution delivered by Herschel. Different technical solutions where proposed in September 2013, including a formation-flying interferometer based on the ESPRIT concept for heterodyne detection. Interferometric missions such as SPIRIT and SPECS were proposed in the US to operate in the same wavelength range. In the field of planetary sciences, a concept of heterodyne thermal infrared observatory named PSIO considers the option of an interferometric architecture (Fletcher et al. 2013 ).
In the light of these important elements, we suggest that in order for infrared space interferometry to become strongly supported as an L-class mission by the largest possible scientific community, the proposed science has to go beyond the theme of the Earth-analog characterization and must reflect the astrophysical interests of a wider community than the original Darwin/TPF project did. Clearly this would require a complete recasting of the science and technological roadmaps to explore overlaps and compatibility between the different proposed methods. For instance the capability of interferometric imaging would become at least as important as the nulling capabilities. But we argue this is the most plausible way to have space interferometry seriously considered in the current context. The re-

cently started Horizon-2020 program by the EC should offer an ideal stage for collaborations aiming at exploring possible convergence, boosting technology and support preparatory missions.

## References


Barclay, Th. et al., 2013, Nature 494, 452

Bonfils, X. et al., 2013, A&A 549, A109

Chabrier, G. et al., 2003, PASP 115, 763

Dressing, C. D. & Charbonneau, D., 2013, ApJ 767, 95

Dumusque, X. et al., 2012, Nature 491, 207

Fletcher, L. N. et al., 2013, http://sci.esa.int/Lmissions2013

France, K. et al., 2013, ApJ 763, 149

Fressin, F. et al., 2013, ApJ 766, 81

Haberle, R. M. et al., 1996, Proc. " Circumstellar Habitable Zones", 29

Heller, R. & Armstrong, J., 2014, Astrobiology 14, 50

Howard, A. et al., 2010, Science 330, 653

Kaltenegger, L. et al., 2010, Astrophys Space Sci 326, 233

Kasting, J. et al., 1993, Icarus 101, 108

Kouveliotou, C. et al., 2013, "Enduring Quest, Daring Visions Report"

Lawson, P. et al., 2009, Astro2010 Papers, no. 53

Léger, A. et al., 2007, arXiv:0707.3385

Léger, A. et al., 2009, A&A 506, 287

Malbet, F., 2012, Exp. Astron. 34, 385

Mayor, M. et al., 2009, A&A 507, 487

Mordasini, C. et al., 2009, A&A 501, 1161

Pierrehumbert, R. T., 2011, ApJ 726, 8

Quirrenbach, A. et al., 2013, http://sci.esa.int/Lmissions2013

Sauvage, M. et al., 2013, http://sci.esa.int/Lmissions2013

Segura, A. et al., 2010, Astrobiology 10, 751

*Improving the performances of current optical interferometers & future designs*
*Proceedings of Haute Provence Observatory Colloquium (23-27 September 2013)*
*Edited by L. Arnold, H. Le Coroller & J. Surdej*

# Session 3. Poster session

Chair: Hervé Le Coroller
Tuesday evening, Sept. $24^{th}$


Jonathan Menu

*Improving the performances of current optical interferometers & future designs*
*Proceedings of Haute Provence Observatory Colloquium (23-27 September 2013)*
*Edited by L. Arnold, H. Le Coroller & J. Surdej*

# Conceptual design of a compact optical synthetic aperture telescope

Neng-hong Zhu[1], Xin-yang Chen[1], Dan Zhou[1], Cong-cong Zhang[1], Li-xin Zheng[1], Chao-yan Wang[1]

[1]*Shanghai Astronomical Observatory, 200030, Shanghai, China*

**Abstract.** Y-4 synthetic aperture telescope consists of four 40cm sub-telescopes that are configured as Y-type array based on an unique AZ-Alt mounting. After passing through every sub-aperture, star lights are transformed into parallel beams, enter relay optics for co-phasing sensing, finally combined by an optical combiner and form interferometric images in image plane. Because all tubes are installed on single mounting, the complicate outer optical delay line can be avoided. Y-4 array telescope is of some advantages such as efficient diameter, angle resolution with respect to some other configurations. Some negative influence of beam combining errors including piston, tip/tilt, and pupil mapping error aiming to Y-4 array is analyzed subsequently. The preliminary mechanical and optics design of Y-4 telescope is introduced respectively.

## 1. Introduction

High sensitivity and resolution are two foremost motivations for building optical telescopes since several centuries all along. These specifications are associated with aperture of telescopes, performance of terminals and atmospheric turbulence closely. To enlarge telescope aperture is a general valid method for scientists. A few of giant optical telescopes projects with 30-40 meters diameter and 2-5 thousands of tons weight are ongoing at present. Unfortunately, so large-scale size and heavy weight will bring overwhelming technological challenges to optics, mechanics and control design and manufacture of giant telescopes. Optical interferometer which is thought as a technique can break through aperture limit is developing subsequently. Two or more than two small telescopes are arranged as an array, and multiple beams are combined to achieve interferometric image with high angular resolution which is proportional with length of baselines (separation between sub-telescopes).

There are two fundamental beam-combining way of interferometry. Michelson interferometry is also called pupil-plane interferometry combines multiple beams from independent light collectors with long baselines (up to several hundred meters) by co-axial way and feeds superimposed beams to detector to obtain interfered fringe. At each baseline orientation, only single spatial frequency point is measured, and the u-v plane must be filled in by adding many non-redundant baselines and rotating baselines over a long period of time (e.g. earth rotation).

Fizeau interferometry which is also called image-plane interferometry has compact telescope arrays and multiple beams are focused to image plane with much shorter baselines by a multi-axial beam combiner. Fizeau interferometers produce direct images with nearly full instant u-v plane coverage by mounting tracking. If amount of sub-apertures is above 3, this interferometer also would be named by synthetic aperture telescope.

A new conception of Y-4 Fizeau synthetic aperture telescope will be introduced in the next chapters. This telescope is composed of four 40cm sub-telescopes that are configured as Y-type array based on an unique Alt-AZ mounting. After passing through every sub-telescope, star lights are transformed into parallel beams, enter relay optics for co-phasing sensing, finally combined by an optical combiner and form interferometric images in image plane. Because all tubes are installed on a single mounting, the complicate outer optical delay line can be avoided. But some high precision sensing and compensation set-up for inner optical path errors induced by manufacturing, installing, gravity, thermal etc. is necessary.

Chapter 2 describes some advantages of Y-4 array according to the characteristics of PSF distribution and u-v plane coverage in contrast to some other array configurations. Chapter 3 analyzes some negative influences of beam combining errors including piston, tip/tilt, and pupil mapping error aiming to Y-4 array. Chapter 4 and Chapter 5 introduce preliminary mechanical and optics design of Y-4 telescope respectively.

## 2. Array configuration

An interferometric intensity formula aiming to an array of multiple apertures is given (Mennesson & Mariotti 1997) .

$$I \propto |\frac{\pi D(1+\cos r)^2}{\lambda}|^2 |\frac{J_1(\pi D \sin r/\lambda)}{\pi D \sin r/\lambda}|^2 |\sum_{k=1}^{n} e^{j2\pi(\frac{L_k r}{\lambda})(\delta_k-\theta)} e^{j\varphi_k}|^2 \tag{1}$$

D is the diameter of sub-aperture, and $J_1$ is the 1st order Bessel function of the first kind. $(L_k, \delta_k)$ is the polar coordinate of each sub-aperture center. A point source is located at angular separation r from reference center. $\theta$ is the azimuth angle which spread from 0 to $2\pi$, and $\varphi_k$ is the phase shift given to each beam before entering the beam combiner. The first item of Equation (1) is constant over a small range of r. The second item is the intensity pattern of a single aperture and the third item is an array interference factor.

In general, imaging quality can be evaluated on the basis of point spread function (PSF). PSF of multiple aperture array obviously depend upon the number of sub-telescopes, the apertures diameter, the length of interferometer arm, and the topological structure of array according to Equation (1). Considering the feasibility of opto-mechanical design and to keep a compact structure as far as possible, we primarily determine the equivalent diameter of synthetic aperture array is about 1m, the diameter of sub-aperture is 40cm, and the amounts is 3 or 4. Fig.1-a, 1-b, 1-c show several optimal symmetrical arrays configuration: square array, Y-3 array and Y-4 array. Some main configuration variables of different arrays are listed in Table 1. Fig.1-d, 1-e and 1-f are simplified sketches of Modulation Transfer Function (MTF) of arrays so called u-v plane coverage.

MTF is used to evaluate the characteristic of transferring intensity contrast for telescopes in spatial frequency domain (Chung 2002) and determine synthetic aperture telescopes angular resolution in practice. Dashed circles indicate special frequency regions realized by each kind of array. A solid circle edge means the cut-off frequency of MTF in which there is no loss of frequency. The radius of solid circle is equivalent to the instantaneous effective diameter of array $D_e$. The larger is $D_e$, the higher is angular resolution. The $D_e$ of Y-4 array is maximum for these three array configuration. MTF of multiple aperture array is unsymmetrical in frequency domain. Fig.2 is the distribution of MTF along with different orientation angle: 10deg and 20deg. The MTF within low frequency band of the square array and Y-4 array is obviously higher than Y-3 array. At the meanwhile, the cut-off special frequency of Y-4 array is higher than square array. The Y-4 array is an optimal configuration.

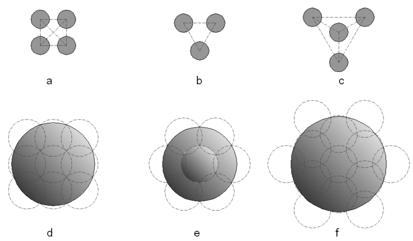


Figure 1.: *Graph of array configuration and u-v coverage.*

Table 1.: *Parameters of different array configuration.*

| Variables | Square array | Y-3 array | Y-4 array |
|---|---|---|---|
| Number of sub-apertures | 4 | 3 | 4 |
| Number of baselines | 6 | 3 | 6 |
| Length of baselines | 565/799mm | 690mm | 650/1126mm |
| Effective diameter | 894mm | 800mm | 1028mm |

## 3. Beam combining errors and total errors budget

For a optical aperture synthesis telescope, its imaging quality will mainly suffer from beam combing errors including piston, tip/tilt and pupil mapping error. As the piston error increases, several major deviations will develop over the envelope of the PSF distribution. Firstly, the main envelope shifts in the direction of the piston error. Secondly, the peak intensity gets reduced compared to the normal PSF without any piston errors resulting in a reduced Strehl Ratio (SR). The size of the main lobe also expands showing a degraded angular resolution. The piston error tolerance should less than 0.1 $\lambda$ if should SR be above 90%.

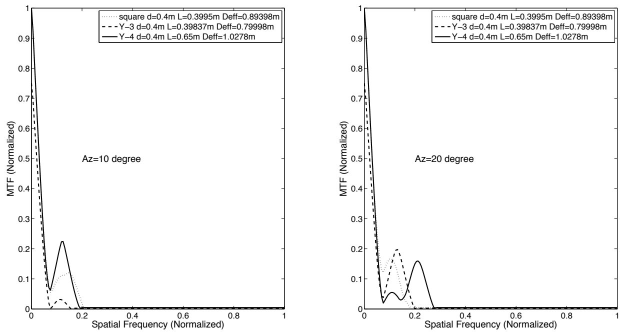


Figure 2.: *MTF of different array configuration.*

Tip/tilt error is usually classified by X axis tip error and Y axis tilt error. The energy of main lobe of PSF distribution will spread to other side lobe as tip/tilt error increases. The response of MTF between low and middle spacial frequency domain will also decline . It also means the imaging quality will degenerate rapidly. For polychromatic light, supposed SR reaches 90%, the tip/tilt error tolerance should be less than 0.3 arcsecond. Pupil mapping errors mainly include shear error and magnification error. In this paper it specially refer to shear error which comes from the incorrect sub-aperture image locations across the beam combiners entrance pupil plane. For a certain Field-of-View(FOV), SR will decrease gradually with pupil mapping error increasing. In particular, the variety of SR following with pupil mapping error is also distinguishing with respect to different FOV. Larger is the FOV, quicker is the decreasing velocity of SR as pupil mapping error increases. It is obvious that pupil mapping error should be limited in order to satisfy a certain FOV and SR. According to our simulation, the pupil mapping error tolerance of Y-4 array telescope should be limited to 0.015 $\lambda$.

Errors analysis is an important design method aiming to all components bring errors to system performance. Each error tolerance strictly defines the rms error which can be introduced during each step of the design, manufacture, assembly and operations. Figure 3 is a total errors budget of Y-4 array telescope (Cao & Wu 2009).

## 4. Mechanism design

Fizeau synthesis aperture telescope is of some mechanical characteristics which are different from classical single aperture telescopes.

(1) Coincidence of tubes fabrication and installation is very strict because of ensuring multiple aperture good co-phasing.

(2) There is a suit of collimation and folding light-path between each telescope main optics and beam combiner. Because these four set of light-path set-up are used to measure and compensate piston and tip/tilt error, the mouting must have higher rigidness and anti-vibration.

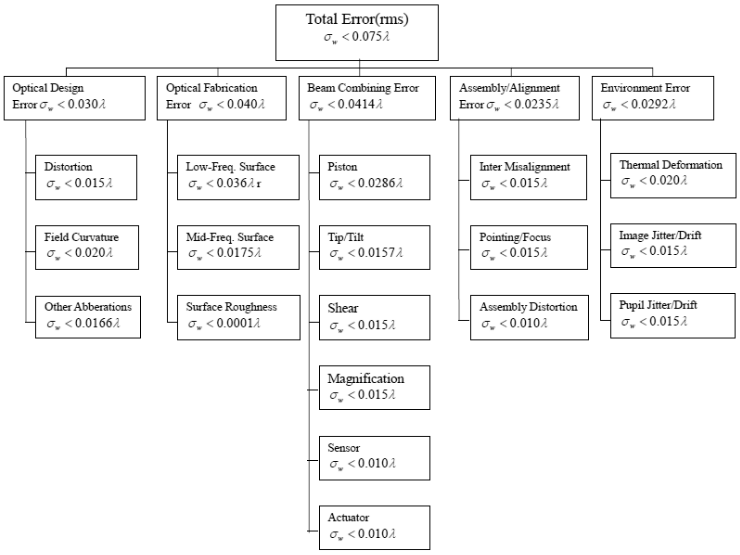


Figure 3.: *Total errors budget of Y-4 array.*

(3) The mounting distortion induced by environment variables such as temperature and wind loads.

On the basis of referring to mechanism design scheme of Large Binocular Telescope(LBT), we also apply C-shape board concept to mechanical structure of Y-4 synthesis aperture telescope. Four sub-telescopes are installed on the a triangle platform which is fixed with two C-shape boards. All collimation and folding light-path set-up are placed on the platform,while the beam combiner is below. The two boards are linked through trusses firmly. Figure 4 is a structure model of Y-4 synthesis aperture telescope.

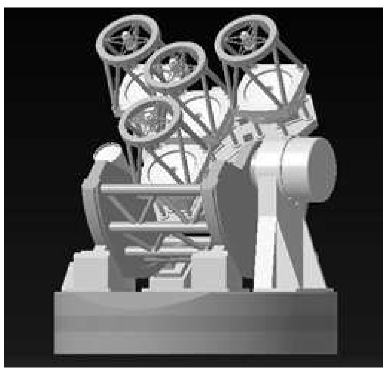

Figure 4.: *Structure model of Y-4 synthesis aperture telescope.*

This scheme shows several significant advantages relative to conventional AZ-ALT tracking mouting of telescopes. Firstly, a whole triangle platform replacing traditional middle block component will enforce rigidness of structure and heighten resonance frequency of mechanical system. Secondly, all sub-telescopes, collimation and folding set-up can be modularized by batch fabrication thanks to same opto-mechanism. So each module can be assembled and adjusted individually on the laboratory. This point is very useful to reducing assembly errors and difficulties on site. Finally, the mounting structure is open entirely,and therefore is good for thermal balance of the whole environment.

### 4.1 Mounting

The tracking mouting consists of the triangle platform and C-shape boards and each other are linked through trusses made of profiled steel. The total mass of mouting is about 3961Kg. We give a certain gravitational acceleration to the whole module and tube payload to the link section. The peak distortion of mounting is about 5.92 $\mu$m. And the finite element modal analysis shows that the minimum resonance frequency is 130.49Hz. In general, the above results confirm this mounting structure is of significant advantage in mechanics.

### 4.2 Sub-telescope tube

The sub-telescope tubes will be supported by trusses which is made of SiC, while the rest part is made of steel. The total mass of each suit of tube is up to 157Kg. The peak distortion of tube is about 7.24 $\mu$m. and the minimum resonance frequency of tube is 122.82Hz.

## 5. Optics design

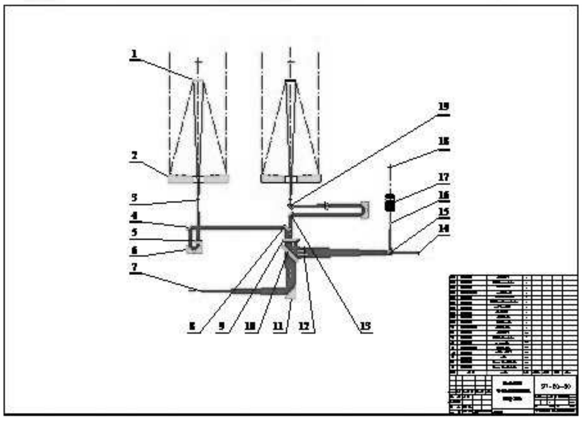

Figure 5.: *Optical layout of Y-4 optical synthesis aperture telescope.*

Figure 5 shows the optical layout of Y-4 optical synthesis aperture telescope. This optical system consists of four sub-telescopes, four collimation & folding optical path set-up, beam combiner and imaging terminal. Incident light will pass through each sub-telescope with 400 mm diameter and collimator lens, and will produce collimated beams with 20 mm diameter. After reflecting by some folding mirrors, then these beams reach to beam combiner together. Finally, form a multiple-axis image at the focus of combiner.

We hope the focal ratio of primary mirror is as short as possible considering cost, optical stability and tracking accuracy. We chose Ritch-Chretien optical structure as main optics of the sub-telescope. The primary mirror of each sub-telescope is of a concave hyperboloidal surface and the secondary mirror is convex hyperboloidal. They are both made of ceramics glass. Thanks to this system can eliminates spherical and comet aberrations well, the diameter of confusion circle is less than $0.7\,''$.

Folding light path consists of field lens and some 45 deg folding mirrors. A double separate objective lens is applied to beam combining. In order to satisfy the Homothetic Rule of optical synthesis aperture telescope, we determine the diameter of beam combiner is 85 mm at least.

## 6. Conclusions

We introduce a conceptual design scheme of Fizeau optical synthesis aperture telescope which consists of 4 sub-telescopes including array configuration, error budget, mechanism and optics design. This kind of compact structure maybe suit for spacial optical interferometer project in future.

## References

Mennesson, B., & Mariotti, J.M. 1997, ICARUS, 128, 202

Soon-Jo Chung. 2002, Design, Implementation and control of a sparse aperture imaging satellite:[D].,

Cao F., Wu Z. 2009, in Fizeau interferometer Conf., Internal report ed. Neng-hong Zhu, 115

*Improving the performances of current optical interferometers & future designs*
*Proceedings of Haute Provence Observatory Colloquium (23-27 September 2013)*
*Edited by L. Arnold, H. Le Coroller & J. Surdej*

# Off-axis nulling transfer function measurement: a first assessment

G. Dalla Vedova[1], J.-L. Menut[1], F. Millour[1], R. Petrov[1], F. Cassaing[2], W. C. Danchi[3], S. Jacquinod[4], E. Lhome[5], B. Lopez[1], J. Lozi[6], A. Marcotto[1], J. Parisot[4], J.-M. Reess[4]

[1] *Laboratoire LAGRANGE, Université de Nice-Sophia Antipolis, OCA, 06108 Nice, France,* [2] *ONERA, F-92322 Châtillon, France,* [3] *NASA Goddard Space Flight Center, Greenbelt, MD 20771, USA,* [4] *LESIA, Observatoire de Paris, 5 Place J. Janssen, 92195 Meudon, France,* [5] *ING, Apartado de correos 321 E-38700 Santa Cruz de la Palma, Canary Islands, Spain,* [6] *The University of Arizona, 1077 N Highland, Tucson Arizona 85721, USA*

**Abstract.** We want to study a polychromatic inverse problem method with nulling interferometers to obtain information on the structures of the exozodiacal light. For this reason, during the first semester of 2013, thanks to the support of the consortium PERSEE, we launched a campaign of laboratory measurements with the nulling interferometric test bench PERSEE, operating with 9 spectral channels between J and K bands. Our objective is to characterise the transfer function, i.e. the map of the null as a function of wavelength for an off-axis source, the null being optimised on the central source or on the source photocenter. We were able to reach on-axis null depths better than $10^{-4}$. This work is part of a broader project aiming at creating a simulator of a nulling interferometer in which typical noises of a real instrument are introduced. We present here our first results.

## 1. Introduction

The observation and the characterisation of dusty debris disks, extrasolar planets, and planetary systems around stars is one of the major astronomical challenge of the 21st century. Direct detection, model fitting, and ultimately imaging of these objects require instruments with very high dynamic range and high angular resolution in order to comply the combination of two major physical constraints. First, there is large flux ratio between the star and the planet or the circumstellar disk, typically $\sim 10^{10}$ in the visible, and $\sim 10^{7}$ in the infrared. Second, the angular separation between a host star and exoplanet in the habitable zone is typically small. For example, the system Earth-Sun at maximum elongation at the distance of 10 pc has an angular separation of the order of 100 mas or 0.5 $\mu$rad which needs an interferometer with a baseline of 20 m at 10 $\mu$m.

Currently, there is a large effort to develop concepts able to detect and characterise Earth-like planets (Quirrenbach 2001). In this context, nulling interferometry could play a key role (Bracewell & MacPhie 1979). In last decades, nulling interferometry has been one of the most studied techniques (Angel & Woolf 1997; Léger et al. 1996a) and these studies led to consider two major projects named DARWIN (Léger et al. 1996b) and TPF-I (Lawson et al. 2007). The goal of these two missions is to detect Earth-like planets into the habitable region and characterise their spectra with eventually markers of the possible presence of life (Danchi et al. 2003). As these instruments are extremely demanding for technical and operational requirements, some intermediate class projects, such as PEGASE (Ollivier et al. 2009) and FKSI (Danchi & Lopez 2007) have been considered. The initial specification was to ensure the exozodiacal light with an accuracy of 1 zodi, i.e. the intensity for a system identical to the solar system, for all Darwin potential targets in order to assess Darwin observations feasibility and priority. Later, it has been understood that this type of M-class space interferometer can have remarkable possibilities to characterise the structures of protoplanetary and debris disks with various signatures of planet presence or formation. A demonstrator PERSEE, acronym of Pegase Experiment for Research and Stabilisation of Extreme Extinction, has been designed and built by a consortium led by CNES and including IAS, LESIA, ONERA, OCA and Thales Alenia Space in order to assess the potential and limits of PEGASE, and lately FKSI.

There is a growing interest in the image reconstruction from interferometric observations, due to the possibility to visualise unsuspected structures and details of the object of interest. Both in model fitting and image reconstruction, the knowledge and the characterisation of the transfer function and the covariance matrix of residuals of the interferometer are critical information, both to optimise the problem inversion and to characterise the quality of the result (Tallon-Bosc 2007; Thiébaut 2009). As a consequence, characterising the off-axis transfer function of a nulling interferometer is of prime interest.

Early in 2013, we started a measurement campaign with the aim of characterising the transfer function with a real nulling interferometer operating in 9 spectral channels in a large spectral band of the infrared. We used the PERSEE test bench to record transmission maps, simulating angularly offset sources with different ranges of baselines and tilts. We obtained a database of measured multi-wavelength transmission maps of a nulling interferometer, and are comparing it with its analytical model (section 3.).

## 2. Measurement campaign

PERSEE is a fibered nulling interferometer demonstrator built with the aim to achieve a stabilised nulling ratio better than $10^{-4}$ in a large spectrum range between bands J and K. Lozi et al. (2013) have demonstrated that a polychromatic nulling depth of $10^{-6}$ with a stability of $10^{-7}$ could be reached over 10 hours simulating conditions of typical perturbations of a spacecraft such as PEGASE. The detailed optical layout made by Thales Alenia Space is recalled in Table 2. and in Fig.1. The bench is equipped with a fringe sensor (FS) based on the ABCD modulation technique (Shao et al. 1988) and a tip-tilt sensor (FRAS) in order to correct respectively internal OPD between the interferometer arms and tilt errors in closed loop. After the combining stage, a Modified Mach-Zehnder (MMZ) (Jacquinod et al. 2008), dichroic plates separate the various spectral channels and direct them in the appropriate detection chains. The $H$ and $K$ channel signals reach, via a single mode fiber, the nitrogen cooled infrared detector. On the

Table 1.: *Optical components of PERSEE*

| | |
|---|---|
| M1 | 45 deg. mirror |
| M4-M5 | nulling periscope |
| M6 | tip-tilt injection |
| M7-M8 | delay line (cat's eye) |
| M11 | FRAS mirror |
| M9 | 30 deg. mirror (MMZ) |
| L3-L4 | separating plates (MMZ) |
| D2 | fringe sensor dichroic |
| M10 | off-axis parabola |
| I | output of MMZ corresponding to the channel A |
| II | output of MMZ corresponding to the channel B |
| III | output of MMZ corresponding to the channel D |
| IV | output of MMZ corresponding to the channel C |

IR camera, we have simultaneously polychromatic measurements in 9 channels from 1.65$\mu m$ to 2.45 $\mu m$. In order to simulate an off-axis source, we introduced on mirrors of PERSEE (M6) a set of commands to drive a displacement in tip-tilt $(\alpha, \beta)$ and OPD $\delta$. These tip-tilt and OPD can be associated with a simulated baseline B by the relationship $\delta = B \cdot \sin(\alpha)$, where $\alpha$ and $\beta$ correspond to an angular position on sky relative to the optical axis of the instrument. With commands injected on mirrors M6, we scanned a near-field close to the axis within an angular separation of two Airy disk diameters, defined by the resolution of the considered pupils. We simultaneously measured the flux on the dark output of the MMZ recombiner (III output or channel D, see Table 2.), and a flux reference for the source fluctuations directly at the output of the collimator (see Fig.1). A measurement corresponds to a scan of a grid of points in the near-field off-axis with a fixed baseline and, for each position $(\alpha, \beta, \delta)$, we recorded 20 frames in 0.2 seconds with the IR camera. We make $\alpha$ and $\delta$ proportional to each other in order to simulate the variation of the transfer function along a 2-telescope baseline. We also measured the photometry of both arms of the interferometer. We normalised the science channels with fluctuations of the source and we evaluated the photometry in both arms $I_A$, $I_B$, and the recombination of both beams of light $I_D$. We define the measured normalised transfer function $\bar{T}^B(\alpha, \beta)$ (Eq.1), and the theoretical transfer function of PERSEE, given in Hénault et al. (2011).

$$\bar{T}^B_{\text{meas}}(\alpha, \beta) = \frac{I_D(\alpha, \beta, \delta)}{I_A(\alpha, \beta, \delta) + I_B(\alpha, \beta, \delta) + 2\sqrt{I_A(\alpha, \beta, \delta) I_B(\alpha, \beta, \delta)}} \tag{1}$$

$$T^B_{\text{theor}}(\alpha, \beta) = |\sin(\alpha B/\lambda) \cdot [\hat{B}_D(\alpha, \beta) \otimes G(\alpha, \beta)]|^2 \tag{2}$$

Where $\hat{B}_D(\alpha, \beta)$ is the complex amplitude generated by an individual subaperture and being back-projected onto the sky. For unobstructed pupils as in PERSEE, it is equal to $2J_1(\rho)/\rho$ where $\rho = \pi D/\lambda$, and $J_1$ is the Bessel function at the first order. $G(\alpha, \beta)$ is the fundamental mode of the exit filtering waveguide, after being projected back on-sky. It can be approximated by a gaussian function. Once we obtain the measured transfer function, we can compare it with the normalised theoretical one $\bar{T}^B_{\text{theor}}(\alpha, \beta) = N \cdot T^B_{\text{theor}}(\alpha, \beta)$, where $N = [\hat{B}_D(\alpha, \beta) \otimes G(\alpha, \beta)]^{-1}$ is the normalisation term.

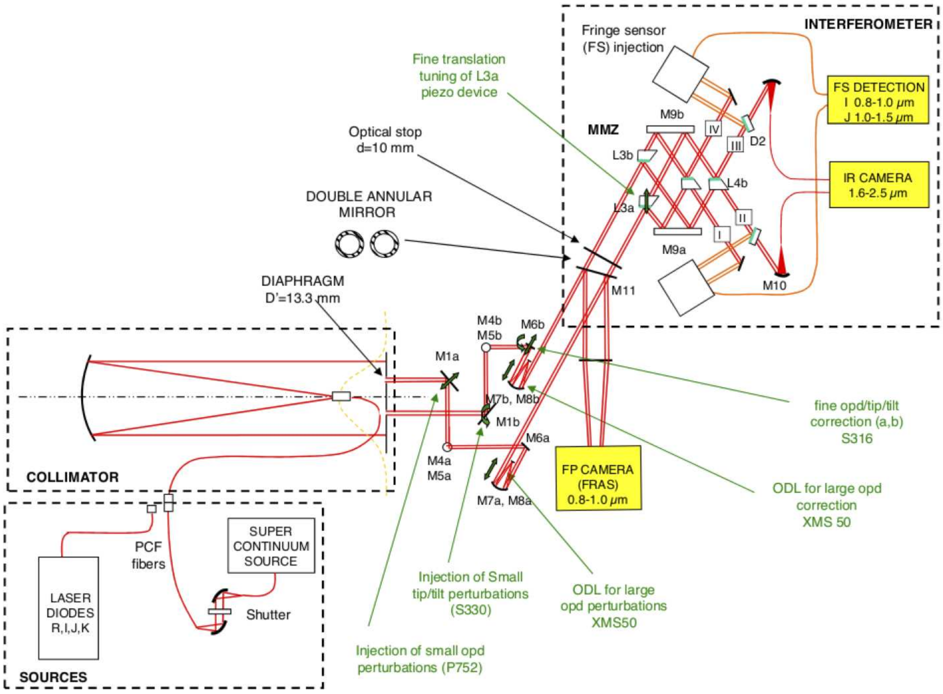


Figure 1.: *Layout scheme of the fibered nulling interferometer demonstrator PERSEE designed by Thales Alenia Space.*

## 3. Results

We present preliminary results for the measure with internal tip-tilt from $-36$ to 36 arcseconds with a maximal OPD of 3.5 $\mu m$. The two apertures of PERSEE have a diameter of 13 mm and are separated by a baseline of 50 mm. It corresponds to a near-field off-axis on the order of $\simeq 1.4$ Airy disk radius and a ratio of baseline to diameter of pupils equal to $B/D = 3.2$ that gives $\sim 7$ fringes in an Airy disk region. For example, if we consider two apertures with a diameter of 10 cm the baseline is equal to 32 cm. Using Eq.1 we produced the map transfer function and its associated variance map shown for the channel $\lambda = 2.45$ $\mu m$ respectively in Fig.2 and Fig.3. Fig.4 shows the theoretical transfer function obtained using Eq.2. The difference between measured and theoretical transfer function is shown in Fig.5. Both theoretical and subtracted maps are obtained for the channel $\lambda = 2.45$ $\mu m$. We see that the measured and modeled maps are fairly similar but with a difference that is larger than the standard deviation. The next step is to tune the model with a simple number of perturbation to obtain a good match with the measures. The value of the best null measured is on the order of magnitude of $10^{-4}$. This value is considered deep enough to detect the zodiacal light with an accuracy of 1 zodi, comparable with the request for the PEGASE mission (Defrère et al. 2008). We hope that this null of $10^{-4}$ is sufficient for a comprehensive analysis of the statistic of the transfer function $\bar{T}^B_{\rm meas}(\alpha, \beta)$. Note that the irregular region in the center of the left side of the measured transfer function has been caused by a sudden slight pressure change in the white room occurred during the measurements, due to the opening of the entrance door.

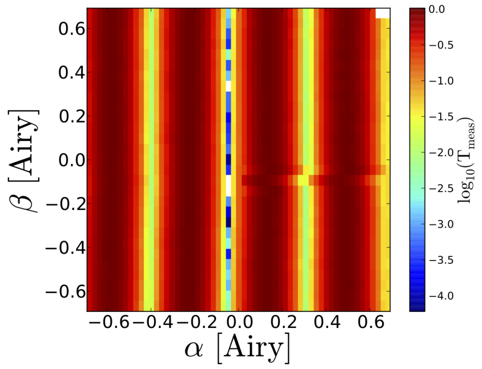


Figure 2.: *measured normalised transfer function* $\bar{T}^{B}_{\text{meas}}(\alpha, \beta)$ *for* $\lambda = 2.45$ $\mu m$.

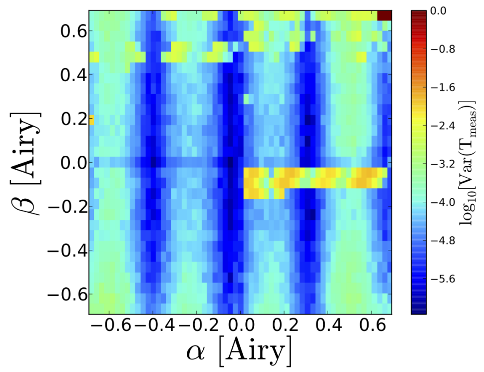


Figure 3.: *variance of the measured normalised transfer function.*

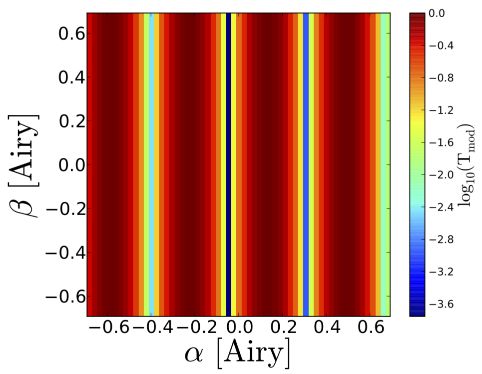


Figure 4.: *theoretical normalised transfer function* $\bar{T}^{B}_{\text{theor}}(\alpha, \beta)$, *for* $\lambda = 2.45$ $\mu m$.

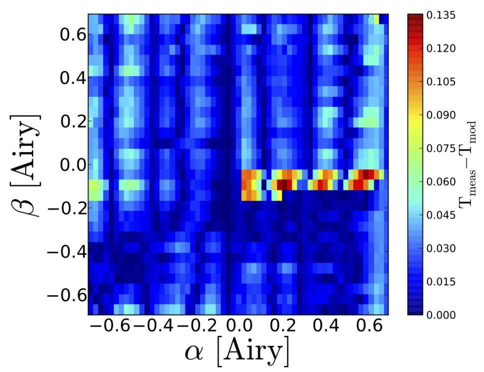


Figure 5.: *map of the subtraction between measured and theoretical transfer function.*

## 4. Conclusions and perspectives

Using the PERSEE test bench, we collected data for a detailed characterisation of the polychromatic transfer function $\bar{T}_B(\alpha, \beta)$ for a realistic fibered nulling interferometer and study its statistics in time and space. We presented preliminary results obtained for the measure with the ratio $B/D = 3.23$. The value of the best null is on the order of $10^{-4}$. If the transfer function is perfectly known, calibrated and stable, the performances of the model fitting or image reconstruction will be limited only by fundamental noises.

The precision and the stability of the transfer function for a nulling interferometer is the main limiting factor for the dynamic range that can be obtained for the investigated structures. Our goal is to analyse the variances and the covariances in time and between channels to evaluate the additional instrumental noise and hence the realistic limits of the approach. This is the starting point for a detailed characterisation of the nulling performances, especially for image reconstruction with an hyper-spectral approach and model fitting of very high-dynamic range scenes such as a star plus an exoplanet, or a star plus a debris disk with gaps.

*Acknowledgements.* The authors would like to thank the following people for the technical help, e-mail exchanges and remarks give during and after the work on the bench: T. Buey[1], J.-M. Le Duigou[2], J. Montri[3], A. Sevin[1].

[1] LESIA, Observatoire de Paris, 5 Place J. Janssen, 92195 Meudon, France, [2] CNES, 18 Av. E. Belin 31401 Toulouse Cedex 9, France, [3] ONERA, F-92322 Châtillon, France, [3] NASA Goddard Space Flight Center, Greenbelt, MD 20771, USA

## References

Angel, J. R. P., & Woolf, N. J. 1997, ApJ, 475, 373

Bracewell, R. N., & MacPhie, R. H. 1979, Icarus, 38, 136

Danchi, W. C. et al. 2003, ApJ, 597, 57

Danchi, W. C. & Lopez, B. 2007, Comptes Rendus Physique, 8, 396

Defrère, D. et al. 2008, A&A, 490, 435

Hénault, F. et al. 2011, Proc. SPIE, 8151, 81510A

Jacquinod, S. et al. 2008, Proc. SPIE, 7013, 70131T

Lawson, P. R. et al. 2007, NASA STI/Recon Technical Report N, 8, 14326

Léger, A. et al. 1996a, Icarus, 123, 249

Léger, A. et al. 1996b, Ap&SS, 241, 135

Lozi, J. et al. 2013, American Astronomical Society Meeting, 221, 328.03

Ollivier, M. et al. 2009, Experimental Astronomy, 23, 403

Quirrenbach, A. 2001, ARA&A, 39, 353

Shao, M. et al. 1988, A&A, 193, 357

Tallon-Bosc, I. et al. 2007, New Astronomy Review, 51, 697

Thiébaut, E. 2009, New Astronomy Review, 53, 312

*Improving the performances of current optical interferometers & future designs*
*Proceedings of Haute Provence Observatory Colloquium (23-27 September 2013)*
*Edited by L. Arnold, H. Le Coroller & J. Surdej*

# A laser ranging method dedicated to path lengths equalization in diluted telescopes

M. Lintz[1], C. Courde[2]

[1] *ARTEMIS, Univ. de Nice, Observatoire de la Côte d'Azur & CNRS, Bd de l'Observatoire, 06304 Nice, France (corresp. author michel.lintz@oca.eu)*

[2] *Univ. Nice Sophia Antipolis, CNRS, IRD, Observatoire de la Côte d'Azur, Géoazur UMR 7329, 250 rue Albert Einstein - 06560 Valbonne - France*

**Abstract.** When implementing a diluted telescope with large dimensions, one has to reach the equal path condition to the different segments of the primary mirror. In this work we suggest a way to implement a fast laser ranging method able to provide the error signal, using phase detection of the microwave modulation of a laser beam.

## 1. Introduction

Beyond classical observation instruments such as telescopes, interferometry takes advantage of the wave nature of light to provide increased angular resolution by combining light beams from optics placed at different locations on a large basis. Interferometric operation is obtained when the different optical paths are equal to within one or a few optical wavelengths. Although the requirement of path equalization can be clearly stated, it can be more difficult to implement, as the paths to equalize are the ones that come from the star or the object to be observed. The situation is somewhat more tractable when one has to set an ensemble of mirrors so as to form a large "diluted" spherical mirror: the sphere geometry can be realized by equalizing the paths from each of the segments to the curvature center of the expected sphere. Alternately, one can use an optics at curvature center (Fig. 1), in a way inspired from Le Coroller et al. (2012). This work addresses the problem of designing a laser ranging scheme that provides a signal proportional to the path difference between two adjacent segments. Two requirements can be stated: i) The measurement of the path length difference should be obtained, with a micron-scale resolution in a time shorter than the typical time scale of atmospheric turbulence, that is, in less than a millisecond. ii) The zero of this measurement should be free of errors to within 1 $\mu$m.

We suggest a measurement scheme that uses an optical beam modulated at high frequency, which is addressed to the first, then the second segment, before the length difference is extracted. Switching from the first to the second mirror can be done in much less than a millisecond.

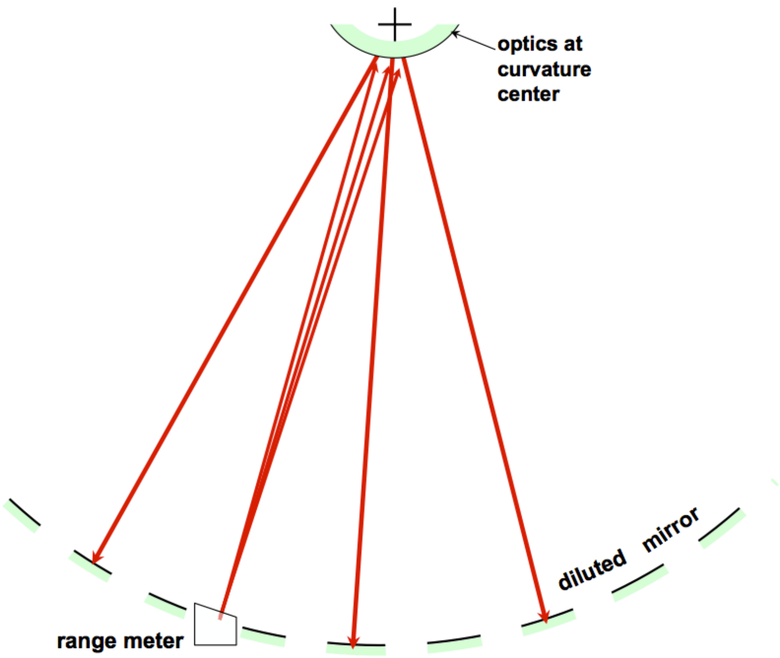


Figure 1.: *Use of laser ranging for optical path equalization via the curvature center.*

## 2. Measurement principles

In the absolute measurement of long distances, one of the most successful ranging schemes is derived from the idea put forward by H. Fizeau (1849). In present day commercial "absolute distance meters", Fizeau's double-pass cogwheel is replaced by a double-pass modulation of the polarization at a frequency around 2GHz. Measuring the modulation frequency for which the double-pass transmitted light is at a minimum prevents from detecting the phase of the return modulation.

The method that uses the phase measurement of a modulated light beam has been known for a long time (Bender 1967), but has not been used in commercial instruments, due to its well-known systematic errors such as electrical or optical crosstalk, or amplitude-to-phase coupling. When it comes to reaching precisions of about 1 $\mu$m, even at frequencies in the range of 10 to 20 GHz, these errors become very large and difficult to reject, as a precision of 1 $\mu$m over the distance corresponds to a precision of $10^{-4}$ cycle of the phase measurement at 15 GHz.

It has been shown that the errors associated to the electrical cross-talk and amplitude-to-phase (AM-to-PM) coupling can be rejected to a large extent by implementing a reference and a measurement arm, and operating at a microwave frequency such that the reference and measurement optical signal are in phase (Courde, Brillet & Lintz 2009). Rejection is obtained if some kind of switch allows to exchange the two optical signals with respect to the detectors: the systematic errors are unchanged in the reversal (while the propagation phase is reversed), and are eliminated by lock-in detection. This measurement scheme has proved capable of a $\approx$ 10 nm resolution on a 10-100 s integration time scale (Courde, Brillet & Lintz 2010).

In the problem of equalizing the distances towards two segments of a diluted mirror, the requirement of measuring a distance with a high accuracy is absent. One needs a signal proportional to the length difference, with well-defined zero. But the requirements for an *absolute* distance measurement are relaxed. For that reason one can devise a measurement set-up that compares the phase of the opto-microwave signal from the two segments. The comparison can be made at short time scale, using polarization control. By switching the polarisation from one to the other linear polarizations, one can address two different directions, hence two different segments of the primary, diluted mirror, using the propagation in a birefringent material.

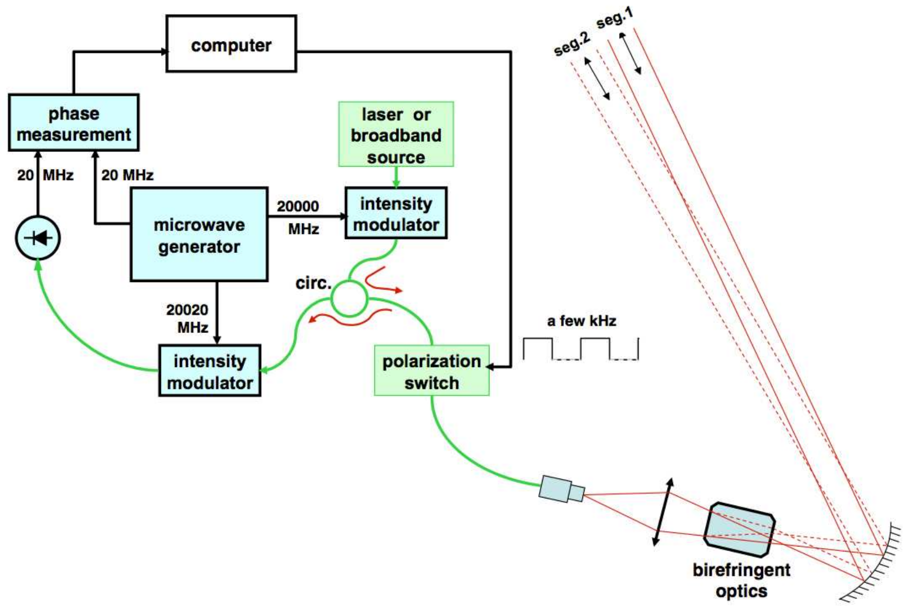


Figure 2.: *Principle setup of a path-difference range-meter with polarization addressing. Green lines: optical fibers. Red lines: laser beams. Black lines: electrical signals. Circ.: fibered optical circulator. The 20 MHz signal is phase-locked to the 20020 MHz - 20000 MHz frequency difference.*

Various kinds of polarization switch are compatible with the $\ll 1$ ms switch time requirement: fibered devices, either electro-optical, magneto-optical or elasto-optical, or free space Pockels cells.

## 3. Systematic errors and noise

Optical cross-talk (such as imperfect polarization extinction) can give rise to potentially large systematic effects. It affects the return polarization by $2\sqrt{\gamma}\cos[2\pi\Delta L/\lambda_{opt}]$ where $\gamma$ is the cross-talk between the two beams and $\Delta L$

the path length difference. It can affect the measured phase if it couples to polarisation defects in the optics that bring the return beam to the photodiode. This contribution can bring large instability to the measured phase, as soon as $\Delta L/\lambda_{opt}$ varies. However it has been shown (Courde et al. 2010) that at equal path length ($\Delta L \ll \Lambda$) this phase error cancels: the interference contribution only affects the amplitude of the signal. If AM-to-PM coupling is adequately dealt with (see below) the interference due to cross talk should have negligible contribution to the phase measurements. The use of a broadband source, rather than a laser source, is another way to reject the consequence of interference due to cross-talk (Courde et al. 2010), or due to a stray beam, whatever its origin, when the stray beam path length difference is larger than the coherence length of the light used for the ranging measurement.

While for Courde et al. (2009, 2010) the modulation frequency is locked to the value that gives equal phase value in the two states of the measurement, here modulation frequency is essentially a free parameter. One can take advantage of this by tuning the frequency to the value for which the electrical cross talk gives no contribution to the phase difference. Once an appropriate value has been obtained, it has no reason to drift, if the setup is not modified.

AM-to-PM coupling has been studied by Phung et al. (2014, this workshop). The most efficient way to remove the AM-to-PM coupling, including the one that results from thermal transients in the photodetector consists in demodulating the microwave optical signal. The phase shifts (at the intermediate frequency, 20 MHz) are then reduced by a factor of 20 GHz / 20 MHz = 1000 and negligible compared to the target accuracy of $10^{-4}$ cycle.

Finally (see Phung 2013, Fig. 6-7 therein), the phase measurement of a 20 GHz modulation has been repeatedly obtained with a noise below $10^{-4}$ cycle for durations of 100 $\mu$s. This corresponds to better than $10^{-4}\Lambda = 10^{-4} \times 15$ mm on the round-trip path length. Thus, the distance to a given segment should be measurable to better than 0.8 $\mu$m, in laboratory conditions, in less than a millisecond.

## 4. Conclusion

The method outlined in this work allows to implement a path length difference measurement adapted to the necessary equalization of the piston of the different segments of a diluted telescope. The laser ranging measurement is obtained by microwave modulation and demodulation of a laser source (or broadband source). Polarization control allows to switch in much less than a millisecond from one segment to the next, a time scale that prevents turbulence or drifts in the microwave instrumentation from adding noise or drifts in the measurement.

## References

Bender, P. L. 1967, Proceedings IEEE 55, 1039

Courde, C., Brillet, A., Lintz, M. 2009, Measurement Science and Technology 20, 127002

Courde, C., Brillet, A., Lintz, M. 2010, Instrumentation Mesure Métrologie 10, 81 (in french)

Fizeau, H. 1849, Comptes Rendus T29, 90, http://www.academie-sciences.fr/activite/archive/dossiers/Fizeau/Fizeau_pdf/Fizeau_pli878.pdf, http://www.academie-sciences.fr/activite/archive/dossiers/Fizeau/Fizeau_pdf/CR1849_p90.pdf

Le Coroller, H. et al. 2012, A&A 539, A59

Phung, D.-H. 2013, Thèse de doctorat de l'Université de Nice, http://tel.archives-ouvertes.fr/docs/00/86/80/28/PDF/2013NICE4038.pdf

Phung, D. H., et al. 2014, in Improving the performances of current optical interferometers & future designs, colloquium held in OHP, France, September 23-27, 2013, edited by L. Arnold, H. Le Coroller & J. Surdej

*Improving the performances of current optical interferometers & future designs*
*Proceedings of Haute Provence Observatory Colloquium (23-27 September 2013)*
*Edited by L. Arnold, H. Le Coroller & J. Surdej*

# Nanometer-scale absolute laser ranging: exploiting a two-mode interference signal for high accuracy distance measurements

D.-H. Phung[1], C. Courde[2], C. Alexandre[3], M. Lintz[1]

[1]*ARTEMIS, Univ. de Nice, Observatoire de la Côte d'Azur & CNRS, Bd de l'Observatoire, 06304 Nice, France (corresp. author michel.lintz@oca.eu)*

[2]*Univ. Nice Sophia Antipolis, CNRS, IRD, Observatoire de la Côte d'Azur, Géoazur UMR 7329, 250 rue Albert Einstein - 06560 Valbonne - France*

[3]*CEDRIC-LAETITIA, CNAM, 292 Rue Saint Martin, 75141, Paris cedex 03, France*

**Abstract.** Absolute distance measurement with accuracy below the micron scale is important in astronomical optical interferometry. We present here an absolute laser rangefinder which relies on the detection of a two mode interference signal. We exploit the specific signature of the signal to extract both the interferometric and synthetic phase measurements, leading to distance measurement with nanometric accuracy. A resolution of 100 pm has been achieved in 75 $\mu$s with a relatively simple laser source. Amplitude to phase coupling in the detection chains turns out to be the largest source of systematic errors. A specific detection scheme is implemented, using optical demodulation of the microwave optical signal, to reduce amplitude-to-phase related systematic errors to below the required level.

## 1. Introduction

Measuring distances is important in many areas of technology. In space geodesy, where formation flight is used for mapping the high harmonics of the earth's gravity field, the measurement of the inter-spacecraft distance variation provides the input for the determination of the gravity field gradients. Astronomical optical interferometry is another domain which requires accurate determination of distances. The phase of the different beams that interfere has to be controlled, to get the required phase condition at recombination (destructive interference in nulling interferometry, constructive interference in imaging techniques, such as diluted telescopes, see Session 6 of this colloquium). Hence absolute distances have to be known to about 1 $\mu$m in ground instruments, where atmospheric turbulence limits the achievable phase stability. In space instruments, much better conditions can in principle be achieved, and accuracy of the absolute distance measurement has to reach the nanometer scale.

In the measurement of long distances, multi-wavelength interferometry has been able to provide both long synthetic wavelength and sub-micron accuracy (Salvadé et al. 2008). Using multiple 40 GHz phase modulations of a CW laser beam, MSTAR (Lay et al. 2003) has reached 100 nm scale accuracy. Frequency combs from femtosecond lasers are increasingly used in absolute distance measurement setups, inspired either from optical linear sampling (Coddington et al. 2009), or from dispersive interferometry (van den Berg et al. 2012). A different approach, that has been considered to some extent by Joo, Kim, & Kim (2008), consists in combining
i) a high precision, interferometric optical phase measurement, wrapped in the $[0,\ \lambda_{opt}]$ interval
ii) a carrier modulation phase measurement at frequency $\approx$ 20 GHz, wrapped in the $[0,\ \Lambda \equiv c/F]$ interval
iii) a time-of-flight measurement of the distance $d$.

If measurement iii) is accurate enough to bring unambiguous meaning to measurement ii), which in turn has good enough accuracy to give absolute significance to measurement i), then absolute distances can be measured with an accuracy far better than an optical wavelength. It appears, however, that long term ($>$ 1 s) drifts in high frequency measurements exceed the limit $\pi\lambda_{opt}/\Lambda$ beyond which measurement ii) fails to provide unambiguous determination of $2d/\lambda_{opt}$.

In this work we demonstrate that this problem is solved by a measurement scheme in which both phase measurements i) and ii) are obtained, in a consistent way, from the same interference measurement, using the 20 GHz beatnote, two-mode laser beam. The two-mode interferometer signal is exploited in a way such that both the optical phase and the synthetic phase are retrieved, separately, after a procedure that lasts about 100 $\mu$s and eliminates long term drifts of the phase and of the gain in microwave detection chains. On a simple set-up on which a $\approx$ 7.5 m optical path is implemented, we show that this measurement scheme can achieve the conditions required to provide nanometer accuracy absolute distance measurements. Among the systematic effects that show up on the two-mode interference measurements, some are related to the detection chains: cyclic errors and, more importantly, amplitude to phase coupling. The latter appears to be very difficult to correct for at the required precision level, due to thermal processes in the photodetectors. We finally present a way to reduce the AM-to-PM effects by a large factor (1000 in our case) so that AM-to-PM coupling is no longer a problem in our detection scheme. The two-mode interference detection scheme appears to provide a signal capable of nanometer accuracy in long (kilometer scale) distance measurements. A resolution of 130 pm has been achieved over measurements that last about 75 $\mu$s, repeated every 135 $\mu$s. The $1/\sqrt{N}$ dependence of the resolution, where $N$ is the number of acquisition cycles, is expected to be obtained if the measured path length is not affected by ambient turbulence or acoustic perturbations.

## 2. Measurement principles

Two narrow-linewidth, single-mode fiber lasers are phase-locked (Fatome et al. 2010, § 5) at a frequency of GHz, to provide a two-mode laser source, of known optical frequencies $[\nu_{opt},\ \nu_{opt} + F]$. The corresponding synthetic wavelength $\Lambda =$

$c/F$ is close to 15 mm. In Fig. 1 below, the two-mode laser beam propagates from BS0 to PhD1 along two different paths: a short reference path, of constant length $l$, and a variable measurement path of length $L$. The interference of these two beams provides the signal from which we extract the quantity to be measured, the length difference $\Delta L \equiv L - l$.

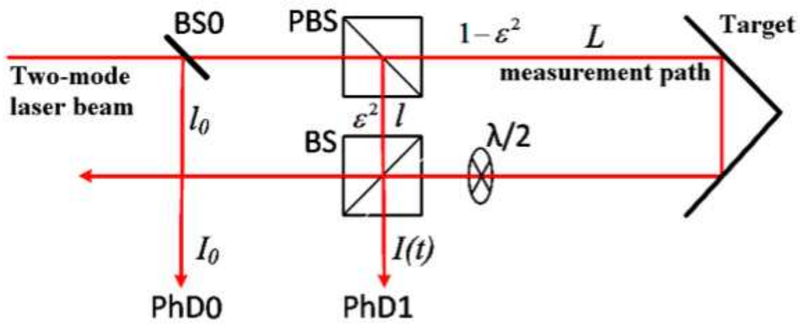


Figure 1.: *Schematic diagram of the telemeter. BS0: beam splitter plate; (P)BS: (polarizing) beam splitter cube.*

The polarization of the initial beam is chosen so that a small fraction of the beam power, $\epsilon^2$ = a few %, propagates, from PBS to BS, along the reference path, with S polarization. The remaining power (fraction $1 - \epsilon^2$) propagates along the measurement path with P polarization (S polarization after the half-wave plate) and interferes with the reference beam. The resulting intensity,

$$\begin{aligned} I(t) = (1-\epsilon^2)\Big[1+\cos\Big(\delta(t-L/c)\Big)\Big] + \epsilon^2\Big[1+\cos\Big(\delta(t-l/c)\Big)\Big] \\ +2\epsilon\sqrt{1-\epsilon^2}\ \cos\Big(\omega(L-l)/c+\delta(L-l)/2c\Big) \\ \times\Big[\cos\Big(\delta(t-(L+l)/2c)\Big)+\cos\Big(\delta(L-l)/2c\Big)\Big], \end{aligned} \tag{1}$$

where $\omega = 2\pi\nu_{opt} = 2\pi c/\lambda_{opt}$ and $\delta = 2\pi F = 2\pi c/\Lambda$, is detected by PhD1. The (reference) photodiode PhD0 delivers a signal whose amplitude and phase are used to eliminate power and phase fluctuations of the laser source. Expression (1) is valid only in vacuum. Application to quantitative measurements in air requires that two indices of refraction, at the two wavelengths, are taken into account.

The measurement exploits the phase $\Phi$ and amplitude $\alpha$ of the $\alpha\cos(\delta t - \Phi)$ terms, oscillating at the microwave frequency $F$. As illustrated in Fig. 2, in which oscillating terms are represented as vectors $\alpha\exp(i\Phi)$ in the complex plane, the measurement signal $A$ is the sum of three terms, $MEAS = (1-\epsilon^2)\exp(i\delta L/c)$, $REF = \epsilon^2\exp(i\delta l/c)$, and the interference contribution:

$$INT = 2\epsilon\sqrt{1-\epsilon^2}\ \cos[(\omega+\delta/2)\Delta L/c] \times \exp\Big(i\delta(L+l)/c\Big). \tag{2}$$

When the optical frequency $\nu_{opt}$ of the two-mode source is scanned over more than the free spectral range $FSR \equiv c/\Delta L$, the tip of the vector $A = MEAS + REF + INT$ travels back and forth along the "segment" (Fig. 2-a), of length $4\epsilon\sqrt{1-\epsilon^2}$, characteristic of optical interference. Any deviation from a strictly linear segment reveals the presence of systematic effects.

The dependence on the target position is more complex. Not only the amplitude of the $INT$ vector changes, but its direction, and the $MEAS$ vector direction also change, producing a circular pattern with a large number ($\omega/\delta \approx 10^4$) of spikes. On Fig. 2-b, the choice of $\omega/\delta \approx 20$ allows for the spikes to be conveniently observable. Each spike corresponds to one fringe of the optical interference.

From a *single* measurement of this complex interference signal, one cannot extract the three contributions separately. However, assuming that a time-of-flight measurement has been done beforehand, with a relative accuracy of $10^{-5}$ or better, one can estimate the free spectral range $FSR$, and perform *three* measurements $A1, A2, A3$ with an optical frequency of $\nu_{opt}$, $\nu_{opt} + FSR/4$, and $\nu_{opt} + FSR/2$, respectively. Then the three data points of the two-mode interference signal can be processed, in a relatively straightforward manner, to compute, separately, the interferometric phase $\Phi_{inter} \equiv 2\pi\Delta L/\lambda_{opt}$ (mod. $2\pi$) and the synthetic phase $\Phi_{synt} \equiv 2\pi\Delta L/\Lambda$ (mod. $2\pi$). Fast ($< 1$ $\mu$s) change of the optical frequency can be achieved using an acousto-optic modulator (AOM). The accuracy of the measurement relies on the accuracy of the knowledge of $\nu_{opt}$ and $F$.

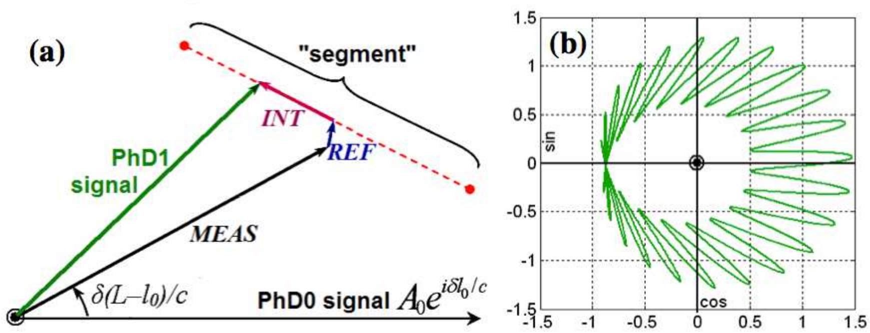


Figure 2.: *Behavior of the two-mode interference signal (PhD1 signal): (a) when the optical frequency of the two-mode source is scanned, (b) when the target moves continuously over one half of the synthetic wavelength, $\Lambda/2$, for $\epsilon = 0.25$. For clarity, $\Lambda/\lambda_{opt}$ is chosen equal to 20.*

## 3. Implementation

In the experimental set-up (Fig. 3) interference takes place at the Glan polarizer which, oriented at 45°, mixes the beams from the reference and measurement arms. Stray contributions to the two-mode interference signal have to be kept below $10^{-4}$. Hence, stray beams have to be kept well below $10^{-8}$: wedged optics are used to prevent interference due to multiple reflections, which are a significant source of systematics. The microwave signals (20.04 GHz) are detected by two 20 GHz bandwidth photodiodes, down-converted to 20 MHz by the mixers, and sampled during 10 $\mu$s by two 250 MS/s, 14 bit analog-to-digital converters.

The FPGA-based phase meter updates the AOM frequency for the $\nu_{opt}$ shifts and calculates the signal amplitudes and phases. Data processing and averaging (Phung 2013) is operated in a way that rejects the slow drifts in the microwave instrumentation, which otherwise would spoil the measurements, adding shifts of $\pm 1$ (or several) times $\lambda_{opt}$ on the measurement of $\Delta L$. Next section describes phase systematic shifts of thermal origin that have requested a change in the detection setup.

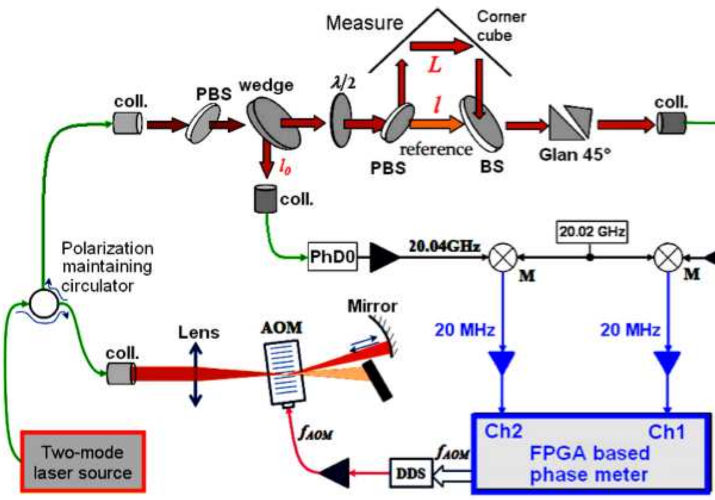


Figure 3.: *Implementation of the range meter. Orange: laser beams; green: optical fiber; black: HF signals; blue: RF signals; coll., fibered collimators; (P)BS: (polarizing) wedged beam splitter plates; Glan* 45°*: air Glan polarizer; DDS: direct digital synthesizer. M: mixers.*

As shown in Fig. 4, successive elementary measurement cycles, repeated every 130 $\mu$s, show the presence of acoustic perturbations, with an amplitude of several nanometers, on the measured length difference. The acoustic perturbations are due to the fans of the electronic equipment in the experimental room, close to the $\approx 7.5$ m round trip measurement arm.

The acoustic perturbations of the measurement path will be absent in the measurement of distances in vacuum, and the resolution, about 130 pm over one elementary measurement cycle, is expected to improve with integration time.

## 4. Amplitude-to-phase (AM-to-PM) effects and their reduction

Systematic errors in the detection chains are of two kinds. The first one is electrical cross-talk, which, if uncorrected for, gives rise to errors of about 10 $\mu$m in the ranging measurements. It can be measured, in phase and amplitude, and can

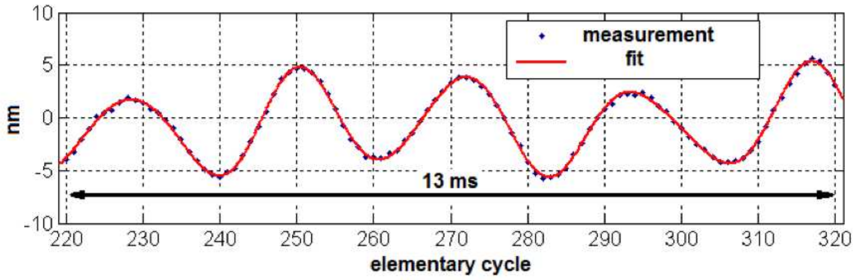


Figure 4.: *One hundred successive length measurements (an offset of $\approx 7.5$ m is subtracted, for clarity). One point corresponds to one $A1 \Rightarrow A2 \Rightarrow A3$ sequence (one "elementary measurement cycle"). The red curve is a fit obtained using 8 harmonic (sine) functions.*

be corrected for, with a good enough accuracy. The second kind of systematics in the detection chain is amplitude-to-phase coupling.

AM-to-PM coupling is well-known in electronics, and has been observed also in high-bandwidth photodiodes. On our set-up, if uncorrected, it gives rise to ranging errors of the order of 100 $\mu$m (Phung 2013). One might think that, knowing the amplitude, AM-to-PM coupling related errors can be corrected for, if the phase-vs-amplitude curve is measured beforehand over the range of experimental values. However, this approach fails with ranging signal data, in which the amplitude changes at microsecond time scales, along a complex pattern. This is due to the fact that AM-to-PM coupling has two contributions related to the physics of the photodiode junction. One is the screening of the applied electric field due to the carriers created in the junction (Taylor et al. 2011, Zhang et al. 2012): it develops at picosecond time scales, and can be considered as instantaneous in our measurements. But the large (up to factors of 3) optical power changes also give rise to another type of AM-to-PM coupling during the $A1 \Rightarrow A2 \Rightarrow A3$ sequence. The heating of the photodiode junction under the Joule power $V_{bias} \times I_{photo}$ (Chen et al. 2009) also changes, giving rise to a *transient* AM-to-PM, at time scales that range from microseconds to milliseconds. As the transient are not exactly exponential with time, correction of the phase systematic errors is not perfect. It removes the errors in the ranging measurement by a considerable factor (from 100 $\mu$m peak-to-peak to 3 $\mu$m, see Fig. 5-a). But on the corrected ranging results, systematic errors are still observable as shifts by + or $-\lambda_{opt}$, which prevent from reaching nanometer scale accuracy.

As suggested by Kim & Kärtner (2010), a modification of the detection setup allows to reduce by a large factor the systematic errors on the phase of the detected signals. It consists in demodulating the 20 GHz signal, not by a microwave mixer (as in Fig. 3), but by an integrated optics intensity modulator placed before the measurement chain photodiode. Then (Phung et al., submitted), the AM-to-PM couplings are expected to be reduced by the ratio of the microwave and intermediate frequencies. On Fig. 5-b, an AM-to-PM coupling is still observable (top graph), but it is attributed to the intermediate frequency amplifier (right blue triangle on Fig. 3). Numerical correction of this systematic phase error is efficient, and the convergence rate reaches 92% while the expected convergence rate is 93.5% (as no 20 GHz modulator was available, we used a 10 GHz modulator, with low 20 GHz modulation efficiency, leading to a reduced signal-to-noise ratio).

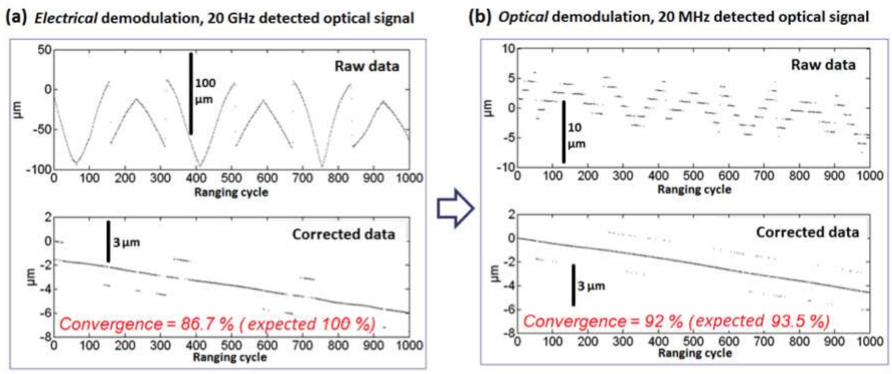


Figure 5.: *Ranging data recorded when the target is slowly moving (2 $\mu$m/minute). The retrieved arm length difference $\Delta L$ is plotted for successive ranging cycles, with an offset of $\approx$ 7.5 m. (a): the set-up of Fig. 3 is used; in the lower graph the data are corrected for electrical cross- talk and AM-to-PM coupling (instantaneous and transient, 20 $\mu$s time constant). (b): detection uses optical demodulation. Due to the low intensity modulation efficiency, noise on the data limits the expected convergence to 93.5%.*

## 5. Conclusion

A two-mode interference signal is used in high sensitivity absolute distance ranging, after a time of flight measurement has provided a preliminary, coarse estimate of the distance. The two-mode interference signal can be processed in a way that both the synthetic wavelength phase, and the optical interference phase can be retrieved, providing, respectively, micron- and nanometer-scale precision. The processing of the data removes the slow drifts that take place in microwave components, by completing an elementary measurement cycle in about 100 $\mu$s. A new length measurement is provided after averaging $\approx$50 ms of data. Large (several times $10^{-3}$ radian) systematic errors due to amplitude-to-phase coupling in the photodiode are removed by optical (rather than electrical) demodulation of the optical 20 GHz signal. Other systematic errors, related to optical interference (Phung 2013, Chapter 5) are kept under control by using wedged optics to prevent stray beams from interfering with the measurement beam or the reference beam. This high accuracy ranging method, allowing a resolution at the 100 pm scale in about 100 $\mu$s, appears to be competitive with other ranging schemes with more sophisticated laser sources.

## References

Chen, H., Beling, A., Pan, H., & Campbell, J. C 2009, IEEE Journal of Quantum Electronics 45, 1537

Coddington, I., Swann, W. C., Nenadovic, L., & Newbury, N. R. 2009, Nature Photonics, 3, 351

Fatome, J., Pitois, S., Fortier, C., Kibler, B., Finot, C., Millot, G., Courde, C., Lintz, M., & Samain, E. 2010, Optics Communications, 283, 2425

Joo, K. N., Kim, Y., & Kim, S. W. 2008, Optics Express, 16, 19799

Kim, J., & Kärtner, F. X. 2010, Laser and Photonics reviews, 4, 432

Lay, O. P., Dubovitsky, S., Peters, R. D., Burger, J. P., Ahn, S.-W., Steier, W. H., Fetterman, H. R., & Chang, Y. 2008, Optics Letters, 28, 890

Phung, D.-H., Alexandre, C., & Lintz, M., 2013, Optics Letters, 38, 281

Phung, D.-H. 2013, Thèse de doctorat de l'Université de Nice, `http://tel.archives-ouvertes.fr/docs/00/86/80/28/PDF/2013NICE4038.pdf`

Phung, D.-H., Merzougui, M., Alexandre, C., & Lintz M., submitted

Salvadé, Y., Schuhler, N., Lévêque S., & Le Floch S. 2008, Applied Optics, 47, 2715

Taylor, J. et al. 2011, IEEE Photonics Journal, 3, 140

van den Berg, S. A., Persijn, S. T., Kok, G. J. P., Zeitouny, M. G., Bhattacharya, N. 2012, Physical Review Letters, 108, 183901

Zhang, W., Li, T., Lours, M., Seidelin, S., Santarelli, G., & Le Coq, Y. 2012, Applied Physics B, 106, 301

*Improving the performances of current optical interferometers & future designs*
*Proceedings of Haute Provence Observatory Colloquium (23-27 September 2013)*
*Edited by L. Arnold, H. Le Coroller & J. Surdej*

# Observing the Sun with micro-interferometric devices: a didactic experiment

D. Defrère[1], O. Absil[2], C. Hanot[3], P. Riaud[2], A. Magette[3], L. Marion[2], O. Wertz[2], F. Finet[2], M. Steenackers[4], S. Habraken[2], A. Surdej[2], & J. Surdej[2]

[1] *Steward Observatory, 633 N. Cherry Avenue, 85721 Tucson, USA*

[2] *Université de Liège, 17 Allée du 6 Août, 4000 Liège, Belgium*

[3] *Techspace Aero, Route de Liers 121, 4041 Milmort, Belgium*

[4] *Technische Universität München, Arcisstraße 21, 80333 München, Germany*

**Abstract.** Measuring the angular diameter of celestial bodies has long been the main purpose of stellar interferometry and was its historical motivation. Nowadays, stellar interferometry is widely used for various other scientific purposes that require very high angular resolution measurements. In terms of angular spatial scales probed, observing distant stars located 10 to 100 pc away with a large hectometric interferometer is equivalent to observing our Sun with a micrometric baseline. Based on this idea, we have manufactured a set of micro-interferometric devices and tested them on the sky. The micro-interferometers consist of a chrome layer deposited on a glass plate that has been drilled by laser lithography to produce micron-sized holes with configurations corresponding to proposed interferometer projects such as CARLINA, ELSA, KEOPS, and OVLA. In this paper, we describe these interferometric devices and present interferometric observations of the Sun made in the framework of Astrophysics lectures being taught at the Liège University. By means of a simple photographic camera placed behind a micro-interferometric device, we observed the Sun and derived its angular size. This experiment provides a very didactic way to easily obtain fringe patterns similar to those that will be obtained with future large imaging arrays. A program written in C also allows to reproduce the various point spread functions and fringe patterns observed with the micro-interferometric devices for different types of sources, including the Sun.

## 1. Introduction

The measurement of stellar angular diameters is the historical motivation of stellar interferometry which is now used for various scientific purposes. Since the first interferometric measurement of the angular diameter of a star in December 1920 (Michelson & Pease 1921), a few hundred stars have been measured with various interferometers worldwide. Such experiments are however relatively complex and require ressources generally beyond those available at the University level. Teaching the basics of stellar interferometry then hardly finds an astrophysical application and remains limited to lab experiments with artificial sources. In this context, we have manufactured a set of micro-interferometric devices that can easily be used in the framework of Astrophysics lectures. The idea is that, in terms of spatial scales probed, observing our Sun with a micrometric baseline is equivalent to observing distant stars located 10 to 100 pc away with a large hectometric interferometer. Indeed, the Sun has an angular diameter $\theta$ typically ranging between 0.524 and 0.542 degree, depending on the Sun-Earth distance. In order to resolve it in the middle of the visible wavelength range ($\lambda$=555.5 nm), a single monolithic pupil should have a linear diameter of approximately 145 $\mu$m (according to the Huygens-Fresnel principle). With an interferometer, the baseline ($b$) leading to fringes with a null visibility can be computed using the expression of the fringe visibility with respect to the baseline length and to the size of the source. Accounting for linear limb-darkening, the fringe visibility can be computed as (Hanbury et al. 1974):

$$\mathcal{V} = \frac{1-u}{(1-u)/2 + u/3} \left( \frac{J_1(z)}{z} + u\sqrt{\frac{\pi}{2}} \frac{J_{3/2}(z)}{z} \right) , \tag{1}$$

where $J_1$ is the Bessel function of the first kind, $u$ the limb-darkening coefficient (0.485 in the case of the Sun, Claret et al. 1995), and $z = \pi b\theta/\lambda$. At $\lambda$=555.5 nm, it is therefore possible to fully resolve the Sun with a baseline of approximately 80 $\mu$m. The expected visibility of the Sun as a function of the baseline length is represented in Fig. 1. By using micro-interferometers with various baselines, it is therefore possible to produce fringes over a wide range of visibilities and derive the diameter of the Sun by model fitting. This experiment has been conducted by students at the Liège University and is described in the present paper.

## 2. The micro-interferometric devices

The micro-interferometers consist of a single glass plate that has been drilled with micron-sized holes by laser lithography. Typically, the holes present a diameter of approximately 10 $\mu$m, and are located several tens of microns from each other to form various kinds of configurations (e.g., 2 holes, 3 holes, VLTI, CARLINA, ELSA, KEOPS, OVLA, ...). A chrome layer is deposited on the plate surface to maximize its opacity around the holes. An example of interferometric plate presenting 49 different hole configurations is shown in Fig. 2 (left) in its mechanical support. To observe the Sun, this support is mounted at the front of a classical digital camera (see Fig. 2, right) and the chosen interferometric configuration aligned properly with micrometric screws. Each configuration can be identified by naked eye or by referring to the blueprint of the device (see Fig 3).

Before observing the Sun with the device, we characterized the PSFs of various configurations. Two examples are shown in Fig 4 with the corresponding configuration displayed in the lower right insets.

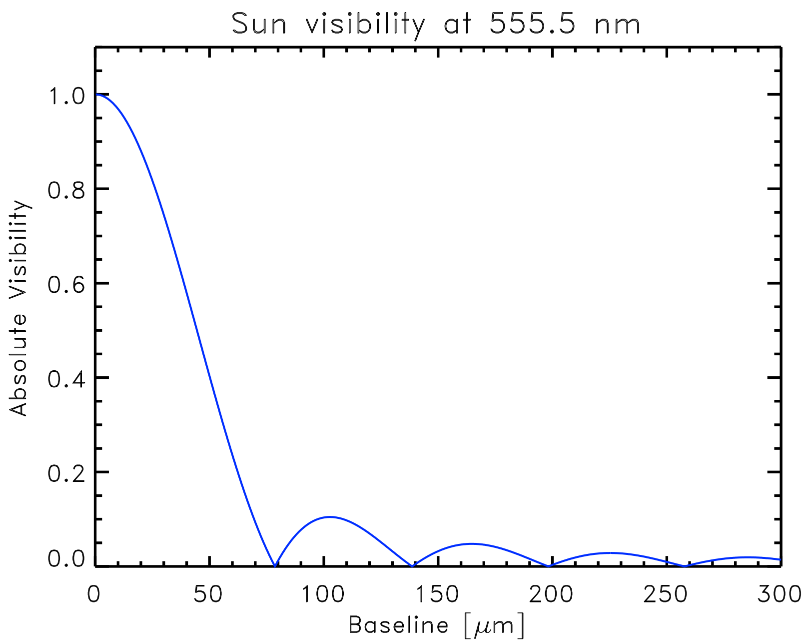


Figure 1.: *Absolute visibility of the Sun with respect to the baseline length at a wavelength of 555.5 nm. Considering a linear limb-darkening coefficient of 0.485 (Claret et al. 1995), the Sun is fully resolved for a baseline of approximately 80 $\mu$m.*

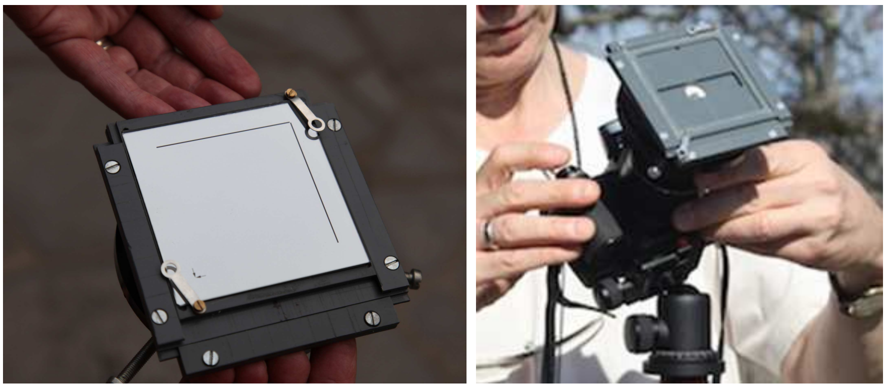

Figure 2.: *Picture of a micro-interferometer plate in its mechanical support (left). This plate contains 49 different interferometric configurations that have been drilled by laser lithography. The plate and its support are mounted at the front of a classical digital camera (right picture).*

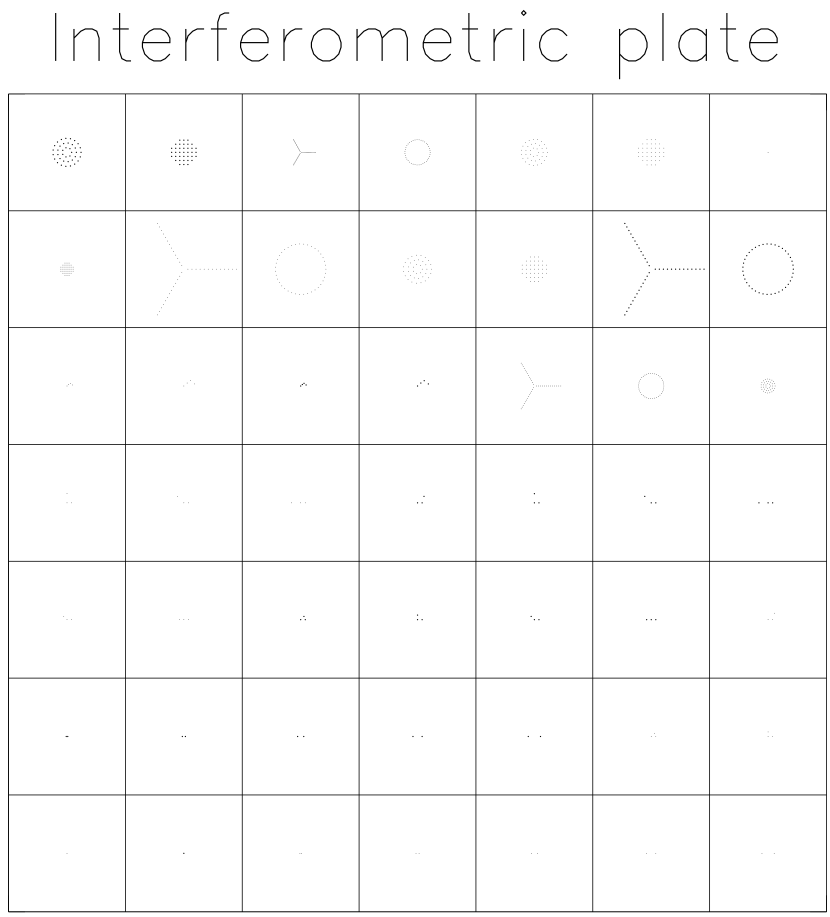


Figure 3.: *Blueprint of the micro-interferometric devices. The hole configurations have been scaled up to match the size of the boxes (preserving the relative scale between each configuration).*

## 3. Observing the Sun

In the framework of Astrophysics lectures being taught at the Liège University, students observed the Sun with the micro-interferometric device. The main goal was to measure the angular diameter of the Sun. This experiment is ideal to get familiar with the notion of fringe visibility and to learn the main steps of interferometric data reduction (i.e., background subtraction and model fitting). Examples of observations obtained on the Sun are shown in Fig. 5 for the 2-hole and ELSA configurations. Generally, the students have measured the diameter of the Sun within a precision of 10%. Attempts to create a "high-resolution" image of the Sun by quickly rotating the interferometric device have been unsuccessful so far, mainly due to the lack of a good and smooth rotation mechanism.

In parallel to the observations, we developed a little C software to help with the preparation of the observations. The software reproduces the fringe pat-

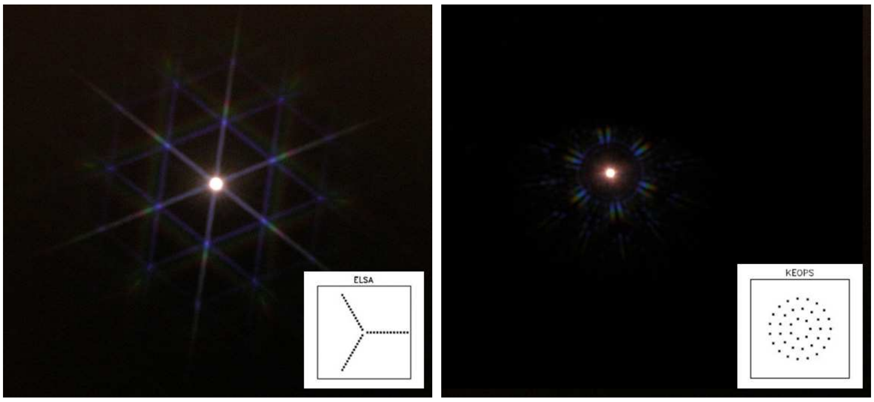


Figure 4.: *Picture of observed PSFs with configurations displayed in the insets (ELSA and KEOPS). The main baseline used is 50 $\mu$m and a hole diameter of 14 $\mu$m.*

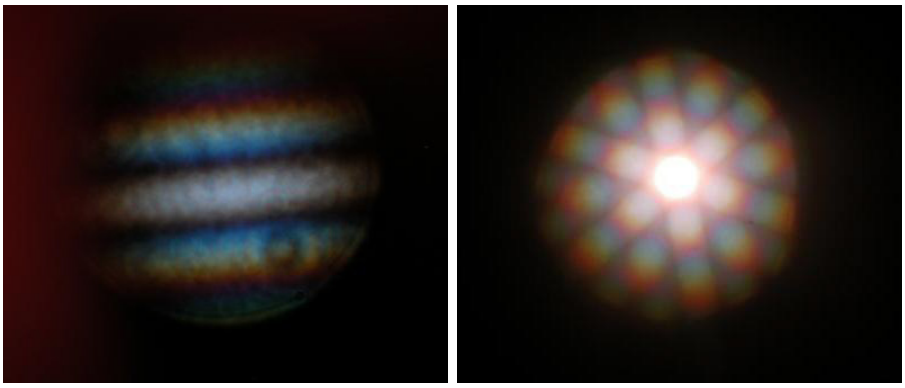

Figure 5.: Left, *First interferometric image of the Sun obtained in April 2010 with a 2-hole configuration (baseline length of 29.4 $\mu$m and hole diameter of 11.8 $\mu$m).* Right, *Observation of the Sun with the ELSA configuration (main baseline length of 24 $\mu$m and hole diameter of 7.2 $\mu$m).*

terns observed with the micro-interferometric devices for various kinds of sources and hole configurations. Input images can also be used which provides a good intuition of interferometric imaging. This software is called $\mu$IDS (i.e., micro-Interferometric Device Simulator) and can be downloaded on the following website: http://www.aeos.ulg.ac.be/upload/uIDS-setup.rar (only available for PC platforms).

## 4. Prospects

Various areas of the proposed experiment can still be improved. On the technical side, the opacity of the interferometric plates is currently relatively poor which impairs the quality of the fringes. We are currently exploring the possibility to use a different material for the plate (e.g., aluminium). We also would like to build a reliable rotating mechanical support in order to produce “high-resolution” images of the Sun. On the software side, we intend to adapt the $\mu$IDS software to the Mac platform.

## References

Michelson A.A. & Pease F.G., 1921, ApJ, 53, 249

Hanbury Brown R., Davis J., Lake R.J.W., & Thompson R.J., 974, MNRAS, 167, 475

Claret A., Diaz-Cordoves J., & Gimenez A. 1995, AAPS, 114, 247

*Improving the performances of current optical interferometers & future designs*
*Proceedings of Haute Provence Observatory Colloquium (23-27 September 2013)*
*Edited by L. Arnold, H. Le Coroller & J. Surdej*

# Session 4. Optimized beam combiners for present and future interferometers

Chair: Fabien Malbet
Wednesday morning, Sept. $25^{th}$

*Improving the performances of current optical interferometers & future designs*
*Proceedings of Haute Provence Observatory Colloquium (23-27 September 2013)*
*Edited by L. Arnold, H. Le Coroller & J. Surdej*

# Interferometric beam combination for a large number of telescopes

P. Kern[1], F. Malbet[1], E. Le Coarer[1]

[1] *UJF-Grenoble 1 / CNRS-INSU, Institut de Planétologie et d'Astrophysique de Grenoble (IPAG), UMR 5274, BP 53, F-38041 Grenoble cedex 9, France*

**Abstract.** We revisit here the system design for the beam combinations of ground based interferometers in the single mode case. We propose an upstream beam distribution using splitting of individual telescope pupils. This solution aims at reducing the constrains of the turbulence, thanks to larger equivalent $D/r_o$ values when injecting in single mode waveguides, and also to increase the field of view imposed by the optical étendue in single mode conditions. A set of elementary beam combiner devices operated in closure phase mode collects the beams delivered by the telescope sub-apertures. The concept brings along also additional interesting features like an easier distribution of the light in parallel instrument or a better use of telescopes of different diameters. Several practical implementations are presented to illustrate the potential of the concept in the case of the combination of 4 or 6 telescopes of the VLTI/ESO in Paranal or CHARA on Mt Wilson.

## 1. Introduction

Single Mode (SM hereafter) interferometry brings along several advantages that have been exploited many times in astrophysics first on IOTA and later on the VLTI and on Chara. The advantages of modal filtering using single mode optical waveguides have been demonstrated (Foresto *et al.* 1997; Mennesson *et al.* 2002). The impact on the achieved performances, the domain of application and comparison to other filtering solutions have been deeply analyzed (Tatulli *et al.* 2004; Tatulli *et al.* 2010).

It has been also identified that the photonics toolbox allows more advanced concepts where the whole beam combiner can be embedded in a single optical chip. Most of the system tasks required for the instrument purposes is then reported in the design of the component (Kern 2001; Malbet *et al.* 1999). It includes optical setups that implement robust and stable multi beam combination. These behaviors made such setups well suited for Closure Phase (CP) measurements. Telescope demonstrations have followed since early 2000s. Among important system features it has been demonstrated that the installation on site of such integrated instrument is highly simplified compared to bulk instruments as soon as the component is properly validated and characterized in laboratory (Berger *et al.* 2010; Le Bouquin *et al.* 2011). Based on photonics experience, we consider here the benefits from the use of multiple identical well known beam combiner chips.

We consider a segmentation of the telescope individual pupils before any injection in SM waveguides that will reduce the turbulence effects (i.e. $D/r_o$ equivalent value) and increase the field of view (FoV) seen by these smaller sub-apertures. The optimum theoretical injection in a SM waveguide is given for the optical étendue of $\lambda^2$, that corresponds to the diffraction pattern of the injection optics. Since the point spread functions (PSF) at the focus of the telescopes is constrained by the atmospheric turbulence, the efficiency of the injection in SM waveguides is directly impacted. When the PSF is limited only by the diffraction conditions the injection in SM guides become theoretically optimum.

Once an optimum injection is performed in the SM waveguides all the delivered beams could be combined using a set of identical integrated optics modules. A first description of a design for interferometry based on these arguments has been given by Guyon (2002). Designs based on pupil segmentation is also the principle of the photonics based instrument dedicated to pupil masking in the single telescope case as proposed in the Dragoonfly and in the FIRST instruments (Perrin *et al.* 2006; Kotani *et al.* 2009; Jovanovic *et al.* 2012). Similarly to this pupil masking scheme we propose a beam combination that allows Closure Phase recovery techniques in order to reject all differential phase disturbances introduced between the optical paths (including atmosphere and optical trains).

## 2. Impact of the turbulence

The effect of turbulence on the injection in SM fiber optics has been analyzed by Cyril Ruilier (1998) showing the following results:

- as soon as $D/r_o \leq .8$ the efficiency of the injection reach 50%,
- the injection fluctuations is highly affected by the ratio $R/r_o$.
- When a tip-tilt correction is applied the fluctuation increases quasi linearly with $D/r_o$ and reach 100% around $D/r_o = 10$.

The Table 1 recall typical value from Ruilier (1998) of the achievable injection and fluctuations according to the seeing condition.

Table 1.: *Injection efficiency ($\eta$) and relative fluctuations (F) according to the seeing condition, respectively without any correction, with Tip-Tilt correction, AO corrections with 11 and 21 Zernike modes.*

| $D/r_o$ | 0.8 | | 1.2 | | 2 | | 4 | | 10 | |
|---|---|---|---|---|---|---|---|---|---|---|
| | $\eta$ | F | $\eta$ | F | $\eta$ | F | $\eta$ | F | $\eta$ | F |
| no cor | 0.6 | 0.3 | 0.45 | 0.45 | 0.2 | 0.8 | 0.08 | 1 | 0.05 | 1 |
| $TT$ | 0.9 | 0.3 | 0.8 | 0.45 | 0.65 | 0.15 | 0.35 | 0.4 | 0.04 | 1 |
| $Z_{11}$ | 0.96 | 0.025 | 0.95 | 0.05 | 0.9 | 0.01 | 0.7 | 0.1 | 0.2 | 0.4 |
| $Z_{21}$ | 0.98 | - | 0.97 | - | 0.9 | | 0.8 - | 0.05 | 0.4 | 0.2 |

Furthermore Ruiler has shown that under a given seeing condition the total coupled power in a SM waveguide saturates for values of $D/r_o > 1$ and

$D/r_o > 4$ respectively without any correction with a Tip-Tilt correction. Increasing the telescope diameter will not increase anymore the power injected in the SM waveguides as soon as this saturation level is reached. The paper analyzes also the impact of the central obscuration that also affect the injection efficiency. In the case of VLT UT, with 1.2m secondary for 8m pupil, the resulting loss for injection is close to 7%.

This analysis shows possible domains of operation. If any adaptive correction is foreseen, it is useful to reach $D/r_o < 1.5$ to achieve efficient injection ($\eta > 40\%$) and moderate fluctuations ($F < 50\%$). In case of higher ratio, the conjunction of AO and of aperture segmentation can be considered but will not bring real system simplification, and similar performances compared to a full AO corrected system using a single waveguide per telescope.

## 3. Setup concept

We decide in this concept to split the beam delivered by each telescope upstream before any other optical function.

A schematic optical layout of the concept is given in Fig. 3. The beam

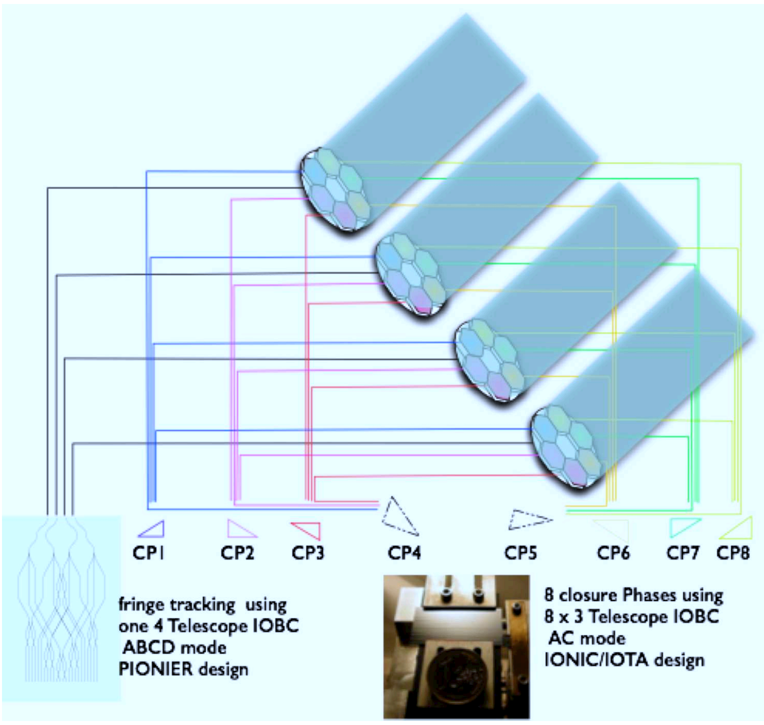


Figure 1.: *Proposed approach for the beam combination: The pupils of the telescopes are divided in sub apertures that fit the turbulent cells ($r_o$). The light from the sub-apertures are then combined to the light of corresponding cells of the other telescopes using SM waveguides. The division can be managed by a lens array that samples the whole telescope pupil image.*

splitting is performed in a plane conjugated to the telescope pupil plane in order to match the individual coherence cells at the highest level. For each sub-aperture, before any beam combination, the signal is injected in SM waveguides that will filter all remaining turbulence effects, providing at the output of the waveguides perfectly plane wavefront.

The central aperture that is strongly affected by the central obscuration of the telescope is not used, or can be used for service functions, for instance for metrology purposes. Consequently the other sub-apertures are not affected by any central obscuration and the overall resulting injection is slightly enhanced. The segmentation do not correct for all phase delays between the sub-apertures either due to atmospheric turbulence, instrumental errors or to SM injection mismatches.

We consider simple individual functions for the beam combination in order to reduce the complexity of the components and of the characterization processes. These characterizations become tedious for combination schemes that deals with large number of optical beams. In the layout presented in this paper, the interferometric combination is done by a set of triplets of beams (or more beams) in order to be able to use closure phase (CPs) technique to overcome any phase disturbance introduced by individual beam paths, either due to turbulence or instrumental effects. In the general case the number of CPs for N telescopes is given by

$$C_N^2 = \frac{N!}{2\,(N-2)!} \tag{1}$$

leading to 3 independent CPs in the 4 telescope case (4 possible triangles) and 10 independent CPs in the 6 telescope case (20 possible triangles). However the instrumental setup must insure that the maximum phase excursion is compatible with the detection of the resulting fringes because of temporal coherence, like for example in the IONIC/IOTA case. This effect can be reduced using a spectral dispersion providing a sufficiently large coherence length.

Beam combination through triplets in a co-axial mode brings the advantage to provide a measurement of the photometry over each individual sub-aperture without any additional dedicated channels. For larger groups of telescopes the beam combination scheme must be chosen properly to have access to this photometry (Blind *et al.* 2011).

For the beam combination, several schemes can be proposed using integrated optics beam combiner (IOBC) solutions. A set of IOBC as the one use for the IONIC/IOTA instrument (Berger *et al.* 2003) (3T-AC-IOBC hereafter) with an AC coding, is well suited for this purpose. One may propose also a component similar to the PIONIER beam combiner (4T-ABCD-IOBC hereafter) as described in Benesty *et al.* (2009) that delivers on-chip solution for the complete coding in 4 phase status without any temporal modulation.

The measurement of the single CP in the 3 telescope case is obtained from the 12 outputs when using an ABCD coding (3 baselines $\times 4$ samples). With 3 free pixels between each output, to avoid any crosstalk effects, each CP needs 48 pixels on the detector. One row of a regular $1K \times 1K$ detector array is able to manage up to 20 identical 3T combiners side by side on a single chip, corresponding to a 6 telescope case. The other dimension of the FPA is fully available for spectral dispersion or for polarization coding. For 6 telescopes at least 10 independent CPs must be measured. The Table 2 lists the possible non-redundant configuration in the case of a 6 telescope array.

Table 2.: *Example of 10 non-redundant triangles using 6 telescopes.*

| | T1 | T2 | T3 | T4 | T5 | T6 |
|---|---|---|---|---|---|---|
| 1 | x | x | x | | | |
| 2 | x | x | | x | | |
| 3 | x | x | | | x | |
| 4 | x | x | | | | x |
| 5 | x | | x | x | | |
| 6 | x | | x | | x | |
| 7 | x | | x | | | x |
| 8 | x | | | x | x | |
| 9 | x | | | x | | x |
| 10 | x | | | | x | x |
| 11 | | x | x | x | | |
| 12 | | x | x | | x | |
| 13 | | x | x | | | x |
| 14 | | x | | x | x | |
| 15 | | x | | x | | x |
| 16 | | x | | | x | x |
| 17 | | | x | x | x | |
| 18 | | | x | x | | x |
| 19 | | | x | | x | x |
| 20 | | | | x | x | x |
| #CP | 10 | 10 | 10 | 10 | 10 | 10 |

When the pupil segmentation provides more beams that required to obtain the full set of independent CPs, the additional CPs can be used to add several identical measurements in order to improved the signal to noise ratio (SNR) especially for shorter base-lines where the visibility signal may become lower.

Some of the additional outputs can also be specifically dedicated to other functions like the fringe sensing, without any additional system complexity. Extra beams can also be used for additional useful functions (fringe tracking), or to improve the u,v plane coverage using slightly different baselines per main apertures. Finally the segmentation can be suitable to optimize the combination when using telescope of different diameters (eg 8m and 1.8m telescope at VLTI) (see Fig. 5).

## 4. Example of dimensioning

We consider here a few illustrating examples, using the facilities of the ESO VLTI in Paranal with 4 main 8-m telescopes (UT) and possibly up to 6 relocatable auxiliary telescopes 1.8-m (AT) [1] and the facilities of CHARA on the Mt Wilson with 6 fixed 1m telescope, in both cases with corresponding 6 delay lines.

Table 3 resumes the dimensioning parameters for medium seeing condition (for Cerro Paranal) for the VLTI and CHARA case.

In this median seeing conditions the phase error within a UT or AT pupil remains smaller than a few $\mu$m as expressed in term of Optical Path Difference (OPD). It means that the phase corrections required between the clusters are

[1] 4 ATs are actually operational on site

Table 3.: *Splitting ratio for a configuration of* 1.8*m telescopes considering the seeing median value at Paranal (according to the ESO web site the median seeing value is* 0.66 *arcsec that corresponds to* $r_o = .15\,m\,@\lambda = .5\,\mu m$*)*

| Spectral band | $I$ | $J$ | $H$ | $K$ |
|---|---|---|---|---|
| Central $\lambda$ | $0.8\,\mu m$ | $1.3\,\mu m$ | $1.6\,\mu m$ | $2.2\,\mu m$ |
| $r_o$ | $24\,cm$ | $40\,cm$ | $48\,cm$ | $66\,cm$ |
| $D/r_o$ over CHARA pupil | 4.2 | 2.5 | 2 | 1.5 |
| CHARA / splitting ratio | 7 | 7 | 7 | 7 |
| resulting $d/r_o$ over sub pupils | $\sim 1$ | 0.84 | 0.65 | 0.5 |
| $D/r_o$ over AT pupil | 7.5 | 4.5 | 3.7 | 2.7 |
| AT / splitting ratio | 19 | 19 | 7 | 7 |
| resulting $d/r_o$ over sub pupils | 1.5 | $\sim 1$ | 1.3 | $\sim 1$ |
| $D/r_0$ over UT pupil | 33 | 20 | 16 | 12 |
| UT / splitting ratio | 61 | 37 | 37 | 19 |
| resulting $d/r_o$ over sub pupils | 3.6 | 2.9 | 2.3 | 2.4 |

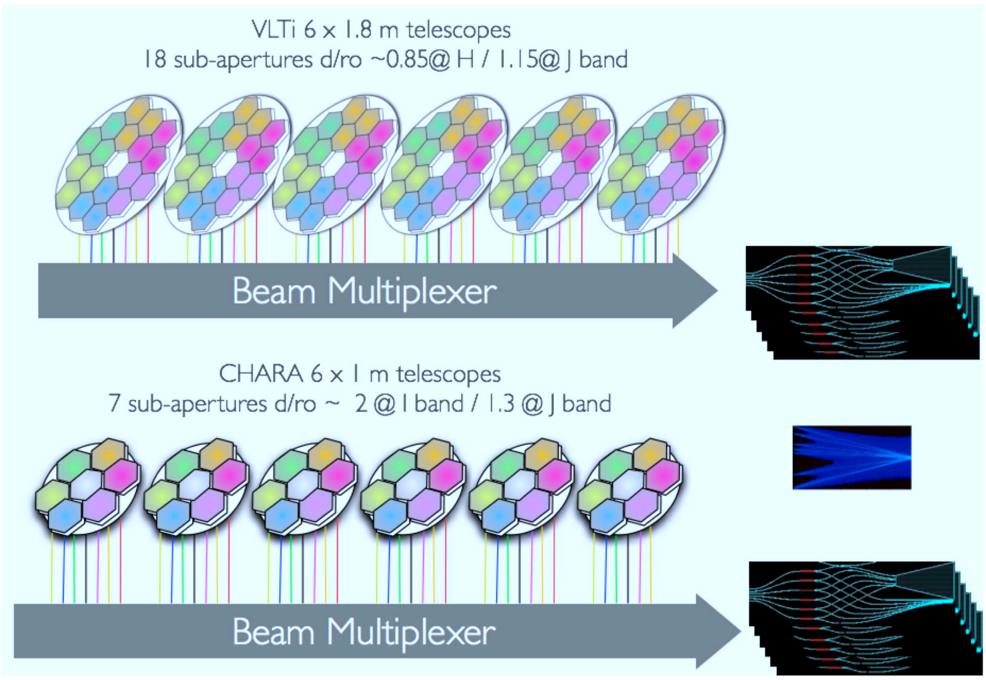


Figure 2.: *System setup for 6 telescopes using a 6T multiaxial combination. The VLTi case with* $6\times1.8m$ *telescopes (top) and the Chara case with* $6\times1m$ *(bottom) are shown. For the VLTi case a suitable* $d/r_o$ *is reached when splitting the pupil into 19 sub apertures in J and H band, requiring* $19\times6T$ *beam-combiners. In the Chara case it is achieved with 7 sub-apertures requiring* $7\times6T$ *beam-combiners (the central aperture is not usable due to the central obscuration).*

smaller or equal to this value, as soon as the OPD between the telescopes are compensated using a coherencing system.

### 4.1 Near IR ($I/J/H/K$ band) configuration with 6 telescopes.

Splitting the main pupil in 7 sub-apertures (CHARA in $I/J$ bands or VLTI in $H/K$ bands) or 19 sub-apertures (AT/VLTI in $I/J$ bands) allows to approach near diffraction limit conditions, with well optimized injection. For such configurations a correction of the tip tilt for each sup-aperture is sufficient to allow achieving a rather perfect injection.

The measurement of the minimum 10 independent CPs of the 6 telescope configuration requires also to split each telescope aperture at least into 7 sub-apertures.

The beam combination can be performed **by cluster of 3 sub-apertures**, for example using a set of 10 3T-beam combiners, similar to the one used for IONIC/IOTA (Berger *et al.* 2003). As mentioned above, this 3T combination does not require dedicated channels to extract the photometry. The measurement of the photometry of each telescope in this setup is naturally derived from the combination of the interferometric signals (Blind *et al.* 2011).

**An all-in-one multiaxial 6T combiner** can also be proposed as shown in Fig. 2). In this case the number of IOBC is the number of sub-apertures. We demonstrated during the phase-A study of the second generation fringe tracker for the VLTI that this "all-in-one" beam combination mode is the most efficient when using very low noise detectors (see for example Blind *et al.* 2011) with Read Out Noise lower than 2 electrons. Such low noise allows the number of pixels to increased without a significant impact on the overall $SNR$ of the interferometric signal detection (see Feautrier & Gach 2013 for the description of the RAPID/APD HgCdTe new generation detectors).

The large number of available $6T$ combinations allows various strategies of operation. For example to split them in two groups: a first one dedicated to fringe tracking, prevailing the shortest baselines in a boot-strapping mode to reconstruct the phase of the network from telescope to telescope and reducing the probability to deal with lower contrast due to resolved stars for the larger baselines. The second group may prevail the larger baselines. Increasing their number can improve the resulting $SNR$ ratio. Depending to the needs for the fringe tracking one may use a more or less large number of sub-apertures for fringe tracking. In an other hand, it may be useful to keep more signal to feed a high resolution spectrograph. However high spectral resolution can also not be useful for all baselines. To conclude this shows that such a setup brings a lot of flexibilities.

### 4.2 Near IR ($K$ band) configuration with $4 \times 8m$ telescopes

These conditions lead to a ratio $D/r_o = 12$ (Table 3). Splitting the main pupil into 19 sub-apertures (5 sub-apertures across) the ratio within each sup-aperture becomes $d/r_o = 2.4$. As mentioned in Roddier (1990) for this value a tip-tilt correction is well suited to achieve near diffraction limited conditions. Associated to the MACAO adaptive optics system operational on each UT, such configuration provide a very efficient injection (Table 1).

A possible scheme would be similar to the one described in Fig. 3. but with

19 sub-apertures (18 apertures operational). With an array of 4 telescopes it is required to record a minimum of 3 independent CPs.
For the beam combination a set of 18 PIONIER-like 4T-ABCD-IOBCs would be suited for the a direct coding of the fringes in groups of 4 sub-apertures (Le Bouquin *et al.* 2011).
A setup using "all-in-one design" multi-axial design is also possible.

If the multiple quadruplets use different positions within the UT main pupils it allows the number of achievable baselines to be increased, introducing new points in the *uv* plane providing additional lengths and angles, for the Fourier reconstruction. In the Fourier plane, instead of a strong frequency peak corresponding to the autocorrelation of the individual telescopes, the transfer function will have clouds of smaller peaks scaled by the smaller sub-apertures (see Fig. 4).

## 5. Practical implementation of the beam splitter

The splitting of individual telescope pupil can be done in the combination room, or even inside a cryostat. It requires to bring an image of the pupils of all the telescopes side by side with the suitable enlargement on a dedicated micro-lens array. Each micro-lens is associated with a fiber optics that will feed the proper input of one of the beam combiners (see Fig. 3 left). Standard micro lens arrays design for SM fiber injection, can be used. Silicon existing micro lens (Suss Optics) are available with an AR coating that allows an operation between 1.3 and $8\mu m$. To change the splitting ratio of the pupil (e.g. 7 to 19 sub-apertures) it requires to change the bundle fibers/microlens.

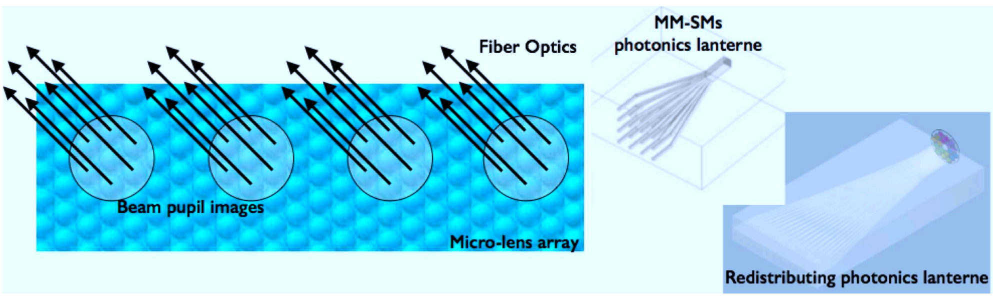


Figure 3.: *The selection of the sub-aperture is done using a micro lens array that feed the injection fibers of the integrated optics beam combiners (left). Photonics lanterns can also be used either to redistribute the beams coming from the different parts of the main pupils to the corresponding fiber optics (right/down), MM/SM lanterns can also be used to collect the flux at the telescope focus and to distribute it in a set of SM waveguides through an adiabatic transition (upper center, credit Robert Thomson). In this case no memory of the location in the pupil is kept.*

An alternate solution to split the beam of individual telescope pupils consists in using photonics lantern (Leon-Saval *et al.* 2005; Thomson *et al.* 2011). This device handles at its input a multi mode (MM hereafter) field, and distributes the light into a set of SM optical fibers thanks to proper adiabatic transitions (see Fig. 3 upper center). The field of view of the MM structure is much larger than the diffraction limited conditions of SM fibers, and can deal with a speckled image. Near infrared devices have been tested and characterized with efficient transmission, a demonstrative device that handles 61 mode exhibits transmissions from the MM to the SM section as low as 0.76 dB **(e.g. 84% transmission)** (Noordegraaf *et al.* 2010). More recent results demonstrate the efficiency of lanterns in near IR spectroscopy ($J$ band) after an adaptive optics system on the WHT with the Canary AO system (Harris *et al.* 2014). An interesting behavior for future mature components of this solution is the possible reduction of the injection losses that is induced by overlapping the fiber mode with the Airy pattern of the image delivered by the telescope (Shaklan & Roddier 1988). In the SM case the injection efficiency is limited to 78%. Much more efficient injection can be expected with MM waveguides, theoretically limited only by Fresnel losses that can also be managed by suitable anti reflection coatings. An implementation of these lanterns in an interferometric setup requires several verifications. Even if first characterizations of lantern have been published, laboratory tests must be performed to analyze how phases are handled in the device. The phase behavior of the lantern is an issue that must be evaluated even if the proposed setup allows rejecting the phase induced effects thanks to a CP detection setup. It must be characterized how the incoming modes contained in the MM field are spread in the individual single mode waveguides, and what is the phase behavior for each SM waveguides. In other word also, what is the effective lobe on the sky due to the MM structure, and what is its stability.

## 6. Discussion

A major advantage of the proposed concept is the possibility to adjust a setup that match the **seeing conditions** at the **wavelength of operation** and the **size of the telescope** to a ratio $D/r_o < 2$.

The flexibility of the proposed setup can be used to match the mode of observation, choosing to put emphasis on specific functions according to the observing conditions, for instance putting more signal either on the FT instrument or to the science instrument.

The **Field of View** is enlarged since it is not any more scaled by the Airy disk of the individual telescopes but by the diffraction pattern of each sub pupil in the lens array case (enlarged by the D/d ratio) and by the MM FoV of the input fiber in the lantern case. For the lantern developed by the Danish team, the MM port has a core diameter of 60 $\mu$m and an estimated numerical aperture of 0.06. These values (FoV and aperture) corresponds to $9''$ for an 1.8 m telescope and $2''$ for an 8 m telescope.

**U-V coverage**: Compared to standard case, breaking all telescope pupils give access to additional CPs. Playing over the diameter of individual telescopes one may have access to slightly different baseline configurations. For instance in a 8m telescope configuration split into 7 sub-apertures one may use external sub-apertures of the main telescope pair for some combinations, and internal ones for some other ones, with difference of lengths between the built baseline of 10.4m. This behavior can be used to improve the $uv$ coverage, with additional available baselines (see Fig. 5). This possibility to improve the $uv$ coverage does not apply in the lantern case, where the input modes are not spatially located within the pupil. This point needs to be properly investigated. Further investigations are required to address the question of the lobe center location in the lantern case.

An improvement of the **SNR** can be expected without any additional correction (Tip Tilt or AO correction) as soon as $d/r_o < 1$ after the splitting of the pupil. In this case the efficiency of the injection can reach $F > 50\%$ and its fluctuations be $\eta < 50\%$. For example in the AT case this $d/r_o$ ratio is obtained by a splitting in 7 segments for $H/K$ bands and in 19 segments for $I/J$ bands where the injection efficiency become respectively $\eta_{HK} < 20\%$ and $\eta_{IJ} < 5\%$ inducing a SNR improvement of a factor 2 to 10 according to the setup and the seeing conditions and when the detection is limited by the photon noise. The evaluation of the SNR improvement in low flux condition cannot be estimated directly and depends strongly of the chosen strategy for the detection, for instance it depends strongly of the number of pixels and of the read out noise for the considered detector. With a noisy camera it is not a good strategy to disperse the collected signal on a too large number of pixels, prevailing for example a co-axial AC or ABCD detection of the fringe over a multi-axial detection. With new APD NIR HgCdTe cameras this limitation will be overcome opening the possibility to use new beam combination strategies.

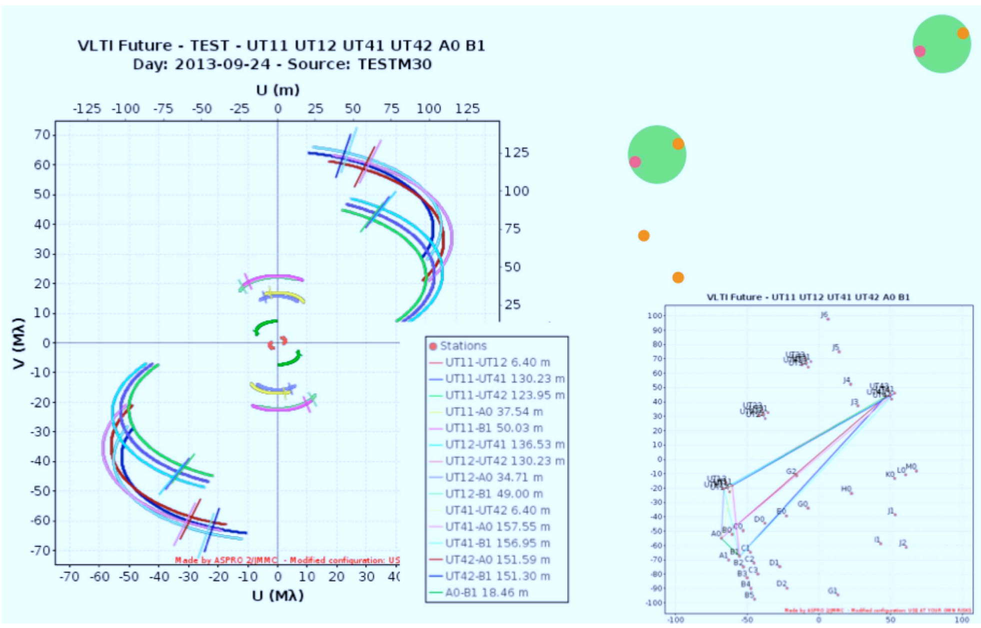


Figure 4.: *Hybrid array case with 1.8 and 8 m telescopes, resulting uv coverage enhancement for a compact array case (credit Gilles Duvert, IPAG).*

Another very interesting capability is to use this flexibility to combine **telescopes of various sizes** (e.g. AT and UT for the VLTI) and splitting them in sub-apertures of equivalent dimension (see Fig. 5). Such a setup avoids a $SNR$ loss due to the difference of diameter of the combined telescopes.

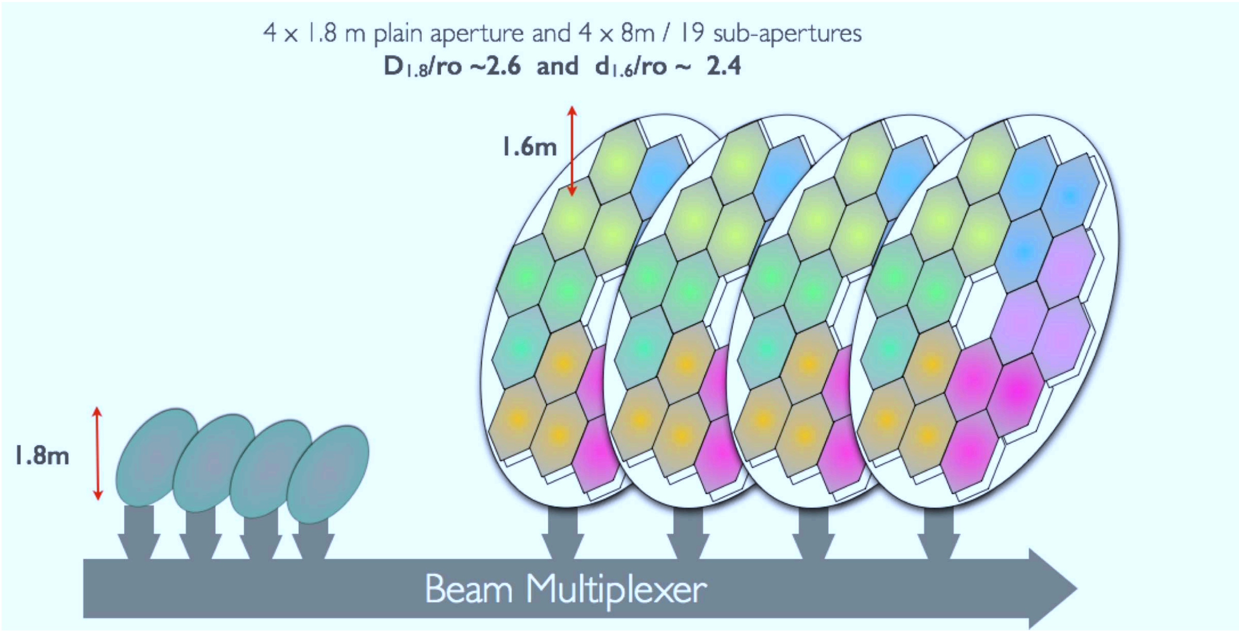


Figure 5.: *Hybrid array case with 1.8 and 8 m telescopes.*

## 7. Conclusion

We proposed a setup for single interferometry interferometry, where the beam distribution is performed in the input pupil plane by a pupil division scaled by the turbulence coherent area $R_o$, leading to a easier injection in the single mode waveguides, and by consequence reducing the need of a correction using an adaptive optics with a large number of actuators.

The proposed interferometric setup is able to simplify a multi-telescope instrument, using simple individual building blocks that have been fully validated for years on IOTA (IONIC/IOTA 3T) or on the VLTI (PIONIER 4T). The main behavior of the proposed setup is to be able to operate a complex interferometric array of telescopes without the need of complex AO systems under high $D/r_o$

conditions, while the combinations are performed between smaller sub-apertures lightly affected by the atmospheric turbulence.

It offers also an enlarged field of view thanks to smaller equivalent instrument pupils. The concept allows to reach shorter wavelengths down to the visible domain using SM waveguides. An other interesting behavior is the possibility to introduce additional points in the U-V plane for short baselines issue from nearby large telescopes.

The proposed setup would be suited for flexible operation according to the considered astrophysical program and to the seeing conditions. It is able to handle a large number of parallel channels, facilitating the realization of small series of simple unit components that can be easily tested and duplicated. Further instrumentation of existing or future telescope arrays (CHARA, VLTI, MROI with up to 10 telescopes), could contemplate such concept that provides an interesting modularity to deal with various astrophysical applications. The application to an hybrid network dealing with telescopes of different sizes is also applicable.

*Acknowledgements.* The authors thank Pierre Benech, Jean Baptiste Lebouquin, and Gilles Duvert for fruitful discussions about this concept.

## References

Benisty, M., Berger, J.-P., Jocou, L., et al. 2009, A&A, 498, 601

Berger, J.-P., Haguenauer, P., Kern, P. Y., et al. 2003, Interferometry for Optical Astronomy II. Edited by Wesley A. Traub . Proceedings of the SPIE, 4838, 1099

Berger, J.-P., Zins, G., Lazareff, B., et al. 2010, in Society of Photo-Optical Instrumentation Engineers (SPIE) Conference, Vol. 7734, Society of Photo-Optical Instrumentation Engineers (SPIE) Conference Series

Blind, N., Absil, O., Bouquin, J.-B. L., Berger, J.-P., & Chelli, A. 2011, A&A, 530, 121

Feautrier, P., & Gach, J. 2013, in Proceedings of the Third AO4ELT Conference, ed. S. Esposito & L. Fini (Firenze: INAF - Osservatorio Astrofisico di Arcetri)

Foresto, V. C. D., Ridgway, S., & Mariotti, J.-M. 1997, A&A Supplement series, 121, 379

Guyon, O. 2002, A&A, 387, 366

Harris, R. J., MacLachlan, D. G., Choudhury, D., et al. 2014, Audio, Transactions of the IRE Professional Group,

Jovanovic, N., Tuthill, P. G., Norris, B., et al. 2012, MNRAS, 427, 806

Kern, P. 2001, Comptes Rendus de l'Académie des Sciences - Séries IV - Physics, 2, 111

Kotani, T., Lacour, S., Perrin, G., Robertson, G., & Tuthill, P. 2009, Optics Express, 17, 1925

Le Bouquin, J., Berger, J., Lazareff, B., & Zins, G. 2011, accepted in A&A

Leon-Saval, S., Birks, T., Bland-Hawthorn, J., & Englund, M. 2005, Optics Letters, 30, 2545

Malbet, F., Kern, P., Schanen-Duport, I., et al. 1999, A&A Supplement series, 138, 135

Mennesson, B., Ollivier, M., & Ruilier, C. 2002, J. Opt Soc Am A, 19, 596

Noordegraaf, D., Skovgaard, P. M. W., Maack, M. D., et al. 2010, Optics Express, 18, 4673

Perrin, G., Lacour, S., Woillez, J., & Thiébaut, E. 2006, MNRAS, 373, 747

Roddier, N. 1990, Optical Engineering, 29, 1174

Ruilier, C. 1998, in Society of Photo-Optical Instrumentation Engineers (SPIE) Conference Series, Vol. 3350, Society of Photo-Optical Instrumentation Engineers (SPIE) Conference Series, ed. R. D. Reasenberg, 319-329

Shaklan, S., & Roddier, F. 1988, Applied Optics, 27, 2334

Tatulli, E., Blind, N., Berger, J. P., Chelli, A., & Malbet, F. 2010, A&A, 524, A65

Tatulli, E., Mège, P., & Chelli, A. 2004, A&A, 418, 1179

Thomson, R., Birks, T., Leon-Saval, S., Kar, A., & Bland-Hawthorn, J. 2011, Optics Express, 19, 5698

*Improving the performances of current optical interferometers & future designs*
*Proceedings of Haute Provence Observatory Colloquium (23-27 September 2013)*
*Edited by L. Arnold, H. Le Coroller & J. Surdej*

# Going deep and precise - the MIDI+FSU experiment - lessons learnt

J.-U. Pott

*Max-Planck Institut für Astronomie, Heidelberg, Germany (jpott@mpia.de)*

**Abstract.** A status review is given on the performance of the $10\mu$m VLTI/MIDI instrument, if supported by external fringe tracking. Highlights are a sensitivity improvement in the science band by about 5x down to 50mJy and similar gains in the precision of the differential phase estimator. It is also being discussed how our data scrutinize the infrastructural capability of the VLTI to do sensitive phase-referenced imaging with the upcoming second generation of beam-combiners, using light of four telescopes at a time.

The material presented at the conference has recently been published and the author proposes to the reader the references below.

## References

Müller, A.; Pott, J.-U. et al. 2010, in Optical and Infrared Interferometry II. Edited by Danchi, William C.; Delplancke, Françoise; Rajagopal, Jayadev K.. Proceedings of the SPIE, Volume 7734, article id. 773420, 15 pp.

Pott, J.-U.; Müller, A. et al. 2012, in Optical and Infrared Interferometry III. Proceedings of the SPIE, Volume 8445, article id. 84450Q, 4 pp.

Müller, A.; Pott, J.-U. et al. 2014, submitted

*Improving the performances of current optical interferometers & future designs*
*Proceedings of Haute Provence Observatory Colloquium (23-27 September 2013)*
*Edited by L. Arnold, H. Le Coroller & J. Surdej*

# PIONIER : A Four Telescope VLTI Instrument

B. Lazareff[1], J.-B. Le Bouquin[1], J.-P. Berger[2], G. Zins[1], P. Haguenauer[3], P. Gitton[3], A. Delboulbe[1], P. Feautrier[1], L. Jocou[1], P. Kern[1], Y. Magnard[1], T. Moulin[1], S. Rochat[1], E. Stadler[1], P. Labeye[4], M. Benisty[1], J. Kluska[1], K. Perraut[1], J. Knudstrup[2], J.-L. Lizon[2], R. Millan-Gabet[5], W. Traub[6], O. Absil[7]

[1] *UJF-Grenoble 1 / CNRS-INSU, Institut de Planétologie et d'Astrophysique de Grenoble (IPAG), UMR 5274, Grenoble, France*

[2] *European Southern Observatory, Karl-Schwarzschild-Str. 2, 85748 Garching bei München, Germany*

[3] *European Southern Observatory, Casilla 19001, Santiago 19, Chile*

[4] *CEA-LETI, MINATEC Campus, 17 rue des Martyrs, 38054 Grenoble Cedex 9, France*

[5] *NASA Exoplanet Science Institute (NExScI), California Institute of Technology, Pasadena, California, USA*

[6] *Jet Propulsion Laboratory, California Institute of Technology, Pasadena, California, USA*

[7] *Institut d'Astrophysique et de Géophysique de Liège (IAGL), University of Liège, 4000 Sart Tilman, Belgium*

**Abstract.** Pionier is a guest instrument, the first four-telescope recombiner at ESO's VLTI. We discuss salient design features and illustrate selected scientific results from the first $2\frac{1}{2}$ years of operation.

## 1. Introduction

In 2009, optical long baseline interferometry started to produce images at milliarcsecond (mas) scale, but the sensitivity limited its scope to stellar physics. The game was essentially dominated by CHARA. The VLTI, with its four 1.8m auxiliary telescope, was ramping up in performance but was limited to a maximum of three-telescope recombiner (AMBER). The second-generation instruments, designed for four-telescope operation, were not due before 2014-2015 (GRAVITY, MATISSE).

IPAG was since long interested in developing aperture synthesis imaging for the observation of pre-main sequence environments. The IONIC intergrated optics four-telescope recombiner had been developed through 10 years of collaboration with LETI. A camera (from IOTA/PTI) was kindly made available by Wes Traub. The opportunity for a fast-track project was identified. A proposal was made to ESO for a visitor instrument, that was approved by the STC in November 2009. A year later, the Pionier instrument was on-sky.

The project could be completed thanks to financial support from Université Joseph Fourier, IPAG, INSU-PNP, INSU-PNPS, and from two ANR grants (Exozodis and 2G VLTI).

## 2. Instrument description

In this section we describe the main features of Pionier. More detailed descriptions can be found in Berger et al. (2010) and Le Bouquin et al. (2011). The subsystems of Pionier are shown on Figure 1.

### 2.1 Injection and calibration

Each of the four beams from the VLTI enters the figure from the right, and is reflected off a dichroic mirror that, if observing in H band, transmits the K band to the IRIS guiding camera. It is then reflected off two plane mirrors in succession. The first one sits on a piezo-electric translation stage, and is used to modulate the optical path (OP) with an amplitude of $400\mu$m. The second, also piezo actuated, is a a tip-tilt used in two ways: (a) align the instrument with the VLTI reference during startup; (b) dynamically respond to the focal plane offsets measured by IRIS. A shutter permits to selectively block each beam. A birefringence compensation device will be discussed in more detail further down. An off-axis parabolic mirror injects the signal into a single-mode fiber, that guides it to the input of the combiner. The four fibers have been carefully matched, not for group delay (which can easily be compensated with the OP piezo), but for dispersion. This is necessary to preserve good fringe contrast near zero OPD. This part of the system is shown on Figure 2.

### 2.2 Birefringence compensation

We now return, in more detail, to birefringence compensation. Astronomical sources are at most weakly polarized. And for natural light, orthogonal polarizations do not interfere. Therefore, it is important to maintain the orientation of the axes up to the IOBC input. In Pionier, this is ensured by using polarization maintaining fibers. By nature, such fibers are strongly birefringent, accumulating one turn of differential phase over a few cm. Despite the careful (dispersion) matching of the fibers, the differential (between telescopes) birefringence is measured to be typically a few fringes. The initial design included a Wollaston prism, to detect separately the fringes in the two orthogonal linear polarizations. To gain in signal-to-noise *and* in readout speed, birefringence compensation has been implemented. A birefringent plate of $LiNbO_3$ is placed in each collimated beam. By changing the inclination of the plate, the phase delay between the two linear polarizations can be adjusted. This adjustment takes place with a Wollaston prism before the detector, allowing one to observe the fringes from the two polarizations. See Figure 3. Once the two polarizations are aligned in group and phase delay, the Wollaston is removed. Twice more light per pixel and half the

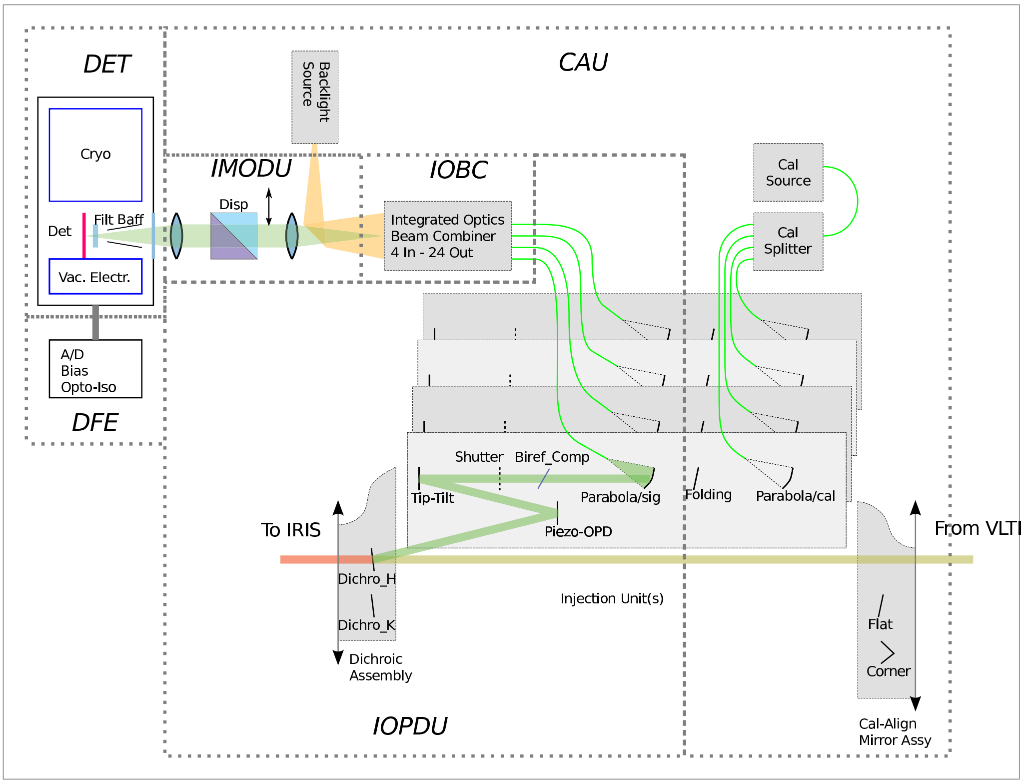


Figure 1.: *System diagram of Pionier. The subsystems are identified as follows. IOPDU: Injection Optics and Delay Unit; CAU: Calibration and Alignment Unit; IOBC: Integrated Optics Beam Combiner; IMODU: Imaging Optics and Dispersion Unit; DET: Detector; DFE: Detector Frontend Electronics.*

number of pixels to be read improves the S/N and allows to better freeze the turbulence. For more details, see Lazareff et al. (2012).

## 2.3 Integrated optics beam combiner

The integrated optics beam combiner (IOBC, Benisty et al. 2009) realizes the crucial function of interferometric recombination in optical waveguides implemented in silicon dioxide, where subsurface ion implantation permits a local increase of the refractive index. See Figure 4. The integration in silicon dioxide of the critical interferometric recombination is a guarantee of stability where it matters most: between the input of the beam splitters and the output of the recombiners. The IOBC has actually been fabricated in two major variants. In the first one, named AC, for each baseline, the two inputs generate two outputs $A = (e_1 + e_2)/\sqrt{2}$ and $C = (e_1 - e_2)/\sqrt{2}$. The second one, named ABCD, generates also: $B = (e_1 + ie_2)/\sqrt{2}$ and $D = (e_1 - ie_2)/\sqrt{2}$. On the balance of pros and cons, the ABCD variant is used the most, allowing a measurement of the bias power underlying (in frequency space) the fringe power, and a robust, unbiased, visibility estimate. The major part of the observing is made in H band, but a K band IOBC is available in selected periods.

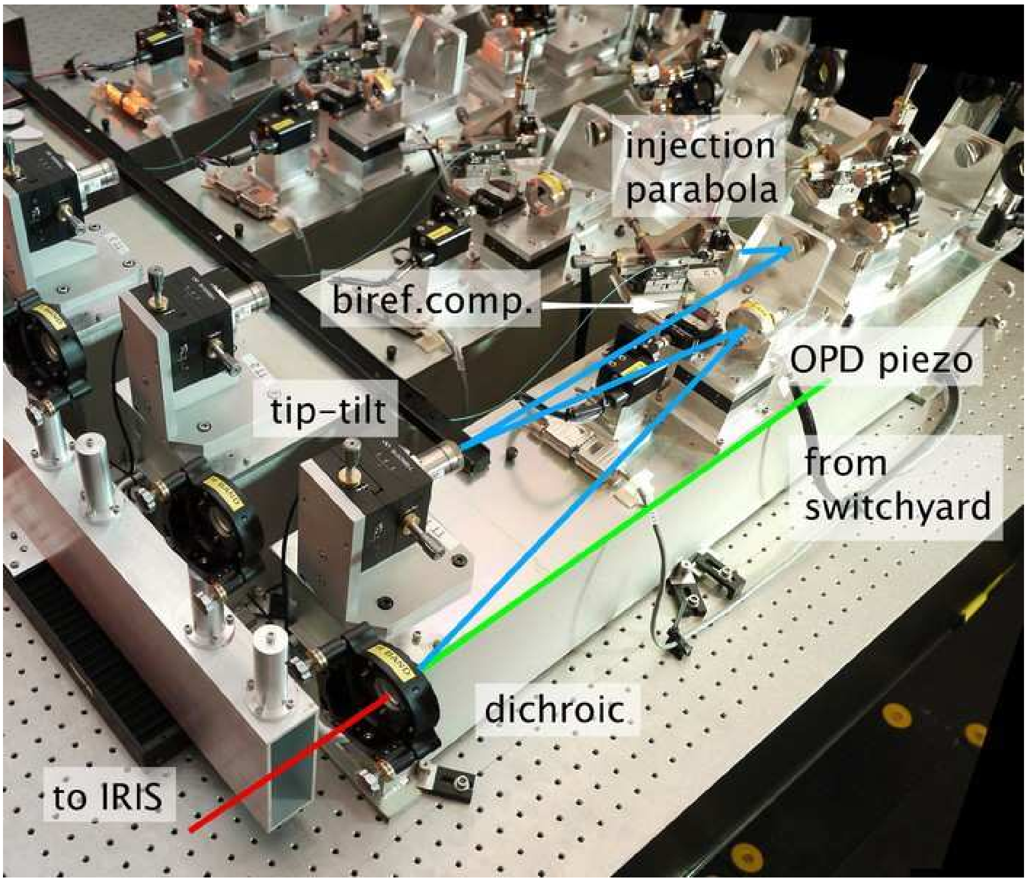


Figure 2.: *A view of the four optical assemblies, implementing the functions of the IOPDU and CAU. The light path from input to the injection parabola is also shown*

### 2.4 Dispersion

Prisms on a motorized stage between the IOBC and the camera provide, in addition to the broadband (1.55-1.80$\mu$m) mode, two dispersion modes: "small", $R \approx 20$ (3 channels), and "large", $R \approx 40$ (7 channels). When the source flux is large enough that one can afford to disperse it (up to H=7 under good conditions), and the coherence time large enough to spend the time to read more pixels, this has two benefits: (a) spectral information, e.g. dust envelope versus star; (b) improved coverage of the UV plane.

### 2.5 Acquisition and data processing

The 12 (AC version) or 24 (ABCD) outputs of the IOBC are imaged on the detector, a Rockwell mercury-cadmium-telluride PICNIC array. The fringes are produced by temporal modulation of the OPD, sweeping the four OP piezo stages at rates $-3s$, $-s$, $+s$, $+3s$, such that the OPD on any baseline is swept at rates between $2s$ and $6s$. We make use of the non-destructive readout of this detector in the so-called Fowler (default) mode. In a typical scan of 1024 steps (lasting

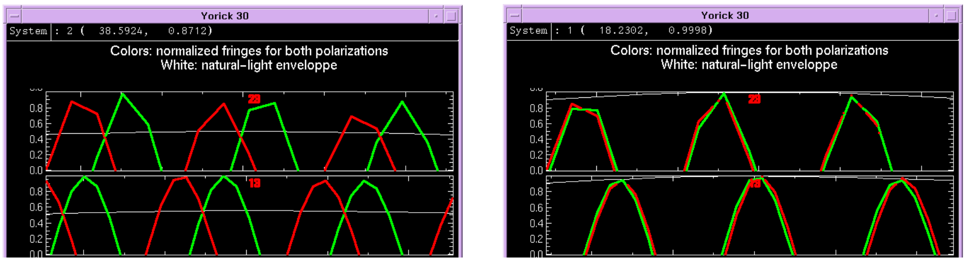


Figure 3.: *Cancellation of the differential birefringence by adjusting the $LiNbO_3$ plates, with the Wollaston prism inserted. Left: fringes from the two linear polarizations are mis-aligned. Right: after alignment is completed. The Wollaston can then be removed for observing, without loss of fringe contrast.*

700ms), the detector is read at each step, and is reset at the end of each scan. The capacity of the detector sites ($\approx 10^5$ electrons) makes this unsuitable for very bright objects (H$\leq$4.5), for which we fall back to a reset-read-read sequence at each scan step.

The fringes are displayed in real-time, both in delay and frequency space. The raw data are processed in two steps: reduction, that produces raw visibilities and closures, and calibration. A quick-look pipeline is running during the observations, providing instant (a few minutes latency) feedback to the observer. Special attention has been paid in the data reduction software (DRS) to cope with changing atmospheric conditions, that affect the width of the fringes in frequency space, and to obtain an unbiased estimate of the underlying "dark" level in frequency space. A detailed discussion of the DRS exceeds the scope of this report.

## 3. Operation and performance

Maybe the first question that a would-be observer will ask is: what is the magnitude limit? The answer: it depends. To illustrate the intrinsic capabilities of Pionier, we show fringes and calibrated visibilities obtained for HD143006 (H=7.7) during the mother of all nights (coherence time >10ms). See Fig. 5. Without spectral dispersion, the limiting magnitude under good weather conditions can exceed H 8.

Observing conditions can degrade below ideal in two ways; seeing decreases the flux coupled into the fiber, and atmospheric piston broadens (in frequency space) the fringes. This is illustrated in Fig. 6. The real-time display of fringes helps the observer to make the right choice of: scan length (integration time), dispersion mode, and targets suited to prevailing conditions.

In some scientific programs, the *accuracy* of the Pionier data is limited not so much by the statistics of photons and of atmospheric phase, but by systematic effects. During the Exozodi program, aimed at the detection of faint debris disks, it was noted that calibrator visibilities had an anomalous scatter on baselines involving AT4. The results started to make sense when visibilities were plotted versus $AZ + Alt$, and can be explained by variable (with pointing) birefringence in the AT4 mirror train, with associated loss of visibility. See Fig. 7. In contrast with the Pionier internal birefringence, that effect is varying with telescope pointing.

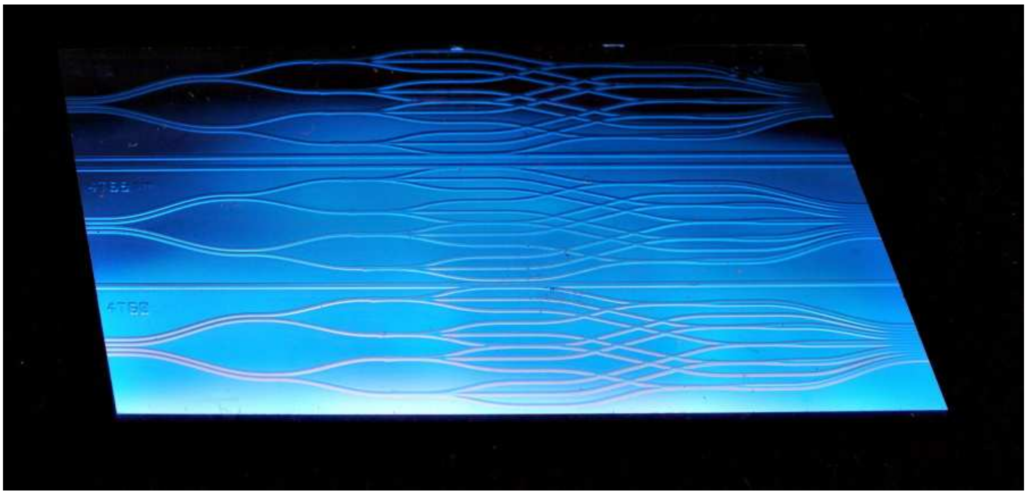

Figure 4.: *The integrated optics beam combiner (IOBC); three identical units on the same fabrication chip. Specular reflection lighting reveals the optical waveguides that reside below the surface. The light from the four telescopes is coupled at the left into the waveguides, each signal is split in three to interfere with the other beams, in the six possible baselines. With a proper design, the waveguides can cross their paths like railway tracks. For each baseline, a coupler (roughly 3/4 to the right) produces from its two inputs the outputs* $A = (e_1 + e_2)/\sqrt{2}$ *and* $C = (e_1 - e_2)/\sqrt{2}$*, for a total of 12 outputs.*

The remedy so far has been to insist on calibrators being within 3deg of each science target (1deg if possible).

## 4. Scientific results

The sensitivity, precision, and efficient coverage of the UV plane by Pionier have enabled scientific programs that were previously excessively time-consuming or just not possible. We select as an example the Herbig AeBe large program. In 30 nights, 50 objects were observed (most in the three VLTI/AT configurations), of which about 30 are clearly resolved, and a handful allow imaging. As an illustration, we show (Fig. 8) the data obtained for HD100546, and two completely independent image reconstructions (Fig. 9) for the dusty environment of HD45677.

A broader view is provided in Fig. 10, showing in matrix form the performance requirements of some of the core science projects of Pionier, and how well they have been fulfilled by the as-built instrument. All programs, with the exception of the search for hot Jupiters, could be carried out in a productive way.

## 5. Status - Lessons learned

Since the commissioning of Pionier, several enhancements have been implemented:

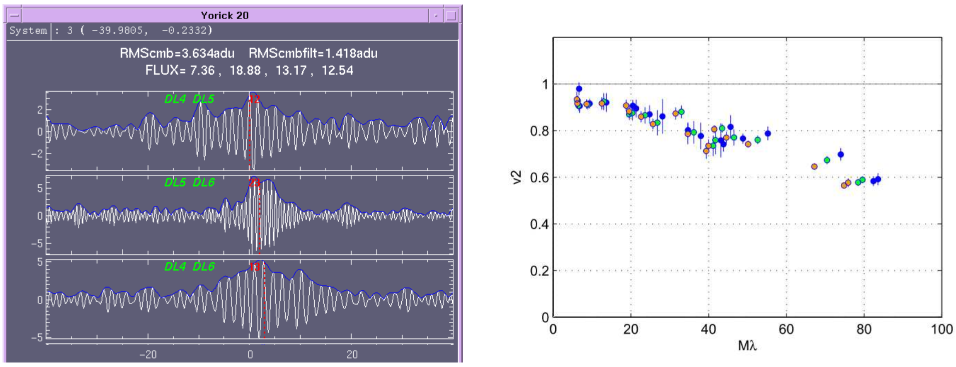


Figure 5.: *Left: fringes from a H=7.7 source during a very good night; only three of the six baselines shown to keep figure compact. Right: calibrated visibilities obtained during that night, color-coded according to the spectral channels.*

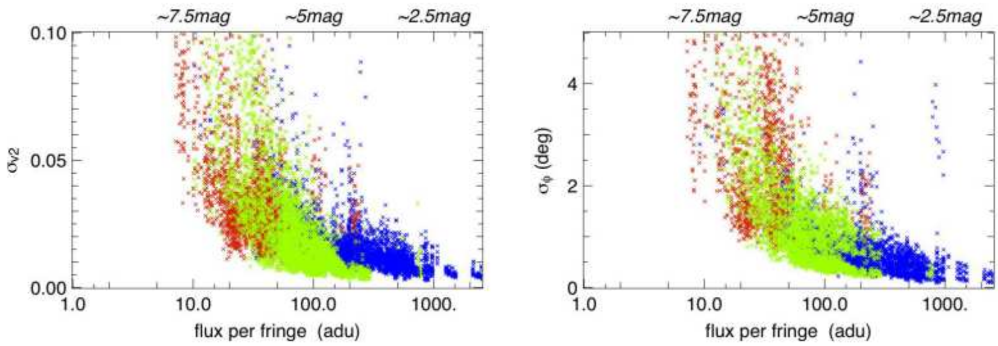


Figure 6.: *Statistical errors on visibilities and closures, versus flux per fringe (detector units), all observations of year 2012. Blue: 7-channel dispersion; green 3-channel; red: undispersed. At any abscissa, the vertical dispersion results from variations in the coherence time; the bottom envelope of the diagram representing the degradation of S/N versus flux. Flux itself results from both the source magnitude and the seeing; the upper scale is for median seeing conditions.*

– Motorize the disperser change, allowing remote operation
– Implement K band
– Identify and eliminate instrument and reduction software systematics
– Upgrade to RAPID camera with APD detectors - pending

The most significant limitations on the performance are:

– Phase piston, from atmosphere (and also the telescopes)
– Coupling loss from atmospheric seeing
– Calibration accuracy including telescope birefringence

The lessons learned:

– Enabling technology (IOBC, 10 yrs of R&D) was a key factor
– Keep It Simple

- Keep proper balance between one-trick pony and swiss knife
- Focused team co-located in one institute, with a good knowledge of the VLTI environment
- Continued development of reduction software as more subtle systematics emerge
- Good interface and cooperation with VLTI team
- Remember that the telescope is also part of the system (birefringence, vibrations)

## References

Benisty, M., et al. 2009, An integrated optics beam combiner for the second generation VLTI instruments, A&A, 498:601-613

Berger, J.-P., et al. 2010, PIONIER: a visitor instrument for VLTI. In Society of Photo-Optical Instrumentation Engineers (SPIE) Conference Series, vol. 7734 of Society of Photo-Optical Instrumentation Engineers (SPIE) Conference Series

Lazareff, B., et al. 2012, A novel technique to control differential birefringence in optical interferometers. Demonstration on the PIONIER-VLTI instrument, A&A, 543:A31

Le Bouquin, J.-B., et al. 2011, PIONIER: a 4-telescope visitor instrument at VLTI, A&A, 535:A67

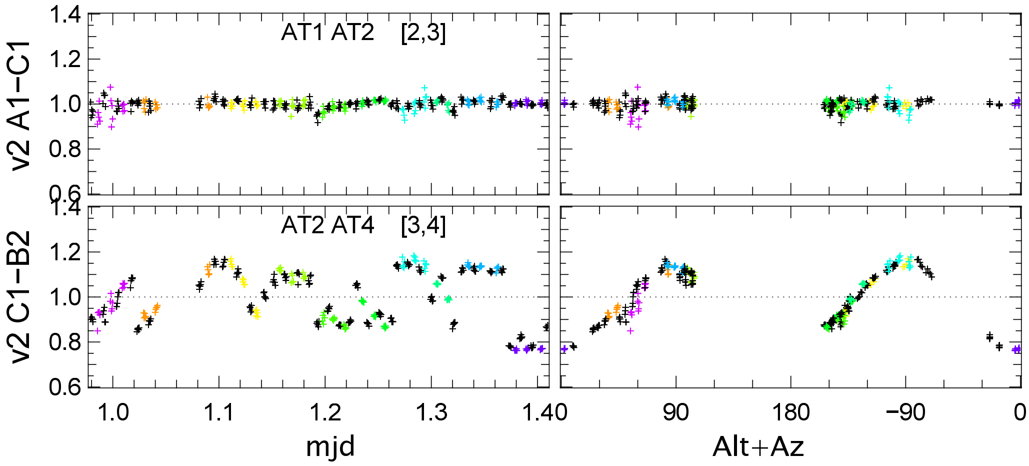


Figure 7.: *Visibilities of calibrators on two baselines, one behaving normally, and another with an anomalous scatter. On the right pane, the values plotted versus AZ + Alt show a telltale cosine pattern.*

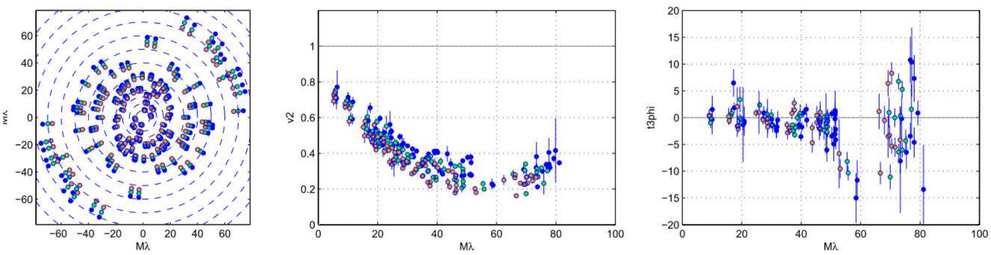

Figure 8.: *Observations of HD100546: UV coverage, visibilities, and phase closures. The data contain a wealth of information: size, radial distribution, and anisotropy of the dust distribution around this Be9 star; e.g. the spread of visibilities* vs *spectral channel readily indicates the dust temperature, and the phase closures indicate a departure from centrosymmetry.*

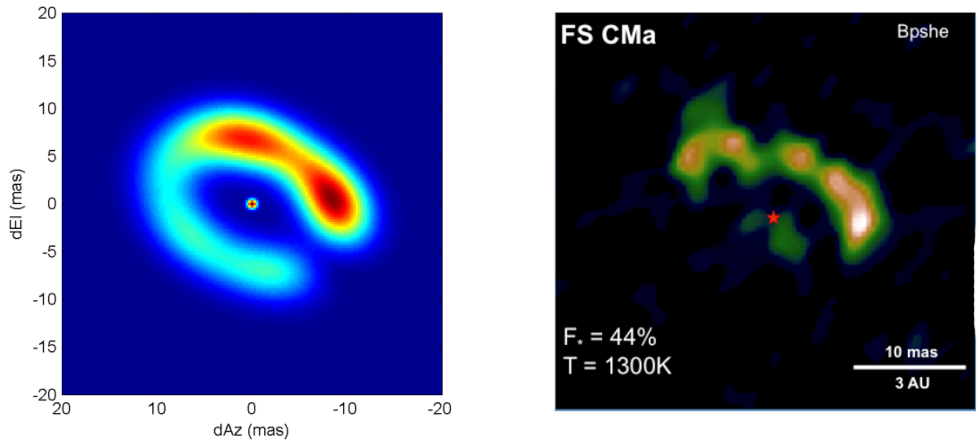


Figure 9.: *Two independent images of HD45677/FSCma from the HAeBe large program. Left: parametric image fitting; right: Mira image reconstruction.*

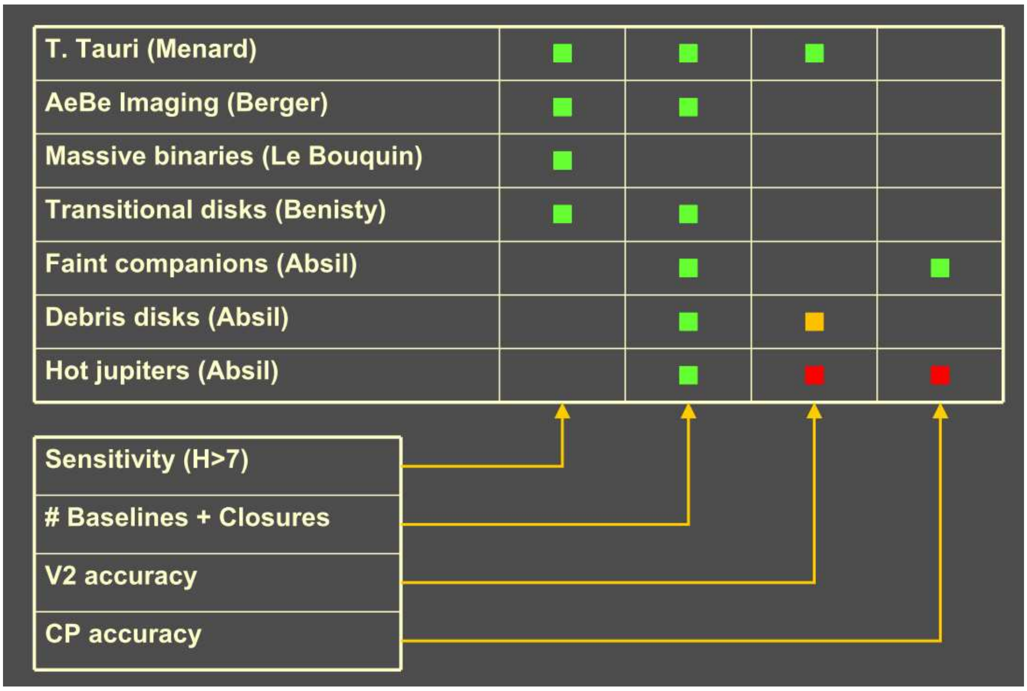


Figure 10.: *Performance requirements for some of the projects that constituted the science case for Pionier. For each project, significant requirements are coded as follows. Green: fully met; orange: requires attention; red: problematic.*

*Improving the performances of current optical interferometers & future designs*
*Proceedings of Haute Provence Observatory Colloquium (23-27 September 2013)*
*Edited by L. Arnold, H. Le Coroller & J. Surdej*
S

# Discrete beam combiners: 3D photonics for future interferometers

S. Minardi, A. Saviauk, F. Dreisow, S. Nolte, & T. Pertsch

*Institute of Applied Physics, Abbe Center of Photonics,*
*Friedrich-Schiller-Universität Jena,*
*Max-Wien-Platz 1,07743 Jena, Germany*

**Abstract.** We present the results of an experimental research aiming at investigating the potential of three-dimensional (3D) photonics for astronomical interferometry. We found that a simple two dimensional array of evanescently coupled waveguides (the so called Discrete Beam Combiner - DBC) can be used to retrieve the mutual coherence properties of light collected by three telescopes with a precision comparable to state-of-the-art interferometric beam combiners. On the basis of these results, we envisage the future use of DBCs in optical/IR interferometry, with particular attention to large arrays of telescopes.

## 1. Introduction

Photonics and, in particular, micro-optical components such as optical fibers and waveguides have started to play a more and more important role in optical/IR astronomical interferometry. Nearly two decades ago it was recognized how optical fibers could be used to perform effective spatial filtering and beam combination of telescopes (Coudé Du Foresto et al. 1996). The instrument FLUOR demonstrated unprecedented accuracy in the measurement of stellar visibilities (Coudé Du Foresto et al. 1998).

It was soon afterwards these pioneering experiments that Kern et al. (1996) proposed the use of planar integrated optical components (2D photonics) to miniaturize even further the optical setup for interferometric beam combination and enhance its thermo-mechanical stability. In the last decade, this proposal lead to the development and on-sky test of several prototypes designed to combine 2 (Berger et al. 2001), 3 (Berger et al. 2003) and 4 (Le Bouquin et al. 2011) telescopes simultaneously. The integrated devices allowed a considerable reduction of the size and maintenance tasks (such as alignment) of the interferometric instruments, while delivering first class scientific results. The main limitation of the planar integrated optics approach is that it is difficult to scale up the devices to allow the combination of a higher number of telescopes and baselines, as would be desirable for interferometric imaging applications. Integrated 8 telescope combiners were proposed but not yet realized (Berger et al. 2000). The difficulty in scaling up planar photonic beam combiners raises from the management of the increasing number of waveguide cross-overs required to distribute the light from the telescopes across the integrated optical chip.

In this context, recent technological advances have opened the perspective to manufacture fully three-dimensional (3D) photonic components, which in principle could solve the problem of scalability of planar integrated beam combiners. The technological platform of 3D photonics is based on the direct writing of transparent materials with tightly focused ultrashort (< 100 fs) laser pulses. Under irradiation of high intensity laser pulses a plasma is formed which develops in defects or a reconfiguration of the local material structure upon recombination. These structural modifications manifest themselves as local variations of the refractive index, which can be positive or negative depending on the type of irradiated material. By scanning the laser beam focus inside the material with a 3-axes positioning system, it is possible to inscribe complex refractive index structures in 3D.

Three dimensional photonic components have been considered very recently for astronomical interferometry as well (Rodenas et al. 2012, Jovanovic et al 2012, Minardi et al. 2012). Rodeans et al. 2012 used curved waveguides and Y-junctions written in chalcogenide glasses to combine three channels simultaneously. While representing the first experimental testbed of 3D photonics for multiple telescope combination, the work also showed the potential of direct laser writing to manufacture waveguides for mid-infared in non-standard glasses. The first 3D component to be tested on-sky was the Dragonfly photonic chip, where waveguides are used to remap 4 pupil apertures into a non redundant linear array of point-like sources for free-space multi-axial beam combination. The potential of pupil remapping techniques resides in the possibility to retrieve high-dynamical range images from seeing limited instruments and with a resolution close to the diffraction limit (Perrin et al. 2006). Finally, in Minardi et al. 2012 laboratory experiments showed that the design of a beam combiner can be radically simplified down to a two-dimensional regular array of coupled waveguides (the discrete beam combiner, DBC) (Minardi & Pertsch 2010). In all three cases, crossovers between waveguides were avoided thanks to the availability of a third dimension.

Here we present the results of an experimental research aiming at investigating the potential of the DBC and in general 3D photonics for astronomical interferometry. We have manufactured several DBC units for the combination of three beams and tested them in the laboratory with monochromatic (Minardi et al. 2012) and polychromatic light (Saviauk et al. 2013). We found that DBCs can measure visibility amplitudes and closure phases over a 50nm-broad visible band with a precision comparable to state-of-the-art interferometric beam combiners. Considering the successful laboratory demonstration of the concept, we will discuss perspectives for the application of DBCs to optical/IR interferometry, with particular attention to large arrays of telescopes.

## 2. Operation principle of a discrete beam combiner

According to the DBC method, to combine N telescopes a regular two dimensional square array of at least N x N evanescently coupled waveguides is used (see Figure 1). The light from the telescopes is injected into selected waveguides of the array. Due to evanescent coupling, light propagating in one waveguide will leak to neighboring waveguides. At a given length of the sample, the N input fields will interfere inside the waveguides with variable amplitude and phase depending on the observed waveguide and length of the sample. As a result, it is possible to retrieve the mutual coherence properties of every possible pair of telescopes from a measurement of the power carried by each waveguide.

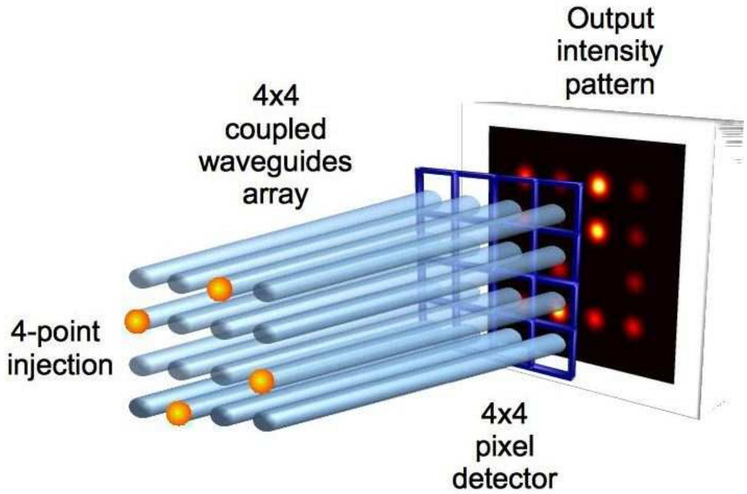


Figure 1.: *Conceptual design of the DBC. Light injected in selected sites of the waveguide array (highlighted in the drawing) is combined within the waveguides thanks to evanescent coupling. The discrete interference pattern is recorded then by an array of detectors matched to the waveguides. This pattern can be related to the mutual coherences of the input fields (see text for details).*

More specifically, the efficient combination of the fields $A_{\mathrm{k}}$ from $N$ telescopes uses an array of $(N+1)\times(N+1)$ waveguides (Minardi 2012). The $(N+1)^2$ output intensities $I_{\mathrm{n}}$ of the waveguide modes at the end of the sample are thus related to the complex visibilities $\Gamma_{\mathrm{jk}} = \Gamma^*_{\mathrm{kj}} =< A_{\mathrm{j}} A^*_{\mathrm{k}} >$ by a real valued, $(N+1)^2 \times N^2$ elements matrix $\{\alpha\}$ (Minardi 2012):

$$I_{\mathrm{n}} = \sum_{\mathrm{k}=1}^{N^2} \alpha_{\mathrm{n,k}} J_{\mathrm{k}}. \tag{1}$$

Here the complex visibilities enter the equation in the form of their quadratures $J_{\mathrm{k}}$, that is the value of the field autocorreleation function (intensities: $\Gamma_{\mathrm{ii}}$) and the real and imaginary components of all possible complex visibilities. The matrix $\{\alpha\}$ is then nothing else that a form of the Visibility to Pixel Matrix (V2PM), usually employed to extract coherence information from multi-axial beam combiners (Tatulli et al. 2007). In terms of the quadratures of the complex visibilities, the commonly measured normalized fringe visibilities are defined as:

$$V_{\mathrm{ij}} = \sqrt{\frac{(\Re\Gamma_{\mathrm{ij}})^2 + (\Im\Gamma_{\mathrm{ij}})^2}{\Gamma_{\mathrm{ii}}\Gamma_{\mathrm{jj}}}} \quad \mathrm{i} \neq \mathrm{j}. \tag{2}$$

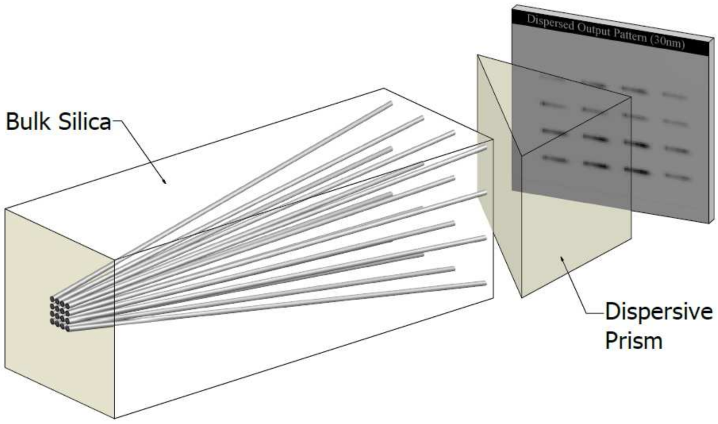


Figure 2.: *Conceptual sketch of a DBC sample for polychromatic operation. The beam combination takes place at the beginning of the tapered array of waveguides, where the inter-waveguide coupling is large. As the light propagates further in the sample, the coupling becomes negligible and the interference pattern of the modes becomes frozen. The waveguides are brought far apart so that an imaging spectrograph (here represented by a prism) can project the spectra of the light carried by the individual waveguides in the gap between them.*

The corresponding phases $\phi_{\mathrm{ij}}$ are defined as:

$$\phi_{\mathrm{ij}} = \tan^{-1} \frac{\Im \Gamma_{\mathrm{ij}}}{\Re \Gamma_{\mathrm{ij}}} \tag{3}$$

The unknowns $J_{\mathrm{k}}$ are retrieved from the individual interference measurements $I_{\mathrm{n}}$ by estimating the pseudo-inverse of the matrix $\alpha$. The matrix elements can be calculated from first principles (Minardi & Pertsch 2010, Minardi 2012), or determined experimentally (Saviauk et al. 2013) by a column-wise calibration procedure, as used by Lacour et al. 2008 for planar photonic beam combiners. The best input configuration, array geometry and length is associated to the matrix $\{\alpha\}$ featuring the smallest condition number, meaning that the error propagation from the measured $I_{\mathrm{n}}$ to the complex visibilities $J_{\mathrm{k}}$ is minimal.

Notice that the coupling between neighboring waveguides is usually very sensitive to the wavelength of light and for this reason we expect the DBC method to work for relatively narrow bandpasses. To increase the operation bandwidth of the component, we designed and tested the tapered DBC component illustrated in Fig. 2. At the beginning of the sample, strong inter-waveguide coupling allows the DBC to operate. The coupling decreases as the waveguides are driven apart, so that the interference pattern formed at the beginning is frozen in the waveguides. At the end of the sample the separation between waveguides is large enough so that it is possible, by means of an imaging spectrograph, to project low resolution frequency spectra of the light coupled in each individual waveguide in the gaps between them. By analyzing the DBC pattern of light at each individual color, it is possible to determine the coherence properties of the combined light wavelength by wavelength.

## 3. Laboratory performance of the discrete beam combiner

We present now the laboratory characterization of a DBC prototype manufactured to combine simultaneously three telescopes and operate between the wavelengths of 640 nm and 690 nm. This wavelength range was dictated by the available white light source and optical equipment of our laboratory, but are representative of what could be achieved at other wavelengths, for instance in the near- or mid-infrared. The setup used to test the DBC is illustrated in Figure 3. The beams of the three telescopes were simulated by the three channels of the modified Mach-Zehnder interferometer of Fig. 3. The complex visibilities arising from the interference of pairs of beams chosen from the three channels represent the visibilities of a baseline (baseline1=Beam1-Beam2, baseline2=Beam1-Beam3, baseline3=Beam2-Beam3). The three beams are focused on the input waveguides of the DBC component, as illustrated in the inset picture. Finally, the output light pattern is dispersed in an imaging spectrograph and recorded on a CCD camera.

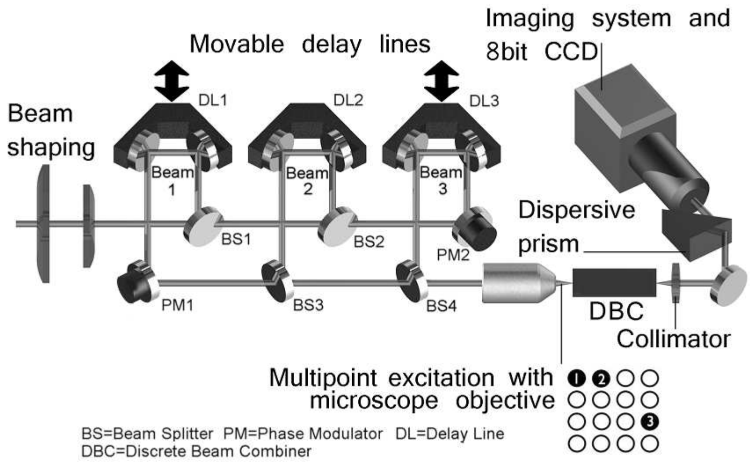


Figure 3.: *The setup of the DBC test-bench. In the inset: the injection points of the light in the DBC component.*

We have characterized the combination performance of the DBC method with polychromatic light. To this end, we have tested the capability to retrieve the photometry, the normalized visibility and the phase of the fringes across the chosen spectral range. Figure 4 addresses the photometric performance and shows the normalized intensities of three input beams as a function of wavelength. The average values of the beam intensities $J_1$, $J_2$ and $J_3$ and their standard deviation were measured. Data show that the mean values have a slightly non-constant trend which is due to the transmission spectrum of the beam splitters in the

Mach-Zehnder interferometer, as proved by the dashed lines representing the model of the beam splitters.

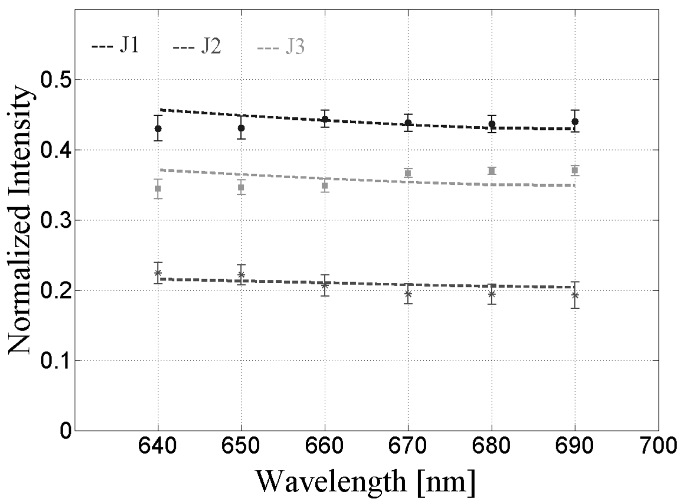


Figure 4.: *The retrieved photometry from DBC measurements at different wavelengths. The slight trend in the photometry is attributed to the transmission spectrum of the beam splitters of the test bench. Lines: fit model of the test bench.*

We next verified that our system can deliver high visibilities throughout the analyzed spectral range. We set the optical path difference between the three input beams to 0 for light at $\lambda_c = 660$ nm. The optical path of the beams 1 and 3 was then modulated independently with a $\pm 6\mu$m stroke with rates of 5.2 $\mu$m/s. The recorded the DBC output was used to retrieve by means of Eq. 2 a time series of the normalized visibilities. The average values of the visibility and its standard deviation are plot as a function of the wavelength in Fig. 4 for the three different baselines of our interferometric setup. The visibility of the three baselines is constant within the error bars and its average value over all baselines and all wavelengths is $0.88 \pm 0.06$, allowing a raw visibility dynamics of about 15. Part of the residual variation of the visibilities over wavelength may be attributed to the chromatic dispersion of the beam splitters.

With the same data we tested also the spectral uniformity of the DBC method in retrieving optical path difference (OPD) data. The measured OPD variation between beams 2 and 3 was 24.6 $\mu$m and was constant within 70 nm across the investigated wavelength range. Another crucial parameter for astronomical imaging is the stability of the closure phase. In our case the closure phase is defined as $\Phi_C = \Phi_{12} + \Phi_{32} - \Phi_{13}$. We have measured the standard deviation of the closure phase for different wavelengths as illustrated in Fig. 9. We have obtained a stability better than $\lambda/36$ over the whole bandwidth of 50 nm with a minimum value of $\lambda/58$ at a wavelength of 650 nm (11 nm optical path difference). Notice that planar beam combiners for astronomical interferometry were reported to have a closure phase stability of $\lambda/144$ at a wavelength of 1550

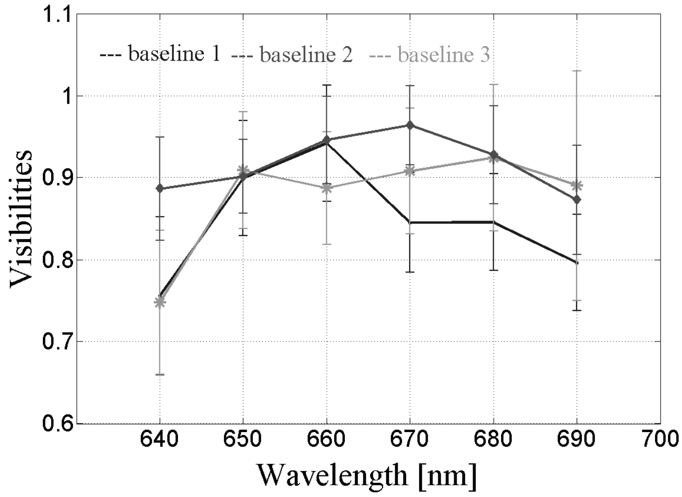


Figure 5.: *The retrieved visibility modulus from DBC measurements at different wavelengths and different baselines.*

nm (Benisty et al. 2009). This corresponds to an optical path difference of 11 nm, as reported in our experiments at the wavelength of 650 nm.

## 4. Applications of DBC and the future of optical/IR interferometers

Applications of DBCs can be found in laser metrology and astronomical interferometry. In its simpler form (straight waveguide array), the DBC can already be used to perform high precision laser metrology simultaneously over many beams, as required for instance for the delay lines of a multi-telescope interferometer. In particular, the possibility to measure the optical path differences between the injected beams would be an advantage for interferometers operating in dual-star mode (Lane & Colavita 2003, Sahlmann et al. 2013), where the precise knowledge of the differential position of delay lines is required to perform astrometric measurements. In the near future it will be possible to extend the dual-star mode to more baselines, so that simultaneous monitoring of several differential delay lines will be required (Gillessen et al. 2012).

Another application for DBC in future interferometers could be the monitoring of optical path differences in networks of optical fibers (Minardi et al. 2009, Spaleniak et al. 2010). Indeed a long term goal for interferometry is the achievement of fibered links between telescopes, a scheme which would allow the realization at sustainable costs of kilometric baseline interferometers (Mariotti et al. 1996, OHANA) The guided wave optics interface of DBC makes them natural candidates to be integrated in fibered optical networks.

Beside these applications, imaging spectro-interferometry is the field where we expect the DBC to have a major impact. Two are the advantages that the application of DBC can bring to this field of astronomy, namely 1) enhanced

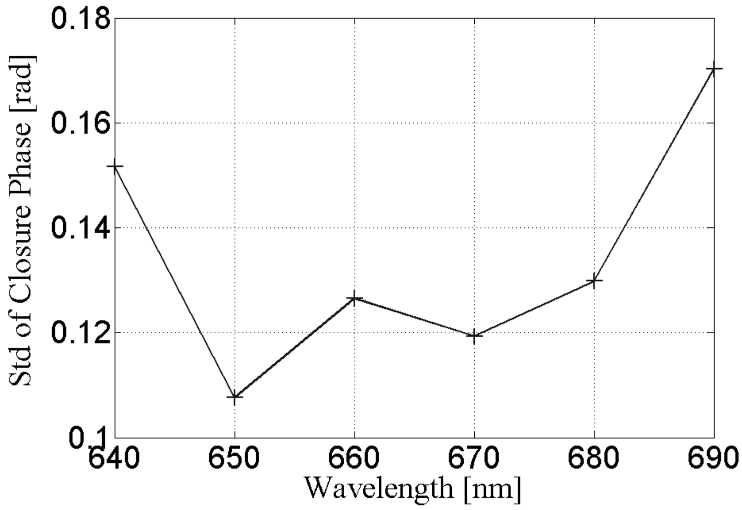


Figure 6.: *The standard deviation of the measurement of the closure phase from DBC data.*

sensitivity and 2) possibility to combine very large arrays of telescopes. As compared to multi-axial combiners (Monnier et al. 2004, Jovanovic et al. 2012), the advantage of the DBC is potentially that of spreading light on a minimal number of pixels per wavelength. Indeed each of the output waveguides could be imaged onto a single pixel of an arrayed detector resulting in $(N+1)^2$ pixels per wavelength required to retrieve the whole coherence portrait of the sampled optical fields. This is much smaller than the number of pixels employed typically in multiaxial combiners (compare e.g. Jovanovic et al. 2012), thus resulting in enhanced sensitivity. There is a slight sensitivity advantage also compared to ABCD integrated beam combiners, where the number of pixels per wavelength scales as $2N(N-1)$ (4 times the number of baselines). DBC combining more than 4 telescopes should be more sensitive than the ABCD combiners, even though slight (for 10 telescopes the advantage is quantified in about 0.5 magnitudes).

The second advantage as compared to current integrated combiners is that DBC could be easily scalable to large number of telescopes while retaining the simplicity of their structure. Numerical simulations have tested the capability of the DBC to combine 6 telescopes (Minardi 2012), but there are no fundamental reasons to prevent from using the scheme for the combination of larger arrays. The difficulty is mainly related to the computational cost of finding the input configuration of the DBC, allowing for a reasonable stability of the coherence reconstruction method (condition number of the V2PM matrix below $\approx 15$).

It is certainly the simplicity of the design and the flexibility of the manufacturing method which makes DBC particularly attractive for astronomical applications. We note that this is particularly true for non-telecom wavelengths such as required for astronomy. Indeed, conventional photonic manufacturing technologies cannot be applied for instance for materials suitable for mid-infrared (such as chalcogenide glasses). Direct laser writing can be used to manufacture

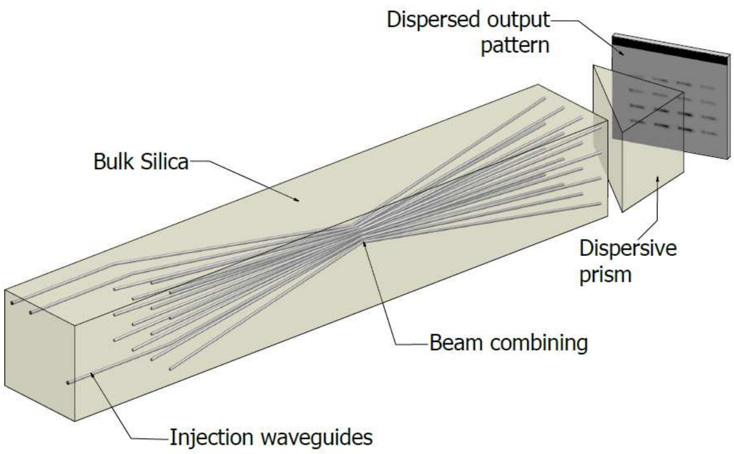


Figure 7.: *Conceptual setup of a component integrating an input modal filtering and beam combination.*

waveguides in a wide range of materials and the DBC scheme offers the simplest 3D photonic circuit that allows the measurement of coherences.

Looking into the future, we may think of a 3D photonic chip integrating several functionalities. An example is given in Figure 7. The chip includes a mode filtering section and a DBC. It could be foreseen that the final dispersive element could also be integrated by connecting the output waveguides through fibers to Arrayed Waveguide Gratings (Cvetojevic et al. 2009) or even more integrated solutions such as the photonic crystal superprism (Momeni et al. 2009).

## 5. Conclusions

We have explored the potential of 3D photonics for applications to astronomical interferometry and found that the design of photonic beam combiners can be greatly simplified by the addition of the third dimension. We investigated in particular the beam combination properties of regular arrays of evanescently coupled waveguides (DBC), showing that they can deliver full interferometric information with a quality comparable to existing beam combiners. Advantage of the DBC scheme is the simplified design and scalability to the combination of large numbers of telescopes (6 or more). The applicability of the DBC can range from metrology to science data collection in multi-telescope interferometers. Future developments of the DBC concept include exploring exotic geometries of the array of waveguides to make the beam combination even more effective.

## References

Benisty, M., et al., 2009, A&A 498, 601

Berger, J.-P., et al. 2000, Proc. SPIE 4006, 986

Berger, J.-P., et al., 2001, A&A 376, L31
Berger, J.-P., et al., 2003, Proc. SPIE 4838, 1099
Coudé Du Foresto, V., et al. 1996 in *Astrofib: Integrated Optics for Astronomical Interferometry*, p. 115
Coudé Du Foresto, V., et al. 1998, Proc. SPIE 3350, 856
Cvetojevic, N., et al., 2009, Opt. Exp. 17, 18643
Gillessen, S., et al., 2012, Proc. SPIE, 8445, 84451O
Itoh, K., et al., 2006, MRS Bulletin 31, 620
Jovanovic, N., et al., 2012, MNRAS 427, 806
Kern, P. , et al., 1996, in *Astrofib: integrated optics for astronomical interferometry*, p. 195
Lacour, S., et al., 2008, Proc. SPIE 7013, 701316
Lane, B. F., & Colavita, M. M., 2003 AJ 125, 1623
Le Bouquin, J.B., et al., 2011, A&A 535, A67
Mariotti, J.M., et al. 1996, A&A 116, 381
Minardi, S., et al., 2009, Astron. Nachr. 330, 518
Minardi, S., & Pertsch, T., 2010, Opt. Lett. 35, 3009
Minardi, S., 2012, MNRAS 422, 2556
Minardi, S., et al., 2012, Opt. Lett. 37, 3030
Momeni, B., et al., 2009, Opt. Comm. 282, 3168
Monnier, J. D., et al., 2004, Proc. SPIE 5491, 1370
Perrin, G., et al., 2006, MNRAS 373, 747
Sahlmann, J., et al., 2013, A&A 551, A52
Saviauk, A., et al., 2013, Appl. Opt. 52, 4556
Spaleniak, I. et al., 2010, Proc. SPIE 7734, 77343Y
Tatulli, E., et al., 2007, A&A 464, 29

*Improving the performances of current optical interferometers & future designs*
*Proceedings of Haute Provence Observatory Colloquium (23-27 September 2013)*
*Edited by L. Arnold, H. Le Coroller & J. Surdej*

# Session 5. Discussion on the future of interferometry

Chair: Jean Surdej
Wednesday evening, Sept. $25^{th}$

A roundtable with the EII/ASHRA/Interferometry Forum groups was organized that evening by Jean Surdej. The main elements of this discussion are given in the colloquium recommendations at the end of this volume, p. 277.

# Session 6. Unique science and technologies that will allow to design future interferometers with extremely high performances

Chair: Frantz Martinache
Thursday morning, Sept. 26$^{th}$

*Improving the performances of current optical interferometers & future designs*
*Proceedings of Haute Provence Observatory Colloquium (23-27 September 2013)*
*Edited by L. Arnold, H. Le Coroller & J. Surdej*

# The CARLINA diluted telescope, a new class of interferometer: Opto-mechanical design and results of the OHP experiment

J. Dejonghe[1], H. Le Coroller[2]*, P. Deram[2] , D. Ricci[3], F. Hespeels[2]

[1]*Laboratoire Lagrange, Observatoire de la Côte d'Azur (OCA), France (Julien.Dejonghe@oca.eu)*

[2]*Observatoire de Haute Provence - UMS Pythéas, 04870 St Michel l'Observatoire, France (herve.lecoroller@lam.fr)*

* *First and second authors contributed equally*

[3]*Institut d'Astrophysique et de Géophysique, Allée du 6 août, 17, B-4000 Liège 1 (Sart-Tilman), Belgium*

**Abstract.** Today, a significant number of optical interferometers are in operation around the world. Baselines longer than 300 meters are reached, and these facilities produce unique high angular resolution data. Nevertheless, the number of telescopes constituting these interferometric arrays is still limited (maximum 6). The Carlina diluted telescope concept represents a novel architecture, similar to that of the Arecibo radio-telescope, except that it works in the optical, and uses a sparse aperture. This particular design allows having a large number of sub-apertures, without significant technical complications, and should provide novel scientific data with rich u-v coverage. In 2003 began at Haute-Provence Observatory (OHP) the construction of a Carlina prototype to explore feasibility and technical solutions necessary to the implementation of this concept. This article summarizes the main technical characteristics of this prototype, and the observations conducted with the full experiment.

## 1. Introduction

After ten years of development, we have just completed the construction of a Carlina prototype at Haute-Provence Observatory. Carlina is a peculiar type of optical interferometer that works without delay-lines, and has a high potential for imaging. An important effort has been put into the development of original solutions required by the peculiar design of Carlina: new mechanical solutions, servo-loops and laser metrology to stabilize the optics borne by a tethered helium balloon. We will mainly describe the general architecture of the prototype, the metrology destined to align the primary mirrors with micrometric precision, and the focal gondola, which is the last module developed and built at OHP. We will present the first observations, and the main results obtained with this prototype.

## 2. Principle of the Carlina architecture

Carlina is a new kind of interferometer: a giant diluted telescope (Le Coroller et al. 2004; Le Coroller et al. 2012) whose primary mirror is constituted of a large number of small segments, distributed on the surface of a large virtual sphere (Fig. 1). This array of fixed sub-apertures produces an image of the sky on the half-radius sphere (focal sphere). A gondola carrying the focal optics is placed on that sphere, where the image of the observed object forms. As explained above, the giant diluted primary mirror is fixed and anchored to the ground. The only moving part is the focal gondola. It is suspended under a cable tripod, whose summit is located at the curvature center of the primary sphere. This cable tripod is kept taut by a pulling force, provided either by a helium balloon, or by a solid structure (pylons, cable attached between two mountains, etc.). Computer controlled winches ensure the guiding of the focal gondola.

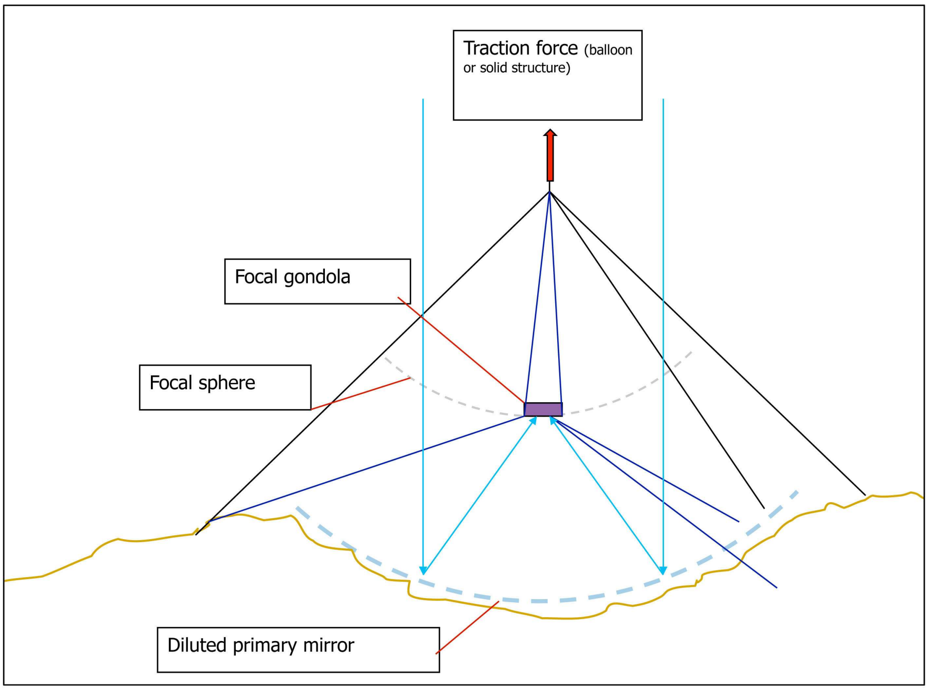


Figure 1.: *Diagram of the Carlina diluted telescope: a spherical diluted primary mirror forms a high resolution of the sky on its focal sphere. A focal optics catches the images of the object. All the system is suspended from cables.*

## 3. The OHP prototype

The prototype built at Haute-Provence Observatory is a scale Carlina implementation. We assembled this prototype to develop and experiment the new and original technical solutions required by this concept. The OHP experiment has been largely described in previous papers (Le Coroller et al. 2012). The primary mirror is made of three segments positioned on a 70-meter radius sphere, forming three baselines of respectively 5, 9 and 10 meters. These mirrors are accurately positioned in Tip-tilt and piston within one micron accuracy thanks to a laser metrology system. The cable tripod, kept taut by the upward pulling force provided by a helium balloon, is stabilized with servo winches. The light (carbon-fiber) focal gondola, carrying an optical corrector and two detectors, tracks the observed object thanks to some motorized winches.

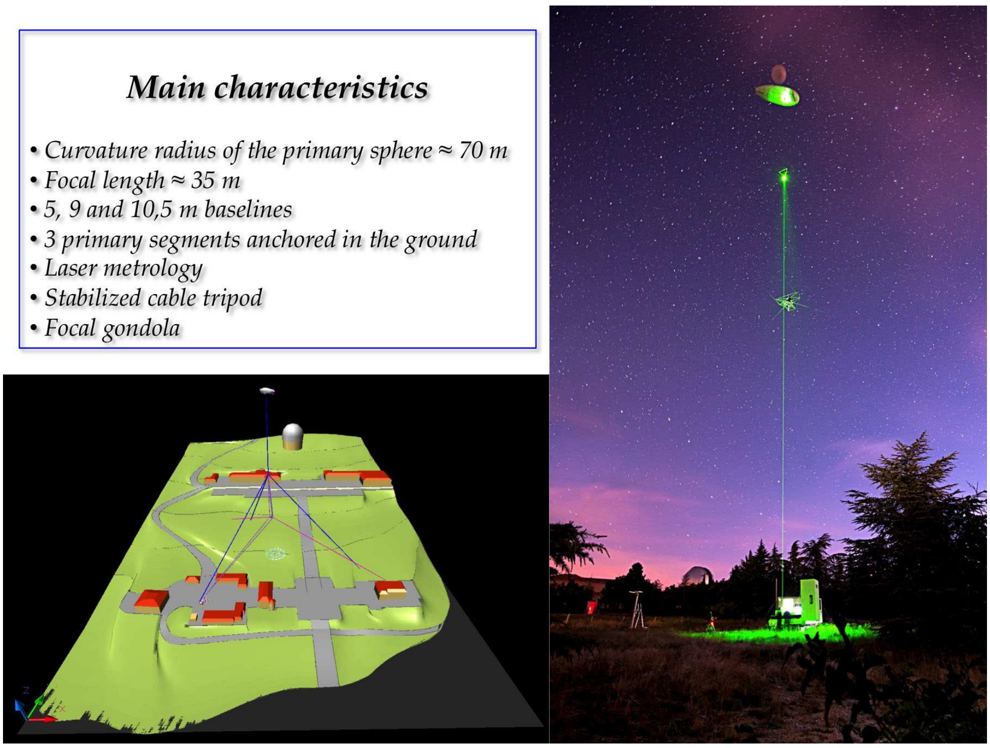


Figure 2.: *Views of the OHP Prototype*

### 3.1 A diluted primary mirror

The primary is made of three 250 mm zerodur segments, anchored to the ground and manually adjustable in tip-tilt and piston. Their support is a rigid carbon-fiber hexapod, topped by a fine adjustment mechanism. To adjust the position of the mirrors and make them fit the 70 m virtual sphere, a two-step method is used: First, a "total station", or tachometer (instrument combining a high-precision theodolite and a laser distance-meter), allows to position a target disposed in three points on the mirror within 100 microns accuracy. Then, a few microns accuracy is reached with the laser metrology system described below. The mechanical mounts that carry the primary mirrors are supposed to ensure high stability, and gives good results on short periods (1 or 2 hours). Nevertheless, some slow drifts in tip-tilt and piston have been observed over longer durations. It was not possible to determine whether this was due to mechanical drifts or ground movements. For a larger project, a permanent servo-loop, using metrology fringes information, would be probably required to automatically adjust the position of the primary segments over long periods.

Figure 3.: *View of the three primary segments: the mirrors are disposed on rigid carbon legs, and manually adjustable in tip-tilt and piston (This pictures has already been published in Le Coroller et al. 2012)*

### 3.2 **The laser metrology**

As explained above, a metrology system is necessary to measure the position of the three primary mirrors. This metrology has been described in detail in Le Coroller et al. 2012. Here, we quickly recall the main lines. The principle implemented here is to light with a white source the three mirrors from the curvature center of the primary sphere and to get the white fringe in the formed image. A super-continuum laser from Leukos Company is used. The basic way to proceed would be to put the laser near the center of curvature, 70 m above the ground, and to get the image back directly on the side of the source. For weight considerations and for accessibility, a convex mirror (called metrology mirror), placed 1 m below the curvature center, is used to project the source and the image at ground level (Fig. 4). We will describe further more in detail the way to attach and stabilize this optics. As we will see after, the metrology mirror is affected by residual oscillations of a few tens of mm amplitude. This produces some sideway motion of the return beam of about 10 to 30 cm. In order to be able to send the beam to the detector despite these motions, a 600 mm field mirror is placed at the focal plane. This mirror forms an image of the pupil near his own focal plane. This image is very stable, and at this level, the three beams coming from the three mirrors are obviously separated. But a few centimeters after this plane, due to the very important diffraction, the beams are again partly superimposed. We choose to put the detector in this "pseudo pupil plane" where the residual motions of the white fringe are drastically reduced (Le Coroller et al. 2012).

The adjustment procedure of the primary mirrors begins by activating the manual tip-tilt screws on their supports, until the three spots are superimposed on the metrology CCD camera. Since the coarse adjustment has previously been done with the "total station", the white fringes can then be found relatively easily and centered in the image (fig. 5) using the piston adjustment. The resolution of this manual procedure may be of order of one fringe or less, but since there are only three mirrors forming a 3-fringe pattern always secant in one point, there is no precise reference for piston adjustment. The fringes are centered in the seeing limited diffraction pattern with an accuracy of a few fringes i.e. few microns. With more than three mirrors, additional fringe patterns should be more precisely positioned in order to have only one cross-point. The metrology to co-spherize the segments of the primary is an active-optic, and does not require an accuracy better than the atmospheric piston.

Nevertheless, in the focal gondola, this method could be used as a fringe tracker sensor (a kind of AO for diluted telescope). For this method, we propose to test a new algorithm: the idea is to find an analytic solution that describes the white fringes pattern. Then, we can fit this equation on the stellar fringes to track the fringes position. This method should be faster than using a Fourier transform to track the fringes phase. Note that a similar method has been used for micro-particle detection in digital holography (Soulez et al. 2007).

### 3.3 A cable giant telescope

Like for the Arecibo radio telescope, the structure of Carlina is made of long cables. The material chosen for all the cables of the experiment is Zylon PBO HM, from Toyobo Company. Its tensile modulus is nearly 3 times higher than the one of high modulus aramid fiber (270 GPa and 109 GPa, respectively), for a similar density. The first part of the structure is the "cable tripod", which provides the support for the entire experiment. The location of the summit of this tripod coincides with curvature center of the primary mirror (Fig. 1 & Fig. 2). An upward force is needed to tauten the cable tripod. The OHP prototype initially used a helium balloon, providing approximately 70 kg of force. With this geometry, the motion of the tripod's summit is kept under a few tens of centimeters while the balloon oscillations in the wind reach 3 to 5 meters. The metrology mirror is placed at the summit of the tripod, where the cables suspending the focal gondola are attached. These two functions don't tolerate

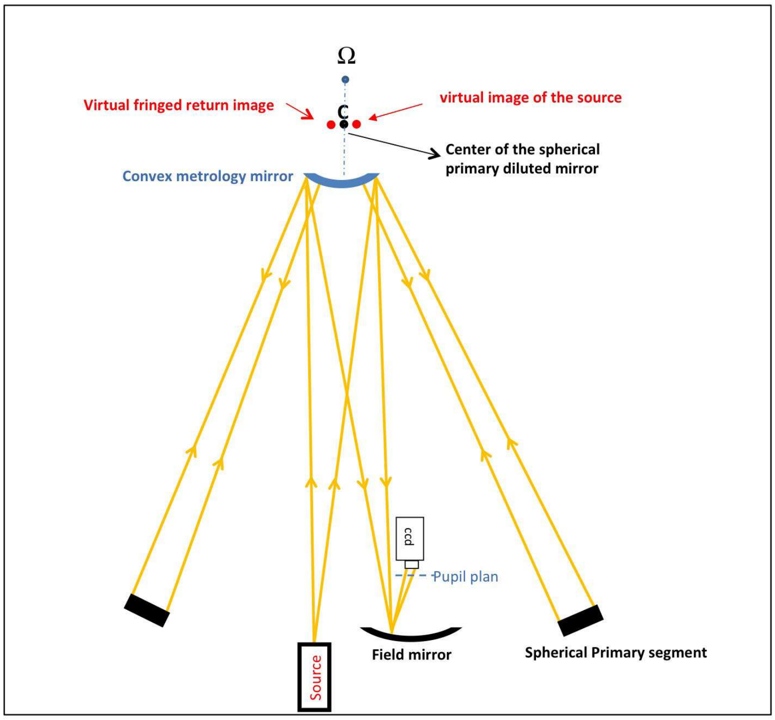


Figure 4.: *Diagram of the laser metrology system: a white source illuminates the primary mirrors from the curvature center of the primary sphere. White fringes are observed in return. For more convenience, the source and the detector are projected at the ground by the convex metrology mirror (Drawing extract from Le Coroller et al. 2012)*

large displacements. As the convex metrology mirror is nearly spherical, it is not the oscillations of the mirror itself that must be reduced, but those of its curvature center. Five degrees of freedom of the mirror have to be blocked by the cable tripod (rotation around the vertical axis has no impact). For this reason, the cable tripod is in reality made of six cables, forming a more rigid double tripod structure, attached to a "girder gondola", or metrology gondola: the upper tripod is attached at the summit of the girder and matches the curvature center Ω of the metrology mirror (see Fig. 6), while the lower tripod is attached at the bottom of the girder, where the metrology mirror is situated. The curvature center of the primary sphere is at the focus of the convex mirror, at the middle of the girder (the girder length is equal to the metrology mirror curvature radius). At the bottom of the girder are also attached the cables of the focal gondola and those of the helium balloon. Thus, the main perturbation forces are applied at the same point. Special motorized winches and a servo-loop system are used to stabilize the lower tripod. This architecture further reduces the oscillations of the summit of the lower tripod down to a few millimeters. The stability of the summit of the upper tripod (curvature center of the metrology mirror) then reaches a few tens

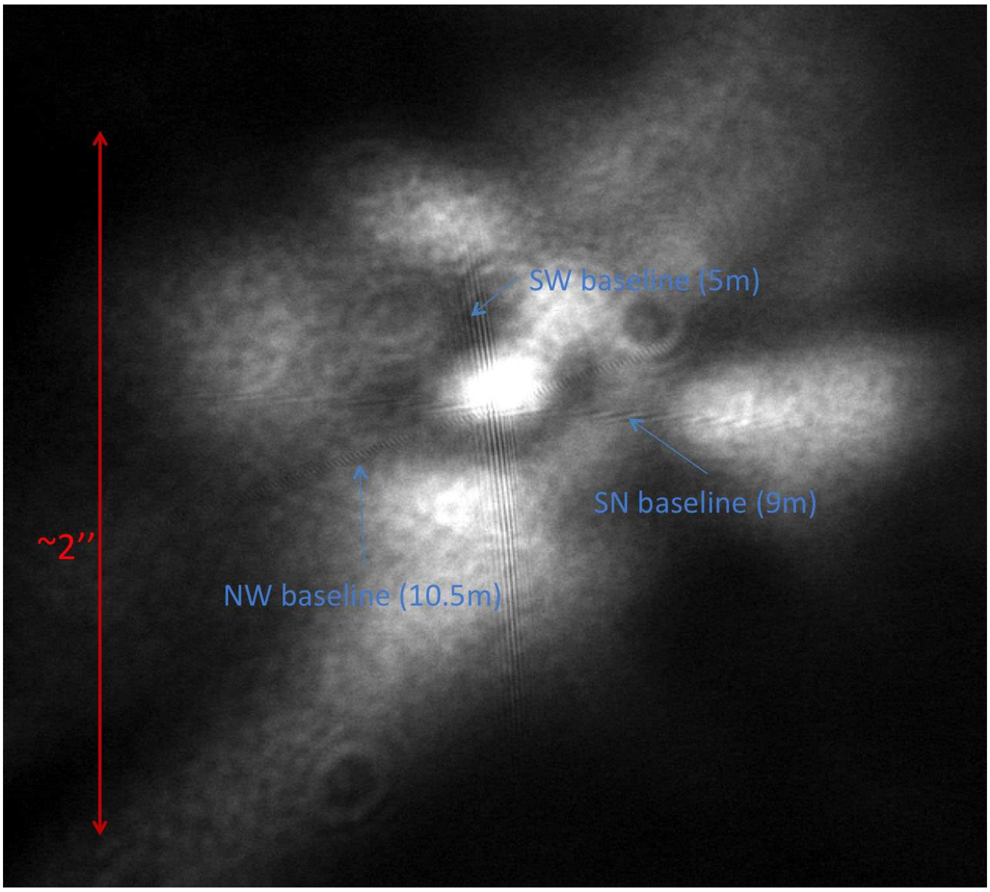


Figure 5.: *Metrology fringes: when the mirrors are correctly adjusted in piston, the 3 fringe patterns are centered in the turbulence spot (picture from Le Coroller et al. 2012).*

of millimeters, while the cables are not motorized. Of course, a fine servo-control system could further improve these performances (Le Coroller et al. 2012).

### 3.4 **Absolute positioning of the metrology gondola**

To position the metrology gondola in the 3-dimensional space, a vertical laser beam is used, to materialize the vertical axis of the entire installation. This laser beam must pass through the curvature center of the primary sphere. The verticality of the laser is obtained thanks to a reflection on a horizontal liquid mirror. The accuracy of this adjustment is $\pm 2$ arcsec.

### 3.5 Actively stabilizing the lower tripod

At ground level, three custom motorized winches allow to control the cables length. To monitor the position of the summit of the lower tripod, a stereoscopic vision system has been developed (Fig. 6). At the summit, two retro-reflectors are

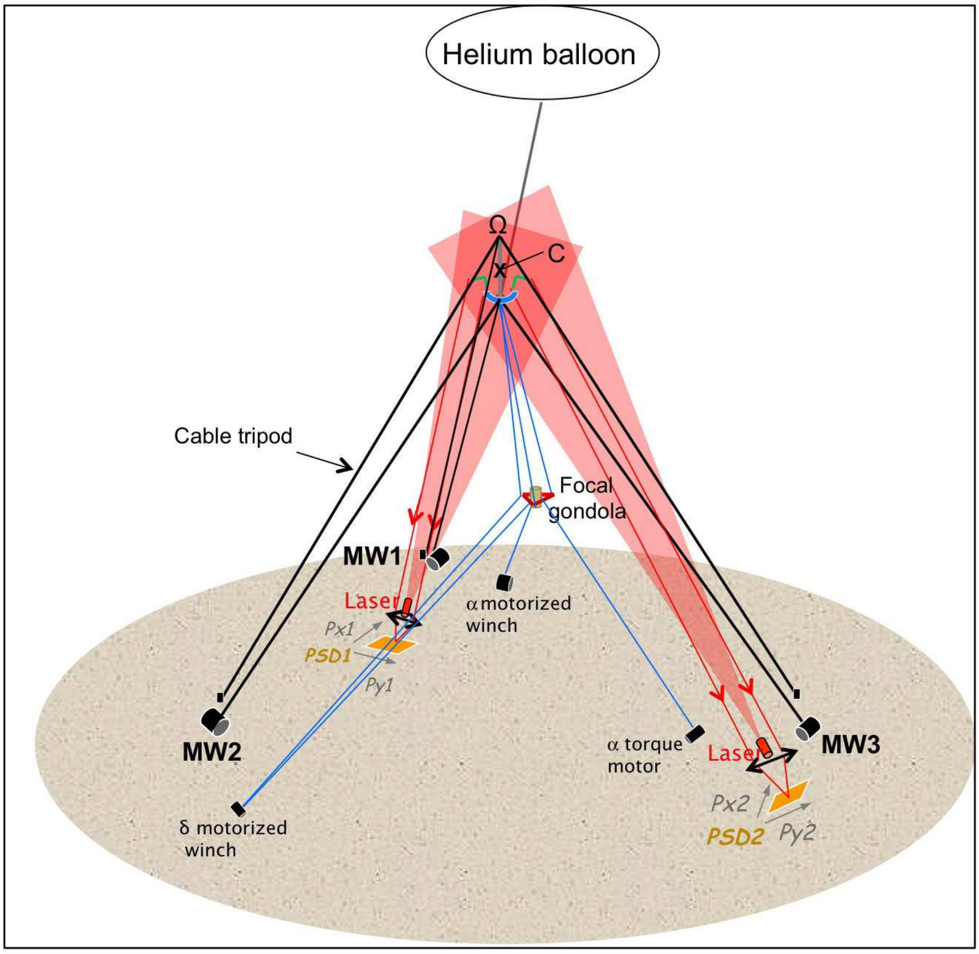


Figure 6.: *The cable structure: a double cable tripod, which summit coincides with the curvature center (C) of the primary sphere, constitutes the support of the experiment. It is tensioned by a traction force, here provided by a helium balloon. The focal gondola is suspended below. The system is stabilized thanks to laser measurements and motorized winches.*

placed. Two lasers light these retro-reflectors from two different locations on the ground. The return light from the reflectors is recorded by two small telescopes, fitted with position sensitive devices (PSD) at their focus. The two PSD gives four coordinates ($P_{x1}$, $P_{y1}$, $P_{x2}$, $P_{y2}$). Using a singular value decomposition, we can find a linear equation: $\Delta L = M.P_{XY}$, where L is the lengh of the cables, M is the matrix of the system, and $P_{xy}$ are the coordinates given by the PSD (Le Coroller et al. 2012).

### 3.6 The tracking system

As we saw earlier, the only moving part of a Carlina diluted telescope is the focal gondola. It is placed on the focal sphere, which is the half-radius sphere concentric to the focal sphere. The observed object, the curvature center (C) and the focal gondola are aligned during the observation. To perform this alignment, the focal gondola is attached in (C), and at the intersection between the polar axis through (C) and the ground, so it can turn around this polar axis, describing an equatorial movement (Fig. 7). The "delta" motorized winch allows changing the declination and apply corrections. The "alpha" motor is used for tracking. The system is kept taut by a torque motor. Indeed, since the "alpha" winch is controlled in velocity and unrolls its cable while tracking, a tension cable is required on the opposite side to provide the appropriate force while rolling. This cable is controlled in force and not in velocity, to avoid hyperstatism and hyperdynamism problems. To achieve this force-controlled rolling, a torque motor was used at first, but we obtained better performance with a long elastic that provided a smoother motion. In a future project, a torque-motor compatible with very low speed, and giving no jolts when the rotor turns from one coil to another, would have to be studied carefully.

### 3.7 The focal gondola

The focal gondola is a carbon fiber truss structure carrying the "focal module" that contains all focal optics. The geometry of the structure and that of the attachments points is optimized to minimize angular oscillations: yaw, pitch and roll (Le Coroller et al. 2012, SPIE). The frame, made of 16 mm diameter carbon tubes and PBO guy-wires, has the shape of a 3 m wide equilateral triangle. The barycenter of this triangle is also the center of gravity of the focal gondola (Fig.8). Three vertical cables coming from the metrology gondola situated 35 m above are attached at the three corners of the triangle (Fig. 7). Tensions in these cables are naturally equal. They sustain the weight of the gondola, and block the rotations around horizontal axis (pitch and roll). With these three cables, the gondola can only rotate around the center of curvature of the primary sphere, and around the optical axis. In order to block the rotation around the optical axis, two "delta" cables, coming from the intersection between the polar axis through (C) and the ground, are attached at both extremities of a carbon tube which passes through the center of gravity of the gondola. It follows that the latter can only rotates around the equatorial axis. Any acceleration of the "delta" cables will produce a real movement along the declination axis, with no parasitic tilt. Finally, to produce the equatorial tracking, the "alpha cable", coming from the alpha winch, is attached at the center of gravity, as well as the "torque cable", which ensure the tension of all the system. Just like for the "delta" cable, any acceleration of the alpha or torque cables will produce a pure equatorial movement, with no undesired tilt, since the cables are attached at the center of gravity of the focal gondola.
The focal gondola is the only moving part of the Carlina diluted telescope. A conventional N-aperture interferometer will require N-1 delay lines, accurately driven during the observation. A real advantage of the Carlina concept is that whatever the number of sub-apertures, there is only one moving part. Nevertheless, as shown in the table below, the challenge in term of control is comparable.

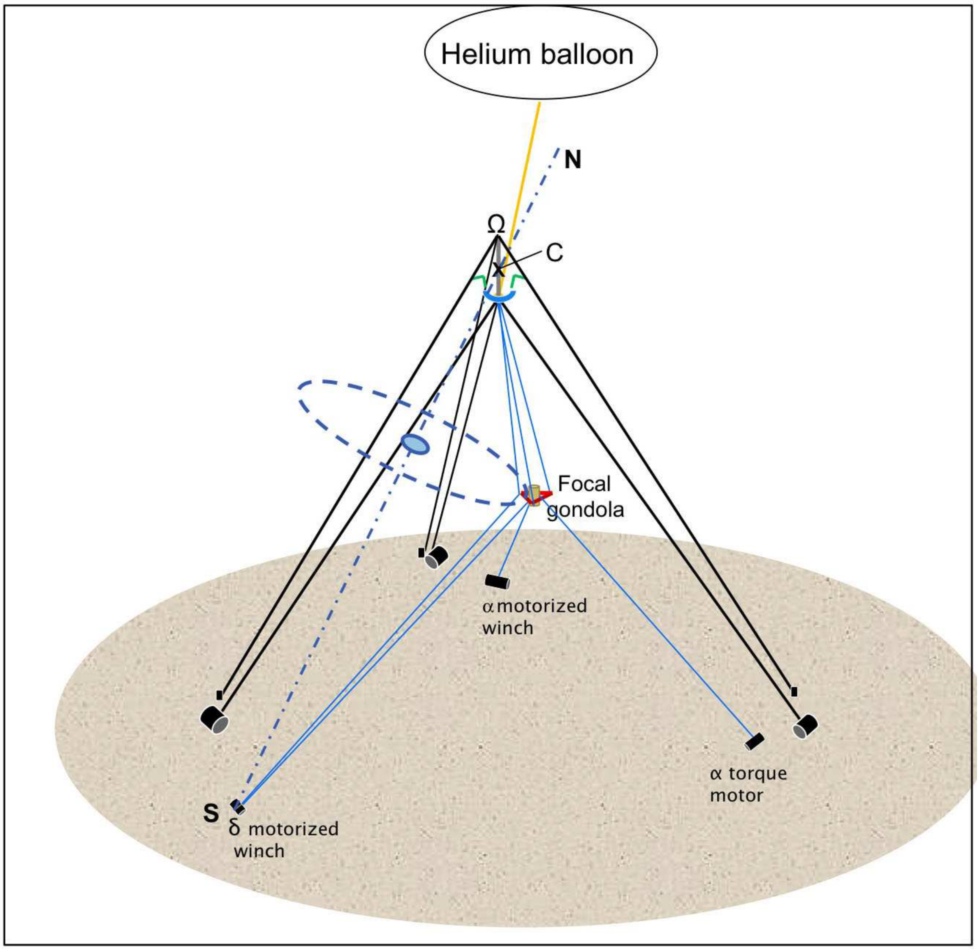


Figure 7.: *The tracking system: The (S-N) axis represents the equatorial axis. As the focal gondola is suspended and attached to the (S) and (C) points, it describes an equatorial movement.*

We can see that if the F-ratio chosen for Carlina is F/2, the max speed of the focal gondola is 4 times higher than the one of the delay lines, as well as the maximum "acceptable" drift (beyond, the fringes are totally blurred). Of course, the maximum drift to get good data must be drastically lower, which is a challenge for a cable-suspended focal gondola.

### 3.8 The focal optics

The focal optics carried by the focal gondola mainly comprises a spherical aberration corrector (because the giant primary is spherical), called Mertz corrector, a pupil densifier, a photon-counting camera, and a guiding camera (Fig. 9).
The Mertz corrector is made of two highly aspherical mirrors, obtained by precision diamond machining. It gives a 40 arcsec guidance field. Over approximately

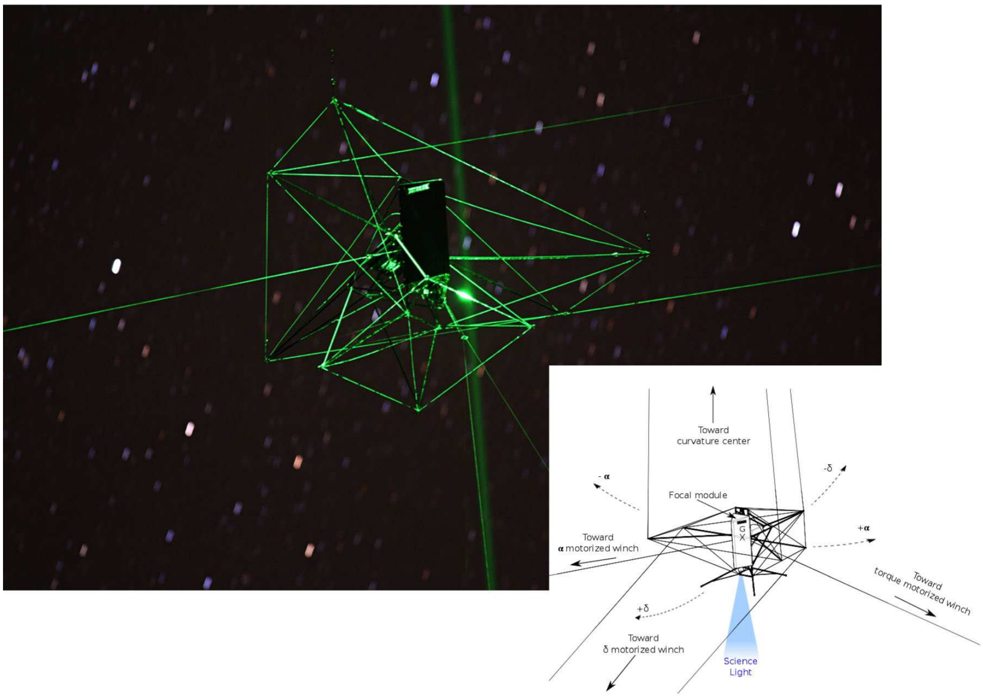


Figure 8.: *The focal gondola: a focal module (containing focal optics and detectors) is inserted into a 3 m triangular carbon structure. The geometry and the attachments positions are optimized to reduce adverse inclinations.*

Table 1.: *Focal Gondola versus Delay line. $R$ is the curvature radius of the diluted telescope's primary mirror; $F$ is the focal length of the primary mirror; $B$ is the maximum baseline; $\lambda$ is the wavelength*

| | Focal Gondola | Delay Line |
|---|---|---|
| Max speed (m/s) | $7.3 \times 10^{-5} \times \frac{R}{2}$<br>($7.3 \times 10^{-5} \times 2B$ at F/2) | $7.3 \times 10^{-5} \times \frac{B}{2}$ |
| Max drift | $\lambda F/B$ per exposure time<br>($2\lambda$ at F/2) | $\frac{\lambda}{2}$ per exposure time |

10 arcsec, the three spots provided by the three primary segments begin to separate.

This corrector gives a focus where the three spots are correctly superimposed, and where the diffraction envelope is about 40 times larger than the fringes. A pupil densifier is an optical device composed of one diverging lens and one con-

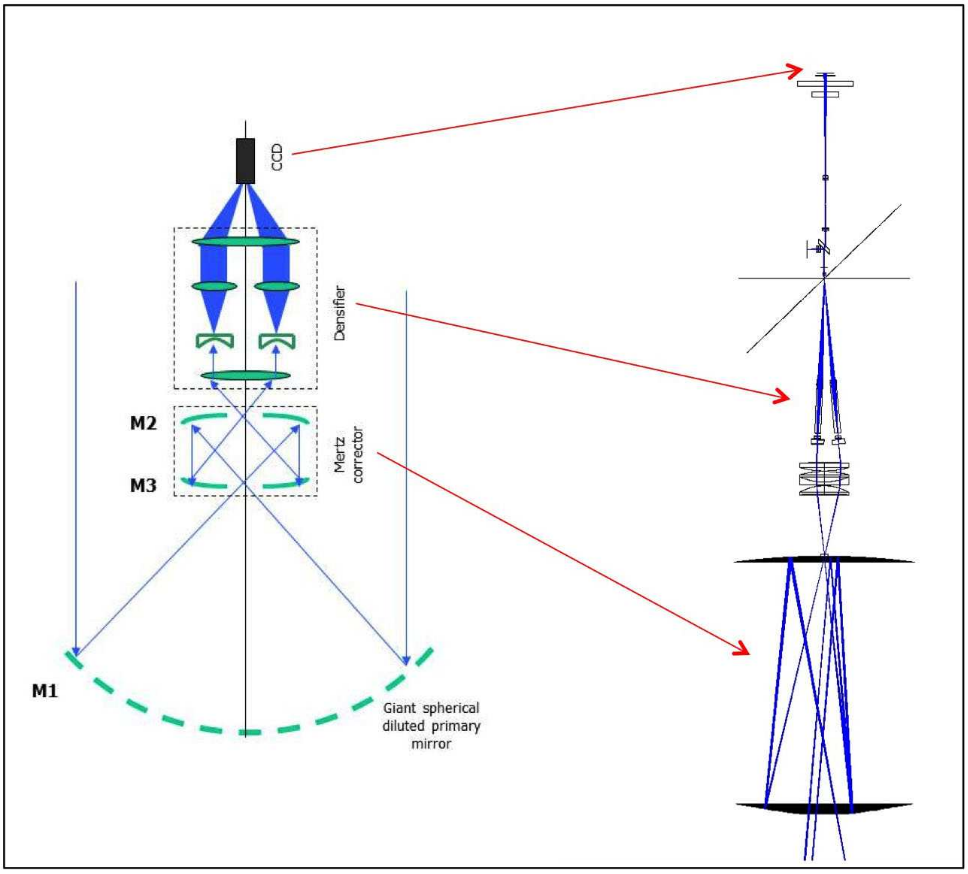


Figure 9.: *The focal optics: a Mertz corrector corrects spherical aberration on the axis. A pupil densifier (device destined to reduce the envelope size versus the fringes size) is disposed into the beam, before the light is directed toward a guiding camera and a photon counting camera.*

verging lens on each beam, destined to reduce the envelope size with regard to the fringes size (Fig. 11). This device is placed in a pupil plan, and must follow the pupil movement during tracking within about 0.1 mm. On the OHP prototype, the densifier is passively positioned, using an equatorial mount oriented by gravity: while the focal gondola tilts during tracking, describing it's equatorial movement, the densifier has to remain always vertical, describing the reverse tilt movement relative to the gondola. This system is mechanically damped, using high viscosity oil.
Successful lab tests and laser sky tests showed the densifier was correctly positioning itself, but the required guidance accuracy (0.1 arcsec) for the focal gondola was impossible to reach without embedded fine motorized guiding system. This severe requirement is due to the fact that in a densified image, two different scales are present: The scale of the fringes is larger than the scale of the envelope. When a tracking error occurs, the fringes rapidly exit the envelope.

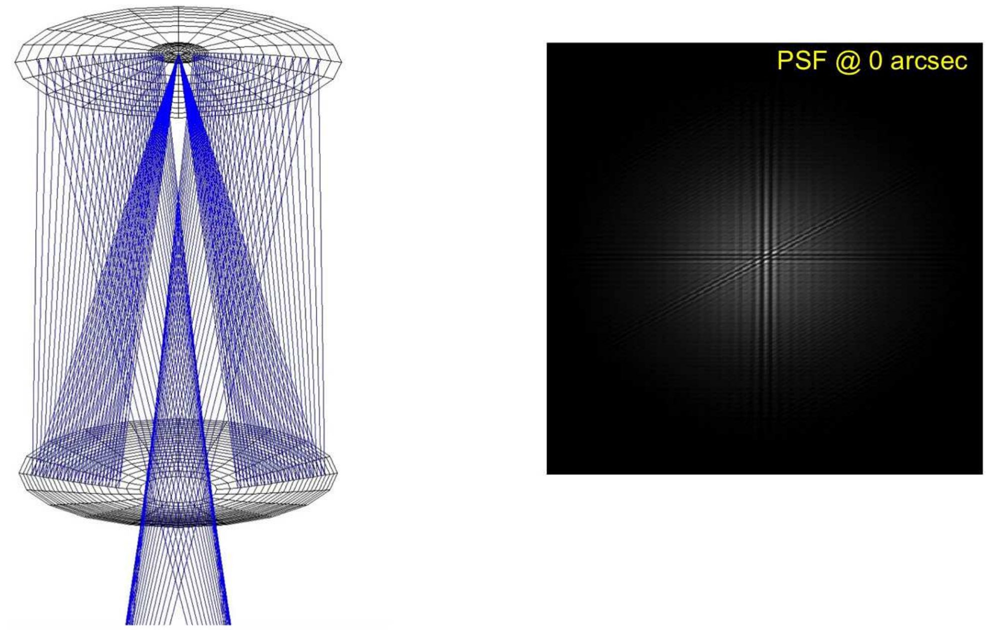


Figure 10.: *The Mertz Corrector, and the resulting PSF, on-axis.*

For this reason, a simplified Fizeau version of the focal optics was developed, by removing the pupil densifier, and modifying the optical design to adapt the size of the images on the science detector and on the guiding detector (Fig. 12). The guidance tolerance was then released to $\pm 1$ arcsec. We obtained good tracking results with very low wind. Nevertheless, better performance could be expectable with fine motorized guiding system in the gondola.

## 4. Observations and results

The construction of the prototype began in 2003 and followed a progressive development, with a certain number of milestones. In May 2004, the first observations with a simplified installation (only two adjacent mirrors, no servo-loop, no metrology, no focal optics in front of the detector) were conducted, and showed a reasonable quality of the tracking, allowing to keep the image of the star on the detector during a few tens of minutes (Le Coroller et al. 2004). In 2007, the Merz corrector was manufactured and tested on the sky with three mirrors regardless of coherence. In 2010, the servo-loop and the laser metrology system were assembled (Le Coroller et al. 2012). Then the complete focal gondola was constructed, and first stellar observations with the entire prototype of a Carlina diluted telescope began in 2012. Experience proved the use of a helium balloon to exhibit some serious drawbacks: not only because of its intrinsic sensitivity to wind, but also because it imposed a complete disassembly of the installation every morning and re-assembly every evening: the balloon cannot stay in flight during the day when the wind speed overcomes 15 km/h. The balloon was even-

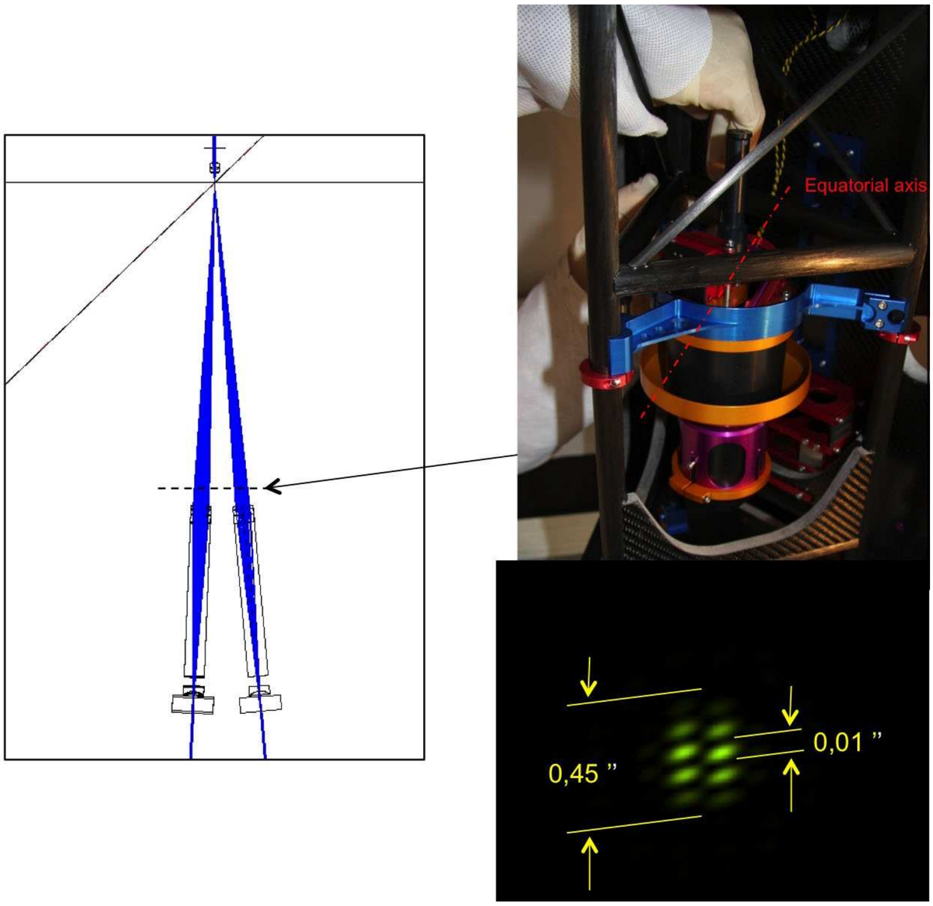


Figure 11.: *The pupil densifier: a pair of diverging/converging lenses are placed into each beam, near a pupil plan. Thos produce a reduction of the envelope sizen abd has no effect on the fringes size. To follow the pupil movement, this device is passively positioned on an "equatorial pendulum".*

tually replaced by a lifting crane for the last observation run, in September 2013 (Fig. 13).

Over the course of a four night run, the prototype was deployed using the crane. After several adjustments, the prototype reached nominal operating performance, each sub-system working as designed: The installation was first positioned using the vertical laser reference. Then, the servo-loop system of the cable tripod was turned on, and the tip-tilt and piston of the primary segments were accurately adjusted, thanks to the metrology system. The white metrology fringes could be kept during the night, with some small adjustments every one or two hours. Several stars could be pointed and tracked correctly, with a variable performance of the tracking, depending on wind conditions.

A preliminary data analysis in September 2013 didn't show the fringes. Recently (February 2014) we improved the analysis procedure, for example by taking

Figure 12.: *Views of the focal module: on the left, initial version with the pupil densifier; on the right, the simplified Fizeau version.*

into account the rotation of the baselines due to the earth-rotation to add more data. Fringes are detected. The analysis method and results will be presented in a forthcoming paper.

Several hypotheses were formulated to explain the difficulty to detect the fringes, although the presence of the white metrology fringes a few minutes before and after each star tracking:

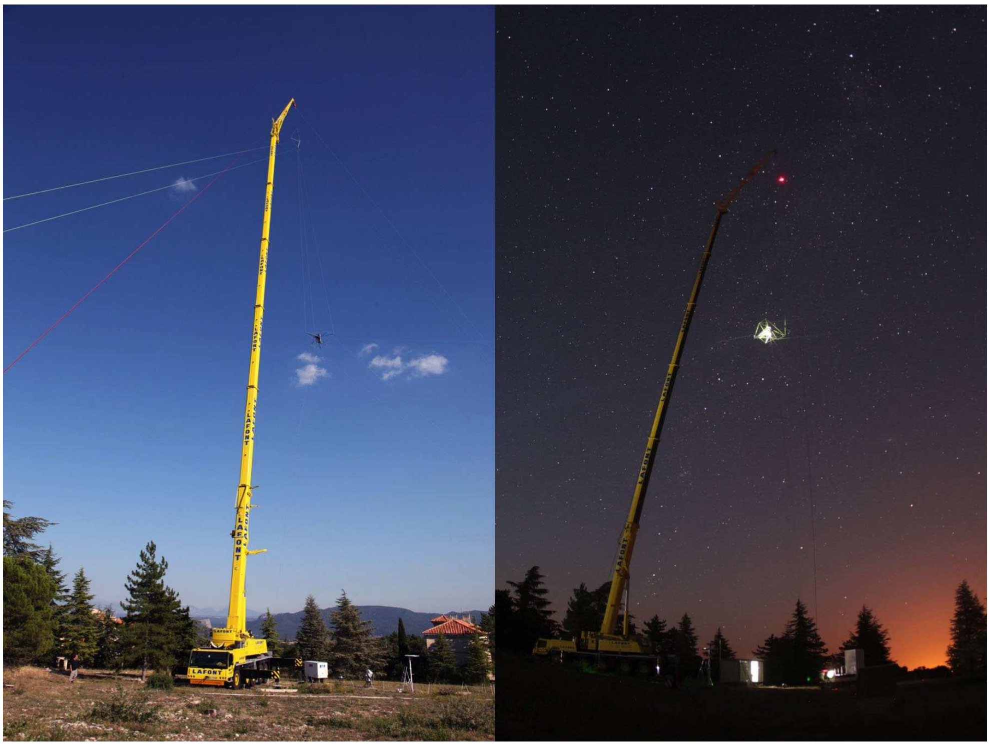

Figure 13.: *The Carlina-OHP experiment in September 2013: the helium balloon was replaced by a crane.*

- Bad geometry of the Mertz corrector: the spherical aberration corrector, made of two high aspheric mirrors, is difficult to test optically in lab. Nevertheless, some measurements had been done on each mirror in 2007, and showed a good shape, with a 5 microns incertitude. Moreover, sky tests (in 2006 and 2013) with three spaced-out mirrors showed that the three spots remained well superimposed during all the tracking.

- The relative ease with which the metrology fringes were obtained could have given too much confidence regarding the possibility to get stellar fringes. Indeed, as explained before, in the laser metrology system, the fringes are formed in a pseudo pupil plan, where the fringe velocity due to residual oscillations of the metrology gondola is drastically reduced, compared with fringes velocity in a focal plane. Even if the oscillations of the focal gondola should be comparable to those of the metrology gondola, the velocity of the focal fringes is 64 times higher (as it has been verified recently with Zemax). It is then possible that the stellar fringes were present, but undetectable because totally scrambled during a 5 ms exposure time. More data taken using a short exposure time (1ms) will be soon reduced.

It therefore appears that a big effort on the gondola stabilization (fine embedded motorized tracking system), much more massive structures and cables with high pre-load, use of inertia wheels, as suggested in T. Andersen's paper (2014), would be necessary for a Carlina diluted telescope to work properly.

## 5. Conclusion

After ten years of development and efforts, the prototype is completed. Original opto-mechanical solutions have been proposed, constructed and tested, to stabilize optical devices attached under cables. For example, the metrology mirror is stabilized within 200 microns accuracy, at 70 meters height! The primary mirrors are adjusted within one micron, thanks to a specific white-laser metrology. We were able to track the stars with 2 arcsec accuracy in very low wind.

Recently (February 2014) we improved the analysis procedure and fringes are detected. The analysis method and results will be presented in more details in a forthcoming paper.

Nevertheless, some solutions to stabilize the focal optics could be studied for a further project.

*Acknowledgements.* This research has been funded by CNRS /ASHRA / OHP / Institut Pytheas, and College de France. We are grateful to Frantz Martinache for some useful corrections and suggestions. We are grateful to the students and to the people who helped us during the long nights of tests.

## References

Andersen, T., Le Coroller, H., O.-Petersen, M., Dejonghe, J. 2014, Linearized Model of an Actively Controlled Cable for a Carlina Diluted Telescope, in *Improving the performances of current optical interferometers & future designs*, Proceedings of Haute Provence Observatory Colloquium (23-27 September 2013) Edited by L. Arnold, H. Le Coroller & J. Surdej

Le Coroller, H., Dejonghe, J., Arpesella, C., Vernet, D., Labeyrie, A. 2004, Tests with a Carlina-type hypertelescope prototype, A & A, 426, 721

Le Coroller, H., Dejonghe, J., Regal, X., Sottile, R., Guillaume, C., Meunier, J.P., Clausse, J.M., Blazit, A., Berio, P., Deram, P., Ricci, D., Le Vansuu, A. 2012, The first diluted telescope ever built in the world, Optical and Infrared Interferometry III. Proceedings of the SPIE, Volume 8445, article id. 844514, 8 pp. (2012).

Le Coroller, H., Dejonghe, J., Regal, X. , Sottile, R. , Mourard, D., Ricci, D., Lardière, O., Le Vansuu, A., Boer, M., De Becker, M., Clausse, J.M.,Guillaume, C., Meunier, J.P., 2012, Tests with a Carlina-type diluted telescope. Primary coherencing, A & A, 539, 59

McAlister, H. A., ten Brummelaar, T. A., Gies, D. R., Huang, W., Bagnuolo, W. G., Shure, M. A.,Sturmann, J., Sturmann, L., Turner, N. H., Taylor, S. F., Berger, D. H., Baines, E. K., Grundstrom, E. and Ogden, C., 2005, APJ, 628, 439

Soulez, F., Denis, L., Thiébaut, E., Fournier, C., Goepfert, C. J., 2007, Opt. Soc. Am., Vol. 24, No. 12, 3708

*Improving the performances of current optical interferometers & future designs*
*Proceedings of Haute Provence Observatory Colloquium (23-27 September 2013)*
*Edited by L. Arnold, H. Le Coroller & J. Surdej*

# Linearized Model of an Actively Controlled Cable for a Carlina Diluted Telescope

Torben Andersen[1], Hervé Le Coroller[2], Mette O.-Petersen[1] & Julien Dejonghe[3]

[1]*Lund Observatory, Box 43, SE-221 00 Lund, Sweden*

[2]*Observatoire de Haute Provence, F-04870 St Michel l'Observatoire, France*

[3]*Laboratoire Lagrange - UMR 7293, Observatoire de la Côte d'Azur, B.P. 4229, F-06304 NICE Cedex 4, France*

**Abstract.** The Carlina thinned pupil telescope has a focal unit ("gondola") suspended by cables over the primary mirror. To predict the structural behavior of the gondola system, a simulation building block of a single cable is needed. A preloaded cable is a strongly non-linear system and can be modeled either with partial differential equations or non-linear finite elements. Using the latter, we set up an iteration procedure for determination of the static cable form and we formulate the necessary second-order differential equations for such a model. We convert them to a set of first-order differential equations (an "ABCD"-model). Symmetrical in-plane eigenmodes and "axial" eigenmodes are the only eigenmodes that play a role in practice for a taut cable. Using the model and a generic suspension, a parameter study is made to find the influence of various design parameters. We conclude that the cable should be as stiff and thick as practically possible with a fairly high preload. Steel or Aramid are suitable materials. Further, placing the cable winches on the gondola and not on the ground does not provide significant advantages. Finally, it seems that use of reaction-wheels and/or reaction-masses will make the way for more accurate control of the gondola position under wind load. An adaptive stage with tip/tilt/piston correction for sub-apertures together with a focus and guiding system for freezing the fringes must also be studied.

## 1. Introduction

The planned Carlina telescope (Le Coroller et al. 2012, Dejonghe et al. 2014) will have a gondola with focal plane optics suspended in a cable net over the primary mirror. The position of the gondola must be controlled accurately by a dynamical control system with cable winches. To model this system, a dynamical, state-space model of a guy wire is needed. We here present such a model and some test runs with conclusions related to choice of design parameters.

Most structures can be adequately described by linear models. However, in some cases non-linear techniques are necessary. Two types of non-linearities are common: Material and geometric non-linearities. Creeping of steel is a well-known example of a material non-linearity. Geometric non-linearities arise when the deformation of a structure is so large that changes of the geometry of the structure play a significant role for the load path in the structure. A wire is a geometrically non-linear system because the system geometry changes due to gravity loads and external forces.

Modeling of suspended cables is difficult but of high interest due to important applications, such as suspension bridges, wire roof structures, guyed antenna masts, semi-submersible drilling rigs, and electrical transmission lines.

The problem related to gondola control for the Carlina is that many simulation and control tools are linear, so it is of interest to establish a linear state-space model of the cable performance. The approach is then to first establish a non-linear model to determine the operating point of the cable and then a linear model describing performance around the operating point.

Two types of models can be used to describe cables, either based on partial differential equations (Irvine 1981, Starossek 1994) or on a finite element representation (Henghold & Russell 1976, Ozdemir 1979, Desai et al. 1988, Tibert 1999, Talvik 2001). In a previous publication (Enmark et al. 2011), a model based upon partial differential equations was used. We here present a cable model based upon a finite element approach (largely following Tibert 1999) and draw some conclusions for the choice of design parameters.

In Section 2, we present the equations for a finite cable element, and in Section 3 we show the algorithms for determination of the static form a of suspended cable. Then, in Section 4, we set up a linear, dynamic model of a cable, valid for small excursions around the operating point, and in Section 5 we comment on the nature of the wind loads. Finally, a generic gondola suspension model is formulated in Section 6 for evaluation of design parameter sensitivity, together with a concluding discussion in Section 7. Through the paper, we illustrate the approach by an example of a cable similar to the ones used for the Carlina.

## 2. Single Element

A finite element model of a cable can be formed as shown in Fig. 1 for a horizontal wire. The cable is divided into a number of elements and corresponding masses are assigned to the nodes between the elements. Under the influence of gravity and preload, the wire assumes a certain form. With modest preloads this is the well-known catenary, whereas it resembles a parabola, when the preload is high. Each node has three translational degrees of freedom.

Figure 2 shows part of a finite element model of a wire for the static case. If the node in B for some reason is displaced from the equilibrium position to position B', two different effects together tend to restore equilibrium. Firstly, elements AB and BC are stretched so in addition to the preload, axial, *elastic* forces turn up. Secondly, due to the displacement of node B, the two preload forces in elements AB and BC change direction, leading to a *geometric* force component $\Delta F_B$ that tends to move the node back from B' to its equilibrium position in B. The two effects can be dealt with separately by use of elastic and geometric stiffness matrices, respectively.

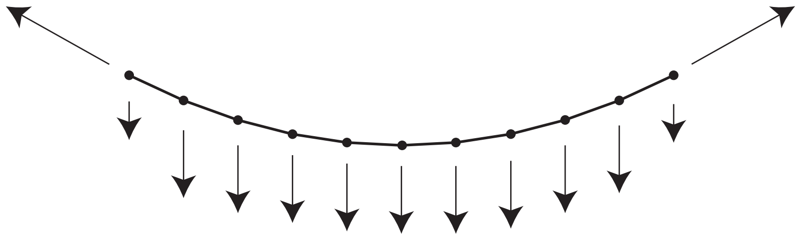

Figure 1.: *Subdivision of a cable into finite elements connected at nodes.*

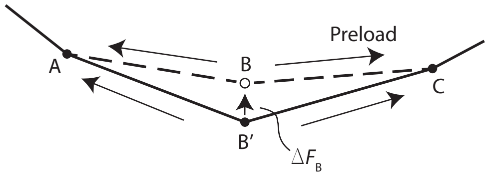


Figure 2.: *Displacing node B to B' creates a geometric restoring force.*

Different cable elements are described in the literature (Gambhir & Barrington De V. Batchelor 1977, Jayaraman & Knudson 1981, Ahmadi-Kashani 1983, Tibert 1999, Ren et al. 2008). For highly preloaded cables, rectilinear elements suffice, whereas curved elements are useful for less preloaded cables. Due to the high preload, simple rectilinear elements (Tibert 1999, Levy & Spillers 2003) can be used for the Carlina.

A rectilinear cable element in 3D Cartesian space $(x, y, z)$ between nodes number $i$ and $j$ is shown in Fig. 3. We first wish to form the elastic stiffness submatrix from which the elastic end node force increments at node $i$ can be determined by multiplication by a displacement vector for the same node. Letting $\mathbf{n_{ij}}$ denote a unit vector directed from node $i$ to node $j$ it can relatively easily be shown (Levy & Spillers 2003) that the elastic stiffness submatrix, $\mathbf{K}_{\mathrm{Ei}}$, for node $i$ is

$$\mathbf{K}_{\mathrm{Ei}} = \frac{AE}{L} \times \mathbf{n}_{\mathrm{ij}}\mathbf{n}_{\mathrm{ij}}^{\mathrm{T}}$$

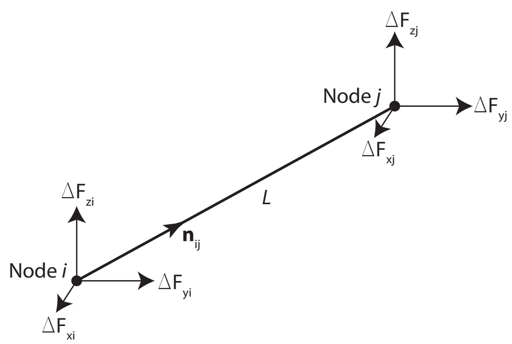


Figure 3.: *An element connecting nodes i and j in 3D space. End point forces in a global coordinate system are shown.*

where the symbols are defined in Table 1 together with some values used in the example of this note. The operator "$\circ^{\mathrm{T}}$" transposes a matrix. For reasons of symmetry, the full, elastic stiffness matrix for the element then is

$$\mathbf{K}_{\mathrm{E}} = \begin{bmatrix} \mathbf{K}_{\mathrm{Ei}} & -\mathbf{K}_{\mathrm{Ei}} \\ -\mathbf{K}_{\mathrm{Ei}} & \mathbf{K}_{\mathrm{Ei}} \end{bmatrix}$$

Table 1.: *Nomenclature with values used in the example.*

| | Definition | Example |
|---|---|---|
| $F_{\mathrm{i}}$ | Axial force in element $i$ | |
| $F$ | Cable preload | 1344 N |
| $A$ | Cable cross section | 2.69 mm$^2$ |
| $E$ | Modulus of elasticity | $7.03 \times 10^{10}$N/m$^2$ |
| $l$ | Cable chord length | 185.8 m |
| $L$ | Length of element | 4.61 m |
| $\rho$ | Mass density | 1440 kg/m$^3$ |
| $\theta$ | Cable inclination angle | 19$^\mathrm{o}$ or 0$^\mathrm{o}$ |
| $g$ | Gravity acceleration | 9.81 m/s$^2$ |
| $(x_{\mathrm{i}}, y_{\mathrm{i}}, z_{\mathrm{i}})$ | Coordinates of end point $i$ | (0 m, 0 m, 0 m) |
| $(x_{\mathrm{j}}, y_{\mathrm{j}}, z_{\mathrm{j}})$ | Coordinates of end point $j$ | (175.68 m, 0 m, 60.49 m) or (185.8 m, 0 m, 0 m) |

Similarly, the geometric stiffness submatrix for the element at node $i$ can be formed (Levy & Spillers 2003). It is

$$\mathbf{K}_{Gi} = \frac{F_i}{L}\left(\mathbf{I} - \mathbf{n_{ij}}\mathbf{n_{ij}^{\mathrm{T}}}\right)$$

where $\mathbf{I}$ is the identity matrix, $F_i$ the axial force in the element and $L$ the length of the element. As expected, the geometric stiffness matrix depends on the load conditions, leading to a nonlinear model. The full, geometric stiffness matrix then is

$$\mathbf{K}_{\mathrm{G}} = \begin{bmatrix} \mathbf{K}_{\mathrm{Gi}} & -\mathbf{K}_{\mathrm{Gi}} \\ -\mathbf{K}_{\mathrm{Gi}} & \mathbf{K}_{\mathrm{Gi}} \end{bmatrix}$$

and the end node force increments (see Fig. 3) for the element are

$$\left\{ \begin{array}{c} \Delta F_{\mathrm{xi}} \\ \Delta F_{\mathrm{yi}} \\ \Delta F_{\mathrm{zi}} \\ \Delta F_{\mathrm{xj}} \\ \Delta F_{\mathrm{yj}} \\ \Delta F_{\mathrm{zj}} \end{array} \right\} = (\mathbf{K}_{\mathrm{E}} + \mathbf{K}_{\mathrm{G}}) \left\{ \begin{array}{c} \Delta x_{\mathrm{i}} \\ \Delta y_{\mathrm{i}} \\ \Delta z_{\mathrm{i}} \\ \Delta x_{\mathrm{j}} \\ \Delta y_{\mathrm{j}} \\ \Delta z_{\mathrm{j}} \end{array} \right\}$$

where $\{\Delta x_{\mathrm{i}}, \Delta y_{\mathrm{i}}, \Delta z_{\mathrm{i}}, \Delta x_{\mathrm{j}}, \Delta y_{\mathrm{j}}, \Delta z_{\mathrm{j}}\}^{\mathrm{T}}$ are the node displacements in directions $x$, $y$, and $z$ for nodes $i$ and $j$ with respect to the position at which the stiffness matrices were evaluated.

The matrix $\mathbf{K} = \mathbf{K}_\mathrm{E} + \mathbf{K}_\mathrm{G}$ is the *tangent stiffness matrix* that describes cable element performance in the vicinity of the node locations at which it was evaluated.

The mass matrix can be formed by simply lumping the mass of the cable to the two end nodes. The mass matrix for a single element then is

$$\mathbf{M} = \frac{1}{2} AL\rho\mathbf{I}$$

## 3. Cable Static Form

### 3.1 Approximate Static Form

A cable fixed in the ends and loaded by gravity is taken as taut if the maximum gravity deflection of the cable from its chord is less than about 1/8 of the chord length. Based upon partial differential equations, it is shown by Irvine (1999) that the static gravity deflection for a taut cable is nearly parabolic. For a horizontal cable oriented along the $x$-axis, the gravity deflection is

$$z = -\frac{\rho Agl^2}{2F} \left( \frac{x - x_1}{l} \left( 1 - \frac{x - x_1}{l} \right) \right) \tag{1}$$

where $x_1$ is the x-coordinate of the first end point of the cable and $F$ the tension force in the cable (taken to be uniform over the length of the cable). For inclined cables, the same expression applies when the gravity vector is scaled appropriately.

For more complex cable networks one may instead use the *force density* method (Schek 1974) which gives a linear set of equations under the assumption that the force per length unit is known. This is a valid approximation for some complex structures.

### 3.2 Iterative Static Solution

The solution to the static problem dealt with above is only approximate. In the following, an approach for a more exact determination of the static equilibrium form under the influence of gravity and preload is presented. For this, an iterative procedure is necessary.

We first combine all degrees of freedom of the cable into a single global vector. The assumed equilibrium coordinate vector, $\mathbf{u}$, is

$$\mathbf{u} = \left\{ x_1, y_1, z_1, x_2, y_2, z_2, \ldots, x_{(\mathrm{n_e}+1)}, y_{(\mathrm{n_e}+1)}, z_{(\mathrm{n_e}+1)} \right\}^\mathrm{T}$$

where $x_\mathrm{i}$, $y_\mathrm{i}$, and $z_\mathrm{i}$ are the coordinates of node $i$ and $n_\mathrm{e}$ the number of elements used. This is the first estimate used for the iteration. A good starting point is the node locations found in Sect. 3.1 using an approximate tension force. It is our objective to arrive at a more precise version of this vector. A global vector, $\Delta\mathbf{u}$, with the excursions from the equilibrium is defined as

$$\Delta\mathbf{u} = \left\{ \Delta x_1, \Delta y_1, \Delta z_1, \Delta x_2, \Delta y_2, \ldots, \Delta x_{(\mathrm{n_e}+1)}, \Delta y_{(\mathrm{n_e}+1)}, \Delta z_{(\mathrm{n_e}+1)} \right\}^\mathrm{T}$$

where $\Delta x_\mathrm{i}$, $\Delta y_\mathrm{i}$, and $\Delta z_\mathrm{i}$ are displacements from the assumed equilibrium for node $i$.

Next, we assemble the global elastic and geometric stiffness matrices, and the global mass matrix, using the expressions for a single element of Sect. 2., and we do this for the node locations defined by $\mathbf{u}$. We here denominate the global elastic matrix by $\mathbf{K}_\mathrm{E}$ and get:

$$\mathbf{K}_\mathrm{E} = \begin{bmatrix} \mathbf{K}_\mathrm{E1} & -\mathbf{K}_\mathrm{E1} & & & & & \\ -\mathbf{K}_\mathrm{E1} & \mathbf{K}_\mathrm{E1}+\mathbf{K}_\mathrm{E2} & -\mathbf{K}_\mathrm{E2} & & & & \\ & & \ddots & & & & \\ & & -\mathbf{K}_\mathrm{E(i-1)} & \mathbf{K}_\mathrm{E(i-1)}+\mathbf{K}_\mathrm{Ei} & -\mathbf{K}_\mathrm{Ei} & & \\ & & & \ddots & & & \\ & & & -\mathbf{K}_\mathrm{E(n_e-1)} & \mathbf{K}_\mathrm{E(n_e-1)}+\mathbf{K}_\mathrm{En_e} & -\mathbf{K}_\mathrm{En_e} \\ & & & & -\mathbf{K}_\mathrm{En_e} & \mathbf{K}_\mathrm{En_e} \end{bmatrix}$$

Elements not shown are zero. A similar expression holds for the global geometric stiffness matrix, which we here call $\mathbf{K}_\mathrm{G}$. The global mass matrix, which we now call $\mathbf{M}$, simply is

$$\mathbf{M} = \begin{bmatrix} \frac{1}{2}Al\rho & & & & \\ & Al\rho & & & \\ & & \ddots & & \\ & & & Al\rho & \\ & & & & \frac{1}{2}Al\rho \end{bmatrix}$$

The stiffness and mass matrices are $\mathbb{R}^{3(n_e+1)\times 3(n_e+1)}$, sparse, and symmetrical.

For determination of the equilibrium form by iteration we assume that the end points are constrained. Later, when the equilibrium form is known, we will account for displacements of the end points. To constrain the end points, we remove the first and last three rows and columns from the global stiffness matrices (Andersen & Enmark 2011) which we then denote $\mathbf{K}'_\mathrm{E}$, and $\mathbf{K}'_\mathrm{G}$. Also, for the moment we disregard the degrees of freedom for the end points from the displacement vectors, which we then call $\mathbf{u}'$ and $\Delta\mathbf{u}'$.

We compute the gravity load vector for the inner nodes

$$\mathbf{f}'_g = \mathbf{M}' \left\{g_{x2}, g_{y2}, g_{z2}, \ldots, g_{xn_e}, g_{yn_e}, g_{zn_e}\right\}^\mathrm{T}$$

where $g_\mathrm{xi}$, $g_\mathrm{yi}$, and $g_\mathrm{zi}$ are the components of the $i$'th gravity vector and $\mathbf{f}'_g \in \mathbb{R}^{3(n_\mathrm{e}-1)\times 1}$. Obviously other static forces, such as point loads, may also be added here.

To determine the element forces on the nodes, we determine a vector from the first node of element $i$ to the second node:

$$\mathbf{r}_\mathrm{i} = \left\{x_\mathrm{i} - x_\mathrm{i+1}, y_\mathrm{i} - y_\mathrm{i+1}, z_\mathrm{i} - z_\mathrm{i+1}\right\}^\mathrm{T}$$

The length of the element is $\|\mathbf{r}_\mathrm{i}\|$ and a unit vector with the same orientation is

$$\mathbf{n}_\mathrm{i} = \mathbf{r}_\mathrm{i} / \|\mathbf{r}_\mathrm{i}\|$$

The force vector on inner node $i$ $(2 \leq i \leq n_e)$ is

$$\mathbf{f}_i = AE\left(\frac{\|\mathbf{r}_\mathrm{i}\| - l_0}{l_0}\mathbf{n}_\mathrm{i} - \frac{\|\mathbf{r}_\mathrm{i+1}\| - l_0}{l_0}\mathbf{n}_\mathrm{i+1}\right)$$

where $l_0$ is the length of the unloaded element. The global inner force vector $\mathbf{f}'_e \in \mathbb{R}^{3(n_\mathrm{e}-1)\times 1}$ then is

$$\mathbf{f}'_e = \left\{f_{x2}, f_{y2}, f_{z2}, \ldots, f_{x(n_\mathrm{e}-1)}, f_{y(n_\mathrm{e}-1)}, f_{z(n_\mathrm{e}-1)}\right\}^\mathrm{T}$$

When in equilibrium, $\mathbf{f}'_\mathbf{g}$ and $\mathbf{f}'_\mathbf{e}$ will outbalance each other. When not in equilibrium, the unbalance is

$$\Delta\mathbf{f}' = \mathbf{f}'_g - \mathbf{f}'_e$$

A correction to the estimated inner node coordinates can be found using a combination of the elastic and geometric stiffness matrices:

$$\left(\mathbf{K}'_\mathrm{E} + \mathbf{K}'_\mathrm{G}\right)\Delta\mathbf{u}' = \Delta\mathbf{f}'$$

The equation must be solved for $\Delta\mathbf{u}'$. Using the assignment symbol ":=", the new estimate for $\mathbf{u}'$ then is:

$$\mathbf{u}' := \mathbf{u}' + \Delta\mathbf{u}'$$

with which the iteration can recommence. A stop criterion can be formed by monitoring the relative error

$$\epsilon = \frac{\|\Delta\mathbf{f}'\|}{\|\mathbf{f}'_\mathbf{g}\|}$$

and then interrupt the iteration when $\epsilon < \epsilon_0$, where $\epsilon_0$ is in the range 0.001-0.1. It is possible to reduce computation time by only recalculating the stiffness matrices at certain intervals. Near the end of the iteration, the stiffness matrices only change little. However, for the present application, calculation times are generally small on multithreaded work stations.

Using the iteration procedure described, as an example, the form of the cable defined in Table 1 is determined. The model has 40 elements. The cable is assumed to be horizontal for better illustration. The form depends on the unloaded length of the cable, which was selected as 184.4883 m (the chord length is 185.8 m). The sag in the middle was found to be 0.1210 m and the preload 1344 N. Using Irvine's formula (Irvine 1999) with the same preload of 1344 N a value of 0.1219 m is obtained, in good agreement with the result from our model.

In the vicinity of the equilibrium form, the cable model may be taken as linear. The static deflection relative to the equilibrium form for any small static load may then be determined from the linear equation

$$\left(\mathbf{K}'_\mathrm{E} + \mathbf{K}'_\mathrm{G}\right)\Delta\mathbf{u}' = \Delta\mathbf{f}'$$

As an example, Fig. 4 depicts the incremental form change of the same cable used in the example above with gravity load and an additional downward force of 1 N at distance of 139.35 m from the left cable support.

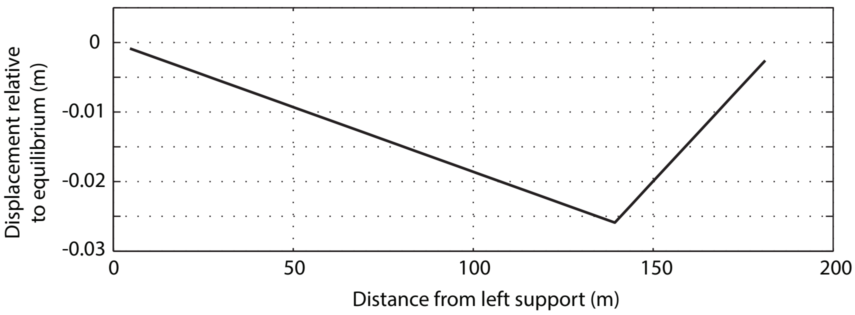


Figure 4.: *Example showing static deflection relative to the equilibrium form due to a downward force of 1 N at a distance 139.35 m from the left support. The two deflection curves seem to be straight lines but that is not exactly the case.*

## 4. Cable Dynamics

### 4.1 Dynamical Finite Element Model

Based on the finite element model formulated in Sect. 2., it is relatively easy to set up a dynamical model of the cable. The model can be formed for the case with fixed end points or with free end points. Using the approach described in Andersen & Enmark (2011), the latter model becomes

$$\mathbf{M}\Delta\ddot{\mathbf{u}} + \mathbf{E}\Delta\dot{\mathbf{u}} + \mathbf{K}\Delta\mathbf{u} = \Delta\mathbf{f} \tag{2}$$

Here, $\mathbf{E}$ is a damping matrix. Using standard solvers, the eigenvalues and eigenvectors can be determined (Andersen & Enmark 2011) from

$$\mathbf{K\Psi} = \mathbf{M\Psi\Omega^2}$$

The columns of $\mathbf{\Psi}$ are the eigenvectors, the diagonal matrix $\mathbf{\Omega}^2$ holds the eigenvalues along the diagonal, and $\mathbf{\Omega}$ the eigenfrequencies. By replacing $\mathbf{M}$ with $\mathbf{M}'$, $\mathbf{K}$ with $\mathbf{K}'$, and $\Delta\mathbf{u}$ with $\Delta\mathbf{u}'$, these equations are also valid for the case where the end points are constrained. We call the corresponding matrices of $\mathbf{\Psi}$ and $\mathbf{\Omega}$ for $\mathbf{\Psi}'$ and $\mathbf{\Omega}'$.

Using the approach, the eigenmodes and eigenfrequencies for the cable of the previous example can be determined. There are two types of eigenmodes, vertical (in-plane) and lateral (out-of-plane), which again can be subdivided into symmetrical and anti-symmetrical eigenmodes. Figure 5 shows low-order in-plane eigenmodes determined for a cable with the characteristics shown in Table 1. For plotting, the eigenmodes have been scaled to a peak displacement of 0.1 m and are shown superimposed on top of the static deflection curve. Table 2 lists the nature of some more important eigenmodes. High-order eigenmodes are not shown because they are generally not important for control system design and wind load studies. Also the model tends to be inaccurate at higher eigenfrequencies. For studies of the effect of flutter (wind-coupled transverse cable vibrations), a finite-element model with many elements would be needed to model high-order eigenmodes accurately.

For the axial eigenmodes, the cable vibrates with a movement along the “axis” of the cable. These modes resemble that of an air column in an organ pipe

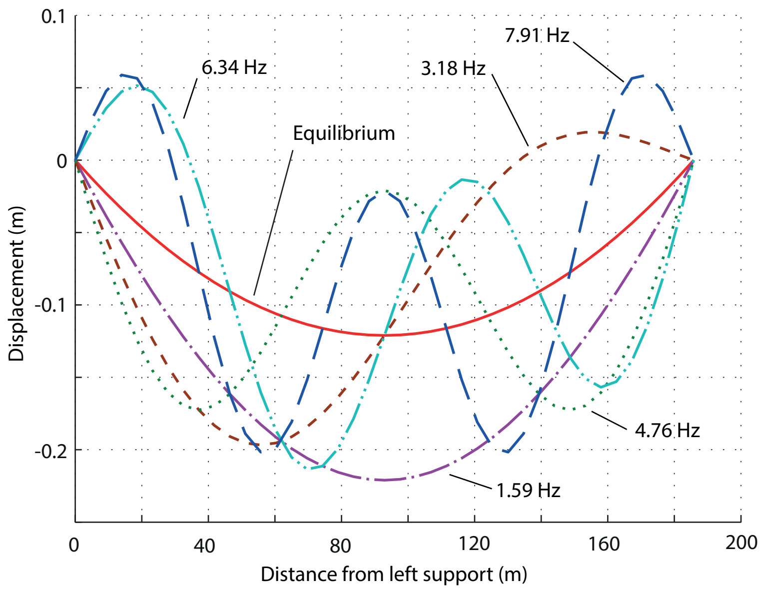


Figure 5.: *Vertical (in-plane) eigenmodes for a cable with the characteristics shown in Table 1.*

Table 2.: *Nature of various modes together with participation factors for a longitudinal translation of one end point. Same example as in Fig. 5.*

| Mode no | Type | Symmetry | Eigenfrequency (Hz) | Participation factor |
|---|---|---|---|---|
| 1 | Out-of-plane | Symmetrical | 1.59 | 0 |
| 2 | In-plane | Symmetrical | 1.59 | 5.63 |
| 3 | In-plane | Anti-symmetrical | 3.18 | 0.4 |
| 4 | Out-of-plane | Anti-symmetrical | 3.18 | 0 |
| 5 | Out-of-plane | Symmetrical | 4.76 | 0 |
| 6 | In-plane | Symmetrical | 4.76 | 1.52 |
| 7 | In-plane | Anti-symmetrical | 6.34 | 0.83 |
| 8 | Out-of-plane | Anti-symmetrical | 6.34 | 0 |
| 9 | Out-of-plane | Symmetrical | 7.90 | 0 |
| 10 | In-plane | Symmetrical | 7.90 | 0.49 |
| 13 | In-plane | Symmetrical | 11.0 | 0.09 |
| 17 | In-plane | Symmetrical | 14.0 | 0.51 |
| 25 | Axial | Symmetrical | 18.9 | 5380 |
| 62 | Axial | Anti-symmetrical | 37.8 | 10700 |
| 81 | Axial | Symmetrical | 56.7 | 16000 |
| 82 | Axial | Anti-symmetrical | 75.4 | 21200 |
| 83 | Axial | Symmetrical | 94.1 | 26200 |

closed in both ends or of a fluid oscillating in a tube. From first-order physics, it is known that the speed of sound, $v$, in a suspended cable is

$$v = \sqrt{\frac{E}{\rho}}$$

For our example, the speed of sound is $4.03 \times 10^3\,\mathrm{m/s}$. With the end nodes constrained there will be resonance, when the period of the oscillation equals the time it takes for the sound to go from one end of the cable to the other end and then be reflected back to first end. Considering also higher-order harmonics, the theoretical eigenfrequencies for axial vibrations then are multipla of the lowest axial eigenfrequency $\nu$:

$$\nu = \frac{v}{2l}$$

For our example, Table 3 lists the axial eigenfrequencies as determined by the finite element model described above and the speed of sound. There is good agreement, in particular for the lower eigenfrequencies shown here, which are the ones of interest.

Table 3.: *Comparison of axial mode eigenfrequencies determined by the finite element model and from speed of sound.*

| Mode no | Eigenfrequency from FE model (Hz) | Eigenfrequency from speed of sound (Hz) |
|---|---|---|
| 25 | 18.9 | 18.8 |
| 62 | 37.8 | 37.6 |
| 81 | 56.7 | 56.4 |
| 82 | 75.4 | 75.2 |
| 83 | 94.1 | 94.0 |

Irvine (1999) has given an analytical approach for determination of eigenfrequencies of a suspended, taut cable. Normalized natural eigenfrequencies, $\omega'$, for symmetrical in-plane eigenmodes can be found as solutions to the transcendental equation

$$\tan\frac{\omega'}{2} = \frac{\omega'}{2} - \frac{4}{\gamma^2}\left(\frac{\omega'}{2}\right)^3 \tag{3}$$

The parameter $\gamma^2$ is

$$\gamma^2 = \frac{(\rho A g \cos\theta)^2\, l^3 EA}{F^3 L_e}$$

where the symbols are defined in Table 1 and the parameter, $L_e$, is

$$L_e \approx l\left(1 + 8\left(\frac{\delta_{l/2}}{l}\right)^2\right),$$

where $\delta_{l/2}$ is the sag at the middle of the cable. For taut cables, $L_e \approx l$.

There are infinitely many solutions to (3) but for our purpose usually only few eigenmodes are of interest. The unnormalized natural eigenfrequencies can be found from

$$\omega = \omega' \sqrt{F/(\rho A)}/l$$

Solving the above transcendental equation iteratively for our example gives the eigenfrequencies shown in Table 4. There is fine agreement with the results from our finite element model, confirming the validity of the model.

Table 4.: *Comparison of symmetrical in-plane eigenfrequencies determined by the finite element model and from Irvine's analytical model.*

| Mode no | Eigenfrequency from FE model (Hz) | Eigenfrequency from Irvine's model (Hz) |
|---|---|---|
| 2 | 1.5913 | 1.5860 |
| 6 | 4.7634 | 4.7572 |
| 10 | 7.9064 | 7.9286 |

The analysis presented above is valid for fixed end points. In practice, one or both end points will be moved during operation. Since the mass of the cable near the end point is small compared to that of the attached parts, and since the rotation angle of winches can be servo-controlled with high bandwidth and stiffness, we can take the position of the end points as controlled input variables, and we are then interested in the cable forces at the end points. To deal with this, and for a moment ignoring damping, we rewrite (2):

$$\mathbf{M}\Delta\ddot{\mathbf{u}} + \mathbf{K}\Delta\mathbf{u} = \Delta\mathbf{f}$$

This is the equation for the full system (including end points). For numerical convenience, we now assume that the degrees of freedom have been resorted, so that the first three components of $\Delta\mathbf{u}$ are those of end point 1 $((\Delta x_1, \Delta y_1, \Delta z_1))$ and the subsequent three components are those of end point 2 $((\Delta x_{\mathrm{n_e}+1}, \Delta y_{\mathrm{n_e}+1}, \Delta z_{\mathrm{n_e}+1}))$, and the remaining unsorted degrees of freedom are for the inner nodes of the cable. This involves switching columns and rows of $\mathbf{M}$ and $\mathbf{K}$ appropriately. We rewrite this equation on the form

$$\begin{bmatrix} \mathbf{M_{11}} & \mathbf{M_{12}} \\ \mathbf{M_{21}} & \mathbf{M_{22}} \end{bmatrix} \begin{Bmatrix} \Delta\ddot{\mathbf{u}}_1 \\ \Delta\ddot{\mathbf{u}}_2 \end{Bmatrix} + \begin{bmatrix} \mathbf{K_{11}} & \mathbf{K_{12}} \\ \mathbf{K_{21}} & \mathbf{K_{22}} \end{bmatrix} \begin{Bmatrix} \Delta\mathbf{u_1} \\ \Delta\mathbf{u_2} \end{Bmatrix} = \begin{Bmatrix} \Delta\mathbf{f_1} \\ \Delta\mathbf{f_2} \end{Bmatrix}$$

where $\mathbf{M_{22}}$ in fact is identical to the previously defined $\mathbf{M}'$, $\mathbf{K_{22}}$ is identical to to $\mathbf{K}'$, and $\Delta\mathbf{u_2}$ identical to $\Delta\mathbf{u}'$. Due to the above assumption, to ignore the influence of end cable mass on the motion of the end points, we let $\mathbf{M_{11}} \approx \mathbf{0}$. Since $\mathbf{M}$ is diagonal, then $\mathbf{M_{12}}$ and $\mathbf{M_{21}}$ are also null matrices. Hence the above equation becomes

$$\mathbf{K}_{11}\Delta\mathbf{u}_1 + \mathbf{K}_{12}\Delta\mathbf{u}' = \Delta\mathbf{f_1} \tag{4}$$

$$\mathbf{M}'\Delta\ddot{\mathbf{u}}' + \mathbf{K}'\Delta\mathbf{u}' = -\mathbf{K}_{21}\Delta\mathbf{u_1} \tag{5}$$

Since we merely wish to study the influence of end point movements, we have here for simplicity assumed that there are no external forces on the cable in addition to those at the end points. Hence $\Delta\mathbf{f_2} = \mathbf{0}$ and $\Delta\mathbf{f_1}$ is equal to the forces at the end points. Then $\Delta\mathbf{u_1}$ is known, whereas $\Delta\mathbf{f_1}$ and $\Delta\mathbf{u}'$ are unknown. We can study the influence of end point movements by solving the equations for the end-constrained case with a load vector equal to $-\mathbf{K_{21}}\boldsymbol{\Delta}\mathbf{u_1}$. Subsequently, the end point forces can be found from (4).

### 4.2 State-space Model

The above model is a second-order linear model. To fully exploit the many useful control engineering tools, we convert the model to a first-order state-space model on the usual ABCD form:

$$\begin{aligned}\dot{\mathbf{v}} &= \mathbf{A}\mathbf{v} + \mathbf{B}\mathbf{w}\\ \mathbf{y} &= \mathbf{C}\mathbf{v} + \mathbf{D}\mathbf{w}\end{aligned}$$

where $\mathbf{A}$ is the *system matrix*, $\mathbf{B}$ the *input matrix*, $\mathbf{C}$ the *output matrix*, $\mathbf{D}$ the *feed-through matrix*, $\mathbf{v}$ is a state-space vector, $\mathbf{w}$ an input vector, and $\mathbf{y}$ an output vector. To determine the ABCD matrices, we first need to mass-normalize the eigenvectors. If $\boldsymbol{\psi}$ is an eigenvector, then the product of $\boldsymbol{\psi}$ and a constant will also be an eigenvector. We choose the constant for each eigenvector as described in Andersen & Enmark (2011) such that $\boldsymbol{\Psi}'^{T}_{\mathrm{m}}\mathbf{M}'\boldsymbol{\Psi}'_{\mathrm{m}} = \mathbf{I}$, where $\boldsymbol{\Psi}'_{\mathrm{m}}$ then is the eigenvector matrix holding the mass-normalized eigenvectors. Further using the methods presented in Andersen & Enmark (2011), we convert the second-order model derived above to ABCD form:

$$\begin{aligned}\mathbf{A} &= \begin{bmatrix}\mathbf{0} & \mathbf{I}\\ -(\boldsymbol{\Omega}')^2 & -2\mathbf{Z}\boldsymbol{\Omega}'\end{bmatrix}\\ \mathbf{B}_{\mathrm{ends}} &= -\begin{bmatrix}\mathbf{0}\\ \boldsymbol{\Psi}'^{T}_{\mathrm{m}}\end{bmatrix}\mathbf{K_{21}}\\ \mathbf{B}_{\mathrm{wind}} &= \begin{bmatrix}\mathbf{0}\\ \boldsymbol{\Psi}'^{T}_{\mathrm{m}}\end{bmatrix}\\ \mathbf{C}_{\mathrm{ends}} &= \mathbf{K_{12}}\begin{bmatrix}\boldsymbol{\Psi}'_{\mathrm{m}} & \mathbf{0}\end{bmatrix}\\ \mathbf{D}_{\mathrm{ends}} &= \mathbf{K_{11}}\end{aligned}$$

The matrix $\mathbf{B}_{\mathrm{ends}}$ relates to an input originating from a translation along either of the six degrees of the end points and the matrix $\mathbf{B}_{\mathrm{wind}}$ deals with a force input in three degrees of freedom for each of the internal nodes of the cable. The matrix $\mathbf{Z}$ is a diagonal matrix holding the assumed damping ratios for each of the modal coordinates.

This first-order model has twice as many degrees of freedom as the original second-order model. It is possible to perform a model reduction by disregarding those degrees of freedom that are outside the frequency range of interest. This is done by including only modes up to a certain order. In addition, eigenmodes that are known not to play a role, such as out-of-plane modes and anti-symmetrical in-plane modes, can be omitted. The eigenvector matrix then becomes rectangular with as many columns as there are eigenmodes retained and $\mathbf{A}$ becomes quadratic with as many rows and columns as there are eigenmodes retained. A substantial order reduction is then achieved.

The ABCD model is a useful building block in any simulation model involving control of a suspended object. Several such blocks can be combined into a large simulation model combining the dynamics of the individual cables and the suspended object.

Using the above model, we can determine *participation factors* as described in Andersen & Enmark (2011). For each mode, the value of the participation factor is a measure of the involvement of the mode when excited by a given input. For instance, the participation factors due to an excitation of the first degree of freedom of the second end point of the cable will be

$$\boldsymbol{\xi} = \boldsymbol{\Psi'}^{T}_{\mathrm{m}} \mathbf{K_{21}} \left\{ \begin{array}{cccccc} 0 & 0 & 0 & 1 & 0 & 0 \end{array} \right\}^{\mathbf{T}}$$

A value near zero of a participation factor signifies that the corresponding mode is poorly excited, whereas a numerically large value means that the mode is strongly excited. Table 2 shows participation factors for some of the more important modes of the cable of our example for an axial movement of an end point. The symmetrical low-order in-plane modes and the axial modes dominate when excited by a horizontal movement of the end point. Out-of-plane modes and anti-symmetrical modes are less important and can, in general, be disregarded in the model.

Using the state-space model, it is straightforward to determine frequency responses illustrating cable performance (Andersen & Enmark 2011). From a scalar input, $w$, to a scalar output, $y$, of the state-space model, the frequency response is

$$G(s) = \frac{y(s)}{w(s)} = \mathbf{C}\left(\mathbf{sI} - \mathbf{A}\right)^{\mathbf{-1}}\mathbf{B} + \mathbf{D} \tag{6}$$

where $\mathbf{C}$ for the single-input-single-output case has only one row, $\mathbf{B}$ only one column, and $\mathbf{D}$ only one column and row (scalar). The expression can be evaluated by setting the Laplace operator $s$ to $\mathrm{i}\omega$, where $\omega$ is the angular frequency. This involves solving a set of linear equations for every frequency at which the frequency response is evaluated. We shall use this expression below.

## 5. Wind Load

Wind will act on the cable/gondola system in two ways, on the gondola and on the suspension cables. To study the wind load on the gondola, outset may be taken in a wind velocity spectrum. We choose a von Karman spectrum (Andersen & Enmark 2011):

$$S(\nu) = \sigma_v^2 \times \frac{4L_{\mathrm{v}}}{\bar{v}} \times \frac{1}{\left(1 + 70.7\left(\nu L_{\mathrm{v}}/\bar{v}\right)^2\right)^{5/6}} \,,$$

where $L_{\mathrm{v}}$ is the *integral scale of turbulence* for longitudinal fluctuations (sometimes also called the outer scale of turbulence), $\bar{v}$ the mean air velocity, $\nu$ the frequency, and $\sigma_v^2$ the turbulence variance. The integral scale of turbulence sets the corner frequency between the Kolmogorov drop-off and the flat part of the spectrum.

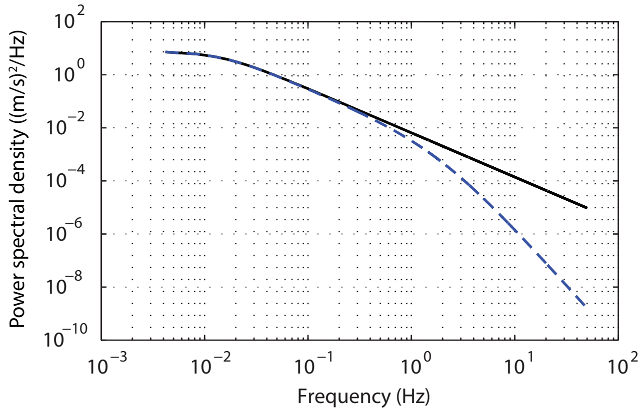


Figure 6.: *Wind velocity power spectral density with values applied for the example. The solid curve does not include cutoff due to high-frequency spatial filtering but the dashed curve does.*

Figure 6 shows the spectrum for the typical values $\bar{v} = 3$ m/s and $L_{\rm v} = 25$ m. The dashed curve includes a weighting factor to account for the high-frequency drop due to lack of coherence over the gondola:

$$\chi = \frac{1}{1 + \left(\frac{\nu}{\nu_{\rm c}}\right)^{4/3}} \tag{7}$$

where

$$\nu_{\rm c} = \frac{\bar{v}}{2l_{\rm s}} \approx \frac{\bar{v}}{2\sqrt{A_{\rm c}}} \ ,$$

where $\bar{v}$ as before is the mean velocity, $l_{\rm s}$ is a characteristic gondola dimension and $A_{\rm c}$ a representative cross sectional area of the gondola. For our example, we used $A_{\rm c} = 0.6$ m$^2$.

The wind force power spectrum can be determined from the wind velocity spectrum (Andersen & Enmark 2011)

$$S_{force}(\nu) = C_{\rm d} \left(\rho_{\rm air}\bar{v}\right)^2 S(\nu) \ .$$

where $C_{\rm d}$ is the drag coefficient of the gondola and $\rho_{\rm air}$ the air density.

The power spectral density of the gondola excursion due to wind load can then be determined from

$$S_{\rm disp}(\nu) = |F(\nu)|^2 \, S_{\rm force}(\nu)$$

where $F(\nu)$ is the frequency response from gondola wind force to gondola displacement. The variance can be found as the area under the power spectral density curve.

There is also a wind load on the cables, potentially exciting in-plane eigenmodes by local, dynamical airflow in vertical direction with eddy sizes in the range 6-30 m. Also, the wind flow may generate flutter by vortex shedding, which will be in the range 100-600 Hz. Due to lack of spatial coherence and the filtering effect of the cable, this will only be an issue near the gondola. This effect has so far not been studied in detail.

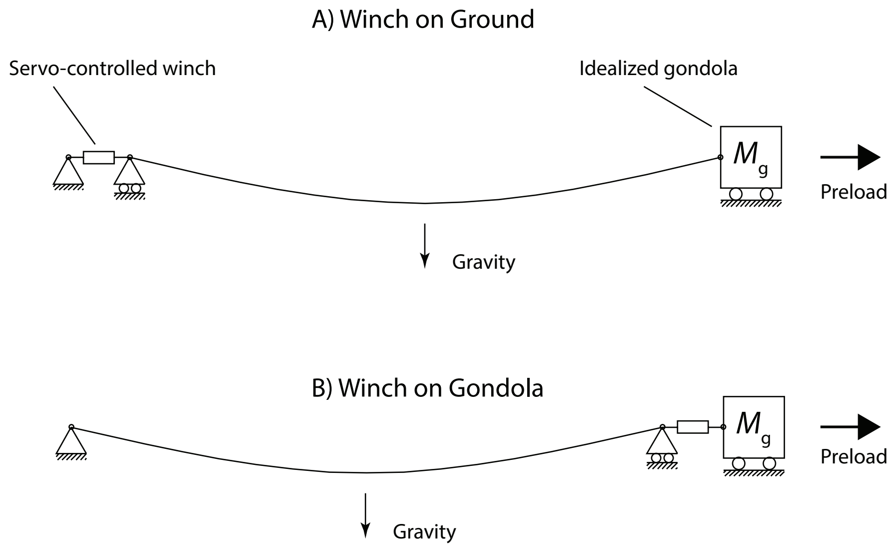


Figure 7.: *Generic gondola suspension model with only one cable to study the influence of design parameters.*

## 6. Design Parameter Selection

### 6.1 Generic Gondola Suspension Model

We now study the influence of various design parameters when using one or more cables for position control of a gondola. To do so, as an abstraction, we assume that the gondola is suspended by a single horizontal cable as shown in A) of Fig. 7. For our example, the gondola mass is taken to be 50 kg and the preload as before 1344 N. The mathematical model is then equal to the state-space model of the cable with the addition of two states for velocity and position of horizontal gondola translation. The frequency response from a horizontal displacement of the left end of the cable to the horizontal position of the gondola for our example can be determined using (6) and is shown in A) of Fig. 8. We have here assumed a damping ratio of 1 percent (although this is merely a rough estimate (Yamaguchi & Jayawardena 1992).

With position feedback from the gondola, it is possible to suppress wind disturbances with a winch control loop that controls the position of the left cable end as shown in the block diagram of Fig. 9. The controller applied for our example is a pure integrator with the addition of a pole/zero notch filter to reduce the influence of the first eigenmode of the gondola suspension. The pole is adjusted to match the first eigenfrequency of the gondola suspension with a damping ratio of 0.05, and the zero is placed at 10 Hz with a damping ratio of 1. It is not possible entirely to cancel the influence of the first eigenmode, so the bandwidth achievable for the closed-loop system will be less than the first eigenfrequency of the gondola suspension system and generally in the range 0.1–1 Hz depending on the choice of various design parameters.

We now turn to a study of the choice of various design parameters using the model and example just described.

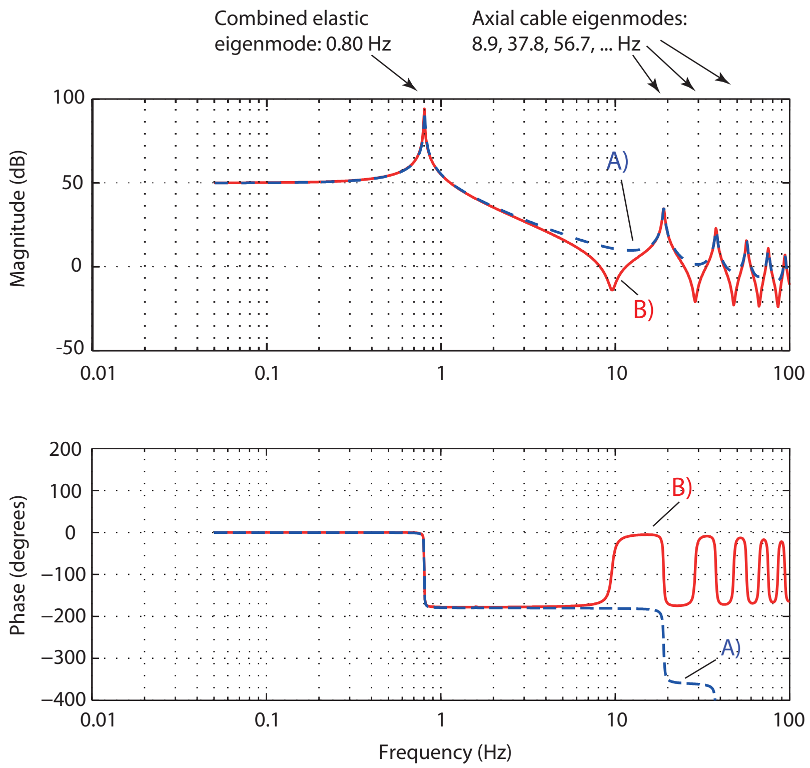


Figure 8.: *Frequency responses for the example introduced in Sect. 3.2. The curve A) takes a displacement of the left cable end as input and displacement of the gondola as output, whereas the curve B) is valid when the winch is placed on the gondola, i.e. with a displacement of the right cable end relative to the gondola.*

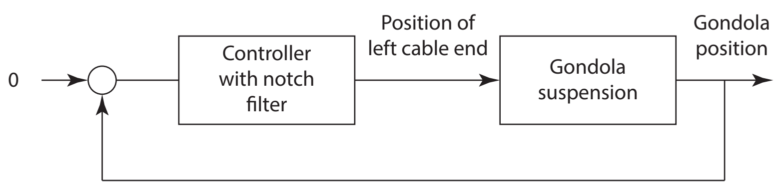


Figure 9.: *Block diagram for the winch control loop described in the text for the example introduced in Sect. 3.2.*

### 6.2 Influence of Modulus of Elasticity

We first study the influence of the cable E-modulus on performance. The E-modulus of the cable depends on the choice of material, and materials with a high E-modulus are generally more expensive than those with a lower value. It is obvious at the outset that the eigenfrequencies are important for servo control of the position of a gondola. For our example, Table 5 shows the influence of the E-modulus on the important eigenfrequencies for three different cables with the same preload but with different E-moduli. Also shown are the static stiffness values of the gondola suspension and the lowest gondola suspension eigenfrequencies.

From Table 5 it is apparent that the E-modulus of the cable should be as high as possible.

Table 5.: *Influence of E-modulus on performance. Same preload for all cases (1344 N).*

| Modulus of elasticity | (GPa) | 70 | 23.4 | 7 |
|---|---|---|---|---|
| Cable eigenfrequency of mode 2 | (Hz) | 1.59 | 1.60 | 1.64 |
| Cable eigenfrequency of mode 6 | (Hz) | 4.76 | 4.80 | 4.91 |
| Cable eigenfrequency of mode 10 | (Hz) | 7.90 | 7.96 | 8.15 |
| Cable eigenfrequency of mode 25 | (Hz) | 18.9 | 11.1 | 6.37 |
| Cable eigenfrequency of mode 62 | (Hz) | 37.8 | 22.2 | 12.7 |
| Static stiffness | (N/m) | 1024 | 346 | 109 |
| Sag | (m) | 0.121 | 0.119 | 0.114 |
| Lowest gondola eigenfrequency | (Hz) | 0.72 | 0.42 | 0.24 |
| Excursion of gondola, RMS | (mm)[1] | 18 | 63 | 196 |

[1] with wind load and closed-loop control of a 50 kg gondola

### 6.3 Choice of Preload

It is also of interest to study the influence of cable preload on performance. Obviously, cable sag depends on the preload, leading to a dependence of the geometric stiffness on preload.

As can be seen in Table 6, use of a too small preload is unattractive because of the drastic decrease in static stiffness of the gondola suspension and low eigenfrequencies. However, above a certain limit, the influence of the preload is marginal because the elastic stiffness dominates over the geometric stiffness.

### 6.4 Influence of Cable Density

Tables 7 and 8 show the influence of cable density on cable performance for our generic suspension model with some representative preloads. As long as the preload is sufficiently high, the density is not a design driver.

### 6.5 Choice of Material

Table 9 lists characteristics of some typical cable materials. With the previous results in mind, we conclude that either an aramid (such as "Kevlar") or regular

Table 6.: *Influence of preload.*

| Cable preload (N) | Length of unstressed cable (m) | Cable sag at equilib-rium (m) | Static Stiffness at end (N/m) | Lowest in-plane cable eigen-frequency (Hz) | Lowest gondola eigen-frequency (Hz) |
|---|---|---|---|---|---|
| 24200 | 183.195 | 0.601 | 9287 | 2.26 | 2.17 |
| 12100 | 184.488 | 0.121 | 9219 | 1.59 | 2.16 |
| 6056 | 185.142 | 0.243 | 9166 | 1.13 | 2.15 |
| 1363 | 185.668 | 1.081 | 7480 | 0.59 | 1.95 |
| 933 | 185.734 | 1.580 | 5380 | 0.57 | 1.65 |
| 361 | 186.000 | 4.088 | 698 | 0.55 | 0.59 |

Table 7.: *Influence of cable density. Case 1: High preload.*

| Density | ($kg/m^3$) | 1440 | 7800 |
|---|---|---|---|
| Preload | (N) | 673 | 614 |
| Sag | (m) | 0.243 | 1.271 |
| Lowest cable eigenfrequency | (Hz) | 1.13 | 0.51 |
| Static stiffness at end | (N/m) | 1019 | 956 |
| Lowest gondola eigenfrequency | (Hz) | 0.72 | 0.71 |

Table 8.: *Influence of cable density. Case 2: Low preload.*

| Density | ($kg/m^3$) | 1440 | 7800 |
|---|---|---|---|
| Preload | (N) | 40 | 174 |
| Sag | (m) | 0.851 | 5.09 |
| Lowest cable eigenfrequency | (Hz) | 0.55 | 0.49 |
| Static stiffness at end | (N/m) | 77.6 | 191 |
| Lowest gondola eigenfrequency | (Hz) | 0.49 | 0.31 |

(galvanized) steel can be applied. Polyester and polyamid, which are widespread rope materials, are not suitable for our application.

Table 9.: *Choice of material.*

| Material | Tensile strength (MPa) | Density (kg/m$^3$ | E-modulus (GPa) |
|---|---|---|---|
| Polypropylene | 60 | 930 | 5 |
| Polyester (Dacron) | 1150 | 910 | 15 |
| Polyamid (Nylon) | 1000 | 1140 | 4 |
| Aramid (Kevlar) | 3000-3500 | 1440 | 70-140 |
| Steel | 1500-2000 | 7800 | 210 |
| Stainless steel (Inox) | 500-1000 | 7850 | 200 |

### 6.6 Choice of Cable Diameter

Table 10 shows performance characteristics for our generic example for four different choices of cable diameter and some representative preloads. Obviously, there is a higher wind drag for a thick cable than for a thin cable. Also, the static gondola suspension stiffness depends on the cable diameter, and the excursions of the gondola due to wind become much higher with a thin cable than with a thick cable. Hence, the cable should be chosen as thick as possible taking into account practical aspects, such as the need for more robust adjoining structures with a thick cable and a high preload.

Table 10.: *Choice of cable diameter.*

| Cable diameter (mm) | Cable mass (kg) | Typical preload (N) | Static stiffness 6 m/s (N/m) | RMS gondola velocity[1] (mm/s) | RMS gondola excursion[1] (mm) |
|---|---|---|---|---|---|
| 1.85 | 0.72 | 1340 | 1020 | 87.5 | 19.6 |
| 3.70 | 2.88 | 5380 | 4100 | 22.3 | 2.60 |
| 5.55 | 6.47 | 12100 | 9200 | 9.4 | 0.73 |
| 7.40 | 11.5 | 21508 | 16400 | 5.3 | 0.31 |

[1] Due to wind at 6 m/s acting on gondola and closed-loop position control with winch.

### 6.7 Location of winch

The winch may be placed on the gondola instead of on the ground as shown in the generic model B) of Fig. 7. The corresponding frequency response from winch position to gondola position is shown in curve B) of Fig. 8. It is equally difficult to stabilize a control system with the winch located on the ground and on the gondola, so there is no real advantage of moving the winch to the gondola.

In addition to the approaches for gondola stabilization studied here, a fast beam steering mirror will be needed to compensate for gondola vibration. This possibility has not yet been studied in detail.

## 7. Discussion

We have set up a linear cable model using a non-linear finite element approach. Model performance agrees well with existing analytical approaches and with speed-of-sound considerations. Also, there is good agreement with the purely analytical model formulated in our previous publication (Enmark et al. 2011). The present model is however preferable due to its simplicity.

Using a cable example with a generic suspension model, we have studied the influence of design parameter selection. We conclude that the preload should be sufficiently high to ensure that the axial elasticity of the cable dominates over the geometrical elasticity. From wind considerations, we find that the wind load on the gondola dominates over wind load on the cable, although vortex shedding (flutter) may be an issue near the gondola.

Aramid and steel are suitable cable materials. The cable diameters should be as large as practically possible.

Gondola motion faster than about 1/2 fringe per millisecond cannot be detected and taken into account with a fast camera working at 1 kHz. This corresponds to 0.5-1 μm/ms in the near infrared. Although we here use a simple, very generic model, the results of Table 10 tend to suggest that the gondola velocity is too high even for short exposures ($> 5.3$ μ/ms), which could explain why no stellar fringes have been detected at the Haute-Provence observatory test site (Dejonghe et al. 2014). A closer study with a full model of all cables is on the way to establish whether this is indeed the case.

Finally, it is apparent that gondola velocity and excursions due to wind are far too high for long exposures without additional corrections, such as tip/tilt beam steering, fringe tracking, etc. It is believed that a much better gondola stability can be obtained using servo-controlled reaction wheels and reaction masses on board the gondola with appropriate angular and linear gondola acceleration, velocity and position feedback. Gyros and accelerometers may be needed. A further study of this possibility is planned.

## References

Kamran Ahmadi-Kashani 1983, Development of cable elements and their applications in the analysis of cable structures. PhD thesis, Division of Structural Engineering, Department of Civil and Structural Engineering, University of Manchester, Institute of Science and Technology.

Torben Andersen and Anita Enmark 2011, Integrated Modeling of Telescopes, Springer.

H. Le Coroller, J. Dejonghe, et al. 2012, “Tests with a Carlina-type Diluted Telescope. Primary Coherencing”, A&A, vol. 539, no. A59, 17pp.

J. Dejonghe et al. 2014, “The Carlina Diluted Telescope: A new class of interferometer. Opto-mechanical design and results of the OHP experiment”, in Proceedings of Haute Provence Observatory Colloquium (23-27 September 2013), L. Arnold, H. Le Coroller, and J. Surdej, eds.

Y. M. Desai, N. Pipplewell, A. H. Shah, and D. N. Buragohain 1988, “Geometric nonlinear static analysis of cable supported structures”, Computers & Structures, vol. 29, no. 6, pp. 1001-1009.

A. Enmark, T. Andersen, M. Owner-Petersen, R. Chakraborty, and A. Labeyrie 2011, "Integrated model of the Carlina Telescope", in Integrated Modeling of Complex Optomechanical Systems, vol. 8336, pp. 83360J-83360J-14.

M.I. Gambhir and Barrington de V. Batchelor 1977, "A finite element for 3-D prestressed cablenets", International Journal for Numerical Methods in Engineering, vol. 11, pp. 1699-1718.

W. M. Henghold and J. J. Russell 1976, "Equilibrium and natural frequencies of cable structures (a nonlinear finite element approach)", Computers & Structures, vol. 6, pp. 267-271.

H. Max Irvine 1981, Cable Structures, The MIT Press.

H. B. Jayaraman and W. C. Knudson 1981, "A curved element for the analysis of cable structures", Computers & Structures, vol. 14, no. 3-4, pp. 325-333.

Robert Levy and William R. Spillers 2003, Analysis of Geometrically Nonlinear Structures. Kluwer Academic Publishers, 2nd ed.

Haluk Ozdemir 1979, "A finite element approach for cable problems", International Journal of Solids and Structures, vol. 15, pp. 427-437.

Wei-Xin Ren, Meng-Gang Huang, and Wei-Hua Hu 2008, "A parabolic cable element for static analysis of cable structures", International Journal for Computer-Aided Engineering and Software, vol. 25, no. 4, pp. 366-384.

H.-J. Schek 1974, "The force density method for form finding and computation of general networks", Computer Methods in Applied Mechanics and Engineering, vol. 3, pp. 115-134.

U. Starossek 1994, "Cable Dynamics - A Review", Structural Engineering International, vol. 3, pp. 171-176.

Ivar Talvik 2001, "Finite element modelling of cable networks with flexible supports", Computers & Structures, vol. 79, pp. 2443-2450.

Gunnar Tibert 1999, Numerical Analyses of Cable Roof Structures. TRITA-BKN Bulletin 46, Kungl. Tekniska Hoögskolan, Institionen för Byggkonstruktion.

Hirold Yamaguchi and Loranjana Jayawardena 1992, "Analytical estimation of structural damping in cable structures", Journal of Wind Engineering and Industrial Aerodynamics, vol. 41-44, pp. 1961-1972.

*Improving the performances of current optical interferometers & future designs*
*Proceedings of Haute Provence Observatory Colloquium (23-27 September 2013)*
*Edited by L. Arnold, H. Le Coroller & J. Surdej*

# OHANA

J. Woillez[1], G. Perrin[2], O. Lai[3,4], F. Reynaud[5], M. Baril[6], Y. Dong[7], P. Fédou[2], T. Kotani[8], S. Vergnole[5], P. Wizinowich[9]

[1] *European Southern Observatory, Karl-Schwarzschild-Str. 2, Garching bei München D-85748, Germany*

[2] *Observatoire de Paris, 5 Place Jules Janssen, F-92190 Meudon, France*

[3] *Gemini Observatory, 670 N. A'ohoku Place, Hilo, HI 96720, USA*

[4] *National Astronomical Observatory of Japan, 650 North A'ohoku Place, Hilo, HI 96720, USA*

[5] *XLIM, 123 avenue Albert Thomas, F-87060 Limoges, France*

[6] *Canada-France-Hawaii Telescope, 65-1238 Mamalahoa Hwy, KAMUELA HI 96743, USA*

[7] *Laboratoire de Physique des Plasmas, École Polytechnique, F-91128 Palaiseau, France*

[8] *National Astronomical Observatory of Japan, 2-21-1 Osawa, Mitaka, Tokyo 181-8588, Japan*

[9] *W. M. Keck Observatory, 65-1120 Mamalahoa Hwy, KAMUELA HI 96743, USA*

**Abstract.** The Optical Hawaiian Array for Nanoradian Astronomy (OHANA) project aims to convert the large adaptive optics equipped telescopes present on top of Mauna Kea into a long-baseline optical interferometer. This contribution gives a brief overview of the timeline and key achievements of the OHANA project, since the Mariotti et al. (1996) founding paper.

## 1. 2000-2006: Components construction and qualification

Obtained in 1999, the first public funding for the project allowed gathering support from the Mauna Kea observatories and start the construction of the components for a demonstrator of the OHANA concept. The first delivered components, an engineering grade NICMOS camera and an optomechanical interface between short single-mode fibers covering the J, H, and K bands, were used to test, in 2002-2003, the adaptive optics coupling performance with the fibers on the Keck, Gemini, and Canada-France-Hawaii telescopes (Woillez et al. 2003, 2004). In parallel, 300 meter-long dispersion-balanced fiber pairs were produced and qualified, at Le Verre Fluoré and Observatoire de Paris for the K-band fluoride glass single mode fibers (Kotani et al. 2005), and at XLIM and Observatoire de Paris for the J-band and H-band polarisation-maintaining fibers (Vergnole et al. 2004, 2005). A beam-combiner, capable of measuring interference and photometric signals due to the combination of co-axial fiber coupler followed by a multi-axial recombination stage, was developed and tested on sky with three technical runs, carried out between 2003 and 2006 on the IOTA interferometer. Finally, Observatoire de Paris (LESIA and GEPI) and INSU technical division completed the construction of a delay line providing an optical delay of 50 meter. This delay line was then shipped for installation at the Canada-France-Hawaii Telescope at the beginning of 2006. At that time, all the components needed for a demonstration between the Canada-France-Hawaii and the Gemini telescopes were ready to be assembled.

## 2. 2004-2009: First fringes on the Keck Interferometer

In the meantime, with coupling tests between adaptive optics and single-mode fibers completed and a pair of 300-meter-long K-band single-mode fibers available and qualified, the project was offered to perform a demonstration on the Keck Interferometer. The goal was to use these single-mode fibers to link the adaptive optics at the Nasmyth focus of the two Keck Telescopes to the already operational interferometric basement, bypassing the existing Keck Interferometer coudé and optical train. The fiber length exceeded the need of an 85 meter baseline: it could have been used on a $\sim 500$ meter baseline. Following an initial installation in August 2008, and two weathered-out attempts in December 2004 and January 2005, first stellar interference fringes by long coherent transport through single-mode fibers were obtained on June 17, 2005 (Perrin et al. 2006). Between 2006 and 2009, two out of four additional attempts to improve on this demonstration were lost to weather. One may have been lost to crossed polarisations resulting from an overlooked difference in the alignment of polarisation in double-pass and single-pass (respectively, laboratory and sky configurations). A final night was lost to operational problem with the adaptive optics. At the end of 2009, the focus of the project shifted to the OHANA Iki on-sky demonstration, hosted by the Canada-France-Hawaii Telescope.

## 3. 2007-2011: OHANA Iki demonstrator

Before embarking directly into the planned connection between the Canada-France-Hawaii and Gemini telescopes, it was considered more prudent to validate on sky using smaller telescopes the individual components assembled in a complete interferometric setup. This is how the OHANA Iki project was born. Two off-the-shelves 20 cm telescopes were equipped with tip/tilt guiders in order to feed the 300 meter long fiber pairs, connected to the delay line installed inside the Canada-France-Hawaii Telescope coudé room, itself linked with short fibers to the beam combiner. The details and first calibrated contrast measurements obtained with this setup in the summer of 2010 are the topic of a publication in preparation.

## 4. Conclusion

The OHANA project was designed in 3 phases: a phase to demonstrate fiber injection at the large telescopes at Mauna Kea, a phase to demonstrate interferometric coupling with long lengths of fibers, and a final phase to build the full OHANA array. The prototypes were made to address the first two phases. Long baseline interferometry with coherent transport of light with fibers was demonstrated with the Keck telescopes and the OHANA Iki experiment using both fluoride glass standard fibers in the K band and silica polarization maintaining fibers in the J and H bands. Those experiments have established fibers as possible candidates to coherently transport light in long baseline interferometers but they have also shown their sensitivity to vibrations. An operational facility would require both mechanical and temperature sensitivities to be tackled with either passive or active systems.

## References

Mariotti, J.-M., Coudé du Foresto, V., Perrin, G., Zhao, P., & Léna, P. 1996, A&AS, 116, 381

Woillez, J., Guerin, J., Perrin, G., et al. 2003, Proc. SPIE, 4838, 1341

Vergnole, S., Delage, L., & Reynaud, F. 2004, Optics Communications, 232, 31

Woillez, J., Perrin, G., Guerin, J., et al. 2004, Proc. SPIE, 5491, 1425

Kotani, T., Perrin, G., Vergnole, S., Woillez, J., & Guerin, J. 2005, Appl.Optics, 44, 5029

Vergnole, S., Kotani, T., Perrin, G., Delage, L., & Reynaud, F. 2005, Optics Communications, 251, 115

Perrin, G., Woillez, J., Lai, O., et al. 2006, Science, 311, 194

Table 1.: *Timeline of the OHANA project*

| | |
|---|---|
| | **Injection tests on Mauna Kea** |
| 2002.08 | CFHT |
| 2002.12 | WMKO |
| 2003.07 | Gemini |
| | **Beam combiner test at IOTA** |
| 2003.06 | First run |
| 2004.10 | Second run |
| 2006.06 | Third run (last IOTA run) |
| | **Keck Interferometer demonstration** |
| 2004.08 | Installation |
| 2004.12.01 | Weathered out |
| 2005.01.31 | Weathered out |
| 2005.06.17 | First fringes on 17 Her (K=4.6) |
| 2006.05.08 | No fringes, polarizations might have been crossed |
| 2007.11.19 | Lost to high humidity |
| 2009.03.07 | Weathered out (guest J. Cavé) |
| 2009.08.09 | Failed to inject in fibers (guest M. Perrin) |
| | **OHANA Iki demonstration** |
| 2007.04 | Delay line installation |
| 2008.04-07 | CFHT-Gemini baseline measurement |
| | (internship: B. Lenoir) |
| 2009.04-05 | Delay line commissioning |
| 2009.04-07 | IKI telescope injection tests |
| | (internship: F. Bouchacourt, G. Zahariade) |
| 2010.04-07 | IKI fringes |
| | (internship: Y. Dong) |

Figure 1.: *A picture showing the Keck Interferometer in the back, and the two OHANA Iki telescopes in the front.*

*Improving the performances of current optical interferometers & future designs*
*Proceedings of Haute Provence Observatory Colloquium (23-27 September 2013)*
*Edited by L. Arnold, H. Le Coroller & J. Surdej*

# Heterodyne Interferometry in InfraRed at OCA-Calern Observatory in the seventies

J. Gay[1] & Y. Rabbia[1]

[1] *Observatoire de la Côte d'Azur, UMR CNRS Lagrange, Nice, France*

**Abstract.** We report on various works carried four decades ago, so as to develop Heterodyne Interferometry in InfraRed (10 $\mu$m) at Calern Observatory (OCA, France), by building an experiment, whose the acronym "SOIRDETE" means "Synthese d'Ouverture en InfraRouge par Detection hETErodyne". Scientific and technical contexts by this time are recalled, as well as basic principles of heterodyne interferometry. The preliminary works and the SOIRDETE experiment are briefly described. Short comments are given in conclusion regarding the difficulties which have prevented the full success of the SOIRDETE experiment.

## 1. Scientific context and technical constraints for InfraRed in the early seventies

InfraRed surveys obtained from ground-based observations have revealed bright sources in this spectral domain, while they were faint or unknown in the visible domain. They are interpreted as stars surrounded by residual matter from a protostellar cloud, which partially (or even totally) absorbs the light from the central star. This circumstellar environment (cooler than the star) radiates in the InfraRed domain, the absorbed energy. The geometry of the stellar environment being unknown (in particular its angular diameter), modeling the radiation processes of these new sources has then become an open issue. An immediate problem was that available facilities and equipments in InfraRed by that time, did not allow measuring these angular diameters which are less than 1 arcsec, (considered at this time as the smallest resolvable angle). Imaging in this range of angular resolution would have needed telescopes with such large diameters as 8m to 10 m (not even in project at that time), adaptive optics systems (yet not defined or not implemented) and bi-dimensional detectors like CCD or CID devices (at the beginning of their forthcoming development). A possible approach for direct imaging could have been the technique of Imaging by Multiplex Encoding (Girard 1970, de Batz et al. 1977), but if it avoids the need for two-dimensional detectors, it does not avoid the need for such large telescopes.

Observation relying on interferometry (which can work with a few small telescopes) appeared then as the only way to reach the angular resolution required for the targeted angular diameters.

Stellar Interferometry basically relies on the measure of the degree of coherence between fields collected by independent telescopes, at several separations and on the use of the Van Cittert and Zernike theorem (Born & Wolf 1975, Rabbia 2005). In other words, it consists of determining discrete values of the spatial spectrum of the source (the Fourier Transform of its brightness distribution).

In InfraRed, two approaches could have been considered: either direct interferometry by mixing optical beams from two telescopes on a unique detector, or heterodyne interferometry, which is transposing to this spectral domain the technique already used by radio astronomers, preserving the phase of the collected fiels and reducing the effect of the huge thermal background from the sky (actually a foreground).

In the InfraRed and visible domains, detection of light is quadratic (incoherent detection). In other words, only the energy conveyed by the electromagnetic field can be recorded, and not its phase, which is the key-information searched for. Direct interferometry (basically a Young's hole scheme), by receiving on the same quadratic detector, two fields collected on separate telescopes, allows in principle to follow the variation of their phase differences (reflecting their optical path differences - hereafter OPD-, continuously changing as the source travels across the sky because of diurnal motion).

Unfortunately this phase difference, highly sensitive to optical paths changes, can not be extracted because a strong spurious phase noise is added by the permanent and random unstabilities caused by the atmosphere and by the instrumental configuration itself. Thus, this approach requires a very demanding control of metrology (OPD's must be less than a fraction of a wavelength) and needs specific techniques (for example fast fast OPD modulation or/and a servo-controlled confiuration, to compensate for unstabilities). Yet, direct interferometry with small telecopes has proven to be efficient in near InfraRed (Mac Carthy et al. 1977, diBenedetto & Rabbia 1987), and in the visible domain (Shao & Staelin 1980, Robbe et al. 1997).

The other choice, the heterodyne approach, is not (at 10 $\mu m$) too much perturbated by turbulence and is greatly relaxing the metrology demands. It has motivated to launch two projects in the early seventies, one at Mount Wilson by the Berkeley University, CA, USA (Johnson et al. 1974), the other (Gay & Journet 1975) at OCA (named CERGA at this time).

## 2. Basic principles of the heterodyne technique

The main feature of this technique is to transpose the frequency of the two collected fields, into a much lower one (so as to allow transmission by cable), while preserving the phase information for each field. This is achieved by receiving on a mono-pixel detector (one for each telescope), a reference field and the collected field. The reference field is named the local oscillator (LO in the following). In our case, it is the light from a CO2 laser around 10 $\mu$m). For each frequency composing the incoherent field from the source, an interference process occurs, giving a "beat" signal at a much lower frequency than the one of the fields. The process is described (broad lines) by the sequence of steps listed here below:
One detector at each telescope. Each detector receives LO and the collected field. Superposition of incident fields made by using a BeamSplitter plate with appropriate coefficients for transmission and reflection (LO must be attenuated).

Quadratic detection (time averaged square modulus of the sum of complex amplitudes) Amplification and low-pass filtering. The signals at output are conveyed by cable to a "mixing element" (correlator) delivering a signal proportional to their product, within which the phase difference $\Delta\phi(t) = \phi_1(t) - \phi_2(t)$ between collected fields is preserved. Another appropriate low-pass filtering is performed (for example by a phase-lock amplifier) delivering a signal proportional to the cosine of $\Delta\phi$ which ( as already mentioned) varies with respect to time because the source moves across the sky. The process is summarized by the mathematical expressions given below, with indexes "0" and "$*$" respectively for the local oscillator and for the collected field , and is illustrated on Figure 1. The expression of the signal from each detector writes:

$$s(t) \propto \mid A_0 \times exp(i\ \omega_0\ t) + A_* \times exp[i(\omega_*\ t + \phi)] \mid^2$$

where the brackets mean here "filtering by the detection chain". After filtering s(t) by the DC blocking capacitor and the bandpass amplifier, we have the so-called heterodyne signal:

$$s_h \propto A_0 \times A_* \times \cos[(\omega_0 - \omega_*)t + \phi].$$

The term at frequency $(\omega_0 + \omega_*)$, expected from algebra, will be eventually filtered in the detection chain. Now we have two heterodyne signals (from two collected fields) sent to the "mixer" which delivers the correlation signal C(t):

$$C(t) \propto A_0 \times A_* \times \Big( \cos[2(\omega_0 - \omega_*)t + \phi_1 + \phi_2] + \cos(\phi_1 - \phi_2) \Big).$$

This correlation signal is then filtered (low pass) so that we obtain the final output signal $V(t)$:

$$V(t) \propto A_0 \times A_* \times \cos[\phi_1(t) - \phi_2(t)] \tag{1}$$

where indexes 1 and 2 refer to the telescopes. The frequency of this signal is related to the motion of the source across the sky. A Synchronous Detection device (in-phase and in-quadrature) tuned to the frequency of the fringe signal might be used to follow the fringes, in spite of turbulence effects and to achieve the last filtering. An alternative configuration uses a simple low-pass filtering and a spectrum analyzer. The process (simplified) is schematically illustrated in Figure 1, where DL means Delay Line, used to compensate for the OPD's between collected field, and LPF stands for Low Pass Filter, SA for spectrum analyser.

Not appearing in equation (1) are the beamsplitter coefficients (implicitly included in amplitudes $A_0$ and $A_*$) and the "degree of coherence $\gamma_{12}$" between collected fields, named "visibility", which samples the spatial spectrum of the source,( one sample for each separation of telescopes). From these data, via the "Van Cittert and Zernike" theorem, angular parameters of the source can be calculated. The proportionality factor also comprises the quantum efficiency of the detector and the energy of the photon at frequency $\nu_0$ (local oscillator).

The source has a large spectral distribution so that the heterodyne signal $s_h(t)$ covers a finite spectral interval resulting from the bandpass of the system [detector, DC blocking capacitor, amplifier]. This is schematically illustrated also

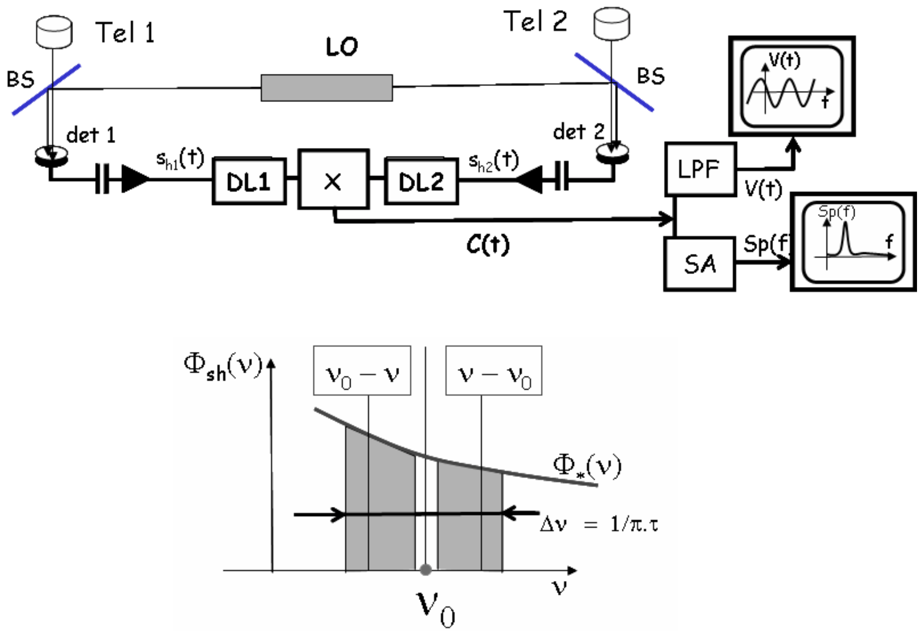


Figure 1.: *Generic set-up and spectral band of work.DL: delay line, LPF: Low Pass Filter, SA: Spectrum Analyzer, $\Phi_*(\nu)$: source's spectrum.*

in Figure 1. Note that more than two telescopes can be used at the same time what enables to simultaneously collect several values of the spatial spectrum.

A critical point is the Signal to Noise Ratio (SNR from now). We simply recall here its expression (Assus et al. 1979):

$$SNR = \frac{\eta}{h\ \nu_0} \times F(\nu_0) \times S \times \sqrt{B \times T} \tag{2}$$

where $\eta$ is the quantum efficiency of the detector, $F(\nu_0)$ is the flux of the source at frequency $\nu_0$, S is the collecting area, B is the electrical bandwidth of the detection chain, and T is the time duration of observation.

## 3. Preliminary works

We give short descriptions of the set-up and of obtained records for three preliminary observations to prepare the SOIRDETE experiment, which will be described in the next section

### 3.1 Heterodyne detection in laboratory with a blackbody

The first preliminary work naturally is the detection of a source in the laboratory. The aim of this work is to implement an optical set-up and to test the detection chain (Gay et al. 1973).

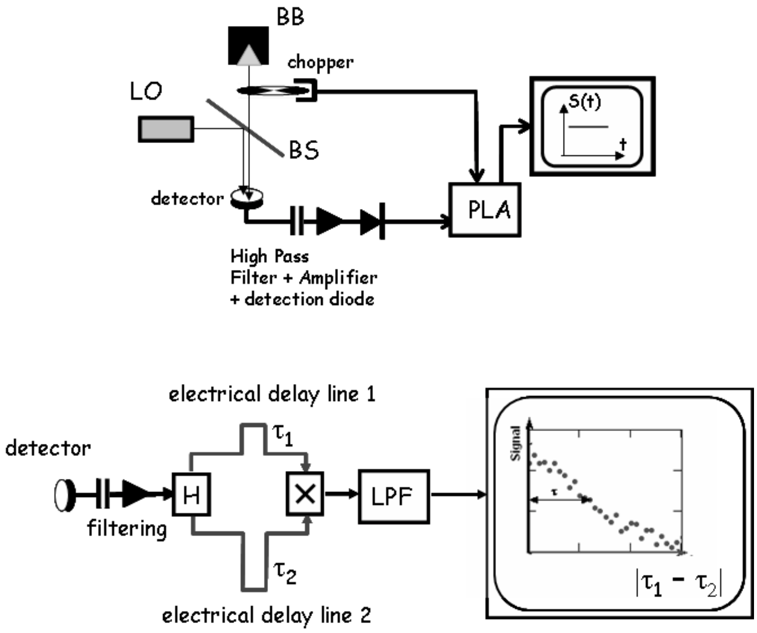


Figure 2.: *Heterodyne detection of a blackbody: detection set-up and auxiliary set-up to measure response time.*

This also allows to optimize adjustments of parameters and to identify from them a standard protocol for handling the set-up. In addition, an auxiliary set-up has been mounted to measure the effective response time of the detection chain, by recording a correlation curve obtained from various phase differences inserted by variable delay lines. The confrontation of the theoretically expectable SNR against the really obtained SNR has proven satisfying. In Figure 2 is shown a schematic description of the generic and the auxiliary configurations.

### 3.2 Heterodyne interferometry with the Sun

This work essentially aimed at illustrating the principle of the heterodyne interferometry approach and has been seen as a demonstrator, showing a slowly drawn fringe pattern, and needing only a small and simple set-up which does not require components with high performance and large dimension (Gay & Journet 1973).

Actually the interferometer could have been accommodated within the hand, and the variable baseline operated manually. Figure 3 shows a schematic description of the set-up, and a record of the fringe signal versus time. Several recorded fringes and the associated visibility curve drawn on paper (at that time, the communication tools was pretty rustic) are shown in Figure 6 at the end of the paper.

### 3.3 Heterodyne detection of Arcturus ($\alpha$ Bootis)

The next step in preliminary works was the heterodyne detection of a star (Arcturus, $\alpha$ Bootis). This has been done using the 1.52 m telescope at the Observa-

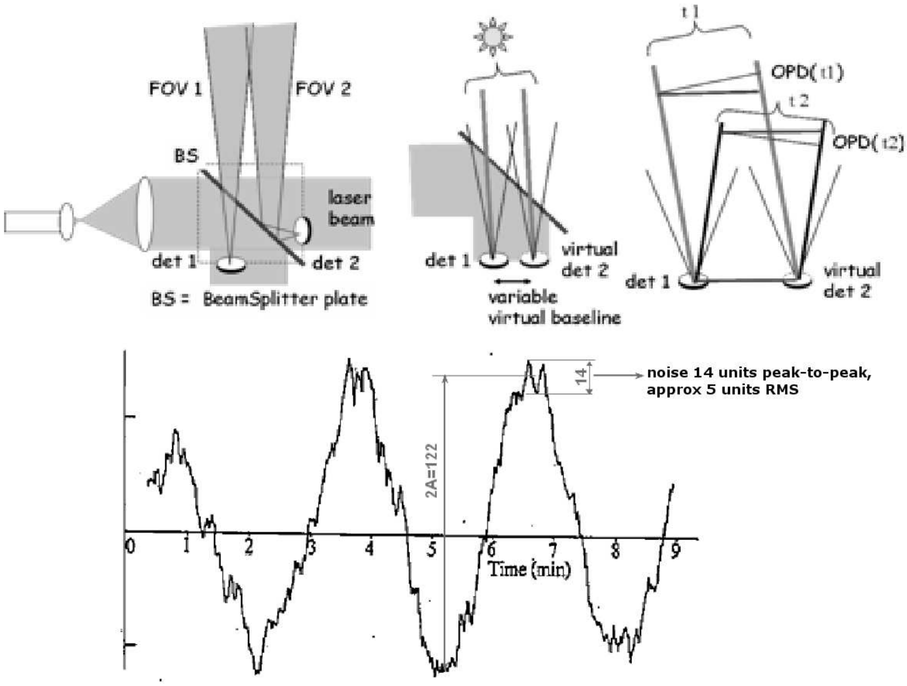


Figure 3.: *Heterodyne interferometry on the Sun, set-up and recording of fringe amplitude. Noise is* $\approx$ *14 units peak-to-peak, thus RMS noise* $\approx 14/3 \approx 5$ *and SNR* $\approx (122/0.62)/(14/3) \approx 40$ *for visibility V=1 (V=0.62 for solar radius=900 arcsec and baseline=0.75 mm at* $\lambda = 11\mu m$*).*

toire de Haute Provence, France (de Batz et al 1973). Figure 4 shows a recorded trace of the detection.

## 4. The SOIRDETE experiment

We list here some instrumental features:

• *Telescopes*: two 1 m telescopes, baseline 15 m East-West, what induces change of baseline length seen from the source from 3 m up to 15 m (supersynthesis).
• *Local Oscillator*: CO2 laser, tuned on CO line P56. This apparently interesting line (faintly absorbed by atmosphere) has been the cause of LO instabilities, preventing permanent capability of detection.
• *Detectors*: cooled HeCdTe photodiodes (liquid nitrogen).
• *Amplifier*: electrical bandwidth 5-500 MHz. This comparatively narrow bandwidth allows comfortable coherence length (about 30 cm) but it is detrimental to the SNR.
• Delay lines: set of switchable coaxial lines of various lengths, under computer control.
• *Site*: Calern observatory, a chalk plateau (altitude 1200 m), poor atmospheric seeing in average.

Figure 1, already shown, describes the instrumental functions, while Figure 5 shows the polaroid photograph (displayed as "negative") of the spectrum of the

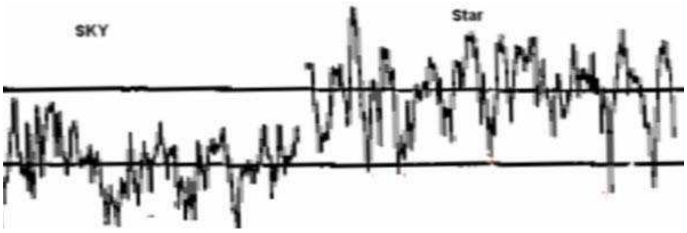


Figure 4.: *Heterodyne detection of Arcturus ($\alpha$ Bootis).*

first fringe signal obtained on Betelgeuse ($\alpha$ Orionis) in August 1978. On the figure 5, the mark $F_0$ indicates the frequency of the fringe signal.

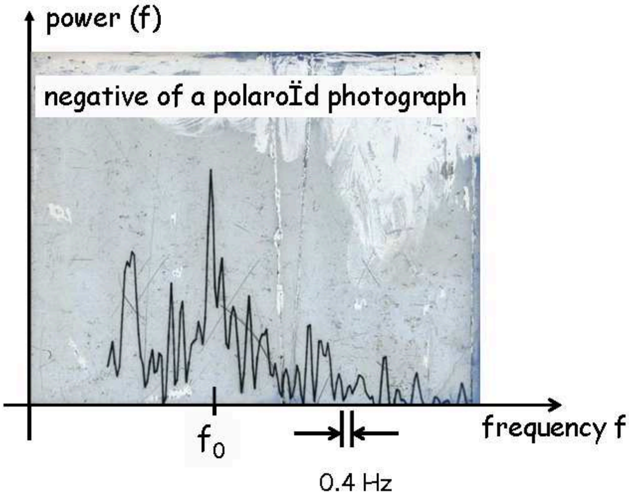


Figure 5.: *Spectral signature of the first fringes obtained on Betelgeuse ($\alpha$ Orionis).*

## 5. Conclusion

The SOIRDETE experience started in 1972, by the building of two domes, two telescopes and the central laboratory, followed by the progressive implementation of the whole experimental configuration in parallel with some preliminary works. The development has been exceedingly long lasting (more than a decade) what gave time to many failures to occur, distributed over the years and over the whole panoply of the numerous components (some being second hand from lend). The last one, putting an end to the experiment, has been an accident which destroyed the laser, the heart of the system. Among the adverse causes can be noted the frequency unstability of the LO, a bad impedance adaption between the detection

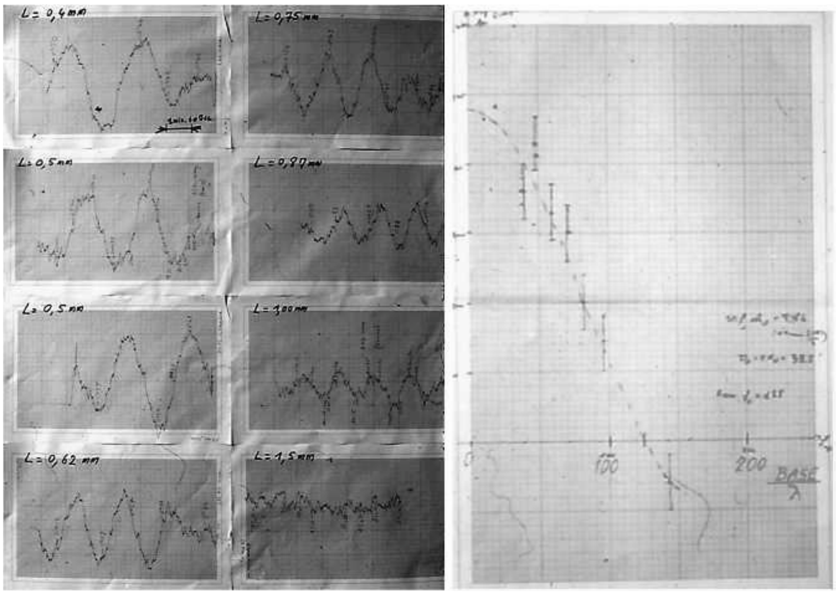


Figure 6.: *Fringes obtained with the Sun as a source, recorded on paper and the resulting visibility curve.*

photodiode and the amplifier (preventing the energy of collected photons to be efficiently transferred) and the rather narrow bandpass of the amplifier, which is (though advantageous regarding the coherence length), correlatively detrimental to the SNR and to the detection capabilities.

Globally it might be noted that in the seventies, modern methods for project management were not popular and not yet well-known. In addition, the pioneering and exploratory nature of SOIRDETE makes them not really applicable in the context, and this has probably been unfortunate. Actually, a detailed analysis of the adverse effects is beyond the scope of this short reminder on the history of SOIRDETE. Today, most of the equipments are used for training activities for students.

Looking at the future, thanks to modern methods of project management and taking into account technological progresses, the heterodyne approach meets a new future, (not limited to InfraRed) regarding the enlargement of the bandpass of the chain, be it by using laser with comb of frequencies or multichannel amplifiers, and by working with dedicated optical fibers and specific numerical techniques.

## References

Assus, P.; Choplin, H.; Corteggiani, J. P.; Cuot, E.; Gay, J.; Journet, A.; Merlin, G.; Rabbia, Y. 1979, Journal of Optics, vol. 10, p. 345-350

Born M. & Wolf E. 1976, "Principles of Optics", Pergamon Press de Batz, B.; Granes, P.; Gay, J.; Journet, A. 1973, Nature Physical Science, Volume 245, Issue 145, pp. 89-90

de Batz, B.; Bensammar, S.; Delavaud, J.; Gay, J.; Journet, A. 1977, Infrared Physics, vol. 17, p. 305-310

di Benedetto, G. P., Rabbia, Y. 1987, A&A, vol. 188, no. 1, p. 114-124

Gay J. & Journet A. 1973, Nature 241, 32-33

Gay J., Journet A., Christophe B. & Robert M. 1973, Applied Physics Letters vol. 22, Issue 9

Girard A., 1971, in proceedings of the AGARD conference, CP-90

Johnson M.A., Betz A.L. & Townes C. H. 1974, Phys. Rev. Letters, 33,1617-1620

McCarthy, D. W.; Low, F. J.; Howell, R. 1977, Optical Engineering, vol. 16, p. 569-574

Rabbia, Y. 2006, EAS Publications Series, Volume 22, pp.293-349

Robbe, S.; Sorrente, B.; Cassaing, F.; Rabbia, Y.; Rousset, G. 1997, A&AS, Vol. 125, 367-380

Shao, M.; Staelin, D. H. 1980, Appl.Opt., vol. 19, p. 1519-1522

*Improving the performances of current optical interferometers & future designs*
*Proceedings of Haute Provence Observatory Colloquium (23-27 September 2013)*
*Edited by L. Arnold, H. Le Coroller & J. Surdej*

# Prospects of Optical Heterodyne Detection for Astronomy and One Photon Interferometry

E. le Coarer[1], A. Chalabaev[1], & G. Duvert[1]

[1] *UJF-Grenoble 1 / CNRS-INSU, Institut de Planétologie et d'Astrophysique de Grenoble, UMR 5274, 38041, Grenoble, France*

**Abstract.** Within the framework of spatial and spectral interferometry, new prospects for optical heterodyne detection in astronomy are sketched in order to take into account the emergence in recent years of frequency comb lasers, absolute time networks and dramatic progress in the field of light detection. We also describe a laboratory experiment of one photon spatial interferometry which indicates a new way to detect photons one by one by using heterodyne technic and to improve significantly the signal to noise ratio.

## 1. Introduction

The heterodyne detection for stellar interferometry in the infrared has been promoted in 1970's (see e.g. Johnson, Betz and Townes, 1977; and review by Gay, 2013 in this volume). The main motivation of the heterodyning is the hope that the signal at the resulting reduced frequency is more easy to be handled than the infrared or optical light and hence a larger baselines are possible. However, the S/N figure of direct interferometry is in general higher. The ratio of S/N of direct and heterodyne detections can be evaluated by the following relation $\frac{1300}{T_D}\sqrt{\frac{\Delta\nu_D}{\Delta\nu_H}}$, where $T_D$ is the noise temperature of the direct detection, roughly $300\,\deg K$, $\Delta\nu_D$ and $\Delta\nu_H \approx 6 \cdot 10^9 Hz$ are the bandwidths of the direct and heterodyne detections respectively (Towns and Wishnow, 2008). The interest of the heterodyne method was hence limited to a small number of special astronomical cases. Nowadays, all stellar interferometers are direct except ISI (for its latest description see Wishnow et al., 2010).

## 2. New Numbers

So far, the heterodyne detection was considered with the use of one laser. Today, one can use the laser frequency combs (Udem, Holzwarth and Haensch, 2002; Steinmetz et al, 2008). Such lasers provides several thousands lines, each of them can be separated by a R=40000 spectrometer. Individual lines may be used as local oscillator. An optical fiber carrying the signal coming from sky and another one carrying the laser signal are placed together in the slit environment in the spectral dispersion direction with a little shift in order to insure the up or down shifting according to the local oscillator. The mixing of light is then operated by the detector itself which also amplifies both signals. Each pixel of the detector is sensitive to the beating terms and acts as a heterodyne channel. A basic approach permits us to gain on the sensitivity as the square root of number of pixel used.

The stability of the frequencies can be insured by high precision metrology network Refimev+ (Refimev project, 2013). A $10^{-17}$ precision and stability can be foreseen in a local telescope network fed by black fibers systems, allowing to date every signal detection at each telescope.

The bandwidth can be as high as several $10^{12} Hz$ using MCT APD detectors acting either as photon counting devices or analog devices. Such devices are able to multiply a photoevents without adding spurious noise (Rothman 2008).

The whole measure of the light coherence can be considered in a more straight way as shows the experiment described below.

## 3. Experiment of spatial interferometry down to one photon

The major renewal of heterodyne detection could be made by the detection of photon itself. Can the mixing of a continuous very stable laser line and a single photon be detected as a single heterodyne event? The noise generated by laser as a level of $\sqrt(N)$, N number of photon in time units. The signal provided by the mixing of one photon and this laser gives a $2\sqrt(N)$ signal level. With this assertion we estimate that it is possible to separate during time an individual heterodyne events in order to record this signal only during few nanoseconds avoiding to record noise during time separating two successive events as it is done in simple photon counting. Because we have not yet demonstrate this detection scheme, we would present here an analogy based on Young interferometry. In this simple set-up of the Young experiment, the laser light is split on two beams by a Y-junction. The light emitted by the fiber end holes gives rise to the interference pattern directly on the detector. The nice system of rings comes from an importune interference on the cryostat window. The Young fringes are the vertical lines.

The high speed of the OCCAM2 detector, 1300 frames/s, makes possible to explore what happens to the Young interference when there are less and less photons per frame coming from one of the the two arms keeping the same flux in the other arm. The Fig. 1 shows the interference in the Fourier space of a very dissymmetric setup. The image of the power spectrum exhibits the expected pics of the visibility on the both side of the central maximum.

We can write the well known relation for the intensity of interference:

$$I = I_{source} + I_{laser} + 2\sqrt{I_{source} I_{laser}} \cdot cos(\omega_{laser} - \omega_{source})t \tag{1}$$

where $I_{source}$ is the light intensity in the attenuated arm of our set-up. We can also write this relation expressing intensities in units of the energy of 1 photon. For $I_{source} = 1$ in this units, we get:

$$I = 1 + I_{laser} + 2\sqrt{I_{laser}} \cdot cos(\omega_{laser} - \omega_{source})t \tag{2}$$

The noise is then $\sqrt{I_{laser}}$ and the intensity of the beat term is $2\sqrt{I_{laser}}$.

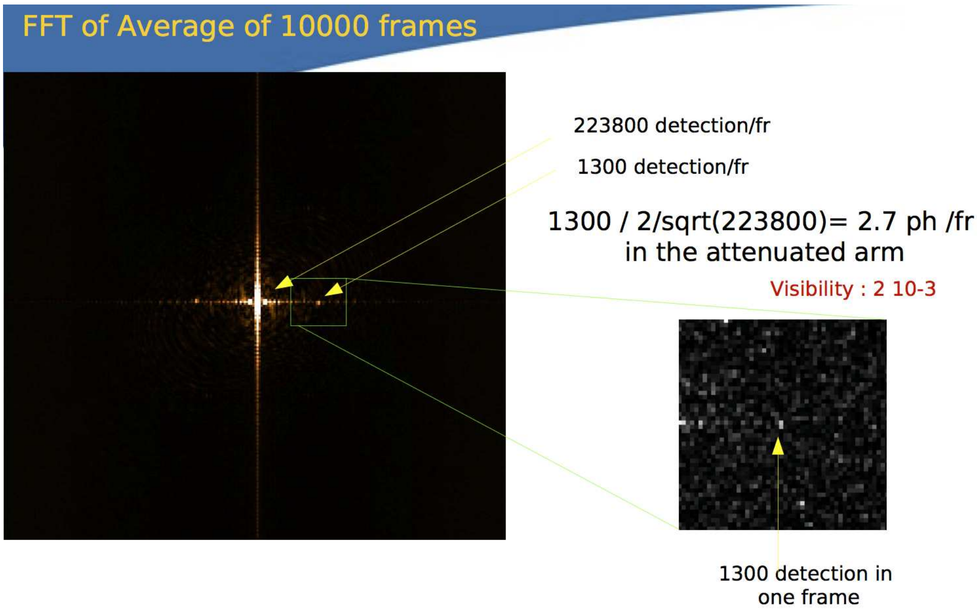


Figure 1.: *The power spectrum*

The amplitude of the central peak of this average of 10000 frames is 223800 detections/frame, that of the secondary peak is 1300 detections/frame. The amplitude of the visibility is $2 \cdot 10^{-3}$.

Given that $I_{laser} >> I_{source}$, and assuming that the detector quantum efficiency is 1, we get $I_{source} = 1300/(2\sqrt{223800}) \approx 3$ photoevents/frame. Fig. 2, we show the evolution of detections on the secondary peak as is they were solely due to the fluctuations of the number of photons in the attenuated arm: 0 photons, 1 photon, and so on. Of course, the amplitude of fluctuations of the laser contribution about 470 photoevents must also be taken into account, however this does not affect the following conclusion: We can detect 1300 photoevents/frame on the secondary peak even if there are only 3 photons in average coming from the source. We can say that the interference is not the combinatory of photons thought as solid particles and counted one by one but a phenomenon implying quanta of electro-magnetic field. One can count 1300 photoevents/frame due to the interference of a laser light with 1, 2 or 3 photon intensity source, and this is encouraging for the prospects of the heterodyne stellar interferometry in the optical and infrared.

## 4. Conclusions

So far, the heterodyne technic at near infrared and visible light domains has been considered as a dead end because of the lack of photon of astronomical sources at a GHz rate. In this communication, we described a new way to use heterodyning, namely, the detection of single photons mixed with high stabilized laser. If we

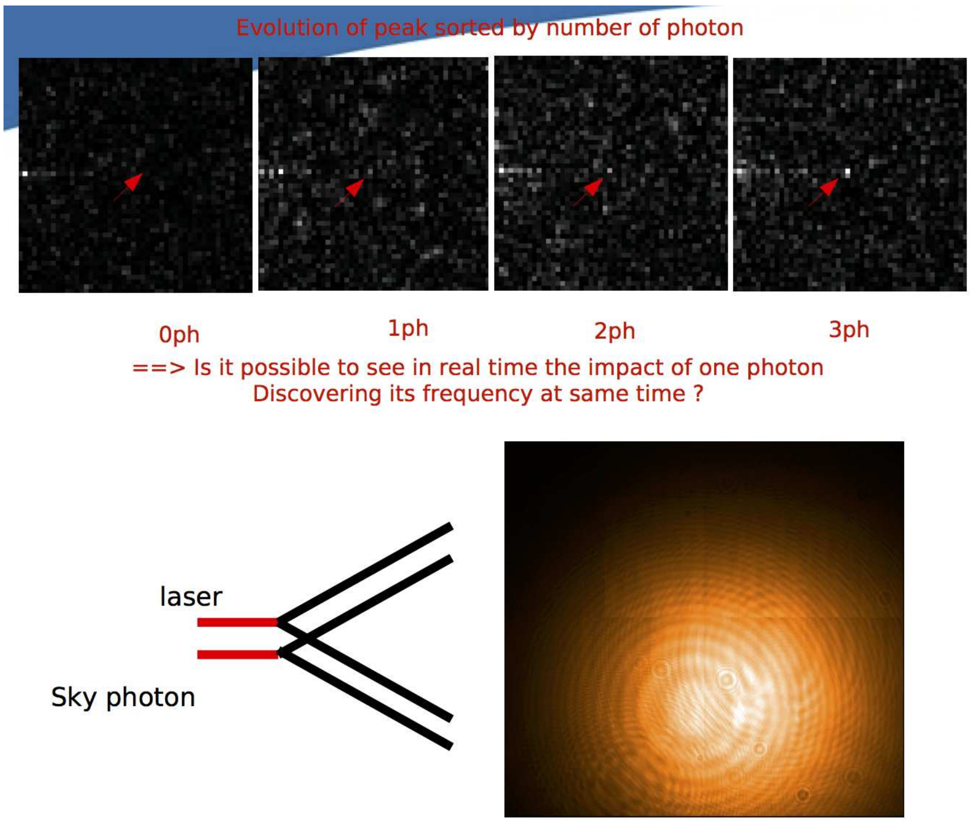


Figure 2.: *Photoevents*

are able to isolate and record the effect of individual photon, the signal to noise of heterodyne interferometry should compete with direct interferometry.

## References

Gay, J., 2013, in *Improving the performances of current optical interferometers & future designs*, colloquium held in OHP, France, September 23-27, 2013, edited by L. Arnold, H. Le Coroller & J. Surdej

Johnson, M. A. and Betz, A. L. and Townes, C. H., 1974, Physical Review Letters, 33,1617

Revimev project, http://syrte.obspm.fr/tfc/frequences_optiques/refimevep_en.php

Steinmetz, T. et al, 2008, Science, 321, 5894,1335

Townes, C. H., Wishnow, E. H., 2008, in *Optical and Infrared Interferometry*, Edited by Schöller M., Danchi W. C., Delplancke F., Proceedings of the SPIE, Volume 7013, article id. 70130D-1

Udem, Th., R. Holzwarth, T. W. Haensch, 2002, Nature 416, 233

Wishnow, E. H. et al, 2010, Proc. SPIE vol. 7734, 773409

Rothman, J., Perrais, G., Ballet, P., Mollard, L., Gout, S., & Chamonal, J. P. 2008, Latest developments of HgCdTe e-APDs at CEA LETI-Minatec, Journal of Electronic Materials, 37(9), 1303-1310.

*Improving the performances of current optical interferometers & future designs*
*Proceedings of Haute Provence Observatory Colloquium (23-27 September 2013)*
*Edited by L. Arnold, H. Le Coroller & J. Surdej*

# Diophantine optics in nulling interferometry: laboratory performances of the chessboard phase shifter

D. Rouan[1], D. Pickel[1], D. Pelat[2], J.M. Reess[1], F. Chemla[3], M. Cohen[3] & O. Dupuis[1]

[1]*LESIA - CNRS - Observatoire de Paris - UPMC - U. Paris-Diderot, Meudon, France*

[2]*LUTH - CNRS - Observatoire de Paris - U. Paris-Diderot, Meudon, France*

[3]*GEPI - CNRS - Observatoire de Paris - U. Paris-Diderot, Meudon, France*

**Abstract.** Among the techniques of very high angular resolution to isolate planetary photons from those of the star - several million times more numerous - a possible one is the nulling interferometry with several telescopes in space. This mode requires an achromatic phase shift of pi in one arm of the interferometer. We introduced several years ago the concept of quasi-achromatic phase shifter based on two chessboard mirrors, each cell introducing a phase shift determined by a mathematical law, so that the behavior of the attenuation of the star as a function of wavelength is flat in a range of more than one octave. This concept is part of broader field that we call diophantine optics and that will be first presented. We then present the experimental validation of such a concept where the chessboard phaser is synthesized using a properly controlled deformable segmented mirror from Boston micro machine with 12x12 actuators. First we introduce the principle of the "chessboard effect", then the dedicated testbench DAMNED will be described in particular the control of the phase through strioscopy. The results on the performances of the device will be presented and the ways of improvement and extension of this concept will be analyzed.

## 1. Introduction

To find one day clues of life on extra-solar planets, or at least characterize them, we need in the future to directly detect photons from exoplanets so as to obtain spectra where specific spectroscopic biomarkers could be found. Among the techniques of very high angular resolution to isolate planetary photons from those of the star - millions to billions times more numerous - a possible one is the nulling interferometry with several telescopes in space. The principle: if the star coincides with a dark fringe it is strongly attenuated, while the planet on a bright fringe is not. This mode requires an achromatic phase shift of $\pi$ in one arm of the interferometer. We introduced in 2008 the concept of a quasi-achromatic phase shifter based on two chessboard mirrors, each cell introducing a phase shift determined by a mathematical law, so that the behavior of the attenuation of the star as a function of wavelength is flat in a range of more than one octave. This concept is part of broader field that we call diophantine optics and which is first presented.

## 2. Diophantine optics

Diophantus of Alexandria is a greek mathematician, known as the father of algebra. He studied polynomial equations with integer coefficients and integer solutions such as $(x-1)(x-2) = x^2 - 3x + 2 = 0$ , called *diophantine equations.* The most famous one is the aegyptian triangle $5^2 = 4^2 + 3^2$ which allowed the builders of the pyramids to make perfectly squared monuments. What could be the relationship between optics and power of integers ? In fact, in optics, constructive or destructive interferences imply that optical path differences (*opd* in the following) are multiple integer (odd or even) of $\lambda/2$ and, besides that, the complex amplitude is a highly non-linear function of the *opd* so that any Taylor development implies powers of integers. This is where diophantine equations appear. The definition one can give of diophantine optics is *the exploitation in optics of some remarkable algebraic relations between powers of integers.* It happens that its application to techniques aiming at direct detection of exoplanets are numerous, probably because of a bias of the first author towards the field of exoplanetary sciences. The website *http://dan.rouan.free.fr/OptiqueDiophantienne/intro.html* gives (in french) a good idea of the basics and some applications, as well as litterature. In the following we give several examples where the concept of diophantine optics has been used.

### 2.1 The hard task of detecting an exoplanet directly

Because of both the extremely high contrast between the planet and the star ($10^{10}$ in visible and $10^7$ in thermal infrared) and the angular proximity of the two objects (sub-seeing), it is well established that direct detection is an extremely difficult problem. Since the mid of the 90's, two main avenues were considered to solve it: in visible/near-IR, the use of single telescope plus adaptive optics and coronagraphy (e.g. Guyon 2007) and in the thermal infrared, the use of coherent recombination of several telescopes in space in a nulling interferometric mode (Bracewell 1978; Leger & Herbst 2007; Cockell et al. 2009). Let's have a look to the kind of plus that diophantine optics can bring to each of those two techniques.

### 2.2 Achromatization of a Four-Quadrant Phase Mask Coronagraph

The Four-Quadrant Phase Mask Coronagraph (FQPMC) was introduced by one of us in 2000 (Rouan et al. 2000). In a certain sense it is already an application of diophantine optics principles since it allows to cancel out to the first order the light of an on-axis star by producing destructive interferences between four sub-beams. This is done thanks to a special component, the four-quadrant phase mask, which is made, in its basic version, of two kind of plates, one for each diagonal, with between them an *opd* difference equal to $\lambda_o/2$; steps follows in the order [0, 1, 0, 1]. A classical FQPMC is by nature chromatic: when $\lambda$ is different from $\lambda_o$ the residual intensity is proportional to $(\delta\lambda/\lambda_o)^2$. Now let's play with combinations of quadrant thicknesses (see Fig. 1) to cancel the first

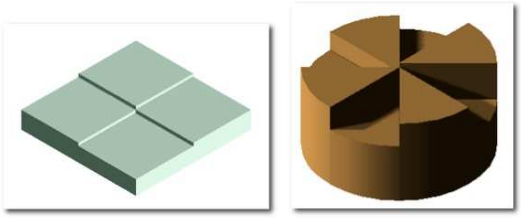

Figure 1.: *Achromatization of a 4QPMC and of a 8QPMC.*

terms of the Taylor development of the complex amplitude $a = \sum \pm \exp(jk\phi)$ where $\phi = \pi\delta\lambda/\lambda_0$ (Rouan et al. 2007). At second order, with steps [0, 1, 2, 1] we obtain $I = (\delta\lambda/\lambda_o)^4$ and at third order, a 8QPMC with steps [1, 8, 3, 6, 2, 7, 2, 7] gives $I = (\delta\lambda/\lambda_o)^6$. We have gained a lot in achromatism performances.

### 2.3 Avoiding long delay lines

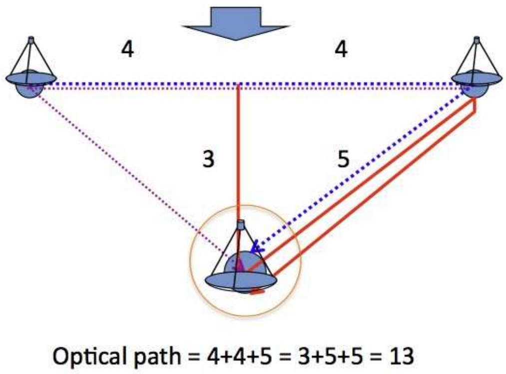


Figure 2.: *Avoiding long delay lines in a 3-telescopes nulling interferometer.*

In a 3-telescopes nulling interferometer in space, as the one proposed for the Pegase experiment (Ollivier et al. 2006), avoiding long delay lines or a fourth spacecraft for recombination is essential, and we proposed a genuine solution based on the Aegyptian triangle, as illustrated on figure 2. The idea is to install on the three spacecrafts, each carrying a telescope, mirrors that allow the light to “circulate” , so as to equalize the *opd* between the different beams before recombination on one of the spacecraft.

### 2.4 Deep nulling interferometers

In a Bracewell nulling interferometer, the stellar disk is generally resolved because of the long baseline. This leads to an uncomplete nulling of the stellar light because of leaks coming from the outer ring of the stellar disk. This is a well known problem and several configurations using more than two telescopes were

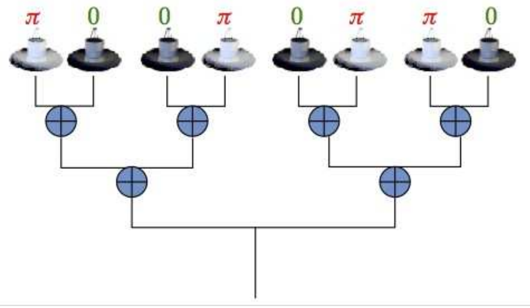


Figure 3.: *Deep nulling interferometers based on the Prouhet-Thué-Morse sequence*

proposed, such as the Angel's cross or the Mariotti's configuration which provide nulling angular function in $\theta^n$ with $n = 4$, instead of $n = 2$ in the Bracewell's configuration. There is indeed a universal rule to obtain any value of $n$ in a multi-telescopes interferometer (Rouan 2007, 2004). It consists in distributing regularly $2^L$ telescopes on a straight line and to introduce a $\pi$ phase shift to those which correspond to a "0" in the Prouhet-Thu-Morse sequence $0110100110010110\cdots$, as illustrated on Fig. 3. This sequence can be constructed recursively and has a fractal structure (Allouche & Shallit 1999). Nulling varies then as $\theta^n$ with $n$ as high as wished. This is so thanks to the remarkable diophantine relation established by Prouhet (1851): $\sum m_0^p = \sum m_1^p$ where $m_0$ are all the ranks of "0" in the PTM sequence from 1 to $2^L$ and $m_1$ are all the ranks of "1". For instance $1+4+6+7 = 2+3+5+8$ and $1^2+4^2+6^2+7^2 = 2^2+3^2+5^2+8^2$. One then shows that the first coefficients, up to L-1, of the Taylor development of the complex amplitude vanish: $a = j\phi \sum(m_0 - m_1) - \phi^2 \sum(m_0^2 - m_1^2) - j\phi^3 \sum(m_0^3 - m_1^3) + ...$, so that the first non-vanishing term varies as $\phi^{L-1} \propto \theta^{L-1}$ when there are $2^L$ telescopes.

## 3. The achromatic chessboard

In nulling inteferometry, as introduced first by (Bracewell 1978), one key element is the sub-system that provides an *achromatic* $\pi$ phase-shift in one arm of the interferometer. Several solutions were proposed, most of them implying an asymmetry between the two arms of the interferometer. A few years ago, we introduced a new concept of achromatic phase shifter, the achromatic chessboard (Rouan & Pelat 2008; Pelat et al. 2010; Pickel et al. 2013). It is based on a single optical device and some unforeseen application of diophantine equations. The wavefront is divided into many sub-pupils thanks to two "chessboards" of phase-shifting cells, each producing an *opd* that is an even (in one arm) or odd (in the other arm) multiple of $\lambda_o/2$, where $\lambda_o$ is a central wavelength in the spectral domain where achromatic phase shift is desired. The main assets of this solution are a) to make the arms of the interferometer fully symmetric and b) to use a unique simple component that can be in bulk optics or consists in a single deformable mirror.

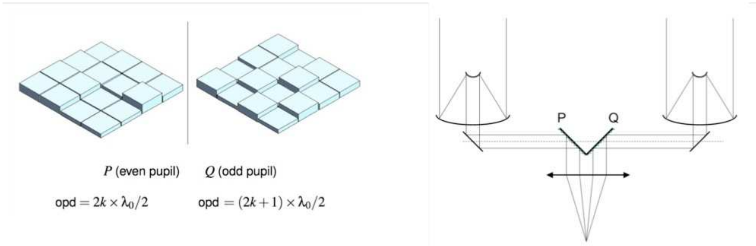


Figure 4.: *The chessboard achromatic phase-shifter; left: the pair of chessboard phase-shifters; right: its implementation in a Bracewell's interferometer.*

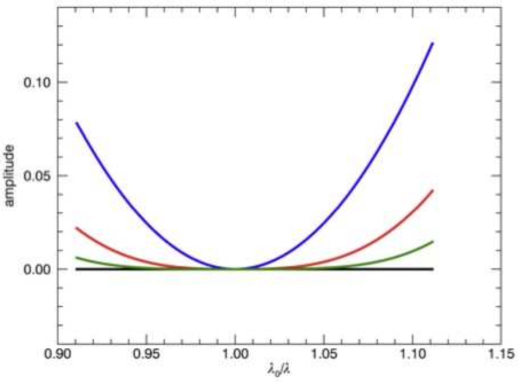


Figure 5.: *The evolution of the nulling factor vs* $\lambda$ *for an interferometer equipped with an achromatic chessboard phase-shifter of increasing order.*

It is the proper distribution of *opd* that is responsible of the quasi-achromatization. Why is it so ? Let's define $z = (-1)^{\lambda_o/\lambda} = \exp(j\pi\lambda_o/\lambda)$, so that the cell with $opd = k\lambda_o/2$ produces a complex amplitude $z^k$. For a basic Bracewell (a unique cell per chessboard), the amplitude is simply $\Lambda = 1 + z$. In other words, $\lambda = \lambda_o$ induces a root of order one on $\Lambda$. To obtain a flat $\Lambda$ around $\lambda_o$, let's consider a multiple root : $\Lambda = (1 + z)^n$, so that the higher $n$, the flatter the nulling vs $\lambda$ around $\lambda_o$, which is exactly the property looked for. Now let's look at the distribution of phase shifts produced by a device that would give this amplitude $\Lambda$ by developing $(1 + z)^n$ using the binomial coefficients: for instance, when $n$=3, we get $(1+z)^3 = 1+3z+3z^2+z^3 = 1+z+z+z+z^2+z^2+z^2+z^3$. Let's associate each term with a cell of a double chessboard, such that there are 1 cell of *opd* 0 ($z^0$), 3 of $\lambda_o/2$ ($z^1$), 3 of $2\lambda_o/2$ ($z^2$) and 1 of $3\lambda_o/2$ ($z^3$). In addition, the odd cells ($z^{2k+1}$) are grouped on one chess board and the even ones ($z^{2k}$) on the second one. The trick is here: when $\lambda = \lambda_o$, each cell produces indeed a 0 or a $\pi$ phase shift as in the classical Bracewell's interferometer, but modulo $2\pi$; this makes the difference. Fig. 6 gives an idea of how chessboards with $n = 3$ or 11 would look.

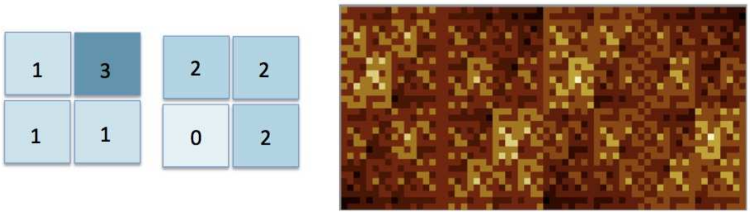


Figure 6.: *Left: the appearance of a chessboard of first order (n=3); right: of order 5 (n=11). The colors code the phase shift and the numbers on left gives the phase shift in unit of* $\pi$.

As regards, the x,y distribution of the cells on the chessboard, there is an optimum configuration that produces the best rejection of light around the optical axis, in about the same way as presented for the *deep nulling interferometer*: it makes use of the diophantine relation established by Prouhet. Let's call $P_r$ and $Q_r$ the physical arrangement of the phase shifters at order $r$. The cells are placed in such a way that $P_r - Q_r$ is a finite difference differential operator of high order. One can achieve this goal with the following iterative arrangement (Pelat et al. 2010): $P_{r+1} = \begin{pmatrix} Q_r+1 & P_r+2 \\ P_r & Q_r+1 \end{pmatrix}, Q_{r+1} = \begin{pmatrix} P_r+1 & Q_r+2 \\ Q_r & P_r+1 \end{pmatrix}$ The theoretical estimate of the absolute maximum bandpass ($n = \infty$) is $\Delta\lambda = 2/3\lambda_o - 2\lambda_o$, i.e. a factor 3 in $\lambda$. For a reasonable value $n = 13$, $\Delta\lambda = 0.65\lambda_o - 1.3\lambda_o$ which covers one octave. This means for instance that the Darwin specs (6 – 18 $\mu$m) are reachable with two components.

## 4. DAMNED, the experimental demonstrator of the achromatic chessboard

DAMNED (Dual Achromatic Mask Nulling Experimental Demonstrator) is the experimental demonstrator we developed. The choice of the visible range was dictated by cost and simplicity: on-the-shelf components and detectors, no cryogeny, *but* it implies much more severe specifications on the *opd* accuracy. A simple design was adopted (Fig. 7): with 2 off-axis parabolas, a chessboard mask, a single-mode fiber optics, we simulate two contiguous telescopes recombined in a Fizeau scheme.

The single-mode fiber is essential in the Fizeau scheme: it allows to sum globally the anti-symmetric amplitude and thus to make the nulling effective. The measurement is achieved by an x-y scanning with the fiber optics head of the spot at the focus of the 2nd parabola. A nanometric resolution is reached thanks to piezo actuators.

We tested first a transmissive chessboard in amorphous silica, manufactured by GEPI (Observatoire de Paris) using Reactive Ion Etching. It features 2 $\times$ 8 $\times$ 8 cells of 600 $\mu$m size. We obtained a typical nulling factor of 3–7 $10^{-3}$ for broad-band filters. Quasi-achromatism is indeed obtained since we get 8 $10^{-3}$ in the broad range 460-840 nm . The medium nulling performance does agree with

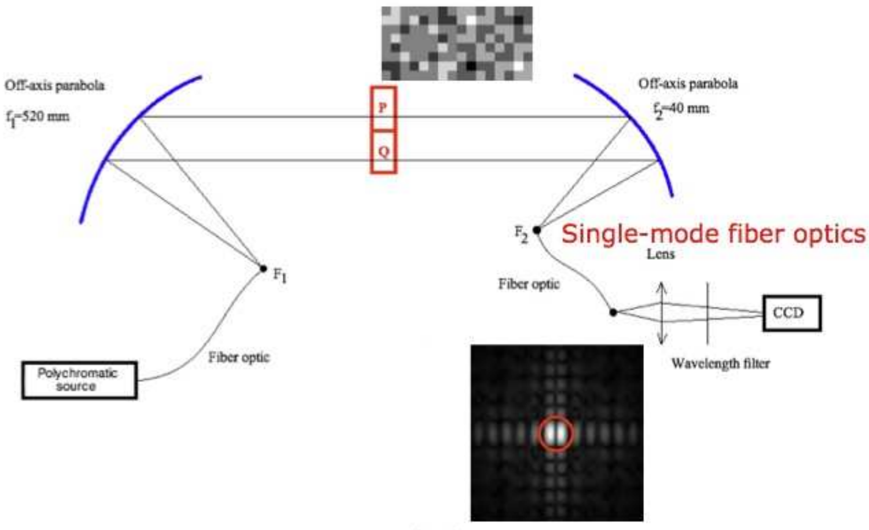


Figure 7.: *Schematics of DAMNED, the laboratory demonstrator.*

numerical simulations using the actual mask cell's thickness: we conclude that performances are limited by the accuracy of steps between cells.

The need for a better accuracy pushed us to change from bulk optics to a deformable mirror controlled in piston. The assets of a phase chessboard synthesized by a segmented deformable mirror are: a) free choice of the central wavelength; b) fine control of each cell's opd; c) versatile way to change the XY distribution; d) open the door to modulation to subtract systematics. Our choice was a segmented Boston Micro-Machine 12 × 12 electrostatic mirror. The optical scheme was then adapted to work in reflection.

Control of flatness is done using phase contrast (i.e. high-pass spatial filtering). The reached accuracy is typically 2–3 nm. A step by step procedure to flatten the DM was designed and appeared to be very efficient as illustrated by Fig. 9

The use of the single mode fiber optics was no longer suited because of the larger PSF (the DM surface is twice smaller than the transmissive mask), so that direct images of the "coffee bean" PSF were done. The performance assessment is less accurate but allowed to check the effectiveness of the nulling. Another method was also tested by scanning all the actuators of the DM while maintaining the nulling pattern, with the source being at a fixed $\lambda$ (laser): this proved to be the clearest demonstration of the achromatic properties, as illustrated on Fig. 10. The performances are similar to the ones of the transmissive chessboard while order is lower (2 × 4×4), a proof that the improvement is real. A nulling of $10^{-2}$ is obtained from 0.4 to 0.8 $\mu$m: the predicted quasi-achromatism is effective!

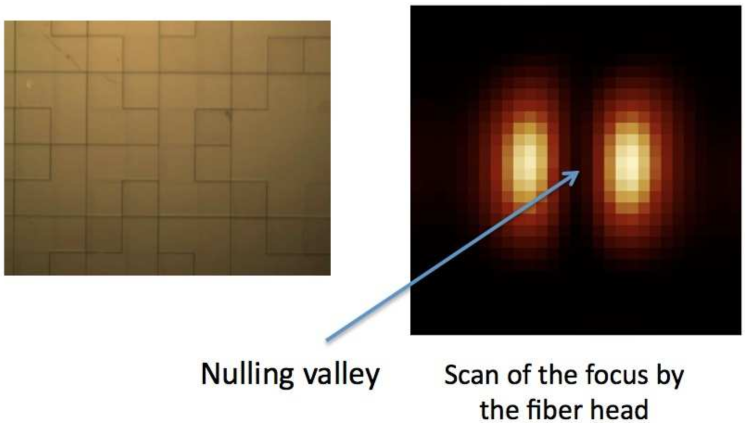


Figure 8.: *Left: macro photo of the transmissive chessboard mask. Right: the result of a x,y scan by the single-mode fiber optics at the focus of the second parabola: the characteristic shape of a coffee bean is observed.*

## 5. Work in progress and conclusion

Present work : we are working on the improvement of the control of the piston accuracy by analyzing the image obtained on several steps; the optical setup is also the object of some tuning and we are implementing spectroscopy for assessing chromatic performance in a one shot.

Future work : we plan to implement modulation between different nulling configurations to measure possible biases.

If we extrapolate the performance to mid-IR, by assuming that the accuracy on piston is the same at 10 $\mu$m, then a null depth of $2\ 10^{-6}$ would be reached on a rather low order ($2 \times 8 \times 8$) chessboard: this is within the Darwin specifications!

In conclusion, we think that we have shown that *diophantine optics* is indeed another way of thinking problems in optics. In some cases it may bring a genuine solution to actual problems. For instance, the need for achromatic $\pi$ phase in nulling interferometry can be solved in an elegant way (one component, symmetry of the arms) thanks to diophantine optics. Using the DAMNED bench, the principle of the achromatic chessboard phase shifter was demonstrated in the lab, both in reflection and transmission. The performances and the mode of operation using a segmented deformable mirror showed that this is a better solution than bulk optics, because it allows to improve the nulling through an active loop. Further developments are currently done to make another step in performances.

*Acknowledgements.* D. Pickel thanks the CNES for the PhD grant that allowed him to accomplish his thesis work on the achromatic chessboard phase shifter.

## References

Allouche J., Shallit J., 1999, in: Helleseth D., Niederreiter H. (eds.), Sequences

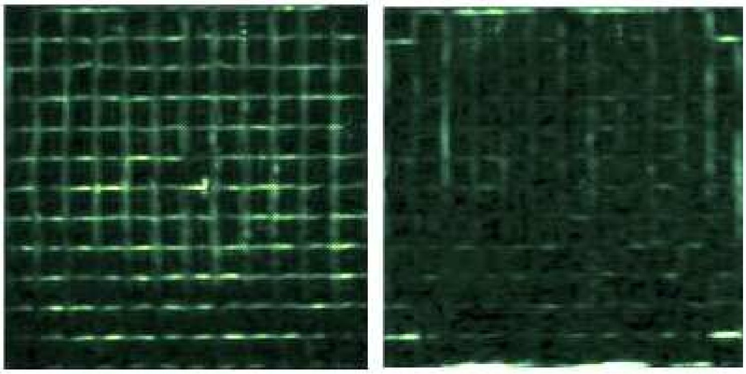

Figure 9.: *The deformable mirror surface before (left) and after (right) flattening.*

and Their Applications: Proceedings of SETA 98, 1–16

Bracewell R.N., Aug. 1978, *Nature* 274, 780

Cockell C.S., Herbst T., Léger A., et al., Mar. 2009, Experimental Astronomy 23, 435

Guyon O., 2007, Comptes Rendus Physique 8, 323

Leger A., Herbst T., Jul. 2007, ArXiv e-prints 707

Ollivier M., Le Duigou J.M., Mourard D., et al., 2006, in: Aime C., Vakili F. (eds.), IAU Colloq. 200: Direct Imaging of Exoplanets: Science & Techniques, 241–246

Pelat D., Rouan D., Pickel D., Dec. 2010, A&A524, A80

Pickel D., Pelat D., Rouan D., et al., Oct. 2013, A&A558, A21

Prouhet E., 1851, Comptes Rendus des Séances de l'Académie des Sciences 33, 225

Rouan D., 2004, in: Aime C., Soummer R. (eds.), EAS Publications Series, vol. 12 of EAS Publications Series, 21–31

Rouan D., Apr. 2007, Comptes Rendus Physique 8, 415

Rouan D., Pelat D., Jun. 2008, A&A484, 581

Rouan D., Riaud P., Boccaletti A., Clénet Y., Labeyrie A., Nov. 2000, PASP112, 1479

Rouan D., Baudrand J., Boccaletti A., et al., Apr. 2007, Comptes Rendus Physique 8, 298

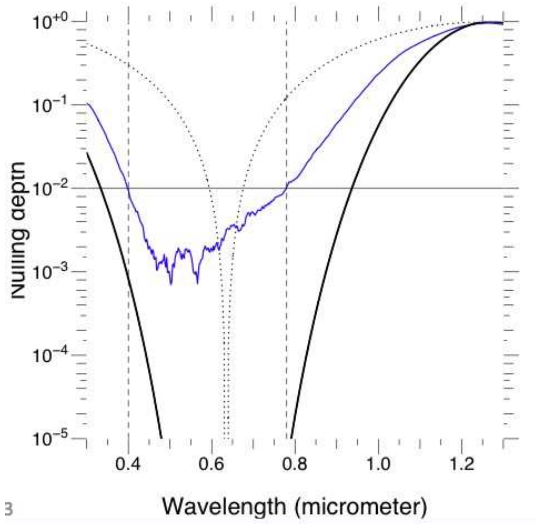


Figure 10.: *The nulling performances vs $\lambda$ of an achromatic chessboard phase shifter based on a 12 $\times$ 12 segmented deformable mirror. Dotted line: case of a classical Bracewell's configuration, blue thin line:the actual performances with a 2 $\times$ 4$\times$4 pattern, black thick line: the performance of a perfect 2 $\times$ 4$\times$4 mask.*

# Session 7. Metrology and astrometry with extremely high accuracy

Chairs: Julien Woillez & Michel Lintz
Thursday afternoon, Sept. 26$^{th}$

*Improving the performances of current optical interferometers & future designs*
*Proceedings of Haute Provence Observatory Colloquium (23-27 September 2013)*
*Edited by L. Arnold, H. Le Coroller & J. Surdej*

# Wavefront sensing with Hypertelescope Laser-Guide-Stars

P. D. Nuñez[1,2] & A. Labeyrie[1]

[1]*Collège de France*

[2]*Laboratoire Lagrange, Observatoire de la Côte d'Azur*

**Abstract.** A Hypertelescope with a spherical architecture is an attractive solution to simultaneously use tens to hundreds of mirrors in a $\sim$ 100 m interferometric array. Provided that phasing is possible, such an instrument will allow us to obtain direct images as well as to push the limiting magnitude in optical interferometry. In order to achieve this a modified laser guide star technique has been proposed. We summarize the status of recent simulation studies of wavefront-sensing with hypertelescopes equipped with laser-guide-stars.

## 1. Introduction

There are proposals to increase the number of apertures in optical interferometry to improve imaging capabilities. The *Carlina* architecture is an optical diluted version of the Arecibo concept, consisting of many small mirrors sparsely arranged on a sphere and having light combined at their common focus. The main advantage of the Carlina architecture is that it will allow the combination of many apertures without the need for optical delay lines. The *Hypertelescope* is a type of interferometer that makes use of pupil densification (Labeyrie 1996), a wavefront manipulation that reduces the size of the diffraction envelope that would be obtained in a direct "Fizeau" combination, concentrating light on a reduced number of fringes. There have been tests of Hypertelescopes with Carlina architectures at the Observatoire de Haute Provence (Dejonghe et al. 2014, Le Coroller et al. 2004) and recently at "Ubaye" in the French southern Alps (Labeyrie et al. 2012).

Hypertelescopes are expected to initially operate in speckle interferometry mode, but will have to be eventually equipped with adaptive optics in order to obtain phased images over long exposures. Several wavefront sensing methods with natural-guide-stars have been proposed (Labeyrie et al. 2002, Mourard et al. 2012) which are essentially extensions of the dispersed fringes method pioneered by Michelson. In the absence of a natural-guide-star, we propose to use a modified Laser-Guide-Star (hereafter LGS) technique that is suitable for diluted apertures as described by Labeyrie (2013) and in more detail by Nuñez et al. (2014).

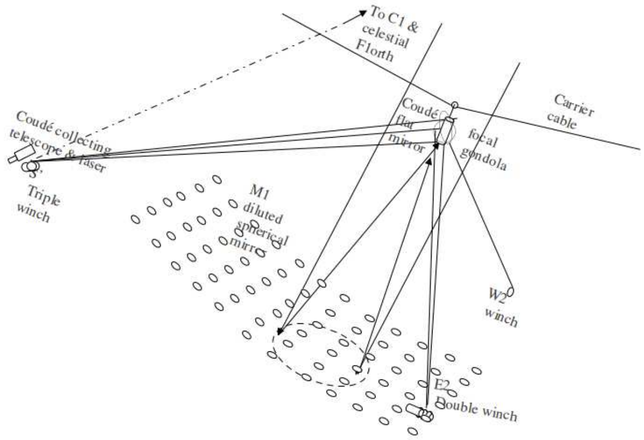


Figure 1.: *The Ubaye Hypertelescope schematic plan: Ground mirrors focus light on a suspended gondola. A coude beam is sent to the southern slope of the valley.*

## 2. The Ubaye Hypertelescope

Tests are being performed in an east-west oriented valley at “la Moutière”. Two $\sim 15$ cm mirrors are used to make a north-south baseline, and a focal gondola is suspended at 101 m from the ground by attaching a $\sim 800$ m cable from both sides of the valley (see Figure 1). Star tracking is achieved by moving the gondola in the west-east direction with the help of auxiliary cables and winches. The gondola has a pupil densifier and a coude-mirror which relays the optical beam to an 8 inch telescope on the southern slope where actual fringes will be acquired. So far, coude-beam acquisition tests have been performed and fringes are expected in the summer of 2014.

## 3. Laser-Guide-Stars for Hypertelescopes

Conventional wavefront sensing schemes used in monolithic apertures cannot be used with large interferometers, e.g. Hypertelescopes, mainly due to the modest sodium layer altitude. This results in the well-known “cone-effect” problem (Tallon & Foy 1990), in which laser light does not sample the same atmosphere as the light from the science target. There is also the fact that “small” ($\sim 10$ m) interferometric baselines already resolve typical artificial laser guide stars. Since a conventional LGS would be resolved, Fourier analysis of direct images cannot be done as in the methods proposed with natural guide stars (e.g. Labeyrie et al. 2002, Mourard et al. 2012).

Therefore, the solution described by Labeyrie (2013) and Nuñez et al. (2014) consists of using using sub-sets of apertures to create an array of spots in the sodium layer and collecting back-scattered light with the same apertures. The cone effect is reduced by using close sub-apertures as the laser emitting optics, and the fringe contrast is retained if exposure times are greater than $\sim 0.3$ ns (the Brownian motion time-scale).

As described in Nuñez et al. (2014), we have considered the case of using quadruplet apertures as the laser emitting optics. We have only studied the case

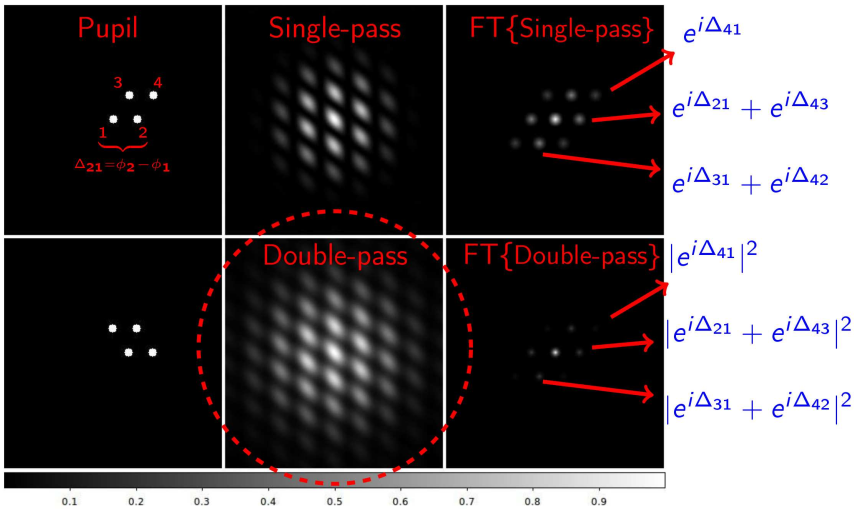


Figure 2.: *Numerical simulations of a Hypertelescope Laser-Guide-Star. A subset of apertures as shown in the top-left corner will form the "single-pass" image in the sodium layer. The "double-pass" image is obtained when the single-pass image is re-imaged with the same pupil. The Fourier transform of the "double–pass" image contains peaks that retain relative piston information ($\Delta_{ij}$ between apertures $i$ and $j$) when there are redundant baselines.*

of small $\sim 15$ cm mirrors, over which the wavefront is approximately uniform, so that only piston errors play an important role.

In Figure 2, we show a simulation of the interference pattern that can formed in the sodium layer by using a quadruplet aperture with redundant baselines. The image formed in the sodium layer (or "single-pass" image) is re-imaged with the same set of sub-apertures to obtain the "double-pass" image in the focal plane of the hypertelescope. The Fourier transform of each image contains peaks corresponding to different baselines as shown in Figure 2. The brightest secondary peaks are the most useful for piston sensing since they retain phase information when there are redundant baselines. Other pupil configurations can be used as long as there are redundant baselines, but the quadruplet configuration seems to be optimal in order to reduce the cone effect (Nuñez et al. 2014).

In order to sense pistons across a large array consisting of many overlapping quadruplets, one must use one laser-guide-star for each quadruplet. Each laser-guide-star allows measuring relative pistons within adjacent apertures, and the absolute piston at each aperture can be found by adding the relative pistons across the array. See Nuñez et al. 2014 for details.

## 4. Simulations

Numerical and laboratory (bench-top) simulations have verified the wavefront sensing technique, estimated its sensitivity and laser power requirements (Nuñez

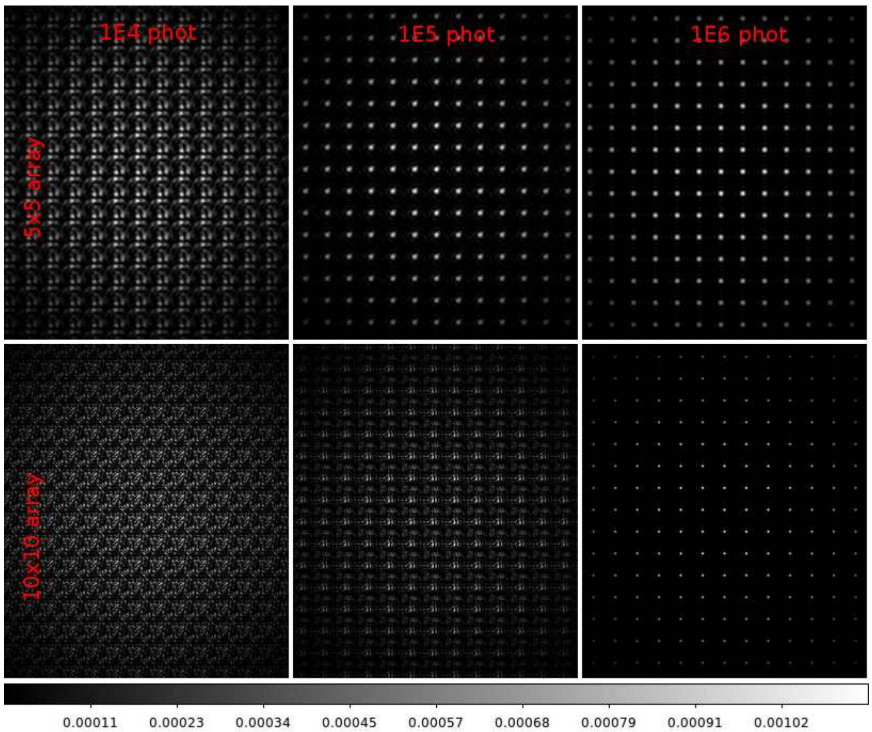


Figure 3.: *The top row corresponds to the corrected PSF of an array of* $5 \times 5$ *telescopes and different number of detected photons per aperture quadruplet, i.e. the number of detected return photons per LGS. The top row corresponds to an array of* $10 \times 10$ *apertures.*

et al. 2014). In Figure 3, we show example numerical simulations of the corrected Point-Spread-Function (PSF) of periodic arrays of $5 \times 5$ apertures and 10 apertures. Note that as the number of photons decreases, the PSF starts to resemble a speckle pattern. Note as well that smaller arrays require less return photons per quadruplet since piston sensing errors are additive across the array.

Laboratory simulations were also performed with a single quadruplet aperture and verify that one can use double-pass images to sense piston errors (see Nuñez et al. 2014 for details). Both laboratory and numerical simulations indicate that $\sim 10^6$ return photons per quadruplet are necessary to perform wavefront sensing for imaging applications (more or less depending on the number of apertures in the array).

## 5. Discussion and Hard points

There are several important challenges that must be overcome in order to build a Hypertelescope equipped with a Laser-Guide-Star. The first is that a laser is needed for each quadruplet, and the laser power required is of the order of $\sim 10\,\mathrm{kW}$ (Nuñez et al. 2014). There is also a phase unwrapping problem: A polychromatic LGS can conceivably be used for this, but numerical simulations have shown that $2\pi$ errors in the measured phase are a common occurrence (Nuñez et al. 2014). The main reason for requiring a large number of return photons when compared to other wavefront sensing methods is that the Hypertelescope-LGS method relies on a fringe contrast measurement rather than a centroid measurement as in the Shack-Hartmann technique.

The issues mentioned above indicate that the subject of Laser-Guide-Stars for optical interferometry still needs significant work, even at the conceptual stage. However, the idea of using the same sub-apertures as laser emitting optics and wavefront sensors, i.e. the "double-pass" scheme, deserves further development. More general pupil configurations should be explored other than the redundant quadruplet case. The pupil redundancy can be somewhat relaxed, requiring only local redundancy, by applying "pin-cushion" distortions of less than the aperture size which also enhance the imaging capabilities of an array. It may also be possible to perform pupil-remapping for the returning image to retain phase information of double-pass images of non-redundant configurations, although this possibility has not yet been investigated. It should also be noted that this wavefront sensing scheme may be applicable to segmented telescopes in general, and a study of higher-order wavefront errors (e.g. tip-tilt) across individual sub-apertures should be performed.

## 6. Conclusions

Using subsets of apertures to form fringes in the sodium layer is a possible way to perform wavefront sensing with diluted apertures and has been studied via simulations. While numerical and laboratory studies have validated the method, initial results suggest that the required photon return rate is too high for an implementation of the method in the near future. More realistic numerical simulations should be performed as well as experiments on the sky, for example, by creating fringes with a masked large telescope such as the European Very Large Telescope.

**References**


Labeyrie, A. 1996, A&A, 118, 517

Labeyrie, A., Allouche, F., Mourard, D., et al. 2012, Proc. SPIE, 8445

Labeyrie, A., 2013, EAS Publication series, 59, 5

Labeyrie, A., Borkowski, V., Martinache, F., et al. 2002, European Southern Observatory Conference and Workshop Proceedings, 58, 109

Mourard, D., Meilland, A., Dali-Ali, W., et al. 2012, Proc. SPIE, 8445,

Le Coroller, H., Dejonghe, J., Arpesella, C., Vernet, D., & Labeyie, A. 2004, A&A, 426, 721

Dejonghe, J., et al. 2014, this conference

Nuñez, P.D., Labeyrie, A., Riaud, P., 2014. MNRAS, in press

Tallon, M., & Foy, R. 1990, A&A, 235, 549

*Improving the performances of current optical interferometers & future designs*
*Proceedings of Haute Provence Observatory Colloquium (23-27 September 2013)*
*Edited by L. Arnold, H. Le Coroller & J. Surdej*

# Spectrally resolved frequency comb interferometry

Steven van den Berg

*VSL, Thijsseweg 11, 2629 JA, Delft, The Netherlands*

**Abstract.** In this contribution a novel method for interferometric distance measurement is presented, that is based on unraveling the spectrum of a femtosecond frequency comb. The light of a frequency comb is sent into a Michelson interferometer. The output of the interferometer is analyzed by a high-resolution spectrometer, resolving the individual comb modes. The path-length difference between the two arms is determined on the level of tens of nm, by utilizing the wealth of information present in the unraveled spectrum, showing homodyne interference for each individual frequency comb mode. The measurement method allows for high-accuracy measurements in combination with a large range of non-ambiguity.

The invention of the femtosecond frequency comb has been a step change in the field of optical-frequency metrology, with a wide outreach to other fields, like high-resolution spectroscopy, femtosecond-pulse shaping and absolute distance measurement. We have investigated the femtosecond frequency comb as a potential new source for accurate absolute long-distance measurements, exploiting the unique properties of the comb and utilizing the direct traceability to the SI second. In this contribution we focus on distance measurement with a mode-resolved frequency comb laser. The frequency comb light is sent into a Michelson interferometer, consisting of a measurement and a reference arm. Subsequently, the interferometer output is analyzed with a high resolution spectrometer based on a virtually imaged phase array (VIPA) and a grating. The VIPA spectrometer unravels the 1 GHz spaced comb frequencies to distinct modes. As a result, interferometry on the level of individual modes (wavelengths) can be observed (see Fig. 1). The distance is determined from both spectral interferometry and massively parallel homodyne interferometry of about 9000 frequency comb modes. We have delivered an experimental proof of principle of homodyne frequency comb interferometry by measuring a short displacement with an unraveled comb and a counting helium-neon laser simultaneously, showing an agreement of tens of nanometers. This new technique can be considered as a combination of multiwavelength interferometry with thousands of continuous wave (cw) lasers and spectral (dispersive) interferometry. It overcomes the limitations of the individual techniques, combining an interferometric scheme with a large range of non-ambiguity. This allows for non-incremental absolute measurement of an arbitrary distance with a single frequency comb laser. We have demonstrated the measurement principle on a short distance of about 15 cm and compared the measured distance to conventional incremental interferometry. An agreement within $\lambda/30$

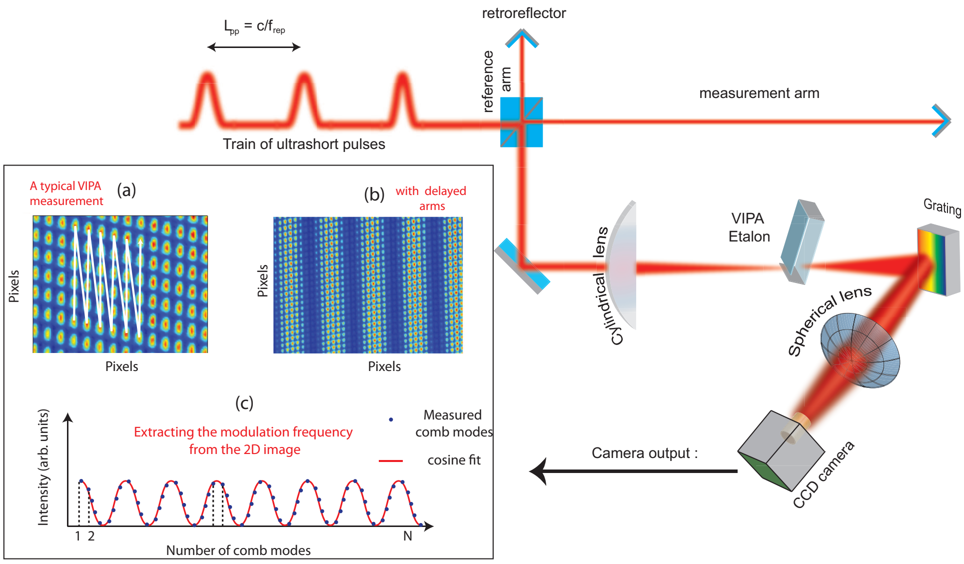


Figure 1.: *Schematic overview of the setup for unraveling the output of a Michelson interferometer into distinct modes. In the inset (a) a small fraction of a typical CCD image is shown, as obtained with the measurement path blocked. Inset (B) shows a part of the CCD image when interference between the two arms occurs. The mode-resolved signal is mapped on a frequency axis by stitching together vertical lines, as schematically indicated by the white arrows (in reality one vertical line consists of about 50 dots). The results is shown in (c).*

is found. It is anticipated that the measurement principle can be extended over much longer measurement ranges and that simplified detection schemes can be developed. A more extensive paper on this work can be found in van den Berg et al. (2012).

## References


S.A. van den Berg, G.J.P. Kok, S.T. Persijn, M.G. Zeitouny and N. Bhattacharya 2012, Many-wavelength interferometry with thousands of lasers for absolute distance measurement, Phys. Rev. Lett., 108, 183901

*Improving the performances of current optical interferometers & future designs*
*Proceedings of Haute Provence Observatory Colloquium (23-27 September 2013)*
*Edited by L. Arnold, H. Le Coroller & J. Surdej*

# Laser ranging by time-of-flight measurement of femtosecond light pulses

Young-Jin Kim

*Korea Advanced Institute of Science and Technology (KAIST), 373-1 Guseong-dong, Yuseong-gu, Daejeon, South Korea (yj.kim@kaist.ac.kr)*

**Abstract.** Time-of-flight (TOF) measurement of femtosecond light pulses was investigated for laser ranging of long distances with sub-micrometer precision in the air. The bandwidth limitation of the photo-detection electronics used in timing femtosecond pulses was overcome by adopting a type-II nonlinear second-harmonic crystal that permits producing the balanced optical cross-correlation signal between two overlapped light pulses. This method offered a sub-femtosecond timing resolution in determining the temporal offset between two pulses through lock-in control of the pulse repetition rate with reference to the atomic clock. The exceptional ranging capability was verified by measuring various distances from 1.5 m to 700 m. This method is found suited for terrestrial land surveying and space missions of formation-flying satellites.

The material presented at the conference has recently been published and the author proposes to the reader the references below.

## References

Joohyung Lee, Young-Jin Kim, Keunwoo Lee, Sanghyun Lee and Seung-Woo Kim, "Time-of-flight measurement with femtosecond light pulses", Nature photonics Vol. 4, 716-720 (2010)

Joohyung Lee, Keunwoo Lee, Sanghyun Lee, Seung-Woo Kim and Young-Jin Kim, "High precision laser ranging by time-of-flight measurement of femtosecond pulses", IOP Meas. Sci. Technol. 23, 065203 (2012)

*Improving the performances of current optical interferometers & future designs*
*Proceedings of Haute Provence Observatory Colloquium (23-27 September 2013)*
*Edited by L. Arnold, H. Le Coroller & J. Surdej*

# Session 8. Problems related to the sensitivity of interferometers and quality of the observables in interferometry

Chair: Denis Defrère
Friday morning, Sept. $27^{th}$

*Improving the performances of current optical interferometers & future designs*
*Proceedings of Haute Provence Observatory Colloquium (23-27 September 2013)*
*Edited by L. Arnold, H. Le Coroller & J. Surdej*

# Some Astronomical Applications of High Accuracy Stellar Interferometry

B. Mennesson

*Jet Propulsion Laboratory, California Institute of Technology, 4800 Oak Grove Dr, Pasadena CA 91009, USA*

**Abstract.**
Optical astronomical interferometry has seen spectacular progress over the last two decades, notably in terms of spatial/spectral resolution, sensitivity, and in the number of accessible baselines. A significant (x 100) parallel improvement has taken place in the accuracy of interferometric measurements, whether phase or amplitude related. This evolution is important because higher measurement accuracy directly translates into higher contrast observations, which is key for a number of astronomical investigations demanding both high resolution and high contrast at the same time. This includes the characterization of molecular layers in the extended atmospheres of evolved stars, the direct imaging of surface oblateness in fast rotating stars, the direct measurement of Cepheids angular diameter changes vs pulsation - and subsequent distance determination -, the detection of faint exozodiacal dust around mature stars, and the search for sub-stellar companions to nearby stars. The latter two applications have particularly driven the field improvements over the last few years. Contrast levels of 1000:1 or better have now been achieved at several facilities, and there are prospects for an other tenfold gain in the near future, notably with the Large Binocular Telescope Interferometer (LBTI).

## 1. Introduction

Over the last 15-20 years, the main instrumental developments seen in optical interferometry have concentrated on improving critical capabilities: angular resolution (e.g. ten Brummelaar et al. 2005), spectral resolution (e.g. Weigelt et al. 2010), sensitivity (e.g. Woillez et al. 2013, Burtscher et al. 2013) and (u,v) plane coverage (e.g. Kloppenborg et al. 2010, Balan et al. 2010, Le Bouquin et al. 2011). In parallel to these observational efforts, and driven by a number of scientific niches, large progress has also been made in terms of interferometric contrast. The dynamic range achievable by interferometry is directly related to measurement accuracy, whether considering phase or amplitude-based observables. While "high" dynamic range (100:1 or higher) will always be benefitial, it is more or less critical depending on the astronomical application. High contrast is mandatory in some specific fields such as the detection of faint structures in the planet forming region of young and mature stars, or direct measurements of stellar pulsation. Figure 1 sketches what kind of studies are enabled at various interferometric contrast levels, assuming adequate capabilities are available for all other observing parameters.

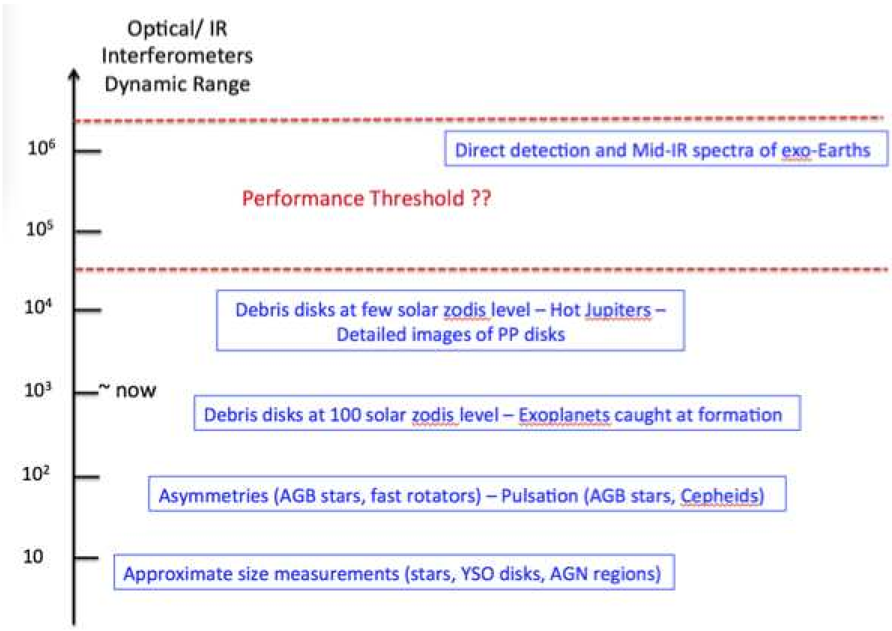


Figure 1.: *Schematic view of astronomical observations enabled by various degrees of interferometric contrast. Each application has its own minimum performance threshold. While broad-band iterferometric contrast better than* $10^6$ *has already been demonstrated in the lab, the current state of the art for astronomical observations is around 1000:1.*

A major driver for the development of high accuracy interferometry has been the direct detection and characterization of exoplanets. It was first proposed for the most challenging application of all in that field: the direct detection of Earth-like extrasolar planets using mid-infrared space nulling interferometry (Bracewell 1978, Leger et al. 1996, Beichman et al. 2006). In that case, a final (post calibration) contrast of $\simeq 10^6$ is required. It has already been successfully demonstrated in the laboratory at both visible (Haguenauer & Serabyn 2006) and mid-infrared wavelengths (Martin & Booth 2010), but remains far above the current on-sky capabilites of stellar interferometers. Indeed, the best point source detection limits reached by stellar interferometry so far are a few 100:1 to $\simeq$ 1000:1, as demonstrated at the VLTI with the PIONIER beam combiner (Absil et al. 2011) and with the CHARA interferometer MIRC instrument (Zhao et al. 2011). Both instruments made use of accurate phase closure measurements in the near infrared (H-band) across 4 or more baselines, with the goal of detecting faint companions to mature stars and eventually search for exoplanets around young stars (PIONIER), or measure spectra of hot Jupiters previously detected by radial velocity studies (MIRC). This 1000:1 point source contrast is also the limit reached by current 8m telescope aperture masking experiments conducted at Keck (NRM: Kraus & Ireland 2012, Hinkley et al. 2011) and at the VLT (NACO/SAM: Huelamo et al. 2011), which also measure interferometric phase closures from a limited number of sub-apertures. In spite of offering similar contrast performance at significantly lower angular resolution than CHARA/MIRC or VLTI/PIONIER, these single dish instruments already provided "images" of planetary candidates caught at formation around a few very young stars. The reason is that operating on large telescopes, non redundant aperture masks have a higher sensitivity, and benefit from a larger number of sub-apertures and baselines. They can also operate at more favorable infrared wavelengths, such as L or M band, where exoplanets are brighter and the required contrast is less. These results make it clear that an LMN band instrument operating at the VLTI Unit Telescopes and providing high accuracy phase closure measurement capability would be able to detect and characterize very young exoplanets around many YSOs. The next generation MATISSE instrument (Lopez et al. 2012) may have the potential for such observations, specially if more emphasis is put on phase closure accuracy over the years. Such studies might be even more compelling with some future dedicated planet formation imaging (PFI: http://planetformationimager.org/ ) interferometric facility, assuming it offers the required combination of sensitivity, (u,v) plane coverage and dynamic range in the near to mid-infrared.

A limit of phase closure measurements, or any interferometric observations based on phase information only, - e.g. differential phase, differential closure phase, closure phase nulling (Duvert et al. 2010) -, is that it is only sensitive to the asymmetric part of the objects brigthness distribution. In particular, it is insensitive to the main emission of circumstellar disks, and can not distinguish between a clump in a bright extended disk and a fainter isolated point source. It is clear that both visibility amplitude and phase information should be measured accurately to best constrain interferometric observations. I concentrate hereafter on the methods used to measure accurate visibility *amplitudes*. As an illustration, I present examples of astronomical objects studied at increasingly high visibility (or equivalently null) accuracy: extended molecular atmospheres around late type stars, Cepheids, warm and hot debris disks around mature stars. I then conclude by discussing new ideas, promising results and future prospects for even higher performance, specially in the context of the LBTI exo-zodi nulling survey (Hinz 2013).

## 2. Applications to the study of stellar atmospheres and pulsation

### 2.1 Fast Rotators

As visibility measurement accuracy gets down to a few percent, an interesting application in stellar physics is the observational study of gravity induced limb darkening in fast rotating stars (i.e. with surface rotational velocites greater than $\simeq$ 100 km/s). The distinctive observational signatures of rapid rotation were first described by von Zeipel (1924), beginning with the expection that centrifugal forces would distort the photospheric shape and that the resulting oblateness would induce lower effective temperatures at the equator, an effect known as gravity darkening. A good illustration of this phenomenon is Altair, a rapidly rotating hot star with a significant ($\simeq$ 14%) disk asymmetry first detected with the Palomar Testbed Interferometer (Van Belle et al. 2001) and whose surface was later imaged in great details by multi-baseline interferometry with CHARA/MIRC (Monnier et al. 2007). MIRC images confirm the basic picture of gravity darkening induced by rapid rotation: they show Altair's photosphere to be oblate with a bright region identifiable as the stellar polar region and a dark equatorial band with approximately 60-70% of the brightness at the pole, broadly consistent with expectations for the near-infrared from previous models. Images show however a stronger darkening along the equator than would be predicted with any von Zeipel-like gravity darkening prescription assuming uniform stellar rotation, and a uniform gravity limb darkening coefficient significantly smaller than in the von Zeipel model. Such accurate imaging studies of gravity darkening have now been carried at NPOI and CHARA on a number of other fast rotators, among which Vega (Aufdenberg et al. 2006), Achernar (Domiciano de Souza), Regulus (McAlister et al. 2005), and Alderamin (Van Belle et al. 2006). Both differential rotation and/or gravity darkening laws versus latitude could explain the observations of Altair and the few other fast rotators observed. Whatever the explanation, these interferometric observations convincingly establish the case for stellar physics beyond the standard models used today to describe fast rotating stars.

### 2.2 Extended molecular layers around late type stars

Historically, the first instrument to provide high visibility accuracy (of the order of 1% or better, Perrin et al. 1998, Merand et al. 2005 ) was the IOTA/FLUOR instrument (Coude du Foresto 1998), which used single-mode waveguides for optical recombination and calibration of atmospheric effects. As these accurate visibility measurements became available, a number of new results were quickly obtained on evolved stars, illustrating the impact of a ten fold gain in visibility accuracy. The effective temperature scale of giants was extended to types later than M6 (Perrin et al. 1998), the photospheric pulsation of R Leonis was detected in the near infrared for the first time (Perrin et al. 1999) and there was now clear evidence for very extended molecular layers ($H_2O$, $CO$, etc) around O-rich Miras and semi-regular variables (Mennesson et al. 2002, Perrin et al. 2004), confirming what was suspected from high resolution spectroscopic observations. The latter discovery, and in particular the results of narrow filter measurements, allowed to reconcile a variety of discrepant "diameter" estimates coming from interferometric observations at different wavelengths and spatial resolutions. High visibility accuracy was key to distinguishing the effect of molecular species variable absorption versus time and wavelength, appearing at mid-spatial frequencies, from that of stellar pulsation, occuring at higher spatial frequencies characteristic of the photosphere. In particular, when taking the contribution of upper molecular layers properly into account, Mira's photospheric radii were found significantly smaller than previously measured, which could favor a fundamental mode of pulsation (Wood 1990). While these now fairly archaic IOTA observations naturally lacked sensitivity and spectral resolution with 40 cm siderostats, they paved the way to next generation fiber based /integrated optics instruments used on larger more sensitive telescope arrays, such as CHARA/MIRC and VLTI PIONIER. As for FLUOR, it is still on the sky in a rejuvenated form. It was moved to the CHARA array in 2005 and was recently upgraded with new optics and acquisition software (Scott 2013, Mennesson 2013).

### 2.3 Cepheids pulsation and circumstellar material

Another application that relies on accurate visibility measurements is the determination of accurate distances to Cepheids, the goal there being to calibrate the Cepheids period - absolute luminosity relation used for the determination of local and cosmological distances, which play themselves a critical role in the determination of the Hubble constant (e.g Sandage et al. 2006). Stellar interferometry allows to directly measure distances to pulsating stars by the way of the parallax pulsation technique, also known as the Baade- Wesselink method (Baade 1926, Wesselink 1946), which compares the actual change in angular diameter and the change in pulsation velocity $V_{rad}$ in order to measure distances. A limitation in using this method however, is that spectroscopy does not directly measures the pulsation velocity, but the projected velocity $V_p = p.V_{rad}$, integrated over the surface on the star, where p is the so-called "projection factor". A first contribution of stellar interferometry has then been to determine this projection factor with a better precision that previously available, applying the Baade Wesselik equation to $\delta$ Cep, the only Cepheid with a well known physical distance, and for which accurate angular diameter measurements were obtained from CHARA (Merand et al. 2005). The p factor value was pinned down to $1.27 \pm 0.04$, while theoretical model predicted values between 1.27 (Nardetto et al. 2004) and 1.45 (Sabbey et al. 1995). A second major contribution of interferometry has been the realization that many Cepheids are surrounded by large envelopes many stellar diameters in size (Kervella et al. 2006, Galenne et al. 2013b) emitting a few percent of the total near infrared flux, and whose characteristics need to be properly taken into account in order to use the Baade-Wesselink method. Finally, recognizing the modeling uncertainties related to these newly discovered complex circumstellar structures around Cepheids, an other powerful approach to the problem of estimating Cepheid distances is the observation of Cepheids in binary systems. This has been the object of recent high accuracy interferometric observations (Galenne et al. 2013a and 2014) providing direct detection of faint stellar companions, accurate measurements of orbital periods, dynamical masses and angular separations, while Kepler's third law provides the physical separation necessary to derive stellar distances.

## 3. Exozodiacal disks

The outer colder parts of debris disks, analogous to our solar system Kuiper belt, were first detected via their mid infrared or far infrared excess emission, and then abundantly imaged at visible to sub-millimeter wavelengths. Conversely, very little is known about the hotter (> 200K) dust component of debris disks, concentrating in the inner few AUs of the stellar environment where rocky planets may have formed, similar to the zodiacal dust found in the inner solar system. Indeed, only a few hot debris disks have been found by Spitzer around mature stars via excess emission at wavelengths of 24 microns or shorter (Su et al. 2006, Wyatt et al. 2007, Lawler et al. 2009, Bryden et al. 2009), and very few have been unambiguously resolved from the ground at mid-infrared wavelengths (e.g. Smith et al. 2009, Stock et al. 2011, Millan-Gabet et al. 2011). This observational difficulty results from several factors: the exozodiacal disks small sizes and their faintness relative to the host stars. Indeed, while cold debris disks cause very significant excesses readily detectable at far infrared wavelengths, exozodiacal material located in the inner few AU only contributes a small fraction of the stellar flux. In order to reliably detect such tiny ($\simeq$ 1% or less) excess emission over that expected from the photosphere, direct imaging is required, with the ability to spatially resolve dust from the central star. In the visible, where dust is essentially seen through starlight scattering, the contrast required is extremely high and only a space or balloon borne coronagraph can provide adequate performance. In the infrared, exozodi disks produce significant thermal emission and contribute a larger fraction of the stellar flux, making it the spectral range of choice for ground-based exozodi studies. With the combination of contrast and spatial scales at play, typically 0.1 to a few AU, such direct infrared observations are best accomplished using high accuracy long baseline interferometry. This was the main goal of the Keck Interferometer Nuller (KIN), a long baseline (85m) high contrast instrument operating between 8 and 13 microns, specially built to spatially resolve faint structures next to bright stars (Colavita et al. 2013, Serabyn et al. 2012, Mennesson et al. 2003). Exozodi observations were carried out with the KIN between 2008 and 2011 through three different Key Science programs (respectively led by Eugene Serabyn, Phil Hinz and Marc Kuchner) and one PI program (led by Mennesson). It targeted 47 nearby main sequence stars overall, 40 of which had no companion known within the interferometric field of view ($\simeq$ 0.5" at FWHM). These KIN observations have just been fully reduced (Mennesson et al. in preparation) and we summarize hereafter some of the key conclusions. These are based on the 8 to 9 microns data alone, which provide the highest signal to noise measurements, with final null accuracies (1 $\sigma$) ranging from of 0.1% to 0.5%, depending on the 10 microns stellar flux. We found only one star with a large excess imputable to dust emission ($\eta$ Crv), while four more stars showed a significant ($> 3\sigma$) excess: $\beta$ Leo, $\beta$ UMa, $\zeta$ Lep and $\gamma$ Oph. Overall, KIN excesses were detected more frequently around A-type stars than later types, and around stars already suspected to have cold dust around them through far infrared excesses, suggesting some dynamical link between the inner (zodi-like) and outer (Kuiper belt like) dust populations. A fairly surprising result is that no significant mid-infrared excess is generally found around sources with a previously reported $\simeq$ 1% near-infrared resolved excess. If dust emission is really at stake in these near-infrared detections (Absil et al. 2013), the absence of a strong mid-infrared counterpart would point to populations of very hot and small (sub-micronic) grains piling up close to the sublimation radius. Since such grains should be rapidly expelled from the inner system by radiation pressure, this would indicate some inordinate replenishment rates or yet poorly understood dynamical effects trapping or maintaining dust close to the sublimation radius. A statistical analysis of the overall measurements also suggests that many of the sample stars have excesses close to the KIN detection limit of a few 100 zodis, and hence constitute prime candidates for more sensitive exo-zodi surveys such as the one just starting with the Large Binocular Telescope Interferometer (LBTI, see section 4.1).

## 4. Future prospects in high contrast interferometry

What is the future of high contrast astronomical interferometry and how do we get there? As the interferometric detection of very faint point sources and especially young and/or hot exoplanets is concerned, there are prospects for reducing current systematics. As explained in section 1, the contrast provided by ground based phase closure measurements is currently limited to 1000:1 or so. This limit is common to long baseline interferometric observations and aperture masking measurements on large telescopes, When dealing with systematics at such low levels, all temporal and spatial effects have to be properly understood and minimized, including the effects of finite integration over spatial, temporal and wavelength domains. Such effects and mitigation strategies have been studied recently by Mike Ireland (2013), who concluded that temporal phase noise and photon noise limited detections should be accessible. Some new ideas have also been proposed to combine nulling with phase closure in order to access deeper point source contrasts than with any of the two techniques used individually.

While exoplanets direct detection will likely continue to drive future improvements in terms of phase closure and differential phase accuracy for high contrast interferometric measurements, we concentrate hereafter on the immediate problem of measuring visibility amplitudes at the $\simeq 10^{-4}$ accuracy level, as required by the LBTI exo-zodi survey. We also discuss a fairly new observing/ data analysis technique which already demonstrated near infrared visibility measurements down to an absolute accuracy of 0.1% or better (Mennesson et al. 2011a & b), and assess its applicability to the LBTI contrast challenge in the mid-infrared.

### 4.1 LBTI Exozodi survey

The Hunt for Observable Signatures of Terrestrial planetary Systems (HOSTS) on the Large Binocular Telescope Interferometer (LBTI) will survey nearby stars for faint exozodiacal dust (exozodi). LBTI-HOSTS (Hinz et al. 2013) should be the first survey capable of measuring exozodi at the 10 zodi level, which corresponds to a null measurement accuracy of $\simeq 10^{-4}$, ten times better than the best results achieved by the KIN survey. Exozodi of this brightness would still be the major source of astrophysical noise for a future space telescope aimed at direct imaging and spectroscopy of habitable zone terrestrial planets. Detections of such warm dust will also reveal new information about planetary system architectures and evolution. The HOSTS survey target list is currently being defined by the LBTI science team (Weinberger et al. 2014) and will reflect both objectives. The space mission-driven approach concentrates on F, G, and K-type stars that are the best targets for future direct observations of exoEarths, thereby providing model-independent ground truth dust observations. However, not every potential target of a future exoEarth mission can be observed with LBTI, and a complementary approach selects targets based only on what exozodi sensitivity could be achieved, without consideration of exoEarth mission constraints. This naturally selects more luminous stars (A and early F-type stars). In both cases, all stars are close enough to Earth that their habitable zones are resolvable by LBTI and bright enough at N-band (10 $\mu$m) to provide excellent sensitivity. Clearly, the LBTI requirement to measure astronomical nulls (or visibilities) down to a relative accuracy level of $10^{-4}$ is a daunting one, specially in the mid-infrared, where warm optics thermal emission is extremely high. There are however several reasons why the LBTI may provide more accurate results that the KIN survey:

- Lower thermal background. With its adaptive secondary mirrors, the LBTI only has 3 warm optics before the cold beam combiner, and the expected total warm train emissivity is 10 to 15%, to be compared to $\simeq 95\%$ at KI. The total number of optics is also less than at KI and the recombination strategy uses a single beam splitter, making the overall instrument transmisison higher than at KI. Overall, the photometric signal to noise is expected to be about ten times higher at any given mid-infrared wavelength, which also opens the door to operation at 10 - 12 microns (rather than 8-9 microns, optimum for sensitivity at Keck), a wavelength range where wavefront correction is better and where the dust over star flux contrast is likely more favorable. Background estimation still remains a difficult task at LBTI: even with the warm optical train low emissivity, background counts are comparable to Vega's flux at 11 microns. In order to measure a $10^{-4}$ null on a 1 Jy star, the thermal background must hence be estimated with no systematic bias down to a few ppm.

– Accurate background estimation. While the KIN used a complex 4-beam phase modulation scheme to reject the large background signal and its slow fluctuations (Serabyn et al. 2012), the LBTI uses simultaneous background measurements in focal plane areas close to the science image. Regular nods of the telescopes are then used to regularly measure the background offset between the 2 regions of the detector. Using nods every 90 seconds and 40 mn of observations, LBTI sky tests have already demonstrated mean background estimation down to a level of 2ppm between 10 and 12 $\mu$m and spectrally white measurement error down to the background photon noise level (Defrere and Mennesson, in preparation).

– No longitudinal dispersion. Because of the common binocular mount used for the observations, the interferometric baseline is always perpendicular to the line of sight and there are no differential longitudinal dispersion or differential atmospheric refraction effects between the 2 beams.

– Smaller baseline. With a 14.4 m center to center baseline, LBTI observations are less sensitive to calibrator diameter uncertainties than the KIN observations. Since the uncertainty on the null goes as the square of the projected baseline, the impact of calibrator diameter uncertainties is reduced by a factor of 30 to 40. Using a smaller baseline and a common mount also significantly reduces the complexity inherent to beam transport and long delay lines.

– A series of two-beam nulling observations conducted in the near infrared at the Palomar Hale Telescope have recently demonstrated the ability to measure astrophysical nulls at a level of a few $10^{-4}$ at $1\sigma$. Moreover, this accuracy could be achieved while the observed mean null levels and temporal fluctuations were 100 higher or more. These Palomar results used the "Null Self Calibration" method (Mennesson et al. 2011b, Hanot et al. 2011), which should be applicable to the LBTI mid-infrared observations, at least to some extent, as explained in the next section.

### 4.2 Null Self Calibration (NSC) method

The NSC method is based on the analysis of the probability distribution of the interferometric signal measured while stabilizing the optical path difference (OPD) around the central dark fringe, i.e. the deepest white light null (Mennesson et al.

2011a, Mennesson et al. 2013). It was first demonstrated with the Palomar Fiber Nuller (PFN), a mini near-infrared (broad K-band) nulling interferometer developed at JPL since 2006 (e.g. Mennesson et al. 2006, Martin et al. 2008), which uses two (3 x 1.5m) sub-aperture beams of the primary mirror located 3.2m apart and recombines them coherently into a common single-mode fiber. The PFN is a visitor instrument installed in the Palomar 200 inch Cassegrain cage and located downstream of the AO system which stabilizes the 2 beams OPD down to $\simeq$ 200 nm rms at K band. Figure 2 shows as an illustration the results obtained on the bright star $\alpha$ Boo, for which consecutive NSC based astrophysical null depth estimates were derived over one hour of observation and remained stable at the few $10^{-4}$ level. Note that for the PFN, we computed the observed distribution of the instantaneous null level (interferometric signal normalized by constructive interference signal). Interestingly, and as shown in the upper two panels, the observing conditions (relative beam intensity, average phase difference and phase jitter) and resulting null level distributions can vary a lot with time, yielding very different average null levels: 0.065 and 0.095 in that case. However, the astronomical null values derived from the NSC fitting method are significantly lower, and much closer to each other: 0.0130 $\pm$ 0.0005 and 0.0132 $\pm$ 0.0006. The advantages of the NSC method is that it uses the whole data distribution (not just its average or some other ensemble characteristics) to make an estimate of the astronomical null or visibility, and that it takes out the coherence loss effects due to opd jitter (piston) and intensity mismatch. The final calibrated visibility estimate derived for $\alpha$ Boo was V= 0.9739 $\pm$ 0.0006 (astronomical null = 0.0132 $\pm$ 0.0003), fully consistent with the value expected from its near infrared diameter measured at much longer baselines. Astrophysical nulls at the $10^{-3}$ level or lower have since been measured on smaller fainter targets, also with accuracies of a few $10^{-4}$ (Mennesson et al. 2011a and subsequent unpublished results).

However, for the NSC method to be effective, four main requirements must be met (e.g. Mennesson et al. 2013): (1) the beams shall eventually be recombined in a common single-mode waveguide, (2) the optical path difference must be stabilized around the central dark fringe with no fringe hop (i.e. $\simeq \lambda/5$ rms jitter is enough), (3) the interferometric signal must be sampled significantly faster than the atmospheric coherence time (or fringe tracker closed loop bandwidth), (4) background and individual beam signals must be recorded close in time to the fringe data. Near infrared feed-forward fringe tracking has recently been demonstrated at the LBTI (Defrere et al. in preparation), providing adequate levels of mid-infrared OPD stabilization (point 2). The LBTI nulling instrument observational procedure has also been designed to meet requirements (3) & (4). In particular, and as stated above, instantaneous background estimation errors are well approximated by zero mean gaussian white noise, and no significant long term bias was found in the background estimates, down to the few ppm level. This means that the mid-infrared background noise behavior will be no different from detector shot noise errors, which are dominating in the case of near infrared PFN observations. The only NSC requirement that is not met by the LBTI nuller is that the instrument is not strictly "single-mode", i.e. that the null observed is not just a function of beam relative intensities and relative piston. Higher order of differential phase aberrations will be present in the measured nulls, because the two telescope beams are not recombined in a common single-mode waveguide (point 1). However, we hope to mitigate such high spatial order effects by only using the central part of the PSF for all null and photometric computations. With

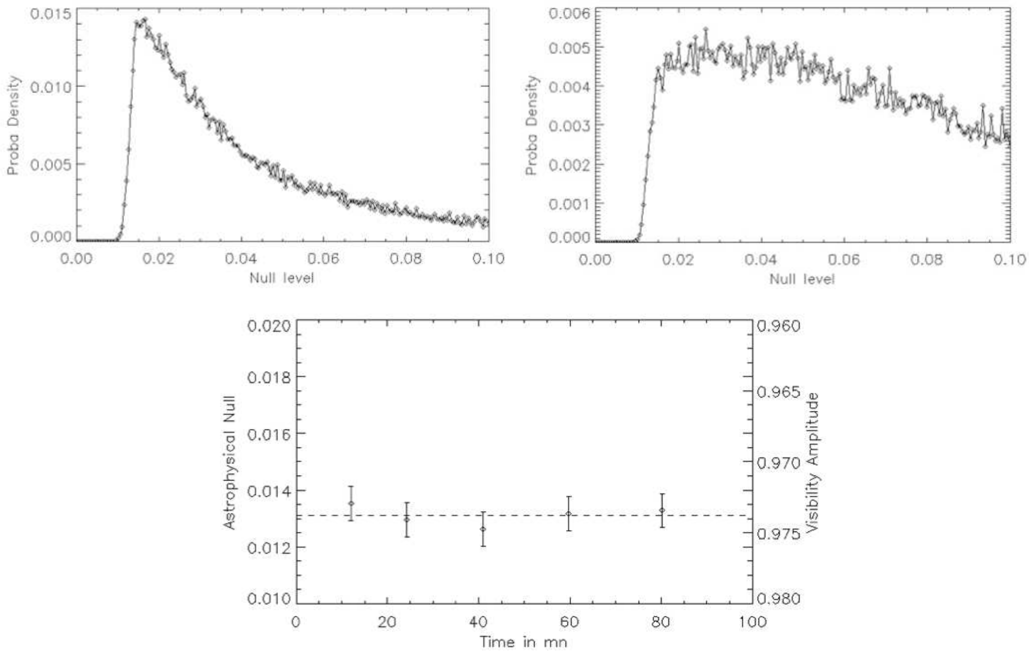


Figure 2.: *Palomar Fiber Nuller measurements of $\alpha$ Boo. Top panels: observed distributions of instantaneous interferometric signals (normalized to constructive interference case to provide an instantaneous null level) recorded at two different times - second and fifth measurements displayed in lower panel-. Lower panel: Object's visibility -right vertical axis- and equivalent astrophysical null depth -left vertical axis- measured as a function of time. No calibrator star was used; visibilities are derived using the null (or visibility) histogram modeling NSC technique (Mennesson et al. 2011a & 2011b, Hanot et al. 2011). All individual visibility error bars are about 0.0006. The final calibrated visibility estimate is V= 0.9739 +/- 0.0006. The dashed line indicates the astronomical null (or visibility) expected at the same spatial frequency, using $\alpha$ Boo's limb darkened diameter measured independently by NIR long baseline interferometry (Perrin et al. 1998, Lacour et al. 2008). A similar data reduction method will be applied to the mid-infrared LBTI nulling survey data.*

mid-infrared Strehl ratios higher than 98% and higher order wavefront errors leaking most light outside of that central diffraction limited area, we expect a small impact on the observed null distribution and the the NSC fitting procedure results.

## 5. Conclusions

High contrast interferometry is coming of age, with a number of facilities having already demonstrated point source detection capabilities approaching 1000:1 at angular scales of just a few milliarcseconds. This is already a remarkable performance given that the multi-baseline imaging systems providing these results are first generation multi-beam combiners, not necessarily optimized for high accuracy phase closure measurements. With some return of experience and the lessons learnt from aperture masking on single telescopes, high contrast long baseline stellar interferometry should be able to access dynamic ranges of $10^4$:1 or so on point sources in the next decade. However, this will only happen if a dedicated effort is pursued in that direction. This could take place at VLTI and CHARA in particular, since they are currently at the forefront of such programs -, or at future interferometric facilities such as the Planet Formation Imager which will likely have ambitious goals in terms of contrast. As the detection of extended sources is concerned, such as circumstellar material around pulsating stars and faint exo-zodi structures around mature stars, high visibility amplitude measurement accuracy is required. In particular, the exo-zodi nulling surveys led in the mid-infrared at the Keck Interferometer and in the near infrared at CHARA (Absil 2013) have already demonstrated contrast limits of 500:1 or more. With its requirement of reaching interferometric contrasts of $10^4$ or so, there is no doubt that the LBTI will stretch nulling (or equivalently visibility) measurement accuracy to its limits for the years to come. In the same way that long baseline phase closure experiments can benefit from aperture masking techniques developed for single telescopes, the LBTI will capitalize on new nulling data reduction techniques elaborated at the Palomar Hale telescope for the Fiber Nuller instrument. Using near infrared nulling on a short 3.2m baseline and the "Null Self Calibration" data reduction method (also applicable to visibilities), the Palomar Fiber Nuller demonstrated null accuracies down to a few $10^{-4}$. These null levels are the deepest reported so far on the sky, and are commensurate with the ambitious LBTI objectives.

*Acknowledgements.* This work was performed at the Jet Propulsion Laboratory, California Institute of Technology, under contract with NASA. The Keck Observatory was made possible through the generous financial support of the W.M. Keck Foundation.

## References

Absil, O., 2011, A&A, 535, 68

Aufdenberg, J.M. et al. 2006, ApJ, 465, 664

Baade, W. 1926, Astronomie Nachrichten, 228, 359

Balan, A. et al. 2010, AJ, 139, 2269

Beichman, C. et al. 2006, SPIE, 6268, 25
Bracewell, R. N., 1978, Nature, 274, 780
Bryden, G. et al. 2009, ApJ, 785, 89
Burtscher, L. et al. 2013, A&A, 558, 149
Colavita, M.M. et al. 2013, PASP, 125, 1226
Coude du Foresto, V. et al. 1998, Proc. SPIE Vol. 3350, p. 856-863, Astronomical Interferometry, Robert D. Reasenberg
Domicinao de Souza, A. et al. 2003, A&A, 407, L47
Duvert, G. et al. 2010, A&A, 509, 66
Galenne, A. et al. 2014, A&A, 561, 3
Galenne, A. et al. 2013b, A&A, 558, 140
Galenne, A. et al. 2013a, A&A, 552, 21
Haguenauer, P. & Serabyn, E. 2006, Applied Optics, 45, 12
Hanot, C., et al. 2011, ApJ 729, 110
Hinkley, S. et al. 2011, ApJ, 730, L21
Hinz, P. 2013, AAS Meeting 221
Huelamo et al. 2011, A&A, 528, 7
Ireland, M. 2013, MNRAS, 433, 1718
Kraus, A. & Ireland, M. 2012, ApJ, 745, 5
Kervella, P. et al. 2006, A&A, 448, 623
Kloppenborg, B. K., et al, 2010, Nature, 464, 870
Lacour, S. et al. 2008, A&A, 485, 561
Lawler, S.M. et al. 2009, ApJ, 705, 89
Le Bouquin, J. B., et al. 2011, A&A, 535, 67
Leger, A. et al. 1996, Icarus, 123, 249
Lopez, B. et al. 2012, Proc. of the SPIE , Vol. 8445
Martin, S. R. & Booth, A. J., 2010, 511, L1
Martin, S. R. et al, 2008, Proc. of the SPIE, Vol. 7013. Edited by Schller, Markus; Danchi, William C.; Delplancke, Franoise.
McAlister, H. A., 2005 et al., 2005, ApJ 628, 439
Mennesson, B. et al. 2013, Journal of Astronomical Instrumentation, Vol. 2, Special Issue Optical and Infrared Interferometry; Guest Editors: Theo ten Brummelaar, Peter Tuthill and Gerald van Belle
Mennesson, B. et al. 2011a, ApJ, 736, 14
Mennesson, B. et al. 2011b, ApJ 743, 178
Mennesson, B. et al. 2006, in SPIE Conf. Ser. 6268, Advances in Stellar Interferometry, ed. J.D. Monnier, M. Scholler, W.C. Danchi, 95
Mennesson, B. et al. 2003, Conference on Towards Other Earths: DARWIN/TPF and the Search for Extrasolar Terrestrial Planets, Edited by M. Fridlund, T. Henning, ESA SP-539, p. 525 - 528
Mennesson, B. et al. 2002, ApJ, 579, 446
Merand, A. et al. 2005, A&A, 438, L9

Merand, A. et al. 2006, in SPIE Conf. Ser. 6268, Advances in Stellar Interferometry, ed. J.D. Monnier, M. Scholler, W.C. Danchi, 46

Millan-Gabet, R. et al. 2011, ApJ, 734, 67

Monnier, J. et al. 2007, Science, 317, 342

Nardetto, N. et al. 2004, A&A, 428, 131

Perrin, G. et al., 2004, A&A, 426, 279

Perrin, G. et al., 1999, A&A, 345, 221

Perrin, G. et al., 1998, A&A, 331, 619

Sabbey C.N. et al. 1995, ApJ, 446, 250

Sandage, A. et al. 2006, ApJ, 653, 843

Scott, N. et al. 2013, Journal of Astronomical Instrumentation, Vol. 2, Special Issue Optical and Infrared Interferometry; Guest Editors: Theo ten Brummelaar, Peter Tuthill and Gerald van Belle

Serabyn, E. 2012, ApJ, 748, 55

Smith, R., Wyatt, M.C. & Haniff, C.A. 2009, A&A503, 265

Stock, N. et al. 2010, ApJ, 724, 1238

Su, K. Y. L. et al. 2006, ApJ, 653, 675

ten Brummelaar, T. A. et al. 2005, ApJ, 628, 453

van Belle G. T. , et al., 2006, ApJ 637, 494

van Belle G. T., et al. 2001, ApJ 559, 1155

Von Zeipel, H. 1924, MNRAS 84, 684

Weigelt, G. et al. 2011, A&A, 527, 103

Weinberger, A. 2014, AAS Meeting 223

Wesselink, A. J., et al., 1946, Bulletin of the Astronomical Institutes of the Netherlands, Vol. 10, p.91

Woillez, J. et al. 2013, in Optical and Infrared Interferometry III. Proceedings of the SPIE, Volume 8445

Wood, P. R. 1990, in From Miras to Planetary Nebulae, ed. M. O. Mennessier & A. Omont (Gif-sur-Yvette: Editions Frontieres), 67

Wyatt, M. et al. 2007, ApJ, 658, 569

Zhao, M., et al. 2011, PASP, 123, 964

*Improving the performances of current optical interferometers & future designs*
*Proceedings of Haute Provence Observatory Colloquium (23-27 September 2013)*
*Edited by L. Arnold, H. Le Coroller & J. Surdej*

# Kernel-phase for interferometry with a rich aperture

F. Martinache[1]

[1] *Laboratoire Lagrange, CNRS UMR 7293, Observatoire de la Côte d'Azur, Nice, France*

**Abstract.** This paper introduces kernel-phase, a framework developed to generalize and extend the application of closure-phase as it is used in the context of non-redundant aperture masking interferometry, that is compatible with a pupil of arbitrary geometry, if wavefront errors are small. This generalization has some powerful applications: large amounts of classical imaging archival AO and/or space borne data can be processed and lead to re-interpretation, in the light of this interferometric point of view of classical telescope image formation. Recent developments involving noise decorrelation procedures take kernel-phase one step closer to being the optimal observable extractable from an AO diffraction limited image or interferogram acquired from a rich interferometric array. While direct applications are so far mostly concerned with AO imaging, the ideas presented here are very relevant to interferometry at large: the framework offers a refreshing look at observing and data reduction strategies, in a manner that scales very well with the complexity of the interferometric array. The paper also shows that the linear algebra formalism used for kernel-phase allows for a very direct and computationally efficient approach to interferometric imaging.

## 1. Introduction

The observational success of optical interferometry relies for the most part on the properties of well defined and therefore well understood observable quantities: the visibility and the closure-phase (when three or more baselines are used simultaneously), used as proxies for measurements of local coherence of the electric field. From a finite number of well characterized visibilities and closure-phases, and without introducing too much a priori information, interferometry makes it possible to infer high-fidelity models or images of a wide variety of sources in a regime of resolution that goes beyond what is usually thought as possible when one is used to dealing with single-telescope observations.

These properties of interferometry, and the fact that it can beat the generally accepted Rayleigh resolution criterion, a regime referred to as super-resolution, have motivated its deployment back on single telescopes, where it is either called non-redundant masking (NRM) or sparse aperture masking (SAM) interferometry, first seeing-limited, and more recently used in conjunction with adaptive optics (AO).

These observations differ from most of the usual long-baseline interferometry in the all-in-one (Fizeau) recombination of a fairly large number of baselines (from tens to hundreds) that lead to interferograms looking not that different from conventional diffraction limited images, except in the structure of point-spread function (PSF) halo. The legacy of long-baseline interferometry is however very strong, and except for some more recent attempts at working in the image plane (Lacour et al, 2011), the bulk of the work is done by working on the Fourier counterpart of the image, where complex visibilities are extracted, to be processed and form squared visibilities and closure-phases, familiar to users of long baseline interferometry.

As we move toward interferometric combiners involving an increasing number of telescopes such as the VLTI 4-telescope combiners MATISSE (Lopez et al, 2012) and GRAVITY (Eisenhauer et al, 2011) or the 6-telescope combiner MIRC (Monnier et al, 2012) for the CHARA array, it seems appropriate to look back and reflect upon what single dish interferometric observations, already effectively combining up to several hundreds of apertures, can teach.

What comes out of this examination is that while it is possible to strictly adhere to the principles of long baseline interferometry, and maintain the use of canonical visibilities and closure-phase, this approach doesn't scale up well. One indeed ends up with a large number of highly correlated observables and is forced to work with a strictly non-redundant pupil that becomes cumbersome and inefficient when working with a large number of apertures.

Recent years have witnessed the introduction of a generalisation of the notion of closure-phase, a concept called kernel-phase that offers an efficient way of working with Fourier-phase information in the context of rich arrays. The framework of kernel-phase relies on a linear approximation that is for now only valid in a regime where piston errors are less than $\sim$1 radian. While the direct application of techniques presented in this paper is limited to this low piston error regime, the general ideas remain relevant to a wider set of conditions. The immediate advantage of kernel-phase over canonical closure-phase is that it can very well be extracted from Fizeau interferograms acquired with a redundant array: the technique is therefore relevant to both sparse pupil interferometry and conventional imaging. Section 2.3 of this paper shows how linear algebra formalism offers a convenient extension of the classical model of closure-phase suited to rich arrays, used in section 3. to introduce a generalisation of the closure-phase: the kernel-phase. Section 4. shows how kernel-phase is used to process AO data for high contrast imaging while section 5. introduces further development that shape the definition of better interferometric observables. Section 6. explores the use of kernel-phase for interferometric imaging.

## 2. A linear model for the Fourier-phase

The basis for the linear model leading to the definition of kernel-phase is easily grasped if one goes back to the NRM scenario and write simple equations for the phase. Fig. 1 describes the mechanism that links pupil phase and Fourier phase for a 9-hole non-redunant mask. A triangle of baselines in the pupil is highlighted along with the corresponding uv-locations in the powerspectrum. Expressions for the phase sampled at those three points are provided. By simply adding them, the piston terms cancels out: the result of this addition, called the closure-phase

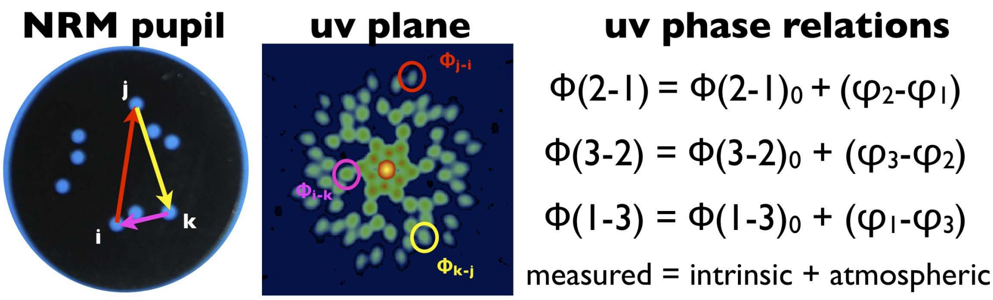


Figure 1.: *Example of closure phase relation. Superimposed on the image of the non-redundant pupil geometry shown in the left panel, is one of the possible closure triangles. The central panel shows the powerspectrum of one image acquired with one such pupil: each active region, often refered to as a splodge, is associated to a baseline in the pupil. The three splodges associated to the baselines chosen in the left panel are highlighted. On the right, are written relations for the phases of each splodge: the measured phase is the sum of a term intrinsic to the target being observed (the "true" phase), and an atmospheric term: the piston along the baseline. The reader will quickly observe that by adding these three relations together, the atmospheric term simply vanishes, leading to a new observable quantity, called the closure-phase.*

is therefore insensitive to residual pupil phase errors and contains information about the observed source only, making it a robust and powerful observable.

The 9-hole NRM used for this example allows to simultaneously measure 36 distinct phases in the uv plane. These 36 relations, all very similar to the ones highlighted in Fig. 1, can be gathered using the following matrix form:

$$\Phi = \Phi_O + \mathbf{A} \cdot \varphi, \tag{1}$$

where $\Phi$ is a 36-component vector encoding the phase sampled in the Fourier plane, $\Phi_O$ a 36-component vector encoding the true target phase information and $\varphi$ a 8-component representing the instrumental pupil phase (9-1 components since one aperture is chosen as piston reference). The important element of this model is the $36 \times 8$ transfer matrix $\mathbf{A}$ that describes the way the pupil phase propagates into the Fourier plane.

For this example, $\mathbf{A}$ is essentially filled with zeros, except for two positions per row, that respectively contain $+1$ and $-1$. In general terms, a closure relation can be thought of as a combination of rows of $\mathbf{A}$ that produce a zero vector. The closure-phase is a special case of linear relation, that simply adds together selected rows of $\mathbf{A}$ to give the zero-vector. More complex relations involving more than three rows of $\mathbf{A}$ can however be produced.

Nevertheless, the total number of independent relations remains constant, and is exactly 28 in this scenario. Closure relations form a basis for the left-hand null space (or Kernel) of $\mathbf{A}$. These relations can be gathered into a left-hand operator $\mathbf{K}$ that acts on $\mathbf{A}$ so that:

$$\mathbf{K} \cdot \mathbf{A} = \mathbf{0}. \tag{2}$$

Although already abstract, the canonical closure-phase is a convenient concept that is easy to grasp. Moreover, it is a natural choice and the only possible closure relation when the pupil is made of only three sub-apertures. In practice for a baseline-rich pupil like the 9-hole case used as an example, closure-phase alone is not the best solution, as similar triangles in the pupil do exhibit correlated closure-phases. The formalism introduced in this section will allow to directly produce relations that produce observables containing decorrelated signals.

## 3. Kernel-phase as a generalized closure-phase

What may at first be perceived as a complicated sleight of hand (the matrix form) to reformulate an otherwise simple and elegant idea (the closure-phase) reveals its true power when one looks beyond the usual strict non-redudant scenario of interferometry. For a rich arbitrarily shaped interferometric aperture such as the one of an unmasked telescope in the context of NRM-interferometry, lies an additional complication: baselines in the pupil are highly redundant and the useful interferometric signal $\Phi_O$ finds itself buried under multiple phase error contributions, resulting into a fairly complex (non-linear) expression for the $k^{\text{th}}$ component of the Fourier phase vector:

$$\Phi^k = \Phi_0^k + \mathrm{Arg}(\mathrm{e}^{\mathrm{j}\Sigma_\mathrm{i}\Delta\varphi_\mathrm{i}}), \tag{3}$$

where $i$ is an index to keep track of the $r$ identical baselines in the pupil, contributing to the same region of the uv plane. With a good wavefront correction (this approach has been validated both on space-based and ground-based data) - eq. 3 can be linearized as follows:

$$\Phi^k = \Phi_0^k + \frac{1}{r}\sum_i \Delta\varphi_i, \tag{4}$$

and the entire problem can again be written in the matrix form of eq. 1, with a modified transfer matrix. In this more general (redundant) scenario, each row of $\mathbf{A}$ now contains more than just two non-zero values. Whereas canonical closure-phases can no longer be extracted from data acquired under such conditions, it is still possible to find a left-hand operator $\mathbf{K}$ that verifies eq. 2.

While it is possible to identify by hand, friendly looking relations very much in the spirit of closure-phases if the pupil geometry is not too complex, it quickly becomes difficult when the transfer matrix $\mathbf{A}$ quickly gets quite big. The linear form of eq. 2 however enables the use of powerful tools of linear algebra, and a very efficient way of building the operator $\mathbf{K}$ is to calculate the singular value decomposition (SVD) of $\mathbf{A}$.

Among its mony other properties, the SVD indeed explicitly constructs an orthonormal basis for the right and left-hand side null-spaces of a matrix. The total number of kernel-phase relations $n_K$ is given by the number of zero singular values of $\mathbf{A}$. The SVD of $\mathbf{A}$ writes as: $\mathbf{A} = \mathbf{U\Sigma V^T}$, where $\mathbf{\Sigma}$ is a diagonal matrix containing the singular values of $\mathbf{A}$, and $\mathbf{U}$ and $\mathbf{V^T}$ are unitary matrices.

One of the best possible set of kernel-phase relations can be found in the columns of $\mathbf{U}$ that correspond to zeros on the diagonal of $\mathbf{\Sigma}$. They form an orthonormal basis for the left null-space (or kernel) of the phase transfer matrix, hence the name kernel-phase.

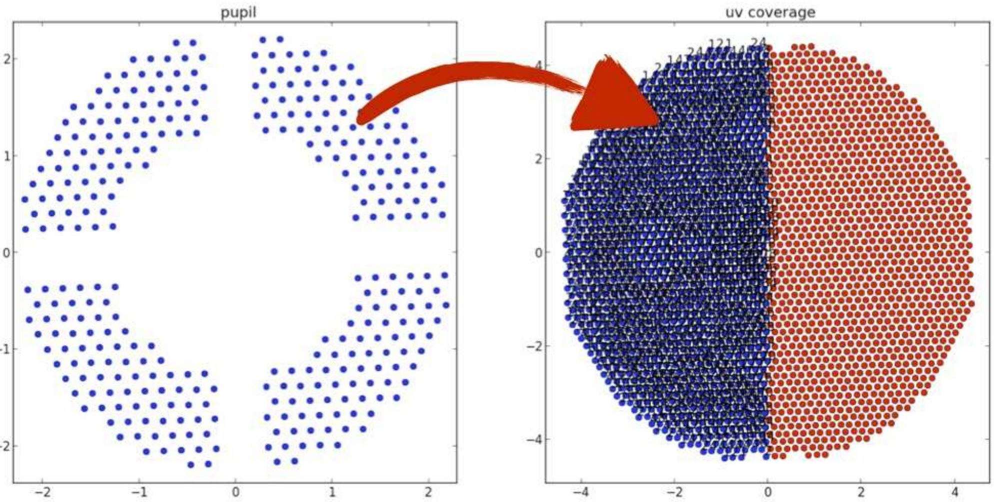


Figure 2.: *Example of discrete model used to construct the operator* **A**. *Left: discrete model of the instrument pupil, here following a regular hexagonal grid. Right: resulting distribution of spatial frequencies sampled by this geometry.*

Gathered into the operator **K**, these relations are then applied to the phase measured in the Fourier plane $\Phi$, to extract information about the target of interest that is immune to residual instrumental phase errors:

$$\mathbf{K} \cdot \Phi = \mathbf{K} \cdot \Phi_O. \tag{5}$$

## 4. Kernel-phase in practice

In practice, finding the phase transfer matrix **A** requires to build a discrete model of the pupil used to acquire the data. Fig. 2 shows the example of a model used to describe the "medium cross pupil" of the Palomar Hale Telescope PHARO instrument. A good discrete model requires a regular grid pattern, whose density is representative of the continuous pupil.

The model shown in Fig. 2 decomposes the telescope pupil into 332 interferometric apertures that map onto a 1128 distinct sample points in the Fourier domain. The SVD of the resulting $1128 \times 332$ operator **A** reveals that using this model, 962 kernel-phases can be extracted from any single image, assuming that it is at least Nyquist-sampled, which means that 85 % (962 kernels out of a total of potentially available 1128 phase samples) of the phase information is directly recoverable.

Once the paving of the uv-plane and the matching kernel-phase relations are identified, they are saved in a template and used for extracting the phase information from the data. Before being Fourier-transformed, frames undergo traditional dark subtraction and flat-fielding procedure. Additionally, to limit the impact of detector readout noise, the data can can be windowed, for instance with a "super-Gaussian" ($\exp -(r/r_0)^4$) radial profile. After the frame is Fourier-transformed, the phase is sampled at the relevant $(u, v)$ coordinates and assembled into the vector $\Phi$. Assuming that the data is at least Nyquist-sampled

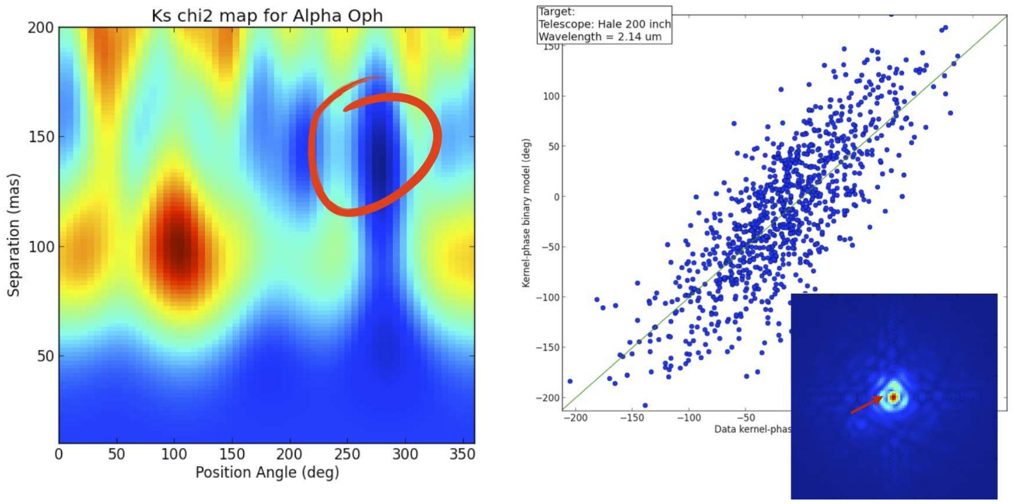


Figure 3.: *Example of kernel-phase result obtained on ground based AO data. Left: map of the $\chi^2$ in the position angle - angular separation space for $\alpha$-Ophiucus, observed with PHARO at the Palomar Hale Telescope, using the model shown in Fig. 2. A red circle highlights the location of the minimum $\chi^2$. Right: correlation plot between the kernel-phase data and the binary model for the corresponding location in the $\chi^2$ space. The image snippet shows (red arrow) that the 30:1 companion is apparently invisible, hidden under the first diffraction ring.*

allows all spatial frequencies to be extracted. Kernel-phase observables $\mathbf{K}\Phi$ are constructed using the pre-determined relations for each frame. Multiple frames on a given target and/or the availability of frames acquired on single stars allow further characterization of the Ker-phase data, using statistics and/or additional calibration.

Fig. 3 showcases the result of such data analysis, using the model of the PHARO medium cross pupil of Fig. 2, and applying to actual AO-corrected data acquired with this instrument. The target, $\alpha$-Ophiucus, is a well known binary with a well characterized, eccentric orbit with an 8.6 year period (Hinkley et al, 2011). The kernel-phase analysis of multiple PHARO frames acquired in the K-band revealed the presence of the 30:1 contrast companion at a position angle 274.6°, but at an angular separation 136.1 mas ($\sim 1.5\lambda/D$), that is directly underneath the first diffraction ring.

After extraction, the kernel-phases are used as constraints in a 3-parameter binary model (separation, position angle and contrast). Conventional likelihood analysis and/or Monte-Carlo simulations provide a binary solution or contrast detection limits. The companion, undetectable in the direct image, due to variance in the PSF, is clearly detected using this approach. The position deduced from the binary model fit is in very good accordance with the ephemerides of the orbit.

## 5. Beyond kernel-phase

By construction, the different signals encoded in kernel-phases form an orthonormal basis, that makes them ideal linearly independent entries for a parametric model such as the one used in the previous example, or a more general image reconstruction software. In practice, this construction however does not guarantee statistical independence. If not accounted for, noise processes affecting the image (where the detection process really happens) can very well lead to correlated Fourier-phases, that will result in correlated observables. In addition to building observables that linearly independent in terms of signal, it is therefore also necessary to make them statistically independent in terms of noise.

This is the observation made by Ireland (2013), who proposes to further improve the observables, by carefully computing the associated covariance matrices for the visibility and the Fourier-phase. Several noise processes are expected to lead to correlated Fourier-phases: photon noise, detector readout noise or lag in the AO correction; are the first of a potentially long list.

It is possible to determine this covariance matrix using simulations or formal calculations for the best understood phenomena. In practice however, the combined effect of all sources of noise can be taken into account by observing a point source calibration star, right before or after the target of interest, under observing conditions (seeing, elevation, source magnitude and color, AO parameters) as close as possible to the ones experienced on the target of interest. The kernel-phases recorded on a point-source should all average to zero, but the statistical properties of the Fourier-phase recorded in multiple successive frames will inform about the correlation properties of the different noise processes.

If one calls this experimental covariance matrix for the Fourier-phase $\mathbf{C}_F = \mathrm{cov}(\Phi)$, the covariance matrix for the kernel-phase $\mathbf{C}_\mathbf{K}$ writes as:

$$\mathbf{C}_K = \mathrm{cov}(\mathbf{K}\Phi) = \mathbf{K} \cdot \mathrm{cov}(\Phi) \cdot \mathbf{K}^\mathrm{T} = \mathbf{K} \cdot \mathbf{C}_\mathrm{F} \cdot \mathbf{K}^\mathrm{T} \tag{6}$$

The covariance being a square, positive semi-definite matrix, it can be diagonalized using a form simpler than that of the SVD:

$$\mathbf{C}_K = \mathbf{S} \cdot \mathbf{D} \cdot \mathbf{S}^\mathbf{T}, \tag{7}$$

where $\mathbf{S}$ is a unitary matrix and $\mathbf{D}$ a diagonal matrix containing the eigen values of $\mathbf{C}_\mathbf{K}$. The important element of this decomposition is $\mathbf{S}$, which allows to turn previously correlated kernel-phases into a set of statistically independent kernel-phases $\theta$:

$$\theta = \mathbf{S} \cdot \mathbf{K} \cdot \Phi. \tag{8}$$

Using photon noise simulations on kernel-phase in the context of high-contrast detection, Ireland (2013) shows that this simple procedure improves the contrast detection limits in a very convincing manner. Kernel-phase, as initially described in (Martinache 2010), exhibits a fairly uniform contrast detection limit beyond a separation greater than $\lambda/D$, which is unlike any standard imaging contrast detection limits rapidly increases as a function of angular separation.

After diagonalizing the effect of photon noise on kernel-phases, using the statistically independent observables introduced in Eq. 8, Ireland (2013) show that contrast detection limits increase as a function of angular separation, and exhibit an overall performance superior over correlated kernel-phases.

## 6. Kernel-phase imaging

Most of work so far done with kernel-phase extracted from AO data has been applied to high contrast detection of binary sources. This application uses the $\chi^2$-minimization approach of a 3-parameter model (angular separation, position angle and contrast). Results of this technique can be found in (Martinache, 2010; 2012) and (Pope et al, 2013).

A binary model search is a very well constrained problem, with only three degrees of freedom for a generally large numbe of kernel-phases. Here we look into the application of a less constrained problem: a more generic imaging test case, like what is routinely done in radio interferometry and can be achieved on some bright sources with long baseline optical interferometry. The Van-Cittert Zernike theorem relates the brightness distribution of the source being observed to measurements of the coherence of the electric field in the uv-plane, itself estimated from the visibility and/or the phase of the interference function.

The quality of the brightness distribution map reconstructed from the interferometric measurements greatly depends on the density of the uv-coverage offered by the array. For a given number of apertures in a sparse geometry, the richest coverage is obtained when a non-redundant pattern is used. Geometries used for NRM-interferometry typically rely on the designs established by Golay (1971) that use three-fold symmetry to produce a compact and dense uv-coverage.

Yet there is a limit to how rich the uv coverage can get while maintaining non-redundancy in a finite spectral bandwidth when the array footprint needs to be contained within say a circle. We have seen that kernel-phase makes strict non-redundancy a non-necessary requirement. A comparative study of several pupil geometries (Martinache, 2012) has shown that even when they provide identical uv-coverage, some configurations do provide a better phase information recovery-rate, defined as the ratio of the number kernel-phase $n_K$ and the number of baselines $n_{UV}$. A good (and often exact) estimate of the number of kernel-phases that can be extracted from an array made of $n_A$ apertures is:

$$n_K = n_{UV} - \frac{n_A}{2}, \tag{9}$$

indicating that for a given uv-coverage, the array with the smallest number of aperture will provide the highest phase information recovery rate: an annular geometry seems to provide an optimal. The results presented in this section use the anticipated geometry of the thirty meter telescope (TMT) primary mirror for a test scenario. The sampling of the uv plane is made so as to produce baselines that match the hexagonal grid of the 492 segments making the primary. Keeping only the outermost 78 segments provides access to the same uv-coverage and results in a total phase information recovery rate $\sim 96$ %, to be compared to the $\sim 75$ % the full pupil would give.

One very convenient consequence of expressing the phase relations in terms of linear algebra (cf. eq. 1) is that the matrix form allows the construction of a pseudo-inverse to the kernel-phase operator $\mathbf{K}^+$.

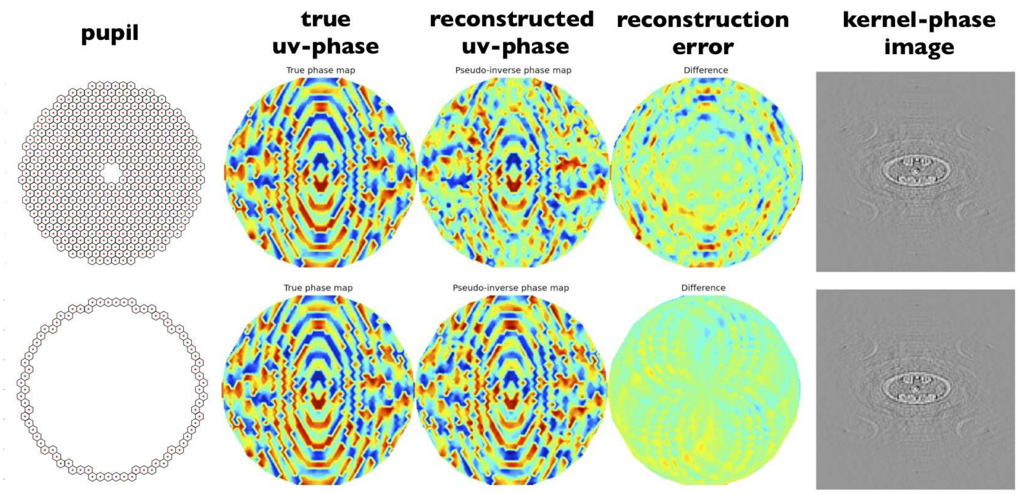


Figure 4.: *Kernel-phase image reconstruction experiment, comparing the phase (and resulting image) reconstruction achieved by a full pupil (top row) to the one achieved by annulus (bottom row). Each row successively shows (from left to right): the pupil, the true uv-phase-map of a simulated source (identical in both cases), the uv-phase-map reconstructed from kernel-phases alone, the reconstruction error and the kernel-phase image, determined from a direct inverse Fourier Transform of the reconstructed phase-map. Note: all six phase-maps use the same color-scale.*

Even for a full-aperture, $\mathbf{K}$ preserves a large fraction of the original uv-phase information while clearing it of all residual wavefront error. The use of a pseudo-inverse $\mathbf{K}^+$ is therefore expected to yield direct access to a reasonably accurate representation of the true object uv-map $\Phi'_O$. The uv-phase estimate:

$$\Phi'_O = \mathbf{K}^+ \cdot \mathbf{K} \cdot \Phi, \tag{10}$$

can directly be used as input for an interferometric imaging program. Fig. 4 compares the phase reconstruction capability of this approach on the full pupil and the annulus. We can verify that both geometries manage to preserve a large fraction of the uv-phase information: while some differences can be appreciated in the fidelity of the pseudo-inverse by comparing the reconstruction error maps, the features of the images determined from direct inverse Fourier transform of the phase-maps, differ very little and are very close to what a reconstruction relying on a perfect knowledge of the phase would achieve. Admittedly, the simulation is simplistic. It nevertheless confirms that the pseudo-inverse approach is sound. The $\mathbf{K}^+ \cdot \mathbf{K}$ operator can easily be used as a way to bypass the abstract kernel-phase intermediate as a direct way to work in uv-phase space. A small fraction of the uv-phase is lost in the process, but the instrumental phase errors are filtered out. These cleaned uv-phase can in turn be related to the source brightness distribution map, like what is shown in Fig. 4.

## 7. Conclusions

This paper has introduced the idea of kernel-phase, a generalization of the more usual notion of closure-phase that can be used in the context of an all-in-one Fizeau combiner, regardless of the array geometry. Kernel-phase relies on a simple linear model that describes the way instrumental phase errors propagate into the uv-plane, and pollute the information relevant to the target of interest. This formal approach allows for the deployment of powerful computational tools: singular value decomposition and pseudo-inverses, which combined with further noise decorrelation procedures, allow for optimal information extraction strategies, relevant to a wide range of applications: from high contrast detections to general interferometric imaging.

To keep things going in one direction, this paper has voluntarily excluded the applications of the linear model relevant to wavefront sensing. Interested readers should refer to (Martinache, 2013) for further details about this complementary problem that isn't concerned with the kernel- but with the eigen-phases of the phase transfer operator **A**.

It should finally be mentioned that the discussion has been restricted to the study of the phase in the uv-plane, and therefore excluded all consideration for the amplitude of the complex visibility. Yet, one knows that simultaneously combining four baselines and more should enable the determination of a closure-amplitude in addition to several kernel-phases. One wonders whether an adaptation of the formalism used here is possible so as to propose a comparable treatment for the amplitude. While this question is being investigated, it is not obvious whether such a treatement is possible.

## References

Eisenhauer, F. et al, 2011, Msngr, 143, 16

Golay, M., 1971, JOSA, 61, 272

Hinkley, S. et al, 2011, ApJ, 726, 104

Ireland, M. J., 2013, MNRAS, 433, 1718

Lacour, S., Tuthill, P., Amico, P., Ireland, M., Ehrenreich, D., Huelamo, N. & Lagrange, A. M., 2011, A&A, 532, 72

Lopez, B. et al, 2012, SPIE, 8445, 84450R

Martinache, F., 2010, ApJ, 724, 464

Martinache, F., 2012, SPIE, 8445, 844504

Martinache, F., 2013, PASP, 125, 422

Monnier, J. D., 2012, SPIE, 8445, 84450Y

Pope, B. et al, 2013, ApJ, 767, 110

*Improving the performances of current optical interferometers & future designs*
*Proceedings of Haute Provence Observatory Colloquium (23-27 September 2013)*
*Edited by L. Arnold, H. Le Coroller & J. Surdej*

# DISCO: a Spatio-Spectral Recombiner for Pupil Remapping Interferometry

F. Millour[1], R. Petrov[1], S. Lagarde[1], P. Berio[1], Y. Bresson[1], L. Abe[1]

[1]*Laboratoire Lagrange, UMR7293, Université de Nice Sophia-Antipolis, CNRS, Observatoire de la Côte d'Azur, Bd. de l'Observatoire, 06304 Nice, France*

**Abstract.** Pupil-remapping is a new high-dynamic range imaging technique that has recently demonstrated feasibility on sky. The current prototypes present however deceiving limiting magnitude, restricting the current use to the brightest stars in the sky. We propose to combine pupil-remapping with spatio-spectral encoding, a technique first applied to the VEGA/CHARA interferometer. The result is an instrument proposal, called "Dividing Interferometer for Stars Characterizations and Observations" (DISCO). The idea is to take profit of wavelength multiplexing when using a spectrograph in order to pack as much as possible the available information, yet providing a potential boost of 1.5 magnitude if used in existing prototypes. We detail in this paper the potential of such a concept.

## 1. Introduction

The need for a better dynamic range in direct imaging techniques is today identified as a top priority for the detection and characterization of extrasolar planets. As an illustration, several high-dynamic range imaging instruments are currently being developed (notably: SPHERE, HICIAO or GPI / Beuzit et al. 2006; Tamura & Abe 2006; Macintosh et al. 2006). These instruments make use of so-called "Extreme-Adaptive Optics" (XAO) in order to make coherent (i.e. interfering) the highest number of photons in the resulting image.

An other way existed before the advent of adaptive optics to get coherent photons: speckle imaging (Labeyrie 1970; Lohmann & Weigelt 1978) makes use of short-integration times to freeze the Earth's atmosphere disturbance and take over its resolution-washing effect. However, the speckle technique and all of its derivatives (speckle masking, segment tilting, lucky imaging, etc.) are bound to waste photons in a way or in another. This is why pupil remapping was proposed by Perrin et al. (2006), to take profit of both fully coherent photons and full-pupil flux collection.

Since the original idea was proposed, pupil remapping has evolved from a pure concept up to a readily demonstrated instrument on-sky (Huby et al. 2012, 2013). The built prototypes have shown the great potential of this technique and also some limitations.

Here, we propose an improvement over the pupil remapping concept as presented in Huby et al. (2012), in order to collect more photons per pixel for a given setup. While this might sound useless for some applications where pixels are "cheap" (like in visible applications), IR wavelength detectors still have limitations on their detector readout noise, making each pixel valuable. A sketch of such an instrument is presented in Fig. 1, which is similar to the proposal of Perrin et al. (2006). It differs mainly in the addition of short-stroke delay lines to control the optical path difference (hereafter OPD) and in the output pupil configuration, which is described in the next section.

We will therefore briefly describe how do we plan to save on pixels, and present optimized OPD configurations to use in such an instrument.

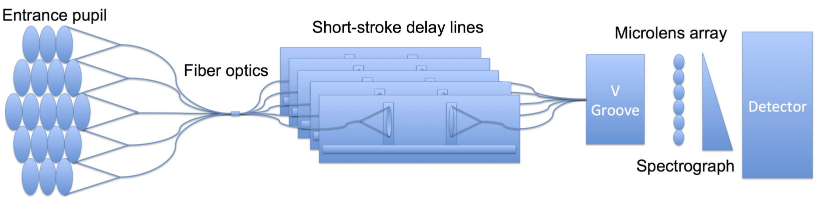


Figure 1.: *A possible setup for DISCO. Please note the similarities with the sketch in Perrin et al. (2006). The differing parts are the short-stroke delay lines and the arrangement of fibers in the V groove, described in the current paper.*

## 2. A recall of the technique and proposal of a new scheme

In an all-in-one multi axial interferometer, several beams are combined altogether, coding the fringes by their frequencies. One baseline corresponds then to one spatial frequency (a "fringe peak") in the Fourier Transform (FT) of the fringe pattern.

It has long been theorized that only a fully non-redundant configuration would allow one to extract the interferometric signal. Hence, several instrument were built on such a beam configuration: the AMBER (Petrov et al. 2007), or MIRC (Monnier et al. 2004) combiner are a few examples.

However, it was proposed in the first times of optical long-baseline interferometry (Vakili & Koechlin 1989), any more recently demonstrated on a wider scale with the VEGA instrument (Mourard et al. 2011), that a fully redundant configuration could also be used given that the fringes could be spectrally dispersed with a sufficient spectral resolution. In such a case, the fringe peaks of several baselines are at the same spatial frequency, noted $V_{pi}$ in order to take the same notation as in Mourard et al. (2011), making them totally cluttered in usual analysis algorithms. However, they can be disentangled by inputting a different fixed OPD, which in turn allows one to change the peaks positions in the wavelength frequency domain, noted $U_{pi}$ in Mourard et al. (2011). A different approach for data analysis has to be used, with the use of 2D FTs instead of 1D FTs, which is extensively described in Mourard et al. (2011). An additional way of uncluttering the fringe peaks is to input an OPD modulation on groups of sub-apertures and to make use of 3-dimensional Fourier Transforms (the third dimension being along time), as was proposed by Vakili & Koechlin (1989).

We reproduce in Fig. 2 the 9 sub-apertures non-redundant output pupil used in the FIRST instrument (Huby et al. 2012), and side to side, the output pupil of a fully redundant configuration.

Figure 2.: *On top is the output pupil of a fully redundant configuration. On the bottom is the non-redundant configuration used in the prototype FIRST instrument.*

Such a configuration saves a great deal of pixels compared to non-redundant configuration, with a given number of sub-apertures and spectral resolution. In the case of 9 sub-apertures, one can save a factor 5, i.e. a direct $\approx 1.5$ magnitude gain given the same spectral resolution.

We evaluate in the next section the requirements and identified limits of such an instrument.

## 3. Optimizing a spatio-spectral interferometer

### 3.1 Spectral resolution

When dealing with fully redundant output pupil for an interferometer, one needs to set a minimum OPD distance between the peaks in order to avoid peaks overlap. On the other hand, the applied OPDs must not exceed a fraction of the coherence length of the fringe pattern, otherwise loss of contrast and under sampling effects would occur.

These conditions provide guidelines that will set the range of spectral resolution and the values of OPD offsets to use in such an instrument.

*Minimal condition*

We recall the minimal condition on the number of spectral channels to use, given in Mourard et al. (2011, equation 13):

$$N_{\mathrm{ch}} \geq 2N_{\mathrm{tel}} \tag{1}$$

This puts a condition on the minimum spectral resolution to use:

$$R \geq 2N_{\mathrm{tel}}\frac{\lambda_0}{\Delta\lambda} \tag{2}$$

with $\lambda_0$ the central wavelength of the observations, and $\Delta\lambda$ the observation bandwidth. For a 9 sub-apertures instrument, working in the K band ($\lambda_0 = 2.2\mu$m, $\Delta\lambda = 0.4\mu$m), this imposes a minimum spectral resolution of $\approx 100$.

However, this is a conservative limit, as there are $N_{\mathrm{tel}} - 1$ fringe peaks for a given frequency, which hence can be compared with $N_{\mathrm{tel}} - 2$ minimal distances. We call CDR the ratio between the largest necessary OPD to input for one given configuration and the shortest distance between two adjacent peaks.

This CDR can be optimized but is always by construction greater or equal to $N_{\rm tel} - 2$ and depends on the number of sub-apertures used. In the example given above, for a 9-subapertures configuration, we get a CDR of 7 (see Table 1). This translates into a minimum spectral resolution of $\approx 80$.

When optimizing the configuration (section 3.3), we can see that this CDR can be used as a criterion to minimize, in order to pack as much as possible the fringe peaks together.

*Atmosphere and/or adaptive optics jitter*

Another criterion to consider is the wobbling of the fringe peaks by natural-atmospheric or adaptive optics-induced OPD. The peaks separation in the $U$ direction must be greater than twice the atmospheric wobbling. If we consider the atmospheric OPD over Paranal which has a peak overrun $\mathrm{OPD_{max}}$ of typically $25\mu$m (Tatulli et al. 2007), this means that two adjacent fringe peaks must be separated typically by $50\mu$m.

This imposes conditions on the coherence length $L_c$, that must follow the condition:

$$L_c \geq 2\mathrm{CDR} \times \mathrm{OPD_{max}} \tag{3}$$

or

$$R \geq \frac{2\mathrm{CDR} \times \mathrm{OPD_{max}}}{\lambda_0} \tag{4}$$

So, still for the 9-telescope configuration example given above, the minimum spectral resolution to use would be $\approx 160$. We see that in such a configuration, the fringes wandering by the atmosphere is by far the most stringent constrain on the spectral resolution. However, the use of adaptive optics prior to the input pupil (by reducing the OPD wandering from $25\mu$m to less than $1\mu$m), or the use of OPD modulation proposed in Vakili & Koechlin (1989) could strongly relax this constrain.

*Fringe peaks overlap*

As was highlighted by J. Monnier during the conference, an overlap of the fringe peaks could occur due to the spectrum shape of the target. Two ways of overcoming this effect were presented in Mourard et al. (2011) by using differential measurements combined with either setting a minimal width of the work channel, or by solving a set of equation describing the peaks overlap.

It is worth to mention that partial peaks overlap could also occur in non-redundant configurations, as happens in the AMBER instrument (Millour et al. 2004; Tatulli et al. 2007). The use of an image-based algorithm (the P2VM) solves this issue, and one could consider also using a 2D-image-based model-fitting algorithm, similar to the P2VM, to avoid the peaks contamination in our case.

### 3.2 OPD offsets optimization

In the literature, a few papers consider the problem of optimizing frequencies in an array. We can cite for example Moffet (1968); Vertatschitsch & Haykin (1986); Ribak et al. (1988); Pearson et al. (1990) for aligned sub-apertures with or without some redundancy, and Golay (1971) for 2D optimization. However, we found no trace of spatio-spectral optimization, except in the two papers Vakili & Koechlin (1989); Mourard et al. (2011) where setups for specific configurations were provided.

In Mourard et al. (2011) are addressed the cases of 3 and 4 telescopes for the spatio-spectral instrument VEGA. In Vakili & Koechlin (1989) is presented an example with 12 telescopes. Since we discuss the possibility to combine tens of sub-apertures for a potential full-pupil instrument, we investigated the optimization of the spatio-spectral scheme for up to 64 sub-apertures, though we present here only a subset, up to 30 sub-apertures.

We considered for this optimization the minimization of the CDR, in order to separate the peaks at maximum. We define this new criterion instead of using moment of inertia or other criteria defined in Golay (1971) because though we end up with 2D fringe peaks patterns, we aim at only optimizing one dimension (the OPD dimension).

We made use of a Monte-Carlo approach similar as in Ribak et al. (1988), using a simulated annealing algorithm. Indeed, the number of fringe peaks for a given configuration scales as $N_{\rm tel}^2$, so the number of distances between fringe peaks to optimize scales as $N_{\rm tel}^4$. Therefore simple optimization methods like gradient descent would fail in finding an acceptable solution.

Table 1 shows the results of our optimization for up to 9 sub-apertures with the corresponding CDR and minimum spectral resolution to use given an uncorrected atmosphere similar to Paranal. Interestingly, these 7 configurations happen to have exactly CDR = $N_{\rm tel} - 2$, i.e. there exist no configurations more compact for these numbers of sub-apertures (though there exist other configurations with the same compactness, in which case we select the configuration with the least number of high-value OPD). The corresponding OPDs are given in $\mu$m for an instrument working in the K-band ($\lambda_0 = 2.2\mu$m, $\Delta\lambda = 0.4\mu$m). We see that a even a moderate spectral resolution of $\approx 160$ can be used to combine 9 telescopes.

Table 1.: *7 most compact optimized OPDs for different interferometer configurations. We provide also the minimum required spectral resolution to avoid fringe peak overlap under a Paranal-like atmosphere in the K-band, and provide the OPDs for this spectral resolution (in $\mu$m)*

| | | | Beam # OPD offset | | | | | | | | |
|---|---|---|---|---|---|---|---|---|---|---|---|
| $N_{\rm tel}$ | CDR | $R_{\rm min}$ | 1 | 2 | 3 | 4 | 5 | 6 | 7 | 8 | 9 |
| 3 | 1 | 33 | -36 | 36 | -36 | | | | | | |
| 4 | 2 | 45 | -50 | 50 | -50 | -50 | | | | | |
| 5 | 3 | 68 | 75 | -75 | -25 | -75 | 75 | | | | |
| 6 | 4 | 91 | -100 | 100 | 0 | 100 | -100 | -100 | | | |
| 7 | 5 | 114 | 25 | -125 | 125 | 75 | 125 | -125 | 25 | | |
| 8 | 6 | 136 | 150 | 50 | -150 | -150 | -50 | 150 | -150 | 150 | |
| 9 | 7 | 159 | -25 | 125 | 175 | -175 | 75 | -175 | 175 | 125 | -25 |

Figure 3 illustrates the appearance of the 2D Fourier transform by materializing the positions of the fringe peaks for 3 to 9 sub-apertures.

We also note that these given offset can be set as fixed OPDs, but can also be set as fringe drift speeds, if one considers a fully redundant interferometer with OPD modulation. In such case, instead of inputting fixed OPDs and analyzing

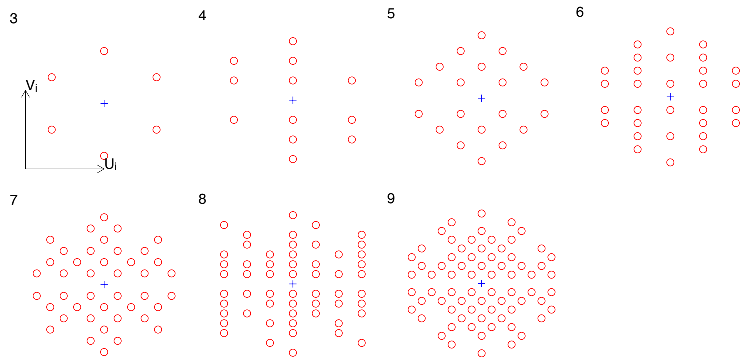


Figure 3.: *The UV fringe peaks relative positions of the most compact optimized OPDs of Table 1.*

the data as a function of wavelength, one can input OPD drifts with drifting speed proportional to the values in Table 1, and analyze the data as a function of time. The great advantage of this alternate solution is to allow for a broadband instrument to be setup. A detailed analysis of such a concept is out of the scope of the current paper.

### 3.3 Avoiding zero OPD

We see in Fig. 3 that up to 6 fringe peaks can be exactly at OPD 0 (for the 8 telescope configuration), which in some cases can be annoying due to the diffraction spike of the zero-frequency photometric peak. A way of overcoming such an issue is to input additional OPD offsets to the ones provided here, which are proportional to the sub-aperture number. Such additional OPD offsets "skew" the peaks position sketch shown in Fig 3 and move all the central fringe peaks away from the zero OPD. Such an additional offset degrades slightly the CDR of the configuration. For example, for sub-aperture, one would need to add to the values of Table 1, OPD offsets of 4, 8, 12, 16, 20, 24, 28, 32 and 36 $\mu$m on each sub-aperture, making none of the fringe peaks at the zero OPD. The final CDR is 7.5 instead of 7.

## 4. Conclusions

We discussed the requirements and limitations of a spatio-spectral recombiner, for a large number of sub-apertures.

We found that 7 configurations exist with the most densely packed fringe peaks, allowing for relatively low spectral resolutions to be used.

These revised configuration provide more densely packed fringe peaks than before, allowing for a gain in spectral resolution and therefore in sensitivity of such an instrument concept.

*Acknowledgements.* We thank J. Monnier and M. Ireland for their questions on the instrumental concept and fringe peaks overlap.

**References**

Beuzit, J.-L., Feldt, M., Mouillet, D., et al. 2006, in IAU Colloq. 200: Direct Imaging of Exoplanets: Science and Techniques, ed. C. Aime & F. Vakili, 317–322

Golay, M. J. E. 1971, Jour. Opt. Soc. America, 61, 272

Huby, E., Duchêne, G., Marchis, F., et al. 2013, A&A, 560, A113

Huby, E., Perrin, G., Marchis, F., et al. 2012, A&A, 541, A55

Labeyrie, A. 1970, A&A, 6, 85

Lohmann, A. W. & Weigelt, G. P. 1978, in Optical Telescopes of the Future, ed. F. Pacini, W. Richter, & R. N. Wilson, 479–494

Macintosh, B., Graham, J., Palmer, D., et al. 2006, in Society of Photo-Optical Instrumentation Engineers (SPIE) Conference Series, Vol. 6272, Society of Photo-Optical Instrumentation Engineers (SPIE) Conference Series

Millour, F., Tatulli, E., Chelli, A. E., et al. 2004, in SPIE Conference series, ed. W. A. Traub., Vol. 5491 (SPIE), 1222

Moffet, A. 1968, IEEE Transactions on Antennas and Propagation, 16, 172

Monnier, J. D., Berger, J.-P., Millan-Gabet, R., & Ten Brummelaar, T. A. 2004, in New Frontiers in Stellar Interferometry, Proceedings of SPIE Volume 5491. Edited by Wesley A. Traub. Bellingham, WA: The International Society for Optical Engineering, 2004., p.1370, ed. W. A. Traub, 1370

Mourard, D., Bério, P., Perraut, K., et al. 2011, A&A, 531, A110

Pearson, T. J., Unnikrishna, P., & Youngjik, L. 1990, IEEE transaction on information theory, 36, 6

Perrin, G., Lacour, S., Woillez, J., & Thiébaut, É. 2006, MNRAS, 373, 747

Petrov, R. G., Malbet, F., Weigelt, G., et al. 2007, A&A, 464, 1

Ribak, E. N., Hochberg, E. B., Page, N. A., Synnott, S. P., & Breckinridge, J. B. 1988, in European Southern Observatory Conference and Workshop Proceedings, Vol. 29, European Southern Observatory Conference and Workshop Proceedings, ed. F. Merkle, 1105–1116

Tamura, M. & Abe, L. 2006, in IAU Colloq. 200: Direct Imaging of Exoplanets: Science and Techniques, ed. C. Aime & F. Vakili, 323–328

Tatulli, E., Millour, F., Chelli, A., et al. 2007, A&A, 464, 29

Vakili, F. & Koechlin, L. 1989, in Society of Photo-Optical Instrumentation Engineers (SPIE) Conference Series, Vol. 1130, Society of Photo-Optical Instrumentation Engineers (SPIE) Conference Series, ed. J.-P. Swings, 109–116

Vertatschitsch, E. & Haykin, S. 1986, Proceedings IEEE, 74, 217

*Improving the performances of current optical interferometers & future designs*
*Proceedings of Haute Provence Observatory Colloquium (23-27 September 2013)*
*Edited by L. Arnold, H. Le Coroller & J. Surdej*

# Session 9. Progress in data reduction and image reconstruction techniques

Chair: Sylvestre Lacour
Friday afternoon, Sept. 27$^{th}$

*Improving the performances of current optical interferometers & future designs*
*Proceedings of Haute Provence Observatory Colloquium (23-27 September 2013)*
*Edited by L. Arnold, H. Le Coroller & J. Surdej*

# An image reconstruction framework for polychromatic interferometry

F. Soulez, É. Thiébaut

*Centre de Recherche Astrophysique de Lyon, 9 avenue Charles André, 69561 Saint Genis Laval cedex, France; Université de Lyon; Université Lyon 1; CNRS, UMR 5574; École Normale Supérieure de Lyon*

**Abstract.** We describe a new approach to implement multi-wavelength image reconstruction in the case where the observed scene is a collection of point-like sources. We show the gain in image quality (both spatially and spectrally) achieved by globally taking into account all the data instead of dealing with independent spectral slices. This is achieved thanks to a regularization which favors spatial sparsity and spectral grouping of the sources. Since the objective function is not differentiable, we had to develop a specialized optimization algorithm.

## 1. Introduction

Optical interferometers provide multiple wavelength measurements. In order to fully exploit the spectral and spatial resolution of these instruments, new algorithms for image reconstruction have to be developed. Early attempts to deal with multi-chromatic interferometric data have consisted in recovering a gray image of the object or independent monochromatic images in some spectral bandwidths. The main challenge is now to recover the full 3-D (spatio-spectral) brightness distribution of the astronomical target given all the available data.

## 2. Direct model

The complex visibility measured at the wavelength $\ell$ and for the baseline $b$ can be discomposed in a real $m_{b,\ell,0}$ and a imaginary part $m_{b,\ell,1}$ that can be modeled as:

$$m_{b,\ell,c} \approx \sum_{n} H_{b,c,n,\ell}\, x_{n,\ell}\,. \tag{1}$$

where $x_{n,\ell}$ is the value of the pixel $n$ in the spectral channel $\ell$. The operator $\mathbf{H}$ is separable along the spectral dimension:

$$\begin{aligned} H_{b,0,n,\ell} &= +\cos(\boldsymbol{\theta}_n^\top \cdot \boldsymbol{B}_b/\lambda_\ell)\,, & (2)\\ H_{b,1,n,\ell} &= -\sin(\boldsymbol{\theta}_n^\top \cdot \boldsymbol{B}_b/\lambda_\ell)\,, & (3)\end{aligned}$$

where $\boldsymbol{B}_b$ is the $b$th baseline, and $\boldsymbol{\theta}_n$ the position of the $n^{\text{th}}$ pixel. As the problem size can be hudge, we use a fast approximation of $\mathbf{H}$ based on the non uniform fast Fourier transform (Keiner et al. 2009). In this approximation $\mathbf{H}$ has the following structure:

$$\mathbf{H} = \mathbf{R} \cdot \mathbf{F} \cdot \mathbf{S} \tag{4}$$

where $\mathbf{F}$ is the discrete Fourier transform computed by the mean of the fast Fourier transform, $\mathbf{R}$ interpolate the gridded spatial frequencies computed by the DFT to the observed spatial frequencies. $\mathbf{S}$ is an operator that precompensates the convolution by the interpolation kernel used in $\mathbf{R}$.

## 3. Inverse problem framework

To solve this problem of hyperspectral image reconstruction, we follow an *inverse problem* approach where the image is estimated according to the measurements, its noise and some priors about the observed object. It can be written as a constrained optimization problem:

$$\boldsymbol{x}^{+} = \underset{\boldsymbol{x}\in\mathbb{X}}{\arg\min}\, f_{\mathsf{prior}}(\boldsymbol{x}) \quad \text{s.c.} \left\{ \begin{array}{l} f_{\mathsf{data}}(\boldsymbol{x}) \leq \eta_1 \\ \mathbf{P}\cdot\boldsymbol{x} = \mathbf{1} \end{array} \right. \tag{5}$$

where

- $\boldsymbol{x} \in \mathbb{X}$ is the vector of parameters in the image domain. It is angularly sampled by $\boldsymbol{\theta}_n \in \mathbb{A}$ and spectraly sampled in $\lambda_\ell \in \mathbb{L}$
- $\mathbb{X}$ is the subspace of $\mathbb{R}^{\mathrm{Card}(\boldsymbol{m})+}$ where lie the positive object parameters $\boldsymbol{x}$,
- $\boldsymbol{m} \in \mathbb{R}^{\mathrm{Card}(\boldsymbol{m})}$ is the vector of complex visibility,
- $f_{\mathsf{data}}(\boldsymbol{x})$ is the likelihood term ensuring the agreement between parameters $\boldsymbol{x}$ and measurements $\boldsymbol{m}$.
- $\mathbf{P}\cdot\boldsymbol{x} = \mathbf{1}$ is the spatial normalization constraint with the spatial integration operator $\mathbf{P}$,
- $f_{\mathsf{prior}}(\boldsymbol{x})$ is a regularization function that enforces some priors.

### 3.1 Likelihood

The likelihood or data fidelity function $f_{\mathsf{data}}(\boldsymbol{x})$ is built according to the direct model and the noise statistics. If the noise is Gaussian, this function is a weighted least square function:

$$f_{\mathsf{data}}(\boldsymbol{x}) = (\mathbf{H}\cdot\boldsymbol{x} - \boldsymbol{y})^{\top}\, \mathbf{C}^{-1}\, (\mathbf{H}\cdot\boldsymbol{x} - \boldsymbol{y}) \;, \tag{6}$$

where $\mathbf{C}$ is the noise covariance matrix. Complex visibilities are mutually independant and only real and complex parts of the same visibility are correlated. Thus, we can write:

$$f_{\mathsf{data}}(\boldsymbol{x}) = \sum_{b,\ell,n} (\mathbf{H}_{b,n,\ell}\cdot\boldsymbol{x}_{n,\ell} - \boldsymbol{m}_{b,\ell})^{\top}\, \mathbf{C}_{b,\ell}^{-1}\, (\mathbf{H}_{b,n,\ell}\cdot\boldsymbol{x}_{n,\ell} - \boldsymbol{m}_{b,\ell}) \;, \tag{7}$$

where $\mathbf{C}_{b,\ell}$ is the $2\times 2$ covariance matrix associated with the measured complex visibility $\boldsymbol{m}_{b,\ell}$.

### 3.2 Regularization

In interferometry, the normalization occurring in the visibility estimation process naturally leads to a strict normalization prior. The parameters space $\mathbb{X}$ is then the subspace where:

$$\boldsymbol{x} \in \mathbb{X} \equiv \begin{cases} \boldsymbol{x} & \geq 0 \\ \sum_n x_{n,\ell} & = 1\,. \end{cases} \tag{8}$$

More specifically, the main scientific goal of the VLTI GRAVITY instrument is to follow stars in the vicinity of the galactic center. At such a distance, those stars are not resolved by the VLTI baselines and there are only few point-like sources in the instrument field of view. Hence non-negativity and spatial sparsity seem to be adapted priors as this will favor having as few as possible bright point-like sources to explain data. In addition, imposing some spectral continuity while favoring spatial sparsity, structured sparsity is an very well adapted prior for such objects. As we have already shown in integral field spectrography (Soulez et al. 2011) or in optical interferometry (Thiébaut et al. 2013), the structured sparsity prior can be enforced by the mean of mixed norms (Fornasier & Rauhut 2008, Kowalski 2009). In hyperspectral case, it writes:

$$f_{\mathsf{prior}}(\boldsymbol{x}) = \sum\nolimits_n \left(\sum\nolimits_\ell x_{n,\ell}^2\right)^{1/2}\,. \tag{9}$$

with $n$ the spatial index (pixel) and $\ell$ the spectral channel. The fact that such a regularization favors spatial sparsity and spectral grouping is a consequence of the triangular inequality (Fornasier & Rauhut 2008).

## 4. Algorithm

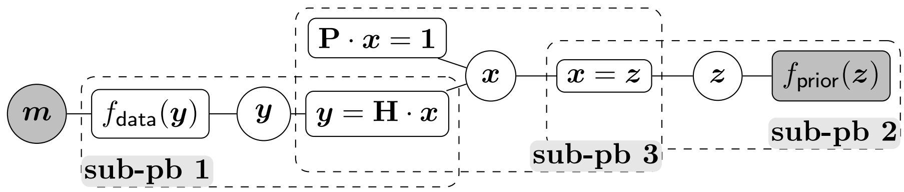


Figure 1.: *Structure of the MiRA3D algorithm*

We propose to solve the image reconstruction problem using an *Alternating Direction of Multipliers Method* (ADMM) (Boyd et al. 2010). Following ADMM strategy, we introduce auxiliary variables $\boldsymbol{y}$ and $\boldsymbol{z}$ to split the complexity of the original problem Eq. (5) which we recast as:

$$\min_{\boldsymbol{x}\geq 0, \boldsymbol{y}, \boldsymbol{z}} \mu\, f_{\mathsf{prior}}(\boldsymbol{z}) + f_{\mathsf{data}}(\boldsymbol{y}) \text{s.t.} \begin{cases} \mathbf{H}\cdot\boldsymbol{x} & = \boldsymbol{y}\,, \\ \boldsymbol{x} & = \boldsymbol{z}\,, \\ \mathbf{P}\cdot\boldsymbol{x} & = \mathbf{1}\,, \\ \boldsymbol{x} & \geq 0\,. \end{cases} \tag{10}$$

Equality constraints can be enforced by means of the augmented Lagrangian which, for Eq. (10), writes:

$$\begin{aligned}\mathcal{L}_\rho(\boldsymbol{x},\boldsymbol{y},\boldsymbol{z},\boldsymbol{u},\boldsymbol{v},\boldsymbol{w}) = {} & f_{\mathsf{data}}(\boldsymbol{y}) + \mu\, f_{\mathsf{prior}}(\boldsymbol{z}) \\ & + \boldsymbol{u}^\top\!\cdot(\mathbf{H}\cdot\boldsymbol{x}-\boldsymbol{y}) + \frac{\rho_1}{2}\,\|\mathbf{H}\cdot\boldsymbol{x}-\boldsymbol{y}\|_2^2 \\ & + \boldsymbol{v}^\top\!\cdot(\boldsymbol{x}-\boldsymbol{z}) + \frac{\rho_2}{2}\,\|\boldsymbol{x}-\boldsymbol{z}\|_2^2\,, \\ & + \boldsymbol{w}^\top\!\cdot(\mathbf{P}\cdot\boldsymbol{x}-\mathbf{1}) + \frac{\rho_3}{2}\,\|\mathbf{P}\cdot\boldsymbol{x}-\mathbf{1}\|_2^2\,, \end{aligned} \tag{11}$$

where $\boldsymbol{u}$, $\boldsymbol{v}$ and $\boldsymbol{w}$ are Lagrangian parameters associated with the constraints $\boldsymbol{y}=\mathbf{H}\cdot\boldsymbol{x}$, $\boldsymbol{x}=\boldsymbol{z}$ and $\mathbf{P}\cdot\boldsymbol{x}=\mathbf{1}$ respectively. $\rho_1>0$, $\rho_2>0$ and $\rho_3>0$ are quadratic weights.

The ADMM consists on minimizing the augmented lagrangian $\mathcal{L}_\rho(\boldsymbol{x},\boldsymbol{y},\boldsymbol{z},\boldsymbol{u},\boldsymbol{v})$ in an alternating manner with respect to each variable $\boldsymbol{x}$, $\boldsymbol{y}$ and $\boldsymbol{z}$ and then updating Lagrangian multipliers $\boldsymbol{u}$, $\boldsymbol{v}$ and $\boldsymbol{w}$:

**Algorithm:** *Solving the problem (10) using ADMM*

Initialization of the object parameters $\boldsymbol{x}^{(0)}$, Lagrangian parameters $\boldsymbol{u}^{(0)}$, $\boldsymbol{v}^{(0)}$ and $\boldsymbol{w}^{(0)}$ and weight $\rho_1$, $\rho_2$ and $\rho_3$. Then set $t=1$ and repeat until convergence:

**Sub-pb 1**: updating $\boldsymbol{y}$:

$$\begin{aligned}\boldsymbol{y}^{(t)} &= \arg\min_{\boldsymbol{y}} \mathcal{L}\big(\boldsymbol{x}^{(t-1)},\boldsymbol{y},\boldsymbol{z}^{(t-1)},\boldsymbol{u}^{(t-1)},\boldsymbol{v}^{(t-1)},\boldsymbol{w}^{(t-1)}\big) \\ &= \arg\min_{\boldsymbol{y}} \Big\{ f_{\mathsf{data}}(\boldsymbol{y}) + \frac{\rho_1}{2}\,\Big\|\boldsymbol{y}-\widetilde{\boldsymbol{y}}^{(t)}\Big\|_2^2 \Big\}\end{aligned} \tag{12}$$

with:

$$\widetilde{\boldsymbol{y}}^{(t)} = \mathbf{H}\cdot\boldsymbol{x}^{(t-1)} + \boldsymbol{u}^{(t-1)}/\rho_1\,; \tag{13}$$

**Sub-pb 2**: updating $\boldsymbol{z}$:

$$\begin{aligned}\boldsymbol{z}^{(t)} &= \arg\min_{\boldsymbol{z}} \mathcal{L}\big(\boldsymbol{y}^{(t)},\boldsymbol{x}^{(t-1)},\boldsymbol{z},\boldsymbol{u}^{(t-1)},\boldsymbol{v}^{(t-1)},\boldsymbol{w}^{(t-1)}\big) \\ &= \arg\min_{\boldsymbol{z}} \Big\{ \mu f_{\mathsf{prior}}(\boldsymbol{z}) + \frac{\rho_2}{2}\,\Big\|\boldsymbol{z}-\widetilde{\boldsymbol{z}}^{(t)}\Big\|_2^2 \Big\}\end{aligned} \tag{14}$$

with:

$$\widetilde{\boldsymbol{z}}^{(t)} = \boldsymbol{x}^{(t-1)} + \boldsymbol{v}^{(t-1)}/\rho_2\,; \tag{15}$$

**Sub-pb 3**: updating $\boldsymbol{x}$:

$$\begin{aligned}\boldsymbol{x}^{(t)} &= \arg\min_{\boldsymbol{x}\ge 0} \mathcal{L}\big(\boldsymbol{x},\boldsymbol{y}^{(t)},\boldsymbol{z}^{(t)},\boldsymbol{u}^{(t-1)},\boldsymbol{v}^{(t-1)},\boldsymbol{w}^{(t-1)}\big) \\ &= \arg\min_{\boldsymbol{x}\ge 0} \Big\{ \frac{\rho_1}{2}\,\Big\|\mathbf{H}\cdot\boldsymbol{x}-\widetilde{\boldsymbol{\gamma}}^{(t)}\Big\|_2^2 + \frac{\rho_2}{2}\,\Big\|\boldsymbol{x}-\widetilde{\boldsymbol{x}}^{(t)}\Big\|^2 + \frac{\rho_3}{2}\,\Big\|\mathbf{P}\cdot\boldsymbol{x}-\widetilde{\boldsymbol{\beta}}^{(t)}\Big\|_2^2 \Big\}\end{aligned} \tag{16}$$

avec:

$$\widetilde{\gamma}^{(t)} = \boldsymbol{y}^{(t)} - \boldsymbol{u}^{(t-1)}/\rho_1\,; \tag{17}$$

$$\widetilde{\boldsymbol{x}}^{(t)} = \boldsymbol{z}^{(t)} - \boldsymbol{v}^{(t-1)}/\rho_2\,; \tag{18}$$

$$\widetilde{\boldsymbol{\beta}}^{(t)} = \mathbf{1} - \boldsymbol{w}^{(t-1)}/\rho_3\,; \tag{19}$$

**4:** updating multipliers $\boldsymbol{u}$, $\boldsymbol{v}$ and $\boldsymbol{w}$:

$$\boldsymbol{u}^{(t)} = \boldsymbol{u}^{(t-1)} + \rho_1 \left(\mathbf{H}\cdot\boldsymbol{x}^{(t)} - \boldsymbol{y}^{(t)}\right)\,, \tag{20}$$

$$\boldsymbol{v}^{(t)} = \boldsymbol{v}^{(t-1)} + \rho_2 \left(\boldsymbol{x}^{(t)} - \boldsymbol{z}^{(t)}\right)\,. \tag{21}$$

$$\boldsymbol{w}^{(t)} = \boldsymbol{w}^{(t-1)} + \rho_3 \left(\boldsymbol{x}^{(t)} - \mathbf{1}\right)\,. \tag{22}$$

This algorithm is illustrated by the schema Fig. 1. It splits the global minimization problem (Eq. (5)) in three successive simpler sub-problems Eq. (12), Eq. (14) and Eq. (16).

### 4.1 Sub-problem 1:

The sub-problem 1 defined by Eq. (12) is a denoising problem with Gaussian prior which have an analytical closed form solution. As complex visibilites are independant it is separable and consist on solving several $2 \times 2$ linear systems:

$$\boldsymbol{y}_{b,\ell}^{(t)} = \left(\mathbf{C}_{b,\ell}^{-1} + \rho_1 \mathbf{I}\right)^{-1} \cdot \left(\mathbf{C}_{b,\ell}^{-1}\cdot\boldsymbol{m}_{b,\ell} + \rho_1 \widetilde{\boldsymbol{y}}_{b,\ell}^{(t)}\right)\,, \tag{23}$$

### 4.2 Sub-problem 2

The sub-problem 2 defined by Eq. (14) is a denoising problem under a group sparsity priors (Thiébaut et al. 2013). For each spectrum, it can be solved independantly applying its so called "proximity operator" (Combettes & Pesquet 2011):

$$\operatorname{prox}_{\alpha f}(\widetilde{\boldsymbol{z}}) \stackrel{\text{def}}{=} \operatorname*{arg\,min}_{\boldsymbol{z}\in\mathbb{R}^{\mathbb{N}}} \left\{\alpha\, f(\boldsymbol{z}) + \frac{1}{2}\,\|\boldsymbol{z} - \widetilde{\boldsymbol{z}}\|_2^2\right\}\,. \tag{24}$$

which is in the case of group sparsity

$$\operatorname{prox}_{\alpha f_{\mathsf{joint}}}(\widetilde{\boldsymbol{z}})_{n,\ell} = \begin{cases} \left(1 - \dfrac{\alpha}{\widetilde{\beta}_n}\right) \widetilde{z}_{n,\ell} & \text{if } \widetilde{\beta}_n > \alpha\,; \\ 0 & \text{else} \end{cases} \tag{25}$$

with $\widetilde{\beta}_n \stackrel{\text{def}}{=} \left(\sum_\ell \widetilde{\boldsymbol{z}}_{n,\ell}^2\right)^{1/2}$ and $\alpha = \mu/\rho_2$.

### 4.3 Sub problem 3

The sub-problem 3 defined Eq. (16) is not separable and does not have a closed form solution. However it is a classical quadratic problem under positivity constraint. We solve it by the mean of the VMLMB algorithm (Thiébaut 2002) that can account for bounds. From the Eckstein-Bertsekas theorem (Eckstein & Bertsekas 1992), it is not necessary to solve this sub-problem exactly to ensure global convergence as long as error on $\boldsymbol{z}$ can be absolutely summed. In practice less than a dozen of iteration is necessary.

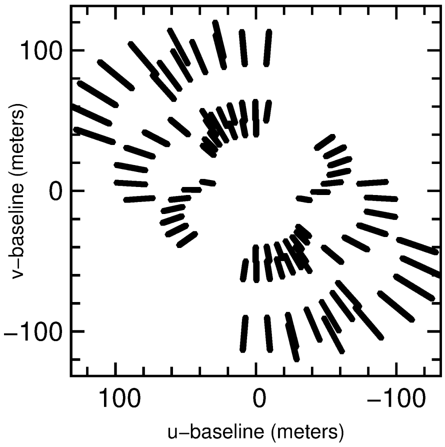


Figure 2.: $(u, v)$ *coverage*

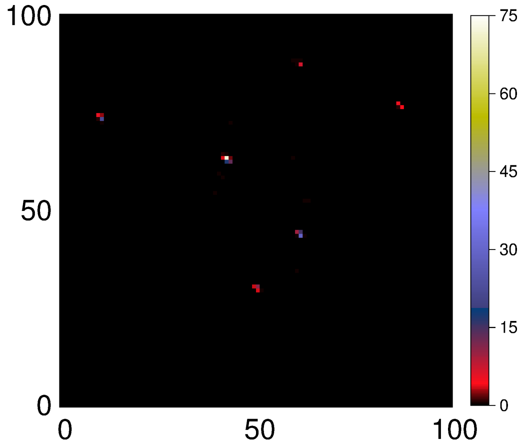


Figure 3.: *Reconstructed image (spectraly integrated)*

## 5. Results

We have tested our method on GRAVITY simulation. It consists on six unresolved stars with different spectra observed by the 4 UTs with 240 spectral channels from 1.95 $\mu$m to 2.45 $\mu$m and 42 baselines (about 10080 complex visibilities). $(u, v)$ coverage is presented Fig. 2.

We reconstruct an hyperspectral image with 240 spectral channels and $100 \times 100$ pixels of size $1 \times 1$ mas. The reconstructed image spectraly integrated in the K band is shown Fig. 3. The six star are recovered and there is not any false detection. The shape of reconstructed star is due to the beam and its centroide indicated its position with an error lower than 0.15 mas. The 6 reconstructed spectra presented in Fig. 4 are very close to the theoretical spectra.

*Acknowledgements.* The authors thank Thibaut Paumard who kindly provides the GRAVITY simulated data. Our algorithm has been implemented and tested with YORICK (`http://yorick.sourceforge.net/`) which is freely available. This work is supported by the POLCA project (*Percées astrophysiques grâce au traitement de données interférométriques polychromatiques* funded by the French ANR: ANR-10-BLAN-0511).

## References

S. Boyd, N. Parikh, E. Chu, B. Peleato, and J. Eckstein. Distributed optimization and statistical learning via the alternating direction method of multipliers. *Foundations and Trends in Machine Learning*, 3:1-122, 2010. doi: 10.1561/2200000016. URL `http://www.stanford.edu/~boyd/papers/pdf/admm_distr_stats.pdf`.

P. L. Combettes and J.-C. Pesquet. *Proximal splitting methods in signal processing*, chapter Fixed-Point Algorithms for Inverse Problems in Science and Engineering, pages 185-212. Springer, New York, 2011.

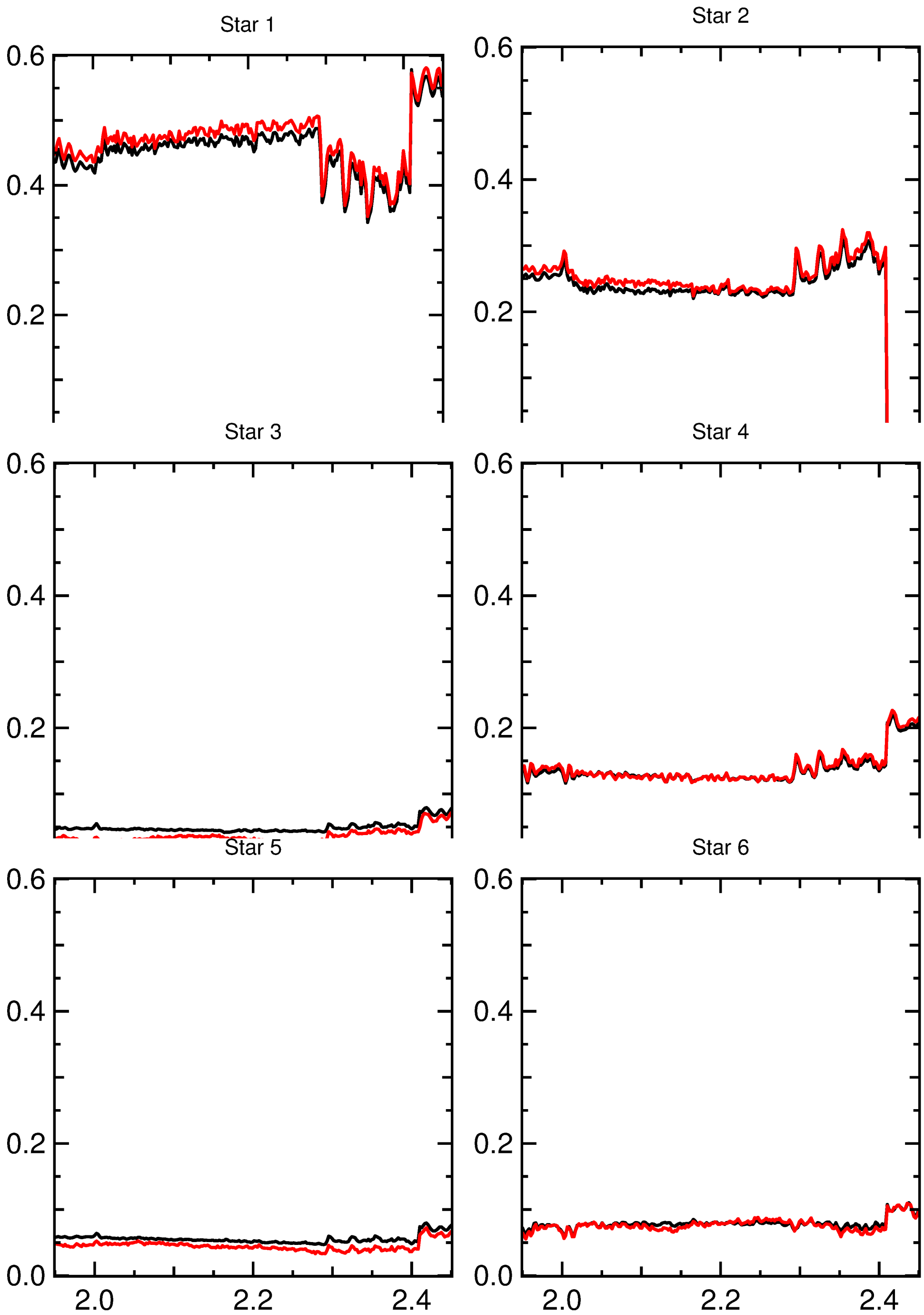


Figure 4.: *Estimated (in black) and theoretical (in red) spectra for the 6 stars.*

J. Eckstein and D. Bertsekas. On the Douglas-Rachford splitting method and the proximal point algorithm for maximal monotone operators. *Mathematical Programming*, 55(1):293-318, 1992.

M. Fornasier and H. Rauhut. Recovery algorithms for vector valued data with joint sparsity constraints. *SIAM Journal on Numerical Analysis*, 46 (2):577-613, 2008.

J. Keiner, S. Kunis, and D. Potts. Using nfft 3-a software library for various nonequispaced fast fourier transforms. *ACM Transactions on Mathematical Software (TOMS)*, 36(4):19, 2009.

M. Kowalski. Sparse regression using mixed norms. *Applied and Computational Harmonic Analysis*, 27(3):303-324, 2009. ISSN 1063-5203. doi: 10.1016/j.acha.2009.05.006. URL `http://www.sciencedirect.com/science/article/pii/S1063520309000608`.

F. Soulez, É. Thiébaut, S. Bongard, and R. Bacon. Restoration of hyperspectral astronomical data from integral field spectrograph. In *3rd Workshop on Hyperspectral Image and Signal Processing (WHISPERS)*, Lisbon, Portugal, 2011. URL `http://core.ieee-whispers.com/`.

É. Thiébaut. Optimization issues in blind deconvolution algorithms. In J.-L. Starck and F. D. Murtagh, editors, *Astronomical Data Analysis II*, volume 4847, pages 174-183, Bellingham, Washington, 2002. SPIE. doi: 10.1117/12.461151.

É. Thiébaut, F. Soulez, and L. Denis. Exploiting spatial sparsity for multiwavelength imaging in optical interferometry. *Journal of the Optical Society of America A*, 30(2):160-170, Feb. 2013.
URL `http://hal.archives-ouvertes.fr/hal-00771800`.

*Improving the performances of current optical interferometers & future designs*
*Proceedings of Haute Provence Observatory Colloquium (23-27 September 2013)*
*Edited by L. Arnold, H. Le Coroller & J. Surdej*

# Imaging Young Stellar Objects with VLTi/PIONIER

J. Kluska[1], F. Malbet[1], J.-P. Berger[2], M. Benisty[1], B. Lazareff[1], J.-B. Le Bouquin[1], F. Baron[3], C. Dominik[4], A. Isella[5], A. Juhasz[6], S. Kraus[7], R. Lachaume[8], F. Ménard[1,9], R. Millan-Gabet[5], J. Monnier[10], C. Pinte[9], F. Soulez[11], M. Tallon[11], W.-F. Thi[1], E. Thiébaut[11] & G. Zins[1]

[1] *UJF-Grenoble 1 / CNRS-INSU, Institut de Planétologie et d'Astrophysique de Grenoble (IPAG) UMR 5274, Grenoble, F-38041, France*

[2] *ESO, Garching, Germany*

[3] *Georgia State University, Atlanta, USA*

[4] *University of Amsterdam, Amsterdam, The Netherlands*

[5] *California Institute of Technology, Pasadena, USA*

[6] *Leiden Observatory, Leiden, The Nertherlands*

[7] *University of Exeter, UK*

[8] *Pontificia Universidad Católica de Chile. Santiago de Chile, Chile*

[9] *UMI-FCA, CNRS y U. de Chile, Chile*

[10] *University of Michigan, Ann Arbor, USA*

[11] *Université de Lyon I, Lyon, France*

**Abstract.** Optical interferometry imaging is designed to help us to reveal complex astronomical sources without a prior model. Among these complex objects are the young stars and their environments, which have a typical morphology with a point-like source, surrounded by circumstellar material with unknown morphology. To image them, we have developed a numerical method that removes completely the stellar point source and reconstructs the rest of the image, using the differences in the spectral behavior between the star and its circumstellar material. We aim to reveal the first Astronomical Units of these objects where many physical phenomena could interplay: the

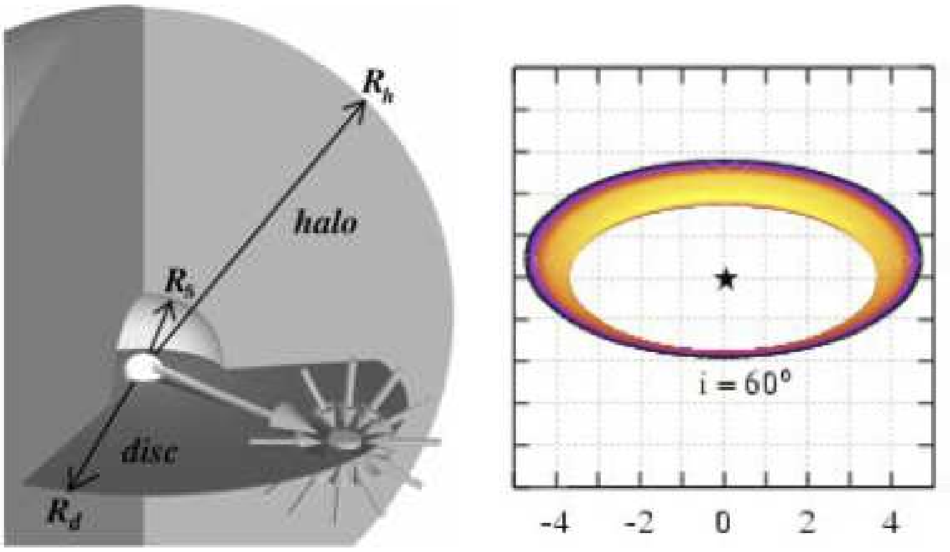


Figure 1.: *Left : Plot from Vinkovic et al. (2003) showing the halo scenario. Right : The puffed-up inner rim scenario proposed by Isella & Natta (2005).*

dust sublimation causing a puffed-up inner rim, a dusty halo, a dusty wind or an inner gaseous component. To investigate more deeply these regions, we carried out the first Large Program survey of HAeBe stars with two main goals: statistics on the geometry of these objects at the first astronomical unit scale and imaging their very close environment. The images reveal the environment, which is not polluted by the star and allows us to derive the best fit for the flux ratio and the spectral slope. We present the first images from this survey and the application of the imaging method on other astronomical objects.

## 1. Introduction

Direct imaging techniques have revealed complex structures around young stellar objects (e.g. Rameau et al. 2013) such as spirals, holes, etc. These features are the consequence of phenomena occurring more closer to the star, like planetary formation. To reach these regions we need more angular resolution. This is where optical interferometry is entering the game.

### 1.1 The inner regions of Young Stellar Objects (YSO).

The inner parts of the Young Stellar Objects are the place of many physical processes. In the near infrared, one of the most contributing phenomena (in the broad band) is the dust sublimation. Dust sublimates at 1500K which is the temperature of the dust at approximately 1 AU of its host star (for Herbig stars). It creates an excess emission in the near infrared but is not well constrain geometrically. Vinkovic et al. (2003) proposed a halo model to explain the excess

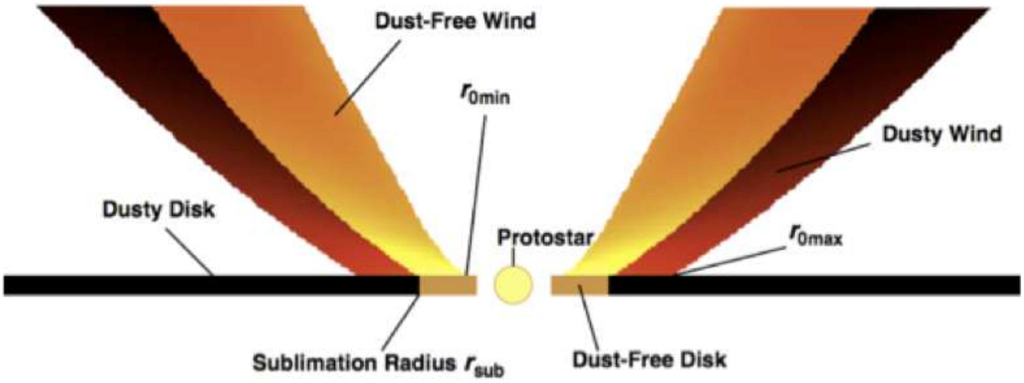


Figure 2.: *The disk wind solution proposed by Bans & Königl (2012).*

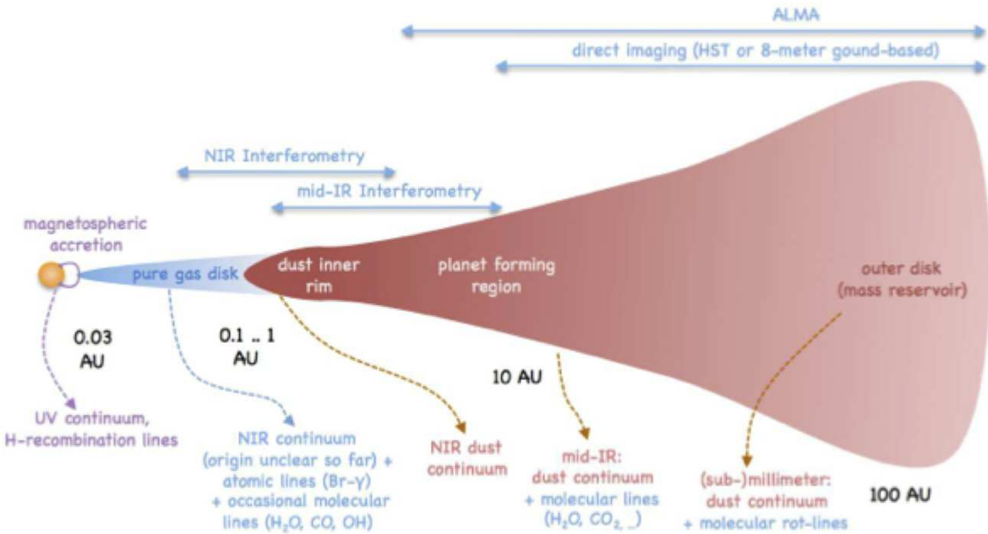


Figure 3.: *This is the sketch from Dullemond & Monnier (2010) of the inner regions of young stellar objects where we expect to see the dust sublimation region, an inner accretion disk and constrain the planetary formation.*

emission in the near infrared and Isella & Natta (2005) proposed a model of a puffed-up inner rim due to dust sublimation (see Fig. 1). More recently, Bans & Königl (2012) published a wind scenario to explain this excess and said that optical interferometry is the tool to distinguish between the scenarios (see Fig. 2).

In addition to dust sublimation, gas could create an accretion disk inside the dust sublimation radius and cause magneto-spheric accretion onto the star. Planetary formation could also perturb the inner rim. We can also expect mass ejection through wind and/or jets that are believed to originate in this inner region. A schematic view is displayed in Fig. 3.

In order to study this complex inner regions and being model independent, we want to make image reconstruction from optical interferometry data.

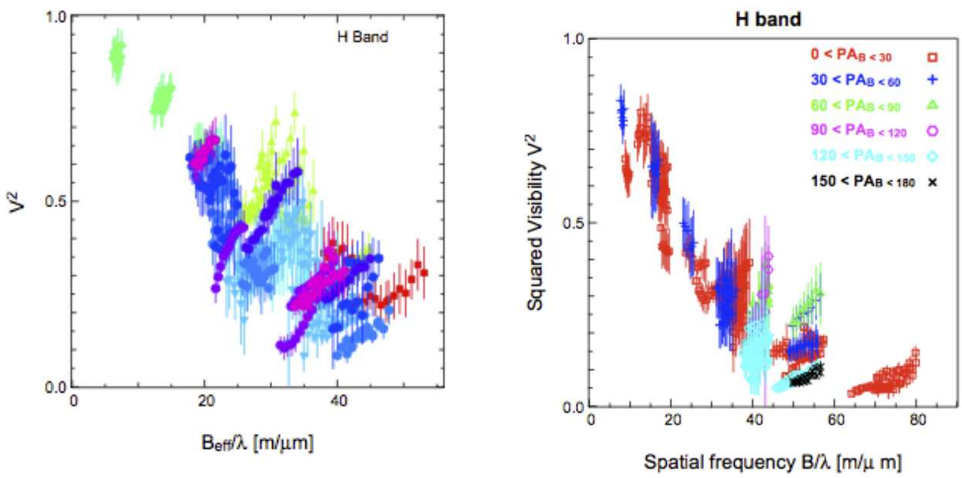


Figure 4.: *Datasets on YSOs obtained with AMBER. HR5999 data is from Benisty et al. (2011) and HD163296 data from Renard et al. (2010). We can clearly see the chromatic effect.*

### 1.2 YSO and chromatism

First reconstructed images of Young Stellar Objects (YSOs) have already been made. For instance Benisty et al. (2011) made an image of HR5999 and Renard et al. (2010) an image of HD163296. These images were obtain with monochromatic image reconstruction algorithms. As we can see on the visibility curves, there is a strong chromatic effect in particular in the $H$-band (see Fig. 4). The longest wavelengths have clearly lower visibilities than the shortest ones. It is an astrophysical effect.

Kluska et al. (2012) showed that if we are in a presence of an unresolved star which is in the Rayleigh-Jeans regime and a resolved environment which is cold ($\approx$ 1500K) we will have such an effect. In the near infrared, the young stellar objects SED is shared between the stellar photosphere flux and the environment one. The changing flux ratio between a resolved environment and a point source creates the chromatic effect seen in the squared visibilities seen in both AMBER (Petrov et al. 2007) and PIONIER (Le Bouquin et al. 2011) data.

## 2. Chromatic method to reconstruct on object

The monochromatic image reconstruction algorithms are not adapted anymore for such a chromaticity. To face this problem two approaches exist. The first one is a three dimensional approach that consists in reconstructing a spectral cube of images adding a trans-spectral regularization term (see Soulez et al.). Another approach, which will be presented here, is the Semi-Parametric Approach for image Reconstruction of Chromatic Objects (SPARCO : Kluska et al. 2014).

### 2.1 Flux parametrization

The chromatic effect needs to be taken into account in a chromatic algorithm. That is why we need to define the flux evolution of both the photosphere and the

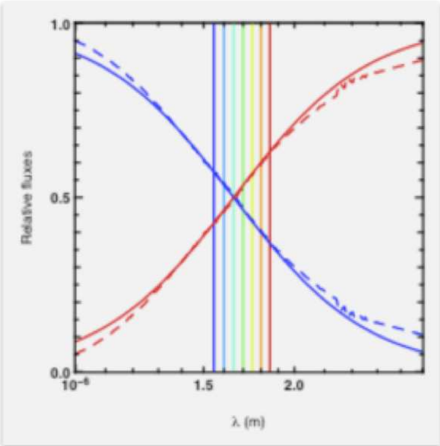


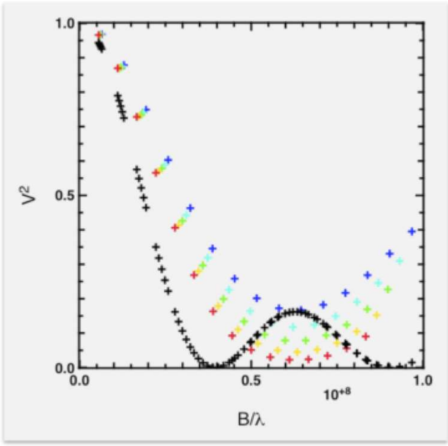


Figure 5.: *Left : fluxes versus wavelength across the H-band. In blue : flux of the photosphere. In red : the flux of the environment. In solid lines : the fluxes defined by Eq. 1. In dashed line : fluxes defined by a photosphere + environment model. Vertical color lines : PIONIER spectral channels. Right : squared visibilities from a ring alone (black) and a ring with a star (color).*

environment. As written in Sect.1.2, the photosphere is in the Rayleigh-Jeans regime and have its flux $F_\lambda \propto \lambda^{-4}$ (or a spectral index of $-4$). The environment flux could also be described as a power-law with a spectral index $d_{\rm env}$ (for 1500K $d_{\rm env} = 0.8$ for $H$-band). To define the total flux we need the fraction of flux of the star $f_*^0$ at $\lambda_0$ (which is an arbitrary chosen wavelength). We can then write the total flux $f_{tot}(\lambda)$ as :

$$f_{tot}(\lambda) = f_*^0 \left(\frac{\lambda}{\lambda_0}\right)^{-4} + (1 - f_*^0) \left(\frac{\lambda}{\lambda_0}\right)^{d_{\rm env}} \qquad (1)$$

where first term is the stellar flux ($f_*(\lambda)$) and the second one is the flux of the environment ($f_{\rm env}$). This flux parametrization is valid in a narrow band such as the $H$-band (see Fig. 5, Left).

### 2.2 Visibility computation

With the fluxes definition, we can compute the total visibilities. To do so we need to set the visibilities for the star and the environment separately. For the photosphere we assume that it is not resolved and its visibility is $V_* = 1$. This assumption is valid considering that a $5R_\odot$ at 140pc (distance of the Taurus star forming region) has a visibility of 0.997 for B=100m in the $H$-band.

The visibility of the environment ($\widetilde{V}_{\rm env}$) will be computed from the image as it is done in monochromatic image reconstruction algorithms. The star is not appearing in the image anymore.

The equation of the total visibility that is fitted to the data is :

$$\widetilde{V}_{\rm tot}\left(\frac{\mathbf{b}}{\lambda}, \lambda\right) = \frac{f_*(\lambda) + f_{\rm env}(\lambda)\widetilde{V}_{\rm env}\left(\frac{\mathbf{b}}{\lambda}\right)}{f_*(\lambda) + f_{\rm env}(\lambda)} \qquad (2)$$

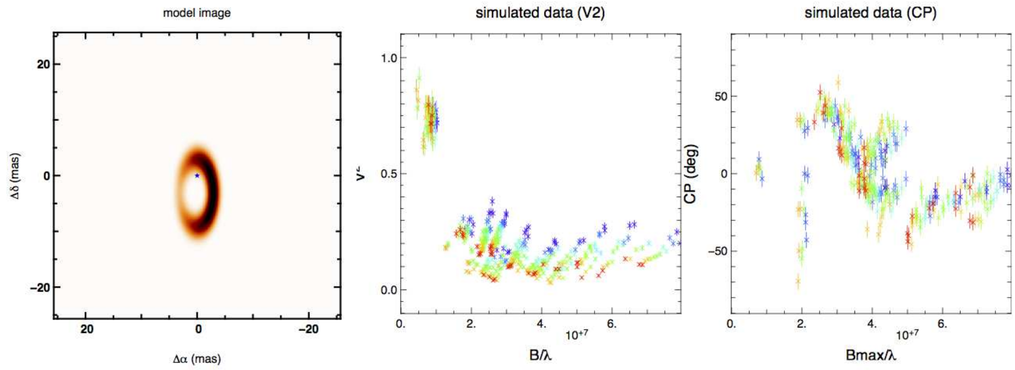


Figure 6.: *Left : The model image. The star is represented with a red star in the middle of the image. The ring is azimuthally modulated and shifted with respect to the star. Center and Right : squared visiblities and closure phases of the model taking a actual $(u, v)$-plan. A gaussian noise was added to this dataset. The colors represent the spectral channels as on the previous figures.*

where $\left(\frac{\mathbf{b}}{\lambda}\right)$ is the spatial frequency (which is the baseline vector divided by the wavelength).

Thanks to the linearity of the Fourier transform we can separate the star from the image of the environment. The algorithm is described more specifically in Kluska et al. (2014). The result of a ring visibility taking into account the chromatic effect i shown Fig. 5 Right.

## 2.3 Validation on a model

The algorithm was tested on a chromatic model of a YSO. It is composed of a star, having 40% of the flux at $1.65\mu$m. The environment is an azimuthally modulated gaussian ring, shifted to the south with respect to the star. The environmental spectral index is set to 1. The model image is showed in Fig. 6. In order to generate a realistic $(u, v)$-plan we have taken an existing one on an object already observed by PIONIER. The $(u, v)$-plan is then not totally optimal. We then generate the squared visibilities ($V^2$) and the closure phases (CP). The whole data set is shown in Fig. 6.

The image reconstructions are shown in Fig. 7. They were performed using the `MiRA` (Thiébaut 2008) algorithm. They were made using three methods :

– An image reconstruction with a monochromatic algorithm. The $\chi^2$ is not satisfactory ($\approx 10$). There are many artifacts in the image due to the chromaticity present in the data.

– An image reconstruction by subtracting the star from the image but without taking into account the chromaticity. The $\chi^2$ is slightly better but the image is still not satisfactory.

– An image reconstruction applying the SPARCO method. This method was tested in both `MiRA` and `MACIM` (Ireland et al. 2006) algorithm with a $\chi^2 = 1.2$. The features of the ring are well retrieved and the artifacts are weak.

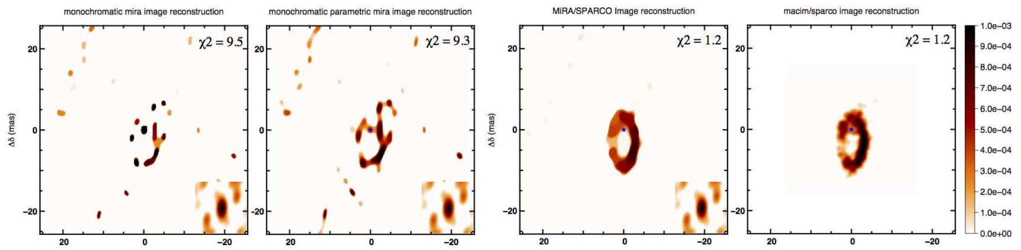


Figure 7.: *Image reconstructions on the model using different methods. Left : classical monochromatic image reconstruction. Center Left : monochromatic image reconstruction subtracting the star. Right : chromatic image reconstruction subtracting the star with* `Mira` *and* `MACIM`*. In the right bottom corner : the dirty beam of the $(u, v)$-plan.*

### 2.4 Chromatic degeneracy

The reconstructions showed in Sect. 2.3 were made setting the chromatic parameters $f_*^0$ and $d_{\mathrm{env}}$ to the right ones (0.4 and 1 respectively).

Without spectrophotometric informations we have no information on these chromatic parameters. What are the effects on the image reconstruction process if the chromatic parameters are wrong ? To test that, we have made a bunch of images that with different values of the chromatic parameters (see Fig. 8). The image with the good parameters is in the center. We have taken a range of spectral indexes for the environment that represent temperatures from 1250K to 1750K (spectral indexes of 2 and 0 respectively). For these temperatures the image does not vary much for a fixed value of the flux ratio. The effects are bigger for the flux ratios. If we put too much flux in the star (50% for instance) the image is filled by artifacts and the ring is dug. But if the stellar to total flux ratio is too low, some flux will be put at the position of the star degrading the quality of the image.

We can also make a $\chi^2$-map of the imager reconstructions in the plan of the chromatic parameters. This map is presented in Fig. 9. We can see there is a smooth valley of $\chi^2$ that indicates a clear degeneracy between the two chromatic parameters. The spectrophotometric data can be used to find the good values of the chromatic parameters.

## 3. Imaging real targets

Once the chromatic image reconstruction method is validated we have applied it on actual datasets. We have conducted a Large Program with the PIONIER instrument on the VLT interferometer. 55 Herbig Ae/Be stars were observed during our 30 nights of observation. A dozen of objects are resolved enough to be imaged. We present images made on two objects in Fig. 10.

These images were obtain by taking the chromatic parameters showing the minimum $\chi^2$ value.

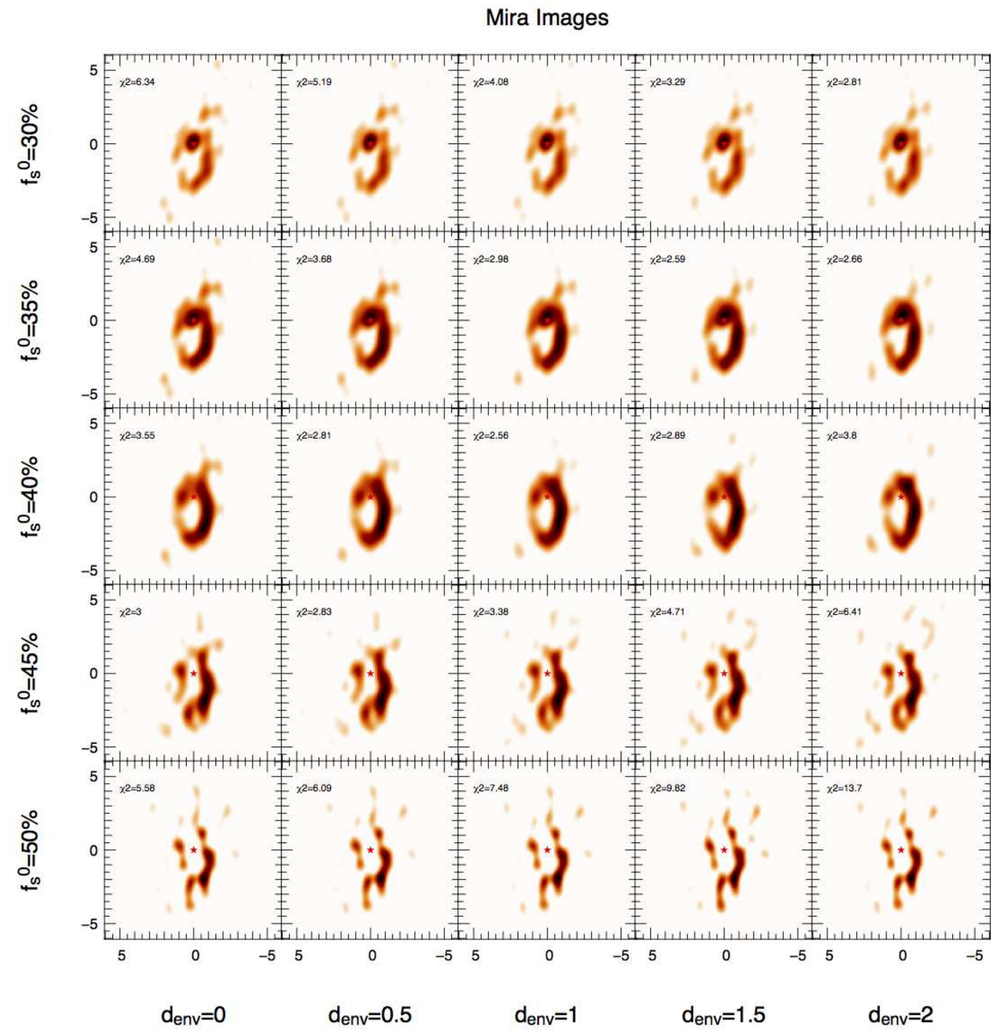


Figure 8.: *The mosaic of chromatic parameters. In the x-axis : the spectral index of the environment ($d_{\rm env}$). In the y-axis : the stellar to total flux ratio ($f_*^0$). The good values are in the center. We can see how an error on a chromatic parameter is affecting the image.*

HD45677 is a Be star which is well resolved for the interferometer. We can clearly see a ring like structure which is brightest in one of his sides. This is most easily interpreted as a inclination effect.

The second object, HD98922, is also a Be star, supposed to be very young. We can clearly see its ring in the image which can be interpreted as the dust sublimation ring.

These images are preliminary and have to be interpreted more precisely. But we can see that the image reconstruction method is able to retrieve a correct brightness distribution of these objects by assuming a correct value for the environment temperature.

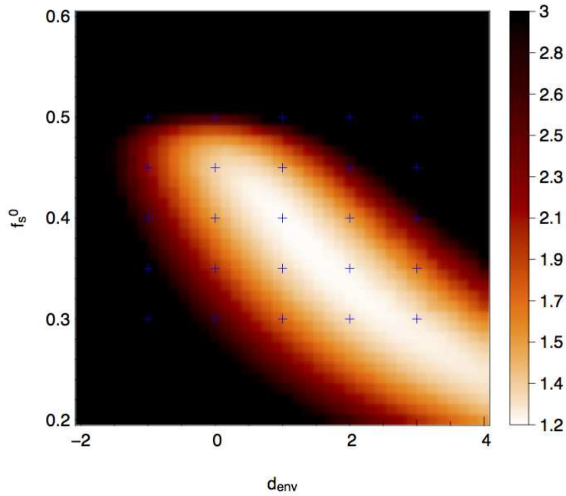


Figure 9.: *The $\chi^2$-map in the space of the chromatic parameters. There is a clear $\chi^2$-valley showing a degeneracy between the two parameters.*

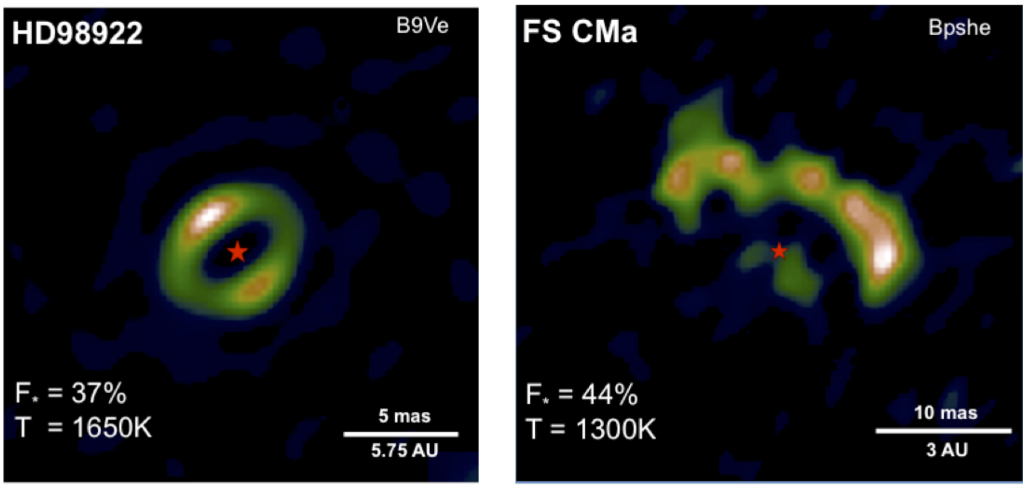


Figure 10.: *Left : an image reconstruction on HD98922. Right : an image reconstruction on HD45677*

## 4. Conclusion

We have presented a new method to perform image reconstructions that takes into account the chromaticity of Young Stellar Objects. To do so it introduces two chromatic parameters that are the stellar to total flux ratio and the spectral index of the environment. This technique is adapted to the case where the flux ratio between the star and its environment is changing across a bandwidth and if it is the main effect.

Nevertheless this method is showing a degeneracy showing a $\chi^2$ valley in the chromatic parameter space. This is why spectro-photometric information is necessary to precisely separate the flux of the star of the environment one and to correctly reconstruct the image.

We showed in the last section the ability of the method to reconstruct images on actual dataset gathered by PIONIER/VLTi on Herbig Ae/Be Stars.

This method can be applied on other astrophysical objects showing a unresolved and a resolved component with different temperatures such as planetary nebulae, AGB stars or Active Galactic Nuclei.

*Acknowledgements.* This work is supported by the French ANR POLCA project (Processing of pOLychromatic interferometriC data for Astrophysics, ANR-10-BLAN-0511).

## References

Bans, A. and Königl, A., 2012, ApJ, 758, 100

Benisty, M., Renard, S., Natta, A., Berger, J.-P., Massi, F., Malbet, F., Garcia, P.-J.-V., Isella, A., Mérand, A., Monin, J.-L., Testi, L., Thiébaut, E., Vannier, M. & Weigelt, G., 2011, A&A, 531, A84

Dullemond, C. P. and Monnier, J. D., 2010, ARA&A, 48, 205

Ireland, M. J., Monnier, J. D. & Thureau, N., 2006, Society of Photo-Optical Instrumentation Engineers (SPIE) Conference Series, 6268, 58

Isella, A. and Natta, A., 2005, A&A, 438, 899

Kluska, J., Malbet, F., Berger, J.-P., Lazareff, B., Le Bouquin, J.-B., Benisty, M., Menard, F., Pinte, C. Millan-Gabet, R., & Traub, W., 2012, Society of Photo-Optical Instrumentation Engineers (SPIE) Conference Series, 8445, 0O

Kluska, J., Malbet, F., Berger, J.-P., Baron, F., Lazareff, B., Le Bouquin, J.-B., Monnier, J. D., Soulez, F. & Thiébaut. E., 2014, A&A, submitted.

Le Bouquin, J.-B., Berger, J.-P., Lazareff, B., Zins, G., Haguenauer, P., Jocou, L., Kern, P., Millan-Gabet, R., Traub, W., Absil, O., Augereau, J.-C., Benisty, M., Blind, N., Bonfils, X., Bourget, P., Delboulbe, A., Feautrier, P., Germain, M. and Gitton, P., Gillier, D., Kiekebusch, M., Kluska, J., Knudstrup, J., Labeye, P., Lizon, J.-L., Monin, J.-L., Magnard, Y., Malbet, F., Maurel, D., Ménard, F., Micallef, M., Michaud, L., Montagnier, G., Morel, S., Moulin, T., Perraut, K., Popovic, D., Rabou, P., Rochat, S., Rojas, C., Roussel, F., Roux, A., Stadler, E., Stefl, S., Tatulli, E. & Ventura, N., 2011, A&A, 535, A67

Petrov, R. G., Malbet, F., Weigelt, G., Antonelli, P., Beckmann, U., Bresson, Y., Chelli, A., Dugué, M., Duvert, G., Gennari, S., Glück, L., Kern, P., Lagarde, S., Le Coarer, E., Lisi, F., Millour, F., Perraut, K., Puget, P., Rantakyrö, F., Robbe-Dubois, S., Roussel, A., Salinari, P., Tatulli, E., Zins, G., Accardo, M., Acke, B., Agabi, K., Altariba, E., Arezki, B., Aristidi, E., Baffa, C., Behrend, J., Blöcker, T., Bonhomme, S., Busoni, S., Cassaing, F., Clausse, J.-M., Colin, J., Connot, C., Delboulbé, A., Domiciano de Souza, A., Driebe, T., Feautrier, P., Ferruzzi, D., Forveille, T., Fossat, E., Foy, R., Fraix-Burnet, D., Gallardo, A., Giani, E., Gil, C., Glentzlin, A., Heiden, M., Heininger, M., Hernandez Utrera, O., Hofmann, K.-H., Kamm, D., Kiekebusch, M., Kraus, S., Le Contel, D., Le

Contel, J.-M., Lesourd, T., Lopez, B., Lopez, M., Magnard, Y., Marconi, A., Mars, G., Martinot-Lagarde, G., Mathias, P., Mège, P., Monin, J.-L., Mouillet, D., Mourard, D., Nussbaum, E., Ohnaka, K., Pacheco, J., Perrier, C., Rabbia, Y., Rebattu, S., Reynaud, F., Richichi, A., Robini, A., Sacchettini, M., Schertl, D., Schöller, M., Solscheid, W., Spang, A., Stee, P., Stefanini, P., Tallon, M., Tallon-Bosc, I., Tasso, D., Testi, L., Vakili, F., von der Lühe, O., Valtier, J.-C., Vannier, M. & Ventura, N., 2007, A&A, 464, 1

Rameau, J., Chauvin, G., Lagrange, A.-M., Thébault, P., Milli, J., Girard, J. H. & Bonnefoy, M., 2012, A&A, 546, A24

Renard, S., Malbet, F., Benisty, M., Thiébaut, E. & Berger, J.-P., 2010, A&A, 519, A26

Thiébaut, E., 2008, Society of Photo-Optical Instrumentation Engineers (SPIE) Conference Series, 7013, 43

Vinković, D., Ivezić, Ž., Miroshnichenko, A. S. & Elitzur, M., 2003, MNRAS, 346, 1151

*Improving the performances of current optical interferometers & future designs*
*Proceedings of Haute Provence Observatory Colloquium (23-27 September 2013)*
*Edited by L. Arnold, H. Le Coroller & J. Surdej*

# Conclusions


Please,
draw me an
interferometer

*Improving the performances of current optical interferometers & future designs*
*Proceedings of Haute Provence Observatory Colloquium (23-27 September 2013)*
*Edited by L. Arnold, H. Le Coroller & J. Surdej*

# Colloquium recommendations: next steps into the future

J. Surdej[1], J.-U. Pott[2]

[1]*Institut d'Astrophysique et de Géophysique, Allée du 6 août, 17, B-4000 Liège 1 (Sart-Tilman), Belgium;*
jsurdej@ulg.ac.be

[2]*Max Planck Institute for Astronomy, Königstuhl 17, 69117 Heidelberg, Germany;*
jpott@mpia.de

**Abstract.** We present an executive summary following the round-table discussion on the Future of Interferometry between members of the EII[1], FIE[2], ASHRA[3], FRINGE[4] and IF[5] working groups organized on 25th September 2013 during the OHP Colloquium *"Improving the performances of current optical interferometers & future designs"*. It was concluded that direct imaging of the planet formation process at AU-scale radii can serve as a versatile science case of broad interest in the astronomical community, which at the same time is sufficiently focussed to help developing the technical roadmap towards the next interferometric facililty. Shortly after the meeting this conclusion was distilled into the *Planet Formation Imager (PFI)* project[6].

A general discussion on the Future of Optical/IR Interferometry has taken place during the OHP Colloquium *"Improving the performances of current optical interferometers & future designs"* organized on 23-27 September 2013 (Saint-Michel l'Observatoire, France) as a continuation of the currently on going community discussions within EII, ASHRA, FRINGE and IF. The round-table participants included: J.-P. Berger, G. van Belle, L. Labadie, H. Le Coroller, J. Monnier, J.-U. Pott, M. Tallon, J. Surdej (chair). Additional participants in the conference room: P. Kern, D. Defrère, G. Duvert, F. Malbet, A. Chelli, F. Martinache, J. Kluska, S. Minardi, D. Buscher, V. Garcia, T. Ten Brummelaar, M. Creech-Eakmann, C. Haniff, M. Ireland, D. Rouan, others.

---

[1]European Interferometry Initiative

[2]Future of Interferometry in Europe

[3]Action Spécifique Haute Résolution Angulaire, France

[4]Frontiers of Interferometry center in Germany

[5]Interferometry Forum

[6]http://www.planetformationimager.org/

It was first reminded that some nine and eight years ago, two European conferences had been organized on the *Science cases for next generation optical/infrared interferometric facilities (the post VLTI era)*[7] and on a *Technology roadmap for future interferometric facilities*.[8]

Amazingly the conclusions of those two conferences established almost 10 years ago are still largely valid today. The urgency of setting up a technology roadmap was already claimed very loudly in 2004. A natural conclusion is of course that it would be totally counter-productive to again carry out a similarly long open-end exercise to define the science goals of a next-generation interferometric facility. Another good reason as to why we should move on is that the optical/IR community has been very active during the past 8 years, establishing several interferometry facility and pathfinder projects. However, most of these pathfinders come to an end, and ELTs are around the corner, probably meaning that if the interferometry community is not settling now on a strong science case for the future, which exploits the unique capabilities of interferometry, the people and groups which are capable of advancing the field will quickly disperse. As a result, the following recommendations were made:

1) In order to establish a credible roadmap for optical/IR interferometry, it was agreed that a very good, unique and common science driver ought to be identified. A very general consensus emerged that the "Planet Formation with a focus on direct observations at AU scale" should be proposed as the main science case. This does not mean that we exclude other important science cases (cf. stellar physics, AGN, ...) but most of us are convinced that a clearly focussed science case will help shaping a good and realistic technology roadmap. Issues that should be very carefully addressed now include: i) to identify the main questions in Planet Formation that can only be tackled by optical/IR interferometry observations, ii) to make sure that the breadth of the science goals matches the significant community funding effort required for any major upgrade / new facility. E.g. the capability to conduct statistically relevant (i.e. sufficiently large) surveys of planet formation at AU scale could play a big role.

2) A white book on the *Future of Interferometry* ought to be ready by 2015, just before the review of the ASTRONET science vision document for the next decades. The perfect complementarity of optical/IR interferometry with respect to other existing and future major facilities (ALMA, JWST, ELTs, SKA, ... ) should be clearly established in that white book. The authors of this article are chairing the writing of this white book, as part of the EII network activities. Interested individuals are encouraged to contact them for further information, or participation (see also the related OLBIN call for participation in fall 2012).

A major consensus at this meeting was that the community effort (including the white book) of the next two years should lead to well established, technically reachable scientific recommendations which should facilitate individual groups to

---

[7]Proceedings of the 37th Liège International Astrophysical Colloquium (23-25 August 2004), Liège University, J. Surdej, D. Caro, A. Detal

[8]Proceedings of the European Interferometry Initiative workshop organized in the context of the 2005 Joint European and National Astronomy meeting 'Distant Worlds' (6-8 July 2005), Liège University, J. Surdej, D. Caro, A. Detal

work towards it by acquiring the respective funding. Current future-oriented interferometric instrumentation research struggles because such a widely accepted goal is missing. If interferometry in the optical near-infrared shall be the technology of choice for a new facility, we need to continue the way to leave the 'nice to have' niche, but establish an *only-optical/IR-interferometry-can-do-this* attitude. The VLTI second generation instrumentation, currently being put in place, and six-telescope imaging efforts at CHARA are right steps in this direction, as evinced by the talk *Science with interferometry* by O. Chesneau at the beginning of this conference.

3) It was discussed that IAU Commission 54 could help organizing a forum meeting on the topics of the Planet Formation Interferometer/Imager (PFI) during the next General Assembly. IAU Commission 54 could also help setting up an ad-hoc international steering committee with additional science and technical working groups in order to define the short term and long term science goals of future facilities addressing as many aspects of Planet Formation as possible and their corresponding top-level requirements (array architecture, size of unit telescopes, operating wavelengths, ...). Similarly, several members of the community committed to discuss the above idea and enlarge the interaction with the wider community at the upcoming SPIE in 2014, Montreal, Canada.

Shortly after the meeting these conclusions were distilled into the foundation of the Planet Formation Imager (PFI) project, please find more related information at:
`http://www.planetformationimager.org/`.

End of Proceedings. OHP, 27 March 2014.

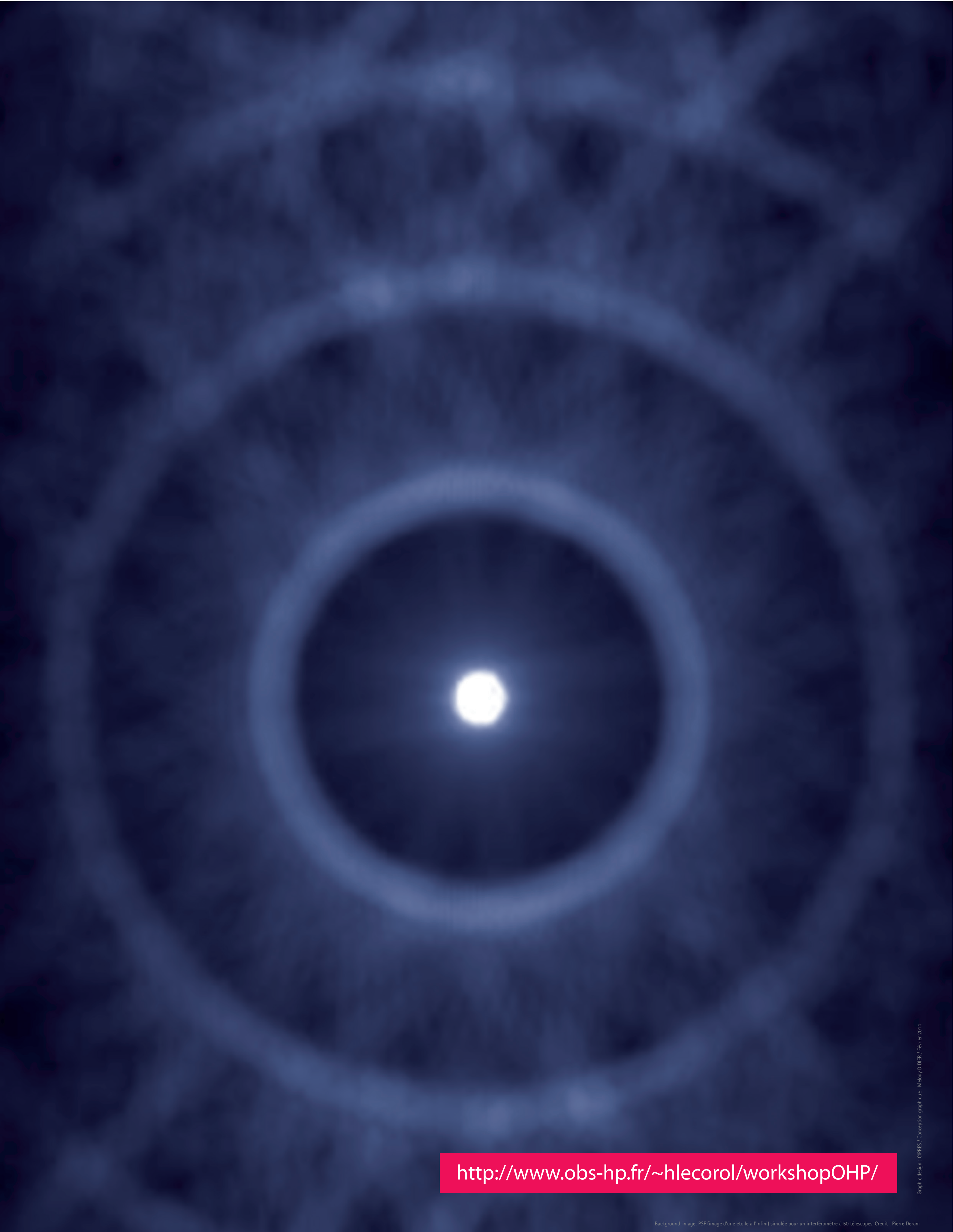

http://www.obs-hp.fr/~hlecorol/workshopOHP/

Graphic design : CIPRES / Conception graphique : Mélody DIDIER / Février 2014

Background-image: PSF (image d'une étoile à l'infini) simulée pour un interféromètre à 50 télescopes. Credit : Pierre Deram

IAU C54 Endorsed